ISSN 2959-0663 (Print)
ISSN 2959-0671 (Online)
ISSN-L 2959-0663

EURASIAN JOURNAL OF CHEMISTRY

2026. Vol. 31 No. 3(123)

ISSN 2959-0663 (Print)
ISSN 2959-0671 (Online)
ISSN-L 2959-0663

EURASIAN JOURNAL OF CHEMISTRY

2026

Volume 31, No. 3 (123)

Founded in 1996

Published 4 times a year

Karaganda
2026

Publisher: **NLC "Karaganda National Research University named after academician Ye.A. Buketov"**
Postal address: 28 University St., Karaganda 100024, Kazakhstan
E-mail: chemistry.vestnik.ksu.kz@gmail.com; ipustolaikina@gmail.com
Tel./fax: +7(7212) 34-19-40.
Web-site: https://ejc.buketov.edu.kz

Editor-in-Chief
Ye.M. Tazhbayev, Doctor of Chemical sciences

Executive Editor
I.A. Pustolaikina, Candidate of Chemical sciences

Editorial board

Z.M. Muldakhmetov,	Academician of NAS RK, Doctor of chem. sciences, Institute of Organic Synthesis and Coal Chemistry of the Republic of Kazakhstan, Karaganda (Kazakhstan);
S.M. Adekenov,	Academician of NAS RK, Doctor of chem. sciences, International Research and Production Holding "Phytochemistry", Karaganda (Kazakhstan);
S.E. Kudaibergenov,	Doctor of chem. sciences, Institute of Polymer Materials and Technologies, Almaty (Kazakhstan);
V.V. Khutoryanskiy,	Professor, University of Reading, Reading (United Kingdom);
Fengyun Ma,	Professor, Xinjiang University, Urumqi (PRC);
Xintai Su,	Professor, South China University of Technology, Guangzhou (PRC);
Lijuan Zhang,	Associate Professor, South China Normal University, Guangzhou (China);
R.R. Rakhimov,	Doctor of chem. sciences, Norfolk State University, Norfolk (USA);
N. Nuraje,	Associate Professor, Nazarbayev University, Astana (Kazakhstan);
S.A. Beznosyuk,	Doctor of phys.-math. sciences, Altai State University, Barnaul (Russia);
B.F. Minaev,	Doctor of chem. sciences, Bohdan Khmelnytsky National University of Cherkasy, Cherkasy (Ukraine);
I.V. Kulakov,	Doctor of chem. sciences, University of Tyumen (Russia);
R.P. Bhole,	PhD, Associate Professor, Dr. D.Y. Patil Institute of Pharmaceutical Sciences and Research, Sant Tukaram Nagar, Pimpri, Pune (India);
S.S. Gurav,	PhD, Professor, Goa College of Pharmacy, Panaji (India);
A.A. Atakhanov,	Doctor of techn. sciences, Institute of Polymer Chemistry and Physics, Tashkent (Uzbekistan);
I.V. Korolkov,	PhD, Associated Professor, Astana branch, Institute of Nuclear Physics of the Republic of Kazakhstan, Astana (Kazakhstan);
A.M. Makasheva,	Doctor of techn. sciences, Zh. Abishev Chemical-Metallurgical Institute, Karaganda (Kazakhstan);
M.I. Baikenov,	Doctor of chem. sciences, Buketov Karaganda National Research University (Kazakhstan);
L.K. Salkeeva,	Doctor of chem. sciences, Buketov Karaganda National Research University (Kazakhstan);
G.I. Dzhardimalieva,	Doctor of chem. sciences, Federal Research Center of Problems of Chemical Physics and Medicinal Chemistry, Russian Academy of Sciences, Chernogolovka, Moscow Region (Russia);
S.K. Filippov,	PhD, Project Leader, DWI-Leibniz Institute for Interactive Materials, Aachen, North Rhine-Westphalia, (Germany);
S.A. Ivasenko,	Doctor of pharm. sciences, Karaganda Medical University (Kazakhstan).

Proofreader I.N. Murtazina
Computer layout V.M. Kobina, V.V. Butyaikin

Eurasian Journal of Chemistry. — 2026. — Vol. 31, No. 3(123). — 143 p.
ISSN 2959-0663 (Print). ISSN 2959-0671 (Online). ISSN-L 2959-0663

Proprietary: NLC "Karaganda National Research University named after academician Ye.A. Buketov".

Registered by the Ministry of Culture and Information of the Republic of Kazakhstan. Re-registration certificate No. KZ02VPY00134144 dated 14.11.2025.

Signed in print 30.09.2026. Format 60×84 1/8. Offset paper. Volume 17,88 p.sh. Circulation 200 copies. Price upon request. Order № 127.

Printed in the Publishing house of NLC "Karaganda National Research University named after academician Ye.A. Buketov".
28 University St., Karaganda 100024, Kazakhstan. Tel.: +7(7212) 35-63-16. E-mail: printed@karnu-buketov.edu.kz

© Karaganda National Research University named after academician Ye.A. Buketov, 2026

CONTENTS

ORGANIC CHEMISTRY

PHYSICAL AND ANALYTICAL CHEMISTRY

INORGANIC CHEMISTRY

CHEMICAL TECHNOLOGY

How to Cite: Salimova, E.V., Gubaidullin, R.R. & Parfenova, L.V. (2026). Synthesis of Amphiphilic Derivatives of Fusidane Triterpenoids. *Eurasian Journal of Chemistry, 31, 3(123), 4–13.* https://doi.org/10.31489/2959-0663/3-26-7

ORGANIC CHEMISTRY

Article

Received: 2 June 2026 | Revised: 14 August 2026 |
Accepted: 18 August 2026 | Published online: 28 August 2026

UDC 544.42+519.242.7

https://doi.org/10.31489/2959-0663/3-26-7

Elena V. Salimova, Rinat R. Gubaidullin, Lyudmila V. Parfenova*

Institute of Petrochemistry and Catalysis, Ufa Federal Research Center of the Russian Academy of Sciences, Ufa, Russia
*(*Corresponding author's e-mail: luda_parfenova@mail.ru)*

Synthesis of Amphiphilic Derivatives of Fusidane Triterpenoids

Fusidic acid exhibits bacteriostatic activity, transitioning to bactericidal at high doses, primarily against Gram-positive bacteria, including methicillin-resistant *Staphylococcus aureus*. This underscores its high potential for functionalizing reactive centers with pharmacophore groups to develop semisynthetic analogs as promising antibiotics. In medicinal chemistry, studies on amphiphilic fusidic acid derivatives with enhanced bioavailability and biological activity are highly relevant. In this work, amphiphilic derivatives of the fusidic acid (FA) were synthesized via quaternization of tertiary amines and pyridines (triethylamine, pyridine, N,N-dimethylaminopyridine, N-methylpiperidine) by bromoethyl fusidate and 3-bromopropylamine methylfusidate. The carboxylic group of FA was brominated using 1,2-dibromoethane in dry acetone with K_2CO_3 under reflux. Reaction of the FA bromo- derivative with tertiary amines and pyridines in DMF at 70 °C afforded ammonium salts in 62–70 % yields. The FA bromoamine, obtained via reductive amination, was involved into the reaction with N-containing compounds in DMF upon heating to yield target products in 60–67 % yields. Structures of novel FA analogs were confirmed by NMR spectroscopy and mass-spectrometry. The obtained FA amphiphilic analogs hold potential for further development of antimicrobial agents.

Keywords: triterpenoids, fusidic acid, amphiphilic derivatives, tertiary amines, quaternization reaction, quaternary ammonium salts, reductive amination.

Introduction

For many years, amphiphilic quaternary ammonium compounds have been widely recognized for their biological activity, primarily as antimicrobial agents [1-11]. Additionally, this class of compounds exhibits antiviral, anticancer [12-17], and membrane-tropic properties [18-20]. Evidently, one of the key reasons underlying the biological activity of amphiphilic compounds is the presence of pharmacophoric ammonium groups, and in some cases, hydrophobic polyalkyl fragments. In this context, functionalizing natural polycyclic terpenoids which possess a hydrophobic carbocyclic core and inherent biological activity–with ammonium groups is of considerable interest.

Fusidane triterpenoids represent a small group of natural compounds produced by various fungal species, each displaying antibacterial activity to varying degrees. Among them, fusidic acid (FA) holds a special place, having found clinical application in the therapy of staphylococcal infections. Since its discovery, multiple functionalizations of FA's reactive centers with pharmacophore groups have been performed, yielding analogs with diverse biological activities [24-29]. However, to the best of our knowledge amphiphilic derivatives of fusidane triterpenoids have not been reported. Taking this into account, within our ongoing research on synthetic transformations of FA [28-34], we have synthesized novel amphiphilic analogs via quaternization of tertiary aliphatic amines and pyridines with bromoethyl fusidate and 3-bromopropylamine methylfusidate.

 © 2026 The Authors. This is an open access article under the CC BY-NC-ND license (http://creativecommons.org/licenses/by-nc-nd/4.0/)

Experimental

^{1}H and ^{13}C NMR spectra were recorded on a Bruker Avance II 500 HD Ascend spectrometer (Germany) [500.17 MHz (^{1}H), 125.78 MHz (^{13}C)]. Samples were prepared in standard 5 mm diameter ampoules. One- and two-dimensional NMR spectra (COSY, HSQC, HMBC, NOESY) were acquired using standard pulse sequences. Melting points were determined on a Stuart SMP3 apparatus (Germany). Optical rotations were measured on a Perkin-Elmer 341 polarimeter (Germany). MALDI TOF/TOF mass spectra were obtained on a Bruker Autoflex™ III Smartbeam spectrometer (Germany) using 3-(4-hydroxy-3,5-dimethoxyphenyl)prop-2-enoic acid (sinapinic acid) as matrix. TLC was performed on Sorbfil plates (Sorbpolymer Ltd., Russia) using $CHCl_3$/MeOH (40:1); spots were visualized with 10 % H_2SO_4 followed by heating at 100–120 °C for 2–3 min. Silica gel (50–160 μm, Sorbpolymer Ltd., Russia) was used for column chromatography. Commercially available reagents of "chemically pure" or "analytical grade" (Acros Organics) were employed. Fusidic acid was purchased from Hangzhou Hyper Chemicals Limited (purity 99.3 %). Methyl fusidate (**7**) and its dioxo derivative (**8**) were prepared according to a literature procedure [30].

2-Bromoethyl (Z)-2-((3S,4S,8S,10S,11R,14S,16S)-16-acetoxy-3,11-dihydroxy-4,8,10,14-tetramethylhexadecahydro-17H-cyclopenta[a]phenanthren-17-ylidene)-6-methylhept-5-enoate (2). K_2CO_3 (0.04 g, 0.28 mmol) and 1,2-dibromoethane (0.17 mL, 1.95 mmol) were added to a solution of fusidic acid **1** (0.20 g, 0.40 mmol) in 20 mL of dry acetone. The reaction mixture was heated at 56 °C for 8 h. Acetone was removed under reduced pressure, the residue was dissolved in 30 mL of EtOAc, washed with H_2O and dried over $CaCl_2$. The solvent was evaporated under reduced pressure and the residue was put under vacuum. Yield of compound **2**: 0.23 g (97 %), white powder. Mp 105–107 °C, $[\alpha]_D^{20} = -17°$ (c 0.82, $CHCl_3$). Spectral data are given in Ref. [35].

Compounds 3–6 (general procedure). Bromoethyl ester **2** (1.00 g, 1.67 mmol) was dissolved in 5 mL of DMF and the corresponding tertiary amine (12 mmol) was added: triethylamine (1.21 g), pyridine (0.95 g), N,N-dimethylaminopyridine (1.47 g), or N-methylpiperidine (1.19 g). The reaction mixture was stirred at 70 °C for 8 h. After completion, the mixture was purified by column chromatography on SiO_2, eluting with $CHCl_3$/MeOH (10:1).

2-(((Z)-2-((3S,4S,8S,10S,11R,14S,16S)-16-acetoxy-3,11-dihydroxy-4,8,10,14-tetramethylhexa-decahydro-17H-cyclopenta[a]phenanthren-17-ylidene)-6-methylhept-5-enoyl)oxy)-N,N,N-triethylethan-1-aminium bromide (3)

Yield 0.72 g (62 %), white powder, mp: 187-189°C, $[\alpha]_D^{19}$ -10° (*c* 0.86, MeOH). ^{1}H NMR (MeOD): δ=0.85 s (3H, H^{18}), 0.88 d (3H, H^{28}, *J* 6.3 Hz), 0.91 s (3H, H^{19}), 0.97-1.09 m (2H, H^{6a}, H^{7a}), 1.12-1.22 m (1H, H^{15a}), 1.32 s (3H, H^{30}), 1.37 t (9H, $H^{4'}$, $H^{6'}$, $H^{8'}$, *J* 7.5 Hz), 1.38-1.47 m (1H, H^{1a}), 1.41-1.51 m (1H, H^5), 1.46-1.55 m (1H, H^9), 1.53-1.61 m (1H, H^{6b}), 1.55 s (3H, H^{27}), 1.61 s (3H, H^{26}), 1.61-1.69 m (1H, H^{7b}), 1.62-1.81 m (2H, H^2), 1.71-1.82 m (1H, H^{12a}), 1.87-2.21 m (2H, H^{23}), 1.96 s [3H, O-C(O)CH_3], 2.01-2.12 m (1H, H^4), 2.05-2.16 m (1H, H^{15b}), 2.06-2.21 m (1H, H^{1b}), 2.24-2.35 m (1H, H^{12b}), 2.25-2.43 m (2H, H^{22}), 3.03 d (1H, H^{13}, *J* 10.1 Hz), 3.38-3.63 m (6H, $H^{3'}$, $H^{5'}$, $H^{7'}$), 3.62-3.72 m (1H, H^3), 3.65-3.81 m (2H, $H^{2'}$), 4.15-4.26 m (1H, $H^{1'a}$), 4.25-4.36 m (1H, H^{11}), 4.50-4.61 m (1H, $H^{1'b}$), 5.01 t (1H, H^{24}, *J* 6.4 Hz), 5.77 d (1H, H^{16}, *J* 6.4 Hz). ^{13}C NMR (MeOD): δ=8.2 ($C^{4'}$, $C^{6'}$, $C^{8'}$), 16.1 (C^{28}), 17.6 (C^{18}), 18.0 (C^{27}), 21.0 (C^6), 21.3 [O-C(O)$\underline{C}H_3$], 23.5 (C^{19}), 23.6 (C^{30}), 25.7 (C^{26}), 28.8 (C^{23}), 28.9 (C^{22}), 29.8 (C^2), 29.9 (C^1), 31.5 (C^7), 35.4 (C^4), 35.5 (C^{12}), 36.6 (C^{10}), 36.7 (C^5), 39.0 (C^{15}), 39.5 (C^8), 44.7 (C^{13}), 48.7 (C^{14}), 49.3 (C^9), 54.4 ($C^{3'}$, $C^{5'}$, $C^{7'}$), 55.7 ($C^{2'}$), 57.5 ($C^{1'}$), 67.8 (C^{11}), 71.2 (C^3), 74.0 (C^{16}), 122.9 (C^{24}), 128.7 (C^{20}), 132.7 (C^{25}), 151.3 (C^{17}), 168.7 (C^{21}), 170.9 [O-$\underline{C}$(O)CH_3].

Calcd, %: C 64.62; H 9.18; Br 11.02; N 1.93; O 13.24. $C_{39}H_{66}BrNO_6$. Found, %: C 64.56; H 9.20; Br 11.05; N 1.92. *m/z* 747.4 $[M+Na]^+$, calcd for $[C_{39}H_{66}BrNO_6Na]^+$ 747.4.

1-(2-(((Z)-2-((3S,4S,8S,10S,11R,14S,16S)-16-acetoxy-3,11-dihydroxy-4,8,10,14-tetramethylhexa-decahydro-17H-cyclopenta[a]phenanthren-17-ylidene)-6-methylhept-5-enoyl)oxy)ethyl)pyridin-1-ium bromide (4)

Yield 0.77 g (68 %), white powder, mp: 179-181°C, $[\alpha]_D^{19}$ +9° (*c* 0.95, $CHCl_3$). ^{1}H NMR ($CDCl_3$): δ=0.87 s (3H, H^{18}), 0.88 d (3H, H^{28}, *J* 6.5 Hz), 0.97 s (3H, H^{19}), 1.03-1.11 m (1H, H^{7a}), 1.05-1.13 m (1H, H^{6a}), 1.14-1.23 m (1H, H^{15a}), 1.36 s (3H, H^{30}), 1.43-1.50 m (1H, H^{1a}), 1.47-1.55 m (1H, H^5), 1.52 s (3H, H^{27}), 1.53-1.60 m (1H, H^9), 1.57-1.67 m (1H, H^{6b}), 1.62-1.70 m (1H, H^{7b}), 1.63 s (3H, H^{26}), 1.66-1.89 m (2H, H^2), 1.75-1.84 m (1H, H^{12a}), 1.94 s [3H, O-C(O)CH_3], 2.01-2.16 m (2H, H^{23}), 2.04-2.13 m (1H, H^4), 2.06-2.17 m (1H, H^{15b}), 2.07-2.17 m (1H, H^{1b}), 2.19-2.31 m (1H, H^{12b}), 2.28-2.44 m (2H, H^{22}), 3.05 d (1H, H^{13}, *J* 8.5 Hz), 3.63-3.69 m (1H, H^3), 4.25-4.35 m (1H, H^{11}), 4.36-4.49 m (1H, $H^{1'a}$), 4.61-4.71 m (1H, $H^{1'b}$), 4.95 t (1H, H^{24},

J 7.1 Hz), 5.03-5.18 m (2H, $H^{2'}$), 5.66 d (1H, H^{16}, *J* 8.5 Hz), 8.19 t (2H, $H^{4'}$, $H^{6'}$, *J* 7.5 Hz), 8.67 t (1H, $H^{5'}$, *J* 7.5 Hz), 9.14 d (2H, $H^{3'}$, $H^{7'}$, *J* 5.5 Hz). ^{13}C NMR ($CDCl_3$), δ=15.7 (C^{28}), 17.3 (C^{27}), 17.5 (C^{18}), 20.7 [O-C(O)<u>C</u>H_3], 21.1 (C^6), 22.8 (C^{30}), 23.6 (C^{19}), 25.7 (C^{26}), 28.4 (C^{23}), 28.7 (C^{22}), 29.6 (C^1, C^2), 31.1 (C^7), 35.2 (C^4), 35.7 (C^{12}), 36.4 (C^{10}), 36.9 (C^5), 38.9 (C^{15}), 39.5 (C^8), 44.5 (C^{13}), 48.6 (C^{14}), 49.4 (C^9), 60.2 ($C^{2'}$), 62.9 ($C^{1'}$), 67.5 (C^{11}), 71.2 (C^3), 74.3 (C^{16}), 122.7 (C^{24}), 128.6 ($C^{4'}$, $C^{6'}$), 128.7 (C^{20}), 132.6 (C^{25}), 145.2 ($C^{3'}$, $C^{7'}$), 146.4 ($C^{5'}$), 151.0 (C^{17}), 169.0 (C^{21}), 171.0 [O-<u>C</u>(O)CH_3]. Calcd, %: C 64.95; H 8.03; Br 11.37; N 1.99; O 13.66. $C_{38}H_{56}BrNO_6$. Found, %: C 64.87; H 8.05; Br 11.40; N 1.98. *m/z* 724.4 $[M+Na]^+$, calcd for $[C_{38}H_{56}BrNO_6Na]^+$ 724.3.

1-(2-(((Z)-2-((3S,4S,8S,10S,11R,14S,16S)-16-acetoxy-3,11-dihydroxy-4,8,10,14-tetramethylhexadecahydro-17H-cyclopenta[a]phenanthren-17-ylidene)-6-methylhept-5-enoyl)oxy)ethyl)-4-(dimethylamino)pyridin-1-ium bromide (5)

Yield 0.78 g (65 %), white powder, mp: 181-183°C, $[\alpha]_D^{19}$ +7° (*c* 0.89, $CHCl_3$). ^{1}H NMR ($CDCl_3$): δ=0.76 s (3H, H^{18}), 0.80 d (3H, H^{28}, *J* 6.5 Hz), 0.83 s (3H, H^{19}), 0.91-1.05 m (2H, H^{6a}, H^{7a}), 1.02-1.12 m (1H, H^{15a}), 1.25 s (3H, H^{30}), 1.30-1.39 m (1H, H^{1a}), 1.33-1.43 m (1H, H^5), 1.38-1.45 m (1H, H^9), 1.40 s (3H, H^{27}), 1.44-1.55 m (1H, H^{6b}), 1.50-1.64 m (1H, H^{7b}), 1.51 s (3H, H^{26}), 1.60-1.77 m (2H, H^2), 1.62-1.72 m (1H, H^{12a}), 1.83 s [3H, O-C(O)CH_3], 1.92-2.02 m (2H, H^{23}), 1.97-2.08 m (1H, H^4), 1.99-2.07 m (1H, H^{15b}), 2.07-2.17 m (1H, H^{1b}), 2.18-2.30 m (2H, H^{22}), 2.19-2.29 m (1H, H^{12b}), 2.97 d (1H, H^{13}, *J* 10.8 Hz), 3.18 s (6H, $H^{8'}$, $H^{9'}$), 3.54-3.63 m (1H, H^3), 4.13-4.23 m (1H, $H^{1'a}$), 4.19-4.27 m (1H, H^{11}), 4.36-4.46 m (1H, $H^{1'b}$), 4.48-4.59 m (1H, $H^{2'a}$), 4.64-4.75 m (1H, $H^{2'b}$), 4.86 t (1H, H^{24}, *J* 6.8 Hz), 5.60 d (1H, H^{16}, *J* 6.8 Hz), 6.88 d (2H, $H^{4'}$, $H^{6'}$, *J* 5.4 Hz), 8.39 d (2H, $H^{3'}$, $H^{7'}$, *J* 5.4 Hz). ^{13}C NMR ($CDCl_3$), δ=16.0 (C^{28}), 17.5 (C^{27}), 17.8 (C^{18}), 21.0 [O-C(O)<u>C</u>H_3], 21.1 (C^6), 23.4 (C^{30}), 23.6 (C^{19}), 25.7 (C^{26}), 28.7 (C^{23}), 28.9 (C^{22}), 29.8 (C^2), 29.9 (C^1), 31.3 (C^7), 35.2 (C^4), 35.5 (C^{12}), 36.5 (C^{10}), 36.9 (C^5), 38.9 (C^{15}), 39.4 (C^8), 40.4 ($C^{8'}$, $C^{9'}$), 44.4 (C^{13}), 48.5 (C^{14}), 49.4 (C^9), 56.1 ($C^{2'}$), 63.2 ($C^{1'}$), 67.5 (C^{11}), 70.9 (C^3), 74.1 (C^{16}), 108.1 ($C^{4'}$, $C^{6'}$), 123.1 (C^{24}), 128.7 (C^{20}), 132.2 (C^{25}), 142.7 ($C^{3'}$, $C^{7'}$), 150.4 (C^{17}), 156.4 ($C^{5'}$), 169.1 (C^{21}), 170.6 [O-<u>C</u>(O)CH_3]. Calcd, %: C 64.42; H 8.24; Br 10.71; N 3.76; O 12.87. $C_{40}H_{61}BrN_2O_6$. Found, %: C 64.49; H 8.22; Br 10.68; N 3.75. *m/z* 767.5 $[M+Na]^+$, calcd for $[C_{40}H_{61}BrN_2O_6Na]^+$ 767.4.

1-(2-(((Z)-2-((3S,4S,8S,10S,11R,14S,16S)-16-acetoxy-3,11-dihydroxy-4,8,10,14-tetramethylhexadecahydro-17H-cyclopenta[a]phenanthren-17-ylidene)-6-methylhept-5-enoyl)oxy)ethyl)-1-methylpiperidin-1-ium bromide (6)

Yield 0.81 g (70 %), white powder, mp: 173-175°C, $[\alpha]_D^{20}$ -12° (*c* 0.67, MeOH). ^{1}H NMR (MeOD): δ=0.88 s (3H, H^{18}), 0.89 d (3H, H^{28}, *J* 6.4 Hz), 0.95 s (3H, H^{19}), 1.04-1.14 m (2H, H^{6a}, H^{7a}), 1.21-1.28 m (1H, H^{15a}), 1.36 s (3H, H^{30}), 1.38-1.47 m (2H, $H^{5'}$), 1.44-1.51 m (1H, H^{1a}), 1.49-1.57 m (1H, H^5), 1.52-1.63 m (4H, $H^{4'}$, $H^{6'}$), 1.53-1.58 m (1H, H^9), 1.55-1.64 m (1H, H^{6b}), 1.58 s (3H, H^{27}), 1.66 s (3H, H^{26}), 1.66-1.72 m (1H, H^{7b}), 1.71-1.86 m (2H, H^2), 1.76-1.85 m (1H, H^{12a}), 1.96 s [3H, O-C(O)CH_3], 1.97-2.19 m (2H, H^{23}), 2.05-2.14 m (1H, H^4), 2.09-2.20 m (1H, H^{1b}), 2.11-2.20 m (1H, H^{15b}), 2.25-2.33 m (1H, H^{12b}), 2.35-2.50 m (2H, H^{22}), 2.44-2.53 m (4H, $H^{3'}$, $H^{7'}$), 2.64 t (2H, $H^{2'}$, *J* 6.1 Hz), 3.02 d (1H, H^{13}, *J* 11.6 Hz), 3.44 s (3H, $H^{8'}$), 3.68-3.73 m (1H, H^3), 4.03-4.09 m (1H, $H^{1'a}$), 4.25-4.30 m (1H, $H^{1'b}$), 4.30-4.35 m (1H, H^{11}), 5.06 t (1H, H^{24}, *J* 6.8 Hz), 5.81 d (1H, H^{16}, *J* 7.8 Hz). ^{13}C NMR (MeOD): δ=15.9 (C^{28}), 17.6 (C^{27}), 17.8 (C^{18}), 20.9 (C^6), 21.0 [O-C(O)<u>C</u>H_3], 23.3 (C^{19}), 23.7 (C^{30}), 23.9 ($C^{5'}$), 25.5 ($C^{4'}$, $C^{6'}$), 25.7 (C^{26}), 28.4 (C^{23}), 28.9 (C^{22}), 29.8 (C^2), 30.0 (C^1), 31.8 (C^7), 35.5 (C^{12}), 35.6 (C^4), 36.6 (C^5), 36.7 (C^{10}), 38.9 (C^{15}), 39.4 (C^8), 44.0 (C^{13}), 48.6 (C^{14}), 49.3 (C^9), 50.5 ($C^{8'}$), 54.6 ($C^{3'}$, $C^{7'}$), 56.8 ($C^{2'}$), 61.6 (C^1), 68.1 (C^{11}), 71.4 (C^3), 74.4 (C^{16}), 123.1 (C^{24}), 130.2 (C^{20}), 132.4 (C^{25}), 148.3 (C^{17}), 170.0 (C^{21}), 170.5 [O-<u>C</u>(O)CH_3]. Calcd, %: C 64.80; H 8.92; Br 11.05; N 1.94; O 13.28. $C_{39}H_{64}BrNO_6$. Found, %: C 64.74; H 8.94; Br 11.07; N 1.95. *m/z* 744.5 $[M+Na]^+$, calcd for $[C_{39}H_{64}BrNO_6Na]^+$ 744.4.

Methyl (Z)-2-((3S,4S,8S,10S,11R,14S,16S)-16-acetoxy-3-((3-bromopropyl)amino)-11-hydroxy-4,8,10,14-tetramethylhexadecahydro-17H-cyclopenta[a]phenanthren-17-ylidene)-6-methylhept-5-enoate (9). A mixture of diketone **8** (1.00 g, 1.92 mmol), titanium(IV) isopropoxide (0.23 g, 0.65 mmol) and 3-bromopropylamine (0.40 g, 2.89 mmol) in 10 mL of absolute methanol was stirred under an argon atmosphere at room temperature for 8 h. Sodium borohydride (0.15 g, 3.96 mmol) was then added at −78 °C and the resulting mixture was stirred for an additional 2 h while warming to 24 °C. Water (5 mL) was added to the reaction mixture, which was stirred at room temperature for 30 min. The precipitate was filtered off, the organic layer was concentrated under reduced pressure and placed under vacuum. The residue was purified by column chromatography on SiO_2, eluting with $CHCl_3$/MeOH (10:1).

Methyl (Z)-2-((3S,4S,8S,10S,11R,14S,16S)-16-acetoxy-3-((3-bromopropyl)amino)-11-hydroxy-4,8,10,14-tetramethylhexadecahydro-17H-cyclopenta[a]phenanthren-17-ylidene)-6-methylhept-5-enoate (9)

Yield 1.05 g (85 %), yellow powder, mp: 198-200°C, $[\alpha]_D^{19}$ +12° (*c* 0.73, $CHCl_3$). ^{1}H NMR ($CDCl_3$): δ=0.88 s (3H, H^{18}), 1.10 d (3H, H^{28}, *J* 6.8 Hz), 1.12 s (3H, H^{19}), 1.14-1.27 m (1H, H^{7a}, 2H, $H^{2'}$), 1.15-1.26 m (1H, H^{15a}), 1.34 s (3H, H^{30}), 1.49-1.60 m (1H, H^{9}), 1.58-1.66 m (1H, H^{7b}), 1.59 s (3H, H^{27}), 1.59-1.72 m (2H, H^{6}), 1.64-1.71 m (1H, H^{1a}), 1.66 s (3H, H^{26}),1.71-1.86 m (2H, H^{4}, H^{12a}), 1.74-1.79 m (1H, H^{2a}), 1.87-1.97 m (1H, $H^{1'a}$), 1.94-2.14 m (2H, H^{23}), 1.97 s [3H, O-C(O)CH_3], 2.01-2.11 m (3H, H^{1b}, H^{2b}, H^{5}), 2.10-2.21 m (1H, H^{15b}), 2.21-2.29 m (1H, H^{12b}), 2.32-2.48 m (2H, H^{22}), 2.56-2.66 m (1H, $H^{1'b}$), 2.66-2.74 m (1H, $H^{3'a}$), 3.04 d (1H, H^{13}, *J* 11.0 Hz), 3.04-3.15 m (1H, H^{3}), 3.32-3.38 m (1H, $H^{3'b}$), 3.63 s (3H, $COOCH_3$), 4.22-4.35 m (1H, H^{11}), 5.08 t (1H, H^{24}, *J* 7.5 Hz), 5.82 d (1H, H^{16}, *J* 8.1 Hz). ^{13}C NMR ($CDCl_3$), δ=14.2 (C^{28}), 17.1 (C^{18}), 17.7 (C^{27}), 18.7 (C^{6}), 20.9 [O-C(O)$\underline{C}H_3$], 22.3 (C^{30}), 25.7 (C^{26}), 28.4 (C^{23}), 28.6 (C^{19}), 28.8 (C^{22}), 29.7 (C^{7}, $C^{2'}$), 29.9 (C^{2}), 30.8 (C^{4}), 31.6 (C^{1}), 36.3 (C^{12}), 36.8 (C^{10}), 38.7 ($C^{3'}$), 38.9 (C^{15}), 39.9 (C^{8}), 42.1 (C^{5}), 43.8 (C^{13}), 48.8 ($C^{1'}$), 49.1 (C^{14}), 50.5 (C^{9}), 51.4 (COO$\underline{C}H_3$), 66.7 (C^{11}), 67.4 (C^{3}), 74.4 (C^{16}), 123.0 (C^{24}), 130.3 (C^{20}), 132.6 (C^{25}), 147.8 (C^{17}), 170.6 (C^{21}), 171.0 [O-$\underline{C}$(O)CH_3]. Calcd, %: C 64.60; H 8.67; Br 12.28; N 2.15; O 12.29. $C_{35}H_{56}BrNO_5$. Found, %: C 64.66; H 8.66; Br 12.25; N 2.16. *m/z* 672.4 $[M+Na]^+$, calcd for $[C_{35}H_{56}BrNO_5Na]^+$ 672.3.

Compounds 10–13 (general procedure). Bromoamine **9** (1.00 g, 1.54 mmol) was dissolved in 5 mL of DMF and the corresponding tertiary amine (11 mmol) was added: triethylamine (1.11 g), pyridine (0.87 g), N, N-dimethylaminopyridine (1.35 g), or N-methylpiperidine (1.09 g). The reaction mixture was stirred at 70 °C for 8 h. After completion, the mixture was purified by column chromatography on SiO_2, eluting with CHCl3/MeOH (4:1).

3-(((3S,4S,8S,10S,11R,14S,16S, Z)-16-acetoxy-11-hydroxy-17-(1-methoxy-6-methyl-1-oxohept-5-en-2-ylidene)-4,8,10,14-tetramethylhexadecahydro-1H-cyclopenta[a]phenanthren-3-yl)amino)-N,N,N-triethylpropan-1-aminium bromide (10)

Yield 0.66 g (60 %), white powder, mp: 195-197°C, $[\alpha]_D^{19}$ +8° (*c* 0.99, MeOH). ^{1}H NMR (MeOD): δ=0.88 s (3H, H^{18}), 1.11 s (3H, H^{19}), 1.17-1.29 m (1H, H^{15a}), 1.18 d (3H, H^{28}, *J* 6.5 Hz), 1.20-1.36 m (1H, H^{7a}), 1.35 s (3H, H^{30}), 1.44 t (9H, $H^{5'}$, $H^{7'}$, $H^{9'}$, *J* 7.2 Hz), 1.52-1.62 m (1H, H^{9}), 1.55-1.64 m (2H, H^{6}), 1.56-1.66 m (2H, H^{2a}, H^{7b}), 1.60 s (3H, H^{27}), 1.63-1.74 m (1H, H^{1a}), 1.67 s (3H, H^{26}), 1.72-1.86 s (2H, $H^{2'}$), 1.74-1.88 m (2H, H^{4}, H^{12a}), 1.75-1.86 m (1H, H^{2b}), 1.92-2.04 m (1H, $H^{1'a}$), 1.97-2.19 m (2H, H^{23}), 1.98 s [3H, O-C(O)CH_3], 2.04-2.14 m (1H, H^{1b}), 2.06-2.16 m (1H, H^{5}), 2.10-2.23 m (1H, H^{15b}), 2.25-2.37 m (1H, H^{12b}), 2.36-2.53 m (2H, H^{22}), 2.63-2.74 m (1H, $H^{1'b}$), 2.96-3.06 m (1H, H^{13}), 3.18 t (6H, $H^{4'}$, $H^{6'}$, $H^{8'}$, *J* 6.1 Hz), 3.19-3.31 m (1H, H^{3}), 3.64 s (3H, $COOCH_3$), 4.14-4.26 m (2H, $H^{3'}$), 4.32-4.47 m (1H, H^{11}), 5.11 t (1H, H^{24}, *J* 6.8 Hz), 5.83 d (1H, H^{16}, *J* 8.1 Hz). ^{13}C NMR (MeOD): δ=8.7 ($C^{5'}$, $C^{7'}$, $C^{9'}$), 14.8 (C^{28}), 17.1 (C^{18}), 17.8 (C^{27}), 18.7 (C^{6}), 21.0 [O-C(O)$\underline{C}H_3$], 22.6 (C^{30}), 22.7 ($C^{2'}$), 25.8 (C^{26}), 28.4 (C^{23}), 28.7 (C^{19}), 28.9 (C^{22}), 29.7 (C^{2}, C^{7}), 31.1 (C^{4}), 31.9 (C^{1}), 36.2 (C^{12}), 36.8 (C^{10}), 38.9 (C^{15}), 39.8 (C^{8}), 42.0 (C^{5}), 43.9 (C^{13}), 46.2 ($C^{4'}$, $C^{6'}$, $C^{8'}$), 48.5 (C^{14}), 49.1 ($C^{1'}$), 50.5 (C^{9}), 51.4 (COO$\underline{C}H_3$), 67.0 (C^{11}), 67.6 (C^{3}), 68.1 ($C^{3'}$), 74.3 (C^{16}), 123.1 (C^{24}), 130.3 (C^{20}), 132.5 (C^{25}), 147.9 (C^{17}), 170.4 (C^{21}), 170.8 [O-$\underline{C}$(O)CH_3]. Calcd, %: C 65.49; H 9.52; Br 10.63; N 3.73; O 10.64. $C_{41}H_{71}BrN_2O_5$. Found, %: C 65.56; H 9.50; Br 10.61; N 3.72. *m/z* 773.5 $[M+Na]^+$, calcd for $[C_{41}H_{71}BrN_2O_5Na]^+$ 773.4.

1-(3-(((3S,4S,8S,10S,11R,14S,16S, Z)-16-acetoxy-11-hydroxy-17-(1-methoxy-6-methyl-1-oxohept-5-en-2-ylidene)-4,8,10,14-tetramethylhexadecahydro-1H-cyclopenta[a]phenanthren-3-yl)amino)propyl)pyridin-1-ium bromide (11)

Yield 0.75 g (67 %), white powder, mp: 182-184°C, $[\alpha]_D^{19}$ -11° (*c* 1.12, MeOH). ^{1}H NMR (MeOD): δ=0.76 s (3H, H^{18}), 1.01 d (3H, H^{28}, *J* 6.5 Hz), 1.02 s (3H, H^{19}), 1.03-1.20 m (1H, H^{15a}), 1.09-1.19 m (1H, H^{7a}), 1.19 s (3H, H^{30}), 1.39-1.45 m (1H, H^{9}), 1.45 s (3H, H^{27}), 1.46-1.59 m (2H, H^{1a}, H^{7b}), 1.53 s (3H, H^{26}), 1.55-1.70 m (2H, H^{6}), 1.63-1.82 m (1H, H^{12a}), 1.69-1.76 m (1H, $H^{2'a}$), 1.73-1.87 m (1H, H^{5}), 1.76-1.91 m (1H, H^{1b}, 2H, H^{2}), 1.83 s [3H, O-C(O)CH_3], 1.84-2.10 m (2H, H^{23}), 1.87-1.98 m (1H, $H^{2'b}$), 1.89-2.10 m (1H, $H^{1'a}$), 1.97-2.12 m (1H, H^{15b}), 2.12-2.29 m (1H, H^{12b}), 2.21-2.52 m (2H, H^{22}), 2.34-2.46 m (1H, H^{4}), 2.37-2.53 m (1H, $H^{1'b}$), 2.91 d (1H, H^{13}, *J* 12.5 Hz), 3.05-3.15 m (1H, H^{3}), 3.50 s (3H, $COOCH_3$), 4.14-4.17 m (2H, $H^{3'}$), 4.16-4.27 m (1H, H^{11}), 4.95 t (1H, H^{24}, *J* 6.5 Hz), 5.68 d (1H, H^{16}, *J* 7.5 Hz), 8.03 t (2H, $H^{5'}$, $H^{7'}$, *J* 7.5 Hz), 8.43 t (1H, $H^{6'}$, *J* 7.5 Hz), 9.19 d (2H, $H^{4'}$, $H^{8'}$, *J* 5.3 Hz). ^{13}C NMR (MeOD): δ=15.0 (C^{28}), 17.1 (C^{18}), 17.7 (C^{27}), 20.8 [O-C(O)$\underline{C}H_3$], 21.0 (C^{6}), 22.5 (C^{30}), 22.6 ($C^{2'}$), 25.6 (C^{26}), 28.4 (C^{23}), 28.7 (C^{22}), 29.3 (C^{19}), 29.5 (C^{2}), 29.5 (C^{7}), 30.0 (C^{1}), 33.2 (C^{4}), 36.3 (C^{12}), 36.4 (C^{10}), 38.9 (C^{15}), 39.5 ($C^{1'}$), 39.6 (C^{8}), 42.7 (C^{5}), 43.7 (C^{13}), 48.4 (C^{14}), 50.6 (C^{9}), 51.3 (COO$\underline{C}H_3$), 62.2 (C^{3}), 66.9 ($C^{3'}$), 67.4 (C^{11}), 74.2 (C^{16}), 123.0

(C^{24}), 128.2 ($C^{5'}$, $C^{7'}$), 130.1 (C^{20}), 132.3 (C^{25}), 145.0 ($C^{6'}$), 145.9 ($C^{4'}$, $C^{8'}$), 148.0 (C^{17}), 170.2 (C^{21}), 170.7 [O-C(O)CH_3]. Calcd, %: C 65.83; H 8.42; Br 10.95; N 3.84; O 10.96. $C_{40}H_{61}BrN_2O_5$. Found, %: C 65.89; H 8.40; Br 10.92; N 3.85. *m/z* 751.3 $[M+Na]^+$, calcd for $[C_{40}H_{61}BrN_2O_5Na]^+$ 751.4.

1-(3-(((3S,4S,8S,10S,11R,14S,16S, Z)-16-acetoxy-11-hydroxy-17-(1-methoxy-6-methyl-1-oxohept-5-en-2-ylidene)-4,8,10,14-tetramethylhexadecahydro-1H-cyclopenta[a]phenanthren-3-yl)amino)propyl)-4-(dimethylamino)pyridin-1-ium bromide (12)

Yield 0.75 g (63 %), white powder, mp: 186-188°C, $[\alpha]_D^{19}$ -5° (*c* 1.11, MeOH). ^{1}H NMR (MeOD): δ=0.81 s (3H, H^{18}), 1.03 d (3H, H^{28}, *J* 6.5 Hz), 1.12-1.22 m (1H, H^{15a}), 1.17 s (3H, H^{19}), 1.18-1.28 m (1H, H^{7a}), 1.24 s (3H, H^{30}), 1.45-1.50 m (1H, H^9), 1.51 s (3H, H^{27}), 1.51-1.65 m (1H, H^{7b}), 1.53-1.60 m (2H, H^6), 1.55-1.60 m (1H, H^{2a}), 1.58 s (3H, H^{26}), 1.65-1.75 m (1H, H^{1a}), 1.71-1.79 m (1H, H^4), 1.72-1.80 m (1H, H^{12a}), 1.74-1.80 m (1H, H^{2b}), 1.83-1.97 m (2H, $H^{2'}$), 1.85-1.95 m (1H, $H^{1'a}$), 1.90 s [3H, O-C(O)CH_3], 1.94-2.14 m (2H, H^{23}), 2.01-2.14 m (1H, H^5), 2.03-2.14 m (1H, H^{1b}), 2.13-2.25 m (1H, H^{15b}), 2.20-2.29 m (1H, H^{12b}), 2.27-2.45 m (2H, H^{22}), 2.34-2.58 m 1H, $H^{1'b}$), 2.96 d (1H, H^{13}, *J* 11.2 Hz), 3.02-3.14 m (1H, H^3), 3.09 s (6H, $H^{9'}$, $H^{10'}$), 3.18-3.56 m (2H, $H^{3'}$), 3.56 s (3H, $COOCH_3$), 4.20-4.33 m (1H, H^{11}), 5.01 t (1H, H^{24}, *J* 6.5 Hz), 5.73 d (1H, H^{16}, *J* 8.1 Hz), 6.63 d (2H, $H^{5'}$, $H^{7'}$, *J* 5.6 Hz), 8.10 d (2H, $H^{4'}$, $H^{8'}$, *J* 5.6 Hz). ^{13}C NMR (MeOD): δ=14.3 (C^{28}), 17.1 (C^{18}), 17.7 (C^{27}), 18.7 (C^6), 20.9 [O-C(O)$\underline{C}H_3$], 22.3 (C^{30}, $C^{2'}$), 25.6 (C^{26}), 28.4 (C^{23}), 28.6 (C^{19}), 28.8 (C^{22}), 29.6 (C^7), 29.6 (C^2), 30.9 (C^4), 31.7 (C^1), 36.3 (C^{12}), 36.6 (C^{10}), 38.9 (C^{15}), 39.7 ($C^{9'}$, $C^{10'}$), 39.8 (C^8), 42.0 (C^5), 43.9 (C^{13}), 48.5 ($C^{1'}$), 49.1 (C^{14}), 50.4 (C^9), 51.3 ($COO\underline{C}H_3$), 63.7 ($C^{3'}$), 66.8 (C^{11}), 67.5 (C^3), 74.3 (C^{16}), 106.7 ($C^{5'}$, $C^{7'}$), 123.0 (C^{24}), 130.1 (C^{20}), 133.1 (C^{25}), 143.0 ($C^{4'}$, $C^{8'}$), 148.0 (C^{17}), 156.2 ($C^{6'}$), 170.5 (C^{21}), 170.8 [O-$\underline{C}$(O)CH_3]. Calcd, %: C 65.27; H 8.61; Br 10.34; N 5.44; O 10.35. $C_{42}H_{66}BrN_3O_5$. Found, %: C 65.34; H 8.59; Br 10.31; N 5.45. *m/z* 794.5 $[M+Na]^+$, calcd for $[C_{42}H_{66}BrN_3O_5Na]^+$ 794.4.

1-(3-(((3S,4S,8S,10S,11R,14S,16S, Z)-16-acetoxy-11-hydroxy-17-(1-methoxy-6-methyl-1-oxohept-5-en-2-ylidene)-4,8,10,14-tetramethylhexadecahydro-1H-cyclopenta[a]phenanthren-3-yl)amino)propyl)-1-methylpiperidin-1-ium bromide (13)

Yield 0.75 g (65 %), white powder, mp: 169-171°C, $[\alpha]_D^{19}$ +6° (*c* 1.10, MeOH). ^{1}H NMR (MeOD): δ=0.85 s (3H, H^{18}), 1.06 d (3H, H^{28}, *J* 6.8 Hz), 1.08 s (3H, H^{19}), 1.14-1.25 m (1H, H^{15a}), 1.18-1.26 m (1H, H^{7a}), 1.30 s (3H, H^{30}), 1.50-1.57 m (1H, H^9), 1.52-1.58 m (2H, H^6), 1.55 s (3H, H^{27}), 1.56-1.63 m (2H, H^{2a}, H^{7b}), 1.58-1.70 m (4H, $H^{5'}$, $H^{7'}$), 1.63-1.70 m (1H, H^{1a}), 1.65 s (3H, H^{26}), 1.72-1.83 m (1H, H^4), 1.75-1.89 m (2H, H^{2b}, H^{12a}, 2H, $H^{2'}$), 1.82-1.92 m (2H, $H^{6'}$), 1.88-1.96 m (1H, $H^{1'a}$), 1.94 s [3H, O-C(O)CH_3], 1.94-2.12 m (2H, H^{23}), 2.00-2.09 m (2H, H^{1b}, H^5), 2.10-2.21 m (1H, H^{15b}), 2.19-2.28 m (1H, H^{12b}), 2.31-2.48 m (2H, H^{22}), 2.59-2.66 m (1H, $H^{1'b}$), 2.95-3.08 m (4H, $H^{4'}$, $H^{8'}$), 2.97-3.10 m (1H, H^{13}), 3.04-3.12 m (1H, H^3), 3.40 s (3H, $H^{9'}$), 3.60 s (3H, $COOCH_3$), 4.09-4.17 m (2H, $H^{3'}$), 4.25-4.34 m (1H, H^{11}), 5.04 t (1H, H^{24}, *J* 6.2 Hz), 5.70 d (1H, H^{16}, *J* 8.1 Hz). ^{13}C NMR (MeOD): δ=14.4 (C^{28}), 17.1 (C^{18}), 17.9 (C^{27}), 18.6 (C^6), 20.9 [O-C(O)$\underline{C}H_3$], 22.1 ($C^{2'}$), 22.3 ($C^{5'}$, $C^{7'}$), 22.3 ($C^{6'}$), 22.6 (C^{30}), 25.6 (C^{26}), 28.3 (C^{23}), 28.6 (C^{19}), 28.8 (C^{22}), 29.6 (C^2, C^7), 30.9 (C^4), 31.7 (C^1), 36.3 (C^{12}), 36.7 (C^{10}), 38.9 (C^{15}), 39.9 (C^8), 42.1 (C^5), 43.8 (C^{13}), 44.5 ($C^{4'}$, $C^{8'}$), 48.5 (C^{14}), 48.7 ($C^{1'}$), 50.0 ($C^{9'}$), 50.5 (C^9), 51.4 ($COO\underline{C}H_3$), 65.6 ($C^{3'}$), 66.7 (C^{11}), 67.6 (C^3), 74.4 (C^{16}), 122.9 (C^{24}), 130.3 (C^{20}), 132.6 (C^{25}), 147.8 (C^{17}), 170.6 (C^{21}), 170.9 [O-$\underline{C}$(O)CH_3]. Calcd, %: C 65.67; H 9.27; Br 10.66; N 3.74; O 10.67. $C_{41}H_{69}BrN_2O_5$. Found, %: C 65.61; H 9.29; Br 10.68; N 3.73. *m/z* 771.4 $[M+Na]^+$, calcd for $[C_{41}H_{69}BrN_2O_5Na]^+$ 771.4.

Results and Discussion

The quaternization reaction is one of the methods for functionalizing organic molecules, involving the introduction of a quaternary ammonium group into the chemical structure. Several variants of this reaction exist, but the most common method entails alkylation of tertiary amines with alkyl halides [**36**]. Bromination of the carboxylic group of FA was carried out by reacting compound **1** with 1,2-dibromoethane under reflux in dry acetone in the presence of K_2CO_3 as base. The reaction afforded bromide **2** with a yield of 97 % (Figure 1) [**35**]. Bromide **2** was then subjected to quaternization with tertiary aliphatic and aromatic amines, such as triethylamine, pyridine, N, N-dimethylaminopyridine, and N-methylpiperidine. The reaction proceeded in DMF at 70 °C. After workup and purification by column chromatography, quaternized derivatives **3–6** were isolated in 62–70 % yields (Figure 1). The lack of a pronounced dependence of the yields on the nucleophilicity of the amine can be attributed to the dominant role of steric hindrance from the fusidane scaffold and the use of a large excess of the amine, which ensures high conversion regardless of the nucleophile's electronic properties.

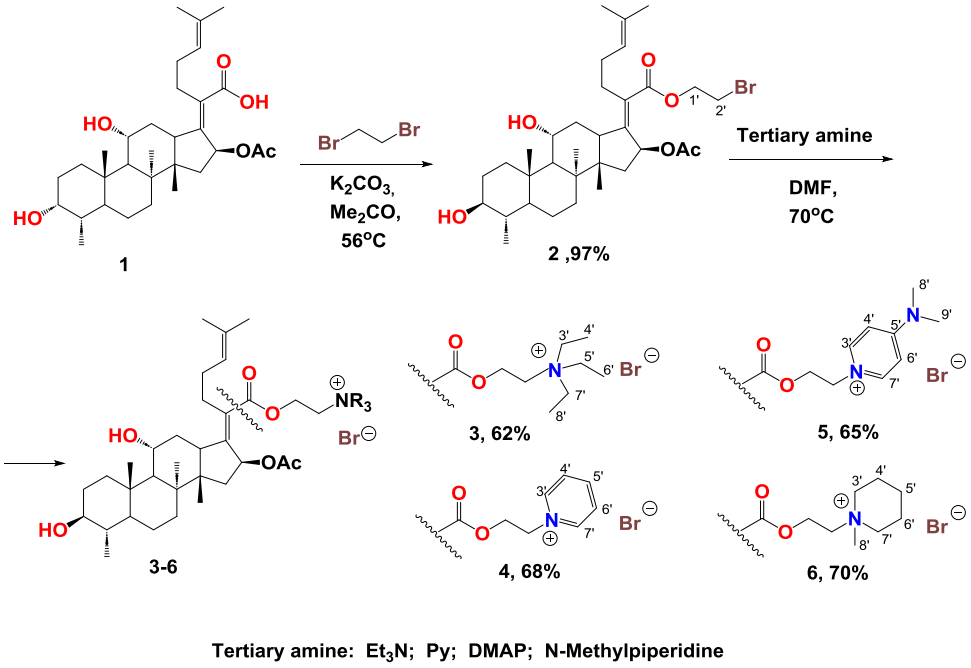

Figure 1. Synthesis of compounds **3-6**

The transformations of compound **2** were confirmed by the **NMR** spectroscopy of the products, particularly by the downfield shift of the aliphatic chain carbon signal of the ester fragment attached to the quaternary nitrogen (δ_C 55.66–60.23 ppm, depending on the substituent at the quaternary nitrogen) compared to the starting bromide (δ_C = 28.35 ppm). Moreover, in the **^{1}H NMR** spectra of compounds **4** and **5**, aromatic proton signals appeared at δ 6.88–9.14 ppm, while for derivative **3**, the **^{13}C NMR** spectrum showed additional signals for the terminal methyl groups of the triethylammonium fragment at δ = 8.20 ppm.

The reductive amination of aldehydes and ketones is one of the most important methods in the pharmaceutical industry due to its versatility and selectivity, enabling the one-step synthesis of amines with varying degrees of substitution [**37**]. Using reductive amination, amine **9** was obtained from the 3,11-dioxo methyl ester derivative of FA (**8**) by reacting the latter with 3-bromopropylamine in MeOH in the presence of Ti(O*i*-Pr)$_4$ catalyst, followed by reduction of the reaction mixture with $NaBH_4$ (Figure 2). The reaction proceeded selectively at the 3-keto group, while the 11-keto group did not undergo amination and was reduced to the hydroxyl function. The transformation of **8** into **9** was confirmed by NMR spectroscopy. In the **^{13}C NMR** spectrum, signals of the two keto groups at δ_C = 215.95 and 209.55 ppm disappeared, and signals of the C atoms at newly formed N-CH-3 and O-CH-11 bonds appeared at δ = 67.42 and 66.98 ppm, respectively. The signal of carbon atom attached to bromine was registered at δ = 38.73 ppm. In the **^{1}H NMR** spectrum of **9**, signals of the CH-3 protons (δ = 3.04–3.15 ppm) and CH-11 protons (δ = 4.22–4.35 ppm) were observed, along with a series of multiplets (δ = 1.14–1.27, 1.87–2.66, and 2.66–3.38 ppm) corresponding to the CH_2 groups of the bromoaminopropane fragment. NOESY spectra confirmed that C-3 acquired β-configuration upon reductive amination, while C-11 retained the α-configuration of the native molecule.

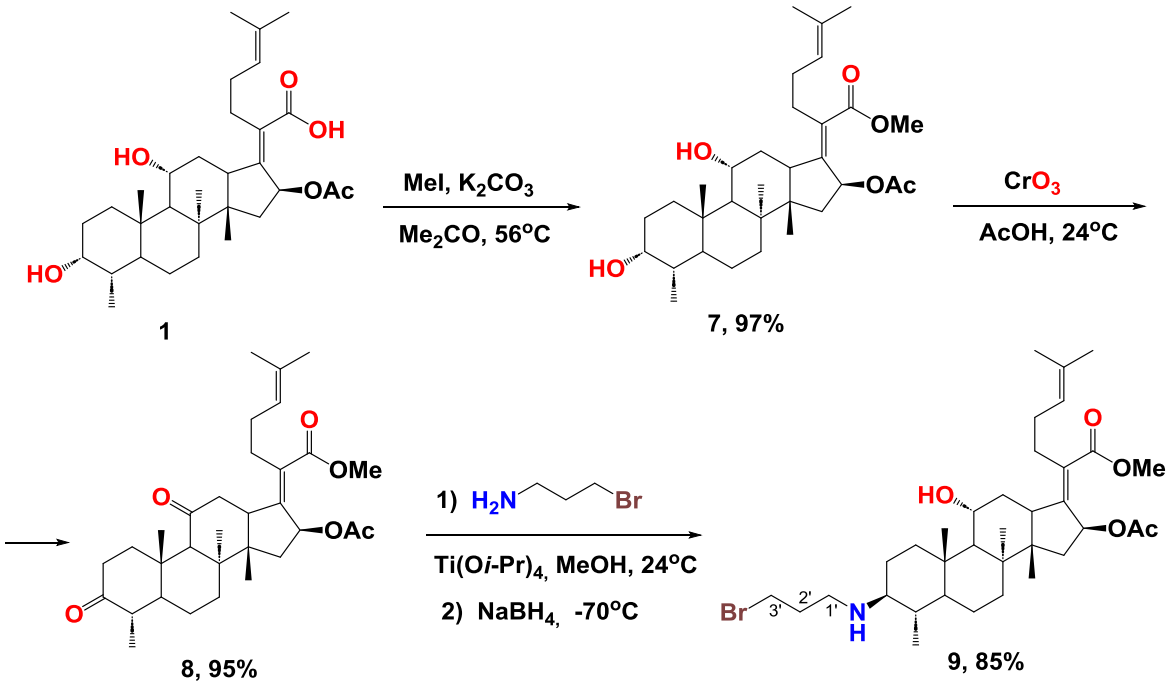

Figure 2. Synthesis of compound **9**

Compound **9** was involved into the reaction with triethylamine, pyridine, N, N-dimethylaminopyridine, and N-methylpiperidine in DMF upon heating, affording amphiphilic derivatives **10–13** in 60–67 % yields (Figure 3). A similar trend was observed for this series, where the yields remained largely unaffected by the amine's nucleophilicity, further supporting the steric control exerted by the bulky triterpenoid core. The structures of the obtained compounds were confirmed by a comprehensive set of spectral studies, including 1D and 2D NMR spectroscopy data.

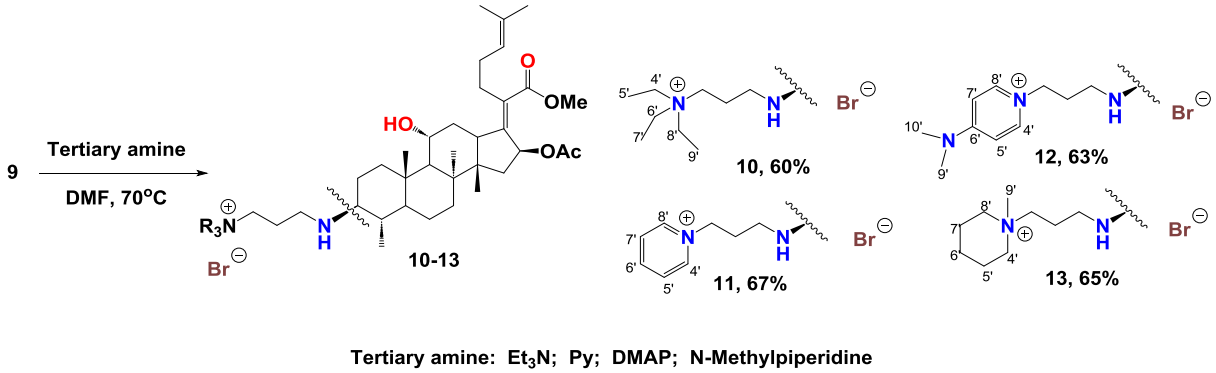

Figure 3. Synthesis of quaternized derivatives **10–13** from compound **9**

Conclusions

Brominated analogs of fusidane triterpenoids were synthesized via esterification of the FA carboxylic group with 1,2-dibromoethane and by reductive amination of the methyl fusidate diketone derivative with 3-bromopropylamine. Quaternization of aliphatic and aromatic tertiary amines with the resulting fusidane bromo derivatives afforded novel amphiphilic fusidic acid analogs, which are of interest as potential antibacterial agents with membrane-tropic activity.

Funding

This study was carried out in the framework of state assignment to the Institute of Petrochemistry and Catalysis (project no. FMRS-2025-0033).

*Author Information**

**The authors' names are presented in the following order: First Name, Middle Name and Last Name*

Elena Viktorovna Salimova — Candidate of Chemical Sciences, Research Fellow, Organic Synthesis Laboratory, Institute of Petrochemistry and Catalysis, Ufa Federal Research Center of the Russian Academy of Sciences, prosp. Oktyabrya, 141, 450075, Ufa, Russia; *e-mail: salimovaev@mail.ru*; https://orcid.org/0000-0002-4328-5080

Rinat Ravilevich Gubaidullin — Candidate of Chemical Sciences, Research Fellow, Organic Synthesis Laboratory, Institute of Petrochemistry and Catalysis, Ufa Federal Research Center of the Russian Academy of Sciences, prosp. Oktyabrya, 141, 450075, Ufa, Russia; *e-mail: rinatg83@mail.ru*; https://orcid.org/0000-0002-9915-0820

Lyudmila Vyacheslavovna Parfenova (*corresponding author*) — Doctor of Chemical Sciences, Head of Organic Synthesis Laboratory, Institute of Petrochemistry and Catalysis, Ufa Federal Research Center of the Russian Academy of Sciences, prosp. Oktyabrya, 141, 450075, Ufa, Russia; *e-mail: luda_parfenova@mail.ru*; https://orcid.org/0000-0003-2816-2178

Author Contributions

The manuscript was written through contributions of all authors. All authors have given approval to the final version of the manuscript. CRediT: **Elena Viktorovna Salimova –** data curation, investigation, methodology, validation, visualization, writing—original draft; **Rinat Ravilevich Gubaidullin –** formal analysis, writing—original draft; **Lyudmila Vyacheslavovna Parfenova –** conceptualization, funding acquisition, resources, supervision, validation, writing-review & editing.

Acknowledgments

Structural studies of the synthesized compounds were performed with the use of the Collective Usage Centre "Agidel" at the Institute of Petrochemistry and Catalysis of the Russian Academy of Sciences (RAS).

Conflicts of Interest

The authors declare no conflict of interest.

References

1 Gerba, C. P. (2015). Quaternary ammonium biocides: Efficacy in application. *Applied and Environmental Microbiology, 81*(2), 464–469. https://doi.org/10.1128/AEM.02633-14

2 Chanawanno, K., Thuptimdang, P., Chantrapromma, S., & Fun, H. K. (2022). New tunable pyridinium benzenesulfonate amphiphiles as anti-MRSA quaternary ammonium compounds (QACs) *Journal of Molecular Structure, 1254*, 132389. https://doi.org/10.1016/j.molstruc.2022.132389

3 Walker, E. B. (2002). Chapter 5. In D.S. Paulson (Ed.), *Handbook of topical antimicrobials: Industrial applications in consumer products and pharmaceuticals*. CRC Press. https://doi.org/10.1201/9780203909256

4 Savage, P. B., Li, C., Taotafa, U., Ding, B., & Guan, Q. (2002). Antibacterial properties of cationic steroid antibiotics. *FEMS Microbiology Letters, 217*(1), 1–7. https://doi.org/10.1111/j.1574-6968.2002.tb11448.x

5 Wessels, S., & Ingmer, H. (2013). Modes of action of three disinfectant active substances: a review. *Regulatory Toxicology and Pharmacology, 67*, 456–467. https://doi.org/10.1016/j.yrtph.2013.09.006

6 Jennings, M. C., Minbiole, K. P. C., & Wuest, W. M. (2015). Quaternary Ammonium Compounds: An Antimicrobial Mainstay and Platform for Innovation to Address Bacterial Resistance. *ACS Infectious Diseases, 1*, 288–303. https://doi.org/10.1021/acsinfecdis.5b00047

7 Schrank, C. L., Minbiole, K. P. C., & Wuest, W. M. (2020). Are Quaternary Ammonium Compounds, the Workhorse Disinfectants, Effective against Severe Acute Respiratory Syndrome-Coronavirus-2?. *ACS Infectious Diseases, 6*, 1553–1557. https://doi.org/10.1021/acsinfecdis.0c00265

8 Chanawanno, K., Chantrapromma, S., Anantapong, T., Kanjana-Opas, A., & Fun, H. K. (2010). Synthesis, structure and *in vitro* antibacterial activities of new hybrid disinfectants quaternary ammonium compounds: Pyridinium and quinolinium stilbene benzenesulfonates. *European Journal of Medicinal Chemistry, 45*, 4199–4208. https://doi.org/10.1016/j.ejmech.2010.06.014

9 Forman, M. E., Jennings, M. C., Wuest, W. M., & Minbiole, K. P. C. (2016). Building a Better Quaternary Ammonium Compound (QAC): Branched Tetracationic Antiseptic Amphiphiles. *ChemMedChem, 11*, 1401–1405. https://doi.org/10.1002/cmdc.201600176

10 Joyce, M. D., Jennings, M. C., Santiago, C. N., Fletcher, M. H., Wuest, W. M., & Mibiole, K. P. (2016). Natural product-derived quaternary ammonium compounds with potent antimicrobial activity. *Journal of Antibiotics, 69*, 344–347. https://doi.org/10.1038/ja.2015.107

11 Sapozhnikov, S. V., Sabirova, A. E., Shtyrlin, N. V., Druk, A. Y., Agafonova, M. N., Chirkova, M. N., Kazakova, R. R., Grishaev, D. Y., Nikishova, T. V., Krylova, E. S., Nikitina, E. V., Kayumov, A. R., & Shtyrlin, Y. G. (2021). Design, synthesis, antibacterial activity and toxicity of novel quaternary ammonium compounds based on pyridoxine and fatty acids. *European Journal of Medicinal Chemistry, 211*, 113100. https://doi.org/10.1016/j.ejmech.2020.113100

12 Yamanaka, T., Bannai, H., Tsujimura, K., Nemoto, M., Kondo, T., & Matsumura, T. (2014). Comparison of the Virucidal Effects of Disinfectant Agents Against Equine Influenza A Virus. *Journal of Equine Veterinary Science, 34*, 715–718. https://doi.org/10.1016/j.jevs.2013.12.010

13 Nyström, L., & Malmsten, M. (2018). Membrane interactions and cell selectivity of amphiphilic anticancer peptides. *Current Opinion in Colloid & Interface Science, 38*, 1–17. https://doi.org/10.1016/j.cocis.2018.06.009

14 Yang, J. S., Song, D., Lee, B., Ko, W. J., Park, S. K., Won, M., Lee, K., Kim, H. M., & Han, G. (2011). Synthesis and biological evaluation of novel aliphatic amido-quaternary ammonium salts for anticancer chemotherapy: Part I. *European Journal of Medicinal Chemistry, 46*, 2861–2866. https://doi.org/10.1016/j.ejmech.2011.04.009

15 Song, D., Yang, J. S., Oh, C., Cui, S., Kim, B. K., Won, M., Lee, J. I., Kim, H. M., & Han, G. (2013). New synthetic aliphatic sulfonamido-quaternary ammonium salts as anticancer chemotherapeutic agents. *European Journal of Medicinal Chemistry, 69*, 670–677. https://doi.org/10.1016/j.ejmech.2013.09.022

16 Dubinin, M. V., Semenova, A. A., Ilzorkina, A. I., Penkov, N. V., Nedopekina, D. A., Sharapov, V. A., Khoroshavina, E. I., Davletshin, E. V., Belosludtseva, N. V., Spivak, A. Y., Belosludtsev, K. N., et al. (2021). Mitochondria-targeted prooxidant effects of betulinic acid conjugated with delocalized lipophilic cation F16. *Free Radical Biology and Medicine, 168*, 55–69. https://doi.org/10.1016/j.freeradbiomed.2021.03.036

17 Dey, G., Bharti, R., Sen, R., & Mandal, M. (2015). Microbial amphiphiles: a class of promising new-generation anticancer agents. *Drug Discovery Today, 20*, 136–146. https://doi.org/10.1016/j.drudis.2014.09.006

18 Ciumac, D., Gong, H., Hu, X., & Lu, J. R. (2019). Membrane targeting cationic antimicrobial peptides. *Journal of Colloid and Interface Science, 537*, 163–185. https://doi.org/10.1016/j.jcis.2018.10.103

19 Dubinin, M. V., Semenova, A. A., Ilzorkina, A. I., Markelova, N. Y., Penkov, N. V., Shakurova, E. R., Belosludtsev, K. N., & Parfenova, L. V. (2021). New quaternized pyridinium derivatives of betulin: Synthesis and evaluation of membranotropic properties on liposomes, pro- and eukaryotic cells, and isolated mitochondria. *Chemico-Biological Interactions, 349*, 109678. https://doi.org/10.1016/j.cbi.2021.109678

20 Pasquale, E. D., Salmi-Smail, C., Brunel, J. M., Sanchez, P., Fantini, J., & Maresca, M. (2010). Biophysical studies of the interaction of squalamine and other cationic amphiphilic molecules with bacterial and eukaryotic membranes: Importance of the distribution coefficient in membrane selectivity. Chemistry and Physics of Lipids, 163, 131–140. https://doi.org/10.1016/j.chemphyslip.2009.10.006

21 Krasutsky, P. A., Avilov, D., Sergeeva, T., Krasutsky, D. A., & Kolomitsyna, O. (2008). *US Patent No. 7,199,114 B2*.

22 Kataev, V. E., Strobykina, I. Yu., & Zakharova, L. Ya. (2014). Quaternary ammonium derivatives of natural terpenoids. Synthesis and properties. *Russian Chemical Bulletin, 63*, 1884–1900. https://doi.org/10.1007/s11172-014-0680-x

23 Zhao, M., Godecke, T., Gunn, J., Duan, J. A., & Che, C. T. (2013). Protostane and Fusidane Triterpenes: A Mini-Review. *Molecules, 18*, 4054–4080. https://doi.org/10.3390/molecules18044054

24 Dziwornu, G. A., Kamunya, S., Ntsabo, T., & Chibale, K. (2019). Novel antimycobacterial C-21 amide derivatives of the antibiotic fusidic acid: synthesis, pharmacological evaluation and rationalization of media-dependent activity using molecular docking studies in the binding site of human serum albumin. *MedChemComm, 10*, 961–969. https://doi.org/10.1039/c9md00161a

25 Guo, M., Ren, Q., Wang, B., Ji, W., Ni, J., Feng, Y., Bi, Y., Tian, J., & Wang, H. (2019). Discovery and synthesis of 3- and 21-substituted fusidic acid derivatives as reversal agents of P-glycoprotein-mediated multidrug resistance. *European Journal of Medicinal Chemistry, 182*, 111668. https://doi.org/10.1016/j.ejmech.2019.111668

26 Ni, J., Guo, M., Cao, Y., Lei, L., Liu, K., Wang, B., Lu, F., Zhai, R., Gao, X., Yan, C., Wang, H., & Bi, Y. (2019). Discovery, synthesis of novel fusidic acid derivatives possessed amino-terminal groups at the 3-hydroxyl position with anticancer activity. *European Journal of Medicinal Chemistry, 162*, 122–131. https://doi.org/10.1016/j.ejmech.2018.10.059

27 Espinoza-Moraga, M., Singh, K., Njoroge, M., Kaur, G., Okombo, J., De Kock, C., Smith, P. J., Wittlin, S., & Chibale, K. (2017). Synthesis and biological characterisation of ester and amide derivatives of fusidic acid as antiplasmodial agents. *Bioorganic & Medicinal Chemistry Letters, 27*, 658–661. https://doi.org/10.1016/j.bmcl.2016.11.077

28 Salimova, E. V., Magafurova, A. A., Tretyakova, E. V., Kukovinets, O. S., & Parfenova, L. V. (2020). Indole Derivatives of Fusidane Triterpenoids: Synthesis and the Antibacterial Activity. *Chemistry of Heterocyclic Compounds, 56*, 800–804. https://doi.org/10.1007/s10593-020-02733-1

29 29. Salimova, E. V., & Parfenova, L. V. (2021). Synthesis and Biological Activity of Oximes, Amines, and Lactams of Fusidane Triterpenoids. *ChemistrySelect, 6*, 8848–8854. https://doi.org/10.1002/slct.202102019

30 Salimova, E. V., Mamaev, A. G., Tretyakova, E. V., Kukovinets, O. S., Mavzyutov, A. R., Shvets, K. Yu., & Parfenova, L. V. (2018). Synthesis and Biological Activity of Cyanoethyl Derivatives of Fusidic Acid. *Russian Journal of Organic Chemistry, 54*, 1411–1418. https://doi.org/10.1134/S1070428018090245

31 Salimova, E. V., Mamaev, A. G., Tretyakova, E. V., Kukovinets, O. S., & Parfenova, L. V. (2018). Reductive amination of fusidane triterpenoid ketones. *Mediterranean Journal of Chemistry, 7*, 198–203. https://doi.org/10.13171/mjc7318106921-salimova

32 Salimova, E. V., Tret'yakova, E. V., & Parfenova, L. V. (2019). Synthesis and cytotoxic activity of 3-amino substituted fusidane triterpenoids. *Medicinal Chemistry Research, 28*, 2171–2183. https://doi.org/10.1007/s00044-019-02445-y

33 Salimova, E. V., Tret'yakova, E. V., Kukovinets, O. S., & Parfenova, L. V. (2020). Beckmann Rearrangement of Oximes of the Fusidane Series. *Russian Journal of Organic Chemistry, 56*, 11–19. https://doi.org/10.31857/S0514749220010036

34 Salimova, E. V., & Parfenova, L. V. (2022). Fischer Reaction in the Synthesis of New Triterpene Indoles of the Fusidane Series. *Russian Journal of Organic Chemistry, 58*, 25–37. https://doi.org/10.1134/S1070428022010031

35 Salimova, E. V., Mannanova, L. R., Kukovinets, O. S., & Parfenova, L. V. (2022). Synthesis of Halo Derivatives of Fusidane Triterpenoids. *Russian Journal of Organic Chemistry, 58*, 968–976. https://doi.org/10.1134/S1070428022070041

36 Geresh, S., Dawadi, R. P., & Arad, S. M. (2000). Chemical modifications of biopolymers: quaternization of the extracellular polysaccharide of the red microalga Porphyridium sp. *Carbohydrate Polymers, 43*, 75–80. https://doi.org/10.1016/S0144-8617(99)00194-0

37 Vila, C., Díaz-García, P., Ladeira, S., Balerdi, M., & Freixa, Z. (2020). Catalytic reductive amination of aldehydes and ketones with nitro compounds: New light on an old reaction. *Frontiers in Chemistry, 8*, 215. https://doi.org/10.3389/fchem.2020.00215

How to Cite: Bedritskikh, K.S., Saeidi, A., Ivanova, A.E., Pestov, A.V., Litvinova, E.A., & Drannikov, A.A. (2026). Sulfoethyl Chitosan: From Synthesis and Physicochemical Characterization to Functional Applications and Patent Perspectives. *Eurasian Journal of Chemistry, 31, 3(123), 14–37.* https://doi.org/10.31489/2959-0663/3-26-12

Review

Received: 25 June 2026 | Revised: 24 August 2026 |
Accepted: 27 August 2026 | Published online: 2 September 2026

UDC 547-31/-39

https://doi.org/10.31489/2959-0663/3-26-12

Ksenia S. Bedritskikh[1,2*], Arsalan Saeidi[1,2], Anna E. Ivanova[1], Alexandr V. Pestov[3], Ekaterina A. Litvinova[1,2,4], Aleksandr A. Drannikov[1,2,5]

[1]*Novosibirsk State Technical University, Novosibirsk, Russia*
[2]*Novosibirsk State University, Novosibirsk, Russia*
[3]*I.Ya. Postovsky Institute of Organic Synthesis, Ural Branch, Russian Academy of Sciences, Yekaterinburg, Russia*
[4]*Samarkand State University named after Sharof Rashidov, Samarkand, Uzbekistan*
[5]*N.N. Vorozhtsov Novosibirsk Institute of Organic Chemistry of Siberian Branch of Russian Academy of Sciences, Novosibirsk, Russia*
*(*Corresponding author's e-mail: k.bedri.16@gmail.com)*

Sulfoethyl Chitosan: From Synthesis and Physicochemical Characterization to Functional Applications and Patent Perspectives

Sulfoethyl chitosan (SEC) is an anionic chitosan derivative obtained through N-, O-, or mixed O, N-substitution with sulfoethyl groups, which significantly enhances water solubility across a wide pH range, imparts strong polyelectrolyte character, and confers heparin-mimicking biological properties. This review provides a comprehensive overview of SEC synthesis approaches, chemoselective routes thereof, and the influence of the degree of substitution (DS) and substitution pattern on solubility, swelling, thermal stability, and metal-ion sorption selectivity. Characterization techniques including ^{1}H NMR, elemental analysis, FT-IR, X-ray diffraction and molecular weight determination approaches are discussed with their specific challenges for polyelectrolyte derivatives, including sample purity and aggregation. The impact of sulfoethylation on biological properties including anticoagulant activity, hemocompatibility, cytotoxicity, antimicrobial effect, DNA protective activity was evaluated for sulfoethylated chitosan and its precursors, chitin and chitin-glucan complex, revealing distinct structure-activity trends governed by the degree of acetylation and substitution pattern. Representative applications include selective solid-phase extraction of copper from environmental waters, anticoagulant coatings, and macroporous cryogels for long-term bacterial stabilization at ambient temperatures over 12 months. Despite its versatility, SEC remains under-patented compared to other chitosan derivatives. Critical knowledge gaps persist, including the absence of systematic DS-bioactivity and regioselectivity-bioactivity relationships and long-term stability studies, which raises doubts on the industrial demand of the biopolymer. Future perspectives emphasize standardized protocols for characterization and for biological activity assessment, pilot manufacturing with reduced toxic and environmental impact, and interdisciplinary efforts to develop advanced functional materials. With focused attention on these priorities, SEC has potential to transition from a laboratory derivative to a commercially viable biopolymer.

Keywords: sulfoethyl chitosan, biopolymer, polysaccharide, sulfoethylation, synthesis, characterization, chitosan derivatives, patent landscape.

Contents

© 2026 The Authors. This is an open access article under the CC BY-NC-ND license (http://creativecommons.org/licenses/by-nc-nd/4.0/

List of abbreviations

AUC: analytical ultracentrifugation
DLS: dynamic light scattering
DS: degree of substitution
FT-IR: Fourier transform Infrared spectroscopy
GA: glutaraldehyde
GlcN: D-glucosamine
GlcNAc: N-acetyl-D-glucosamine
Gp: genipin
IPA: isopropyl alcohol
MKH: Mark-Kuhn-Houwink
MW: molecular weight
NaBES: sodium 2-bromoethylsulfonate
NaCES: sodium 2-chloroethylsulfonate
NaVS: sodium vinylsulfonate
N-SEC: N-sulfoethyl chitosan
O, N-SEC: O, N-sulfoethyl chitosan
O-SEC: O-sulfoethyl chitosan
SEC: sulfoethyl chitosan
SE-C: sulfoethylated chitin
SE-CG: sulfoethylated chitin-glucan complex
SLS: static light scattering

1 Review Plan

This critical review employed a structured literature search to identify all relevant publications on SEC. The search was conducted across major scientific databases including Scopus, Web of Science, PubMed, and Google Scholar, using the following search string: ("sulfoethyl chitosan" OR "N-sulfoethyl chitosan" OR "O-sulfoethyl chitosan" OR "N, O-sulfoethyl chitosan") AND ("synthesis" OR "characterization" OR "application" OR "properties"). No date restrictions were applied to ensure comprehensive coverage of the historical development of SEC chemistry. The search was supplemented by manual screening of reference lists from retrieved articles and review papers to identify additional relevant studies. Inclusion criteria comprised original research articles, review papers, and patent documents reporting on SEC synthesis, physicochemical characterization, or functional applications. Studies were excluded if they (i) focused exclusively on other chitosan derivatives without comparative SEC data, or (ii) lacked sufficient experimental detail for critical evaluation. The retrieved literature was organized thematically according to the three main axes of the review: synthesis methodology, structural characterization, and application domains. This combined approach ensured comprehensive coverage while maintaining focus on the specific chemistry and applications of SEC.

2 Introduction

Chitosan is a naturally derived, cationic biopolymer obtained through the chemical deacetylation of chitin, the second most abundant natural biopolymer after cellulose occurring as a major fraction of the exoskeletal matrices of crustaceans, including either shrimps or crabs, but also derived from insects, as well as the cell walls of certain fungi. As a derivative of chitin, chitosan retains its precursor's structural backbone composed of β-(1→4)-linked D-glucosamine (GlcN) and N-acetyl-D-glucosamine (GlcNAc) units [1, 2].

The presence of free amino groups along its polymeric chain highlights distinguishes chitosan among numerous naturally-derived polymers, providing its advantageous properties, including biodegradability, biocompatibility, mucoadhesivity, and intrinsic antimicrobial activity. In this regard chitosan has been established as a sustainable and environmentally friendly alternative to synthetic polymers in biomedical, pharmaceutical, agricultural, and environmental applications [3-5].

However, the same properties that enable its functionality also impose limitations. Thus, chitosan is only soluble in dilute acidic media with a pH below 6.5, exhibits poor mechanical stability in physiological environments, and offers limited control over its bioactivity profile [6, 7].

These shortcomings have motivated a rich field of chemical modification aimed at tailoring chitosan's physicochemical and biological behavior for specific applications [8, 9]. The resulting wide arsenal of chemical modification strategies has been developed to introduce functional groups into the chitosan backbone. Among the primary targets are the C-2 amino group and the C-3 and C-6 hydroxyl groups, each offering distinct reactivity patterns (Figure 1) [10, 11].

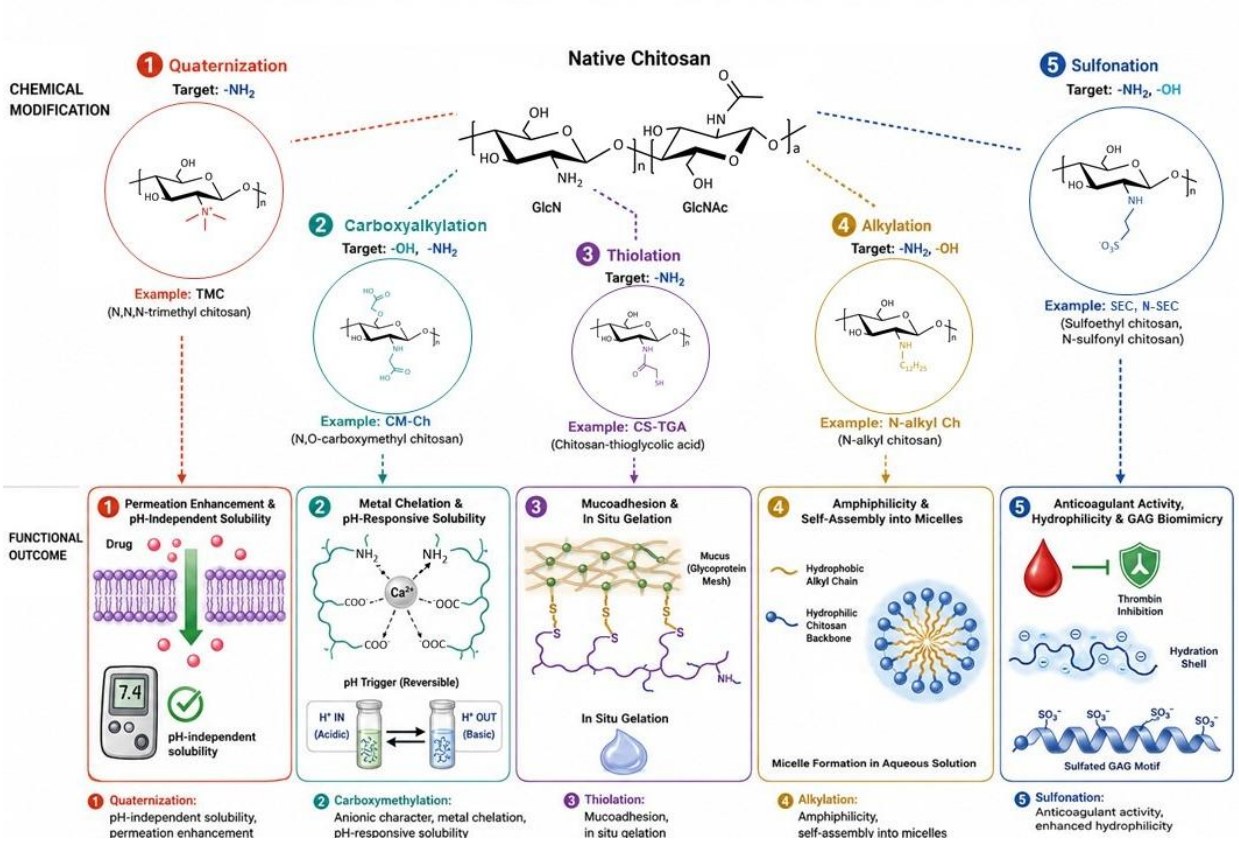

Figure 1. Key targets for chemical modification of chitosan.

Note: The conceptual graphical layout and illustrative elements were assisted using ChatGPT-4o. Chemical structures and reaction schemes were manually verified and curated by the authors for scientific accuracy

For instance, quaternization of the amino group yields N,N,N-trimethyl chitosan, which exhibits enhanced water solubility and permeation-enhancing effects irrespective of pH [12, 13], which allows chitosan's application in drug delivery, while carboxyalkylation, typically at O-6 or N-2 positions, introduces anionic character, enabling pH-responsive solubility and metal chelation [14-17]. Thiolation improves mucoadhesion and in situ gelling capacity via disulfide bond formation with cysteine-rich mucus glycoproteins [18]. And either alkylation or acylation allows modulation of the amphiphilicity, promoting self-assembly into nanoparticles for hydrophobic drug delivery [19].

Each modification, however, involves trade-offs: increased solubility may come at the cost of biodegradability as demonstrated by carboxyalkylation, while enhanced bioactivity may reduce mechanical integrity. Recognizing these patterns is essential before focusing on a particularly promising but underexplored class of modifications — the introduction of sulfo groups.

Sulfo groups (-SO_3H or their anionic form -SO_3^-) take a special place in biopolymer chemistry. Naturally sulfated polysaccharides such as carrageenan obtained from red algae, fucoidan derived from brown algae, or heparin extracted from animal tissues mediate critical biological processes including anticoagulation, antiviral defense, inflammation modulation, and growth factor sequestration [20, 21].

The biological activity of these molecules is strongly correlated with their degree and pattern of sulfation. For example, κ-carrageenan, with one sulfate per disaccharide, primarily formulates gels, while λ-

carrageenan, with three sulfate groups per disaccharide, remains water soluble and exhibits stronger immunomodulatory effects [22-24].

Synthetic introduction of sulfo groups into biopolymers thus represents a rational strategy to mimic nature's sulfated glycosaminoglycans while overcoming the heterogeneity and supply limitations of natural extracts, such as heparin [25, 26].

Compared to carboxyl or amino modifications, sulfo groups confer strong negative charge even at low pH, high hydrophilicity, and specific interactions with positively charged protein domains — properties exploited in heparin-like anticoagulant materials and in scaffolds for growth factor delivery [27-29].

Notably, carrageenan itself has been extensively studied, but its rigid backbone and fixed sulfation pattern limit tunability [30-32]. Chitosan, by contrast, offers a flexible platform where the number and position of sulfo groups can be precisely controlled via synthetic chemistry [33, 34].

Against this backdrop, SEC — a derivative bearing sulfoethyl groups typically introduced via reaction of chitosan with sodium 2-chloroethylsulfonate (NaCES), sodium vinylsulfonate (NaVS) or sodium 2-bromoethylsulfonate (NaBES) — has emerged as a particularly interesting candidate. Early studies suggested that introducing sulfoethyl moieties preserves chitosan's film-forming ability while dramatically improving water solubility and imparting anticoagulant activity reminiscent of heparin [35-39].

However, a comprehensive and critical synthesis of the literature on SEC has been lacking. Individual reports focus either on synthetic optimization, on structural characterization (e.g., degree of substitution, patterns of O- vs N-substitution), on functional properties (solubility, viscosity, thermal stability), or on biological assays. Moreover, contradictions exist regarding the relationship between the degree of substitution (DS) and biological efficacy, and no systematic comparison of different sulfoethylation methods has been published, thus, the present review aims to address this gap.

3 Synthesis and Characterization

3.1 Sulfoethyl Chitosan Synthesis

The first documented synthesis of SEC is attributed to the pioneering work of Nud'ga et al. [40] who produced SEC with a DS of 0.11-0.35 and a sulfur content of 1.39-5.32 % by employing NaCES in the presence of alkali in isopropyl alcohol (IPA) and in mixtures of o-xylene with propyl and IPA. Both O-6- and N-sulfoethylation were confirmed by amino-nitrogen analysis and conductimetric titration. In another study, selective O-substitution was achieved by protecting the amino groups of chitosan with an aromatic aldehyde, resulting in the formation of a Schiff base. The final product had a highest DS of 0.31 [41-43].

Later recorded synthesis was made by Muzzarelli in 1992, who suspended water-insoluble N-carboxymethyl chitosan in IPA, followed by treatment with NaOH and NaCES [41].

A further contribution to understanding the reactivity and optimization of chitosan’s sulfoethylation came from the Nud'ga et al. research group in their 2001 comparative study [44]. Using sodium NaCES in IPA at 80 °C under alkaline conditions within a portionwise addition mechanism, they achieved the DS of 0.35 for chitosan. Under alkaline conditions the authors proposed that NaCES undergoes in situ dehydrohalogenation to form NaVS, after which the reaction proceeds via a Michael-type addition mechanism. The reaction with NaVS in similar conditions had been found significantly more efficient for chitosan sulfoethylation, yielding products with DS values of 0.76-0.98 that were completely soluble in water. Despite requiring an additional step (the preparation of NaVS from NaCES) along with the removal of NaCl, this approach offers substantial advantages, including lower NaOH consumption and minimal deacetylation of the chitin fraction [44].

A significant methodological advancement in the synthesis of SEC was reported by Pestov et al. in 2013, introducing a "synthesis in a gel" technique that has since become a foundational protocol for achieving highly regioselective N-substitution. In contrast to earlier developed heterogeneous methods using NaCES in alkaline organic media, which produced non‑selective N, O‑substitution with low DS ($\leq$ 0.35), the authors suggested a homogeneous protocol: chitosan finely dispersed in 0.8M HCl was left to swell for 10 min formulating a gel, afterwards NaBES was added, and the mixture was stirred at 70 °C heating for 24 h. The resulting reaction media was then neutralized with NaOH, SEC was precipitated with acetone, extracted with hot ethanol, and dried at 50 °C to constant weight. This reaction proceeds via an S_N2 mechanism, primarily resulting in N-substituted chitosan [45].

By performing the reaction in this acidic gel state, the authors suppressed the reactivity of the hydroxyl groups, directing the nucleophilic substitution almost exclusively to the primary amino groups on the chi-

tosan backbone. This strategy enabled the production of N-SEC with a substantially higher DS of up to 0.5. The high N-selectivity observed in neutral or mildly acidic conditions arises from the distinct nucleophilic properties of the functional groups on the chitosan backbone. Although a significant fraction of the primary amino groups is protonated under these conditions, a reactive equilibrium population of free $–NH_2$ remains available. These unprotonated amino groups are strongly nucleophilic and therefore the preferred site of attack. In contrast, the hydroxyl groups stay protonated and, in the absence of their conversion into alkoxide ions, possess only low intrinsic nucleophilicity, effectively suppressing O-substitution. As a result, the reaction proceeds with high selectivity towards nitrogen [46, 47]. In strongly alkaline conditions, however, the situation changes dramatically. The hydroxyl groups are partially deprotonated to form alkoxide ions ($–O^-$), which are much stronger nucleophiles. This leads to competing O-alkylation alongside N-substitution, resulting in reduced selectivity and often a mixture of N- and O-modified products [48-50]. By performing the reaction in a neutral or weakly acidic medium, O-substitution is minimized, enabling clean and highly selective N-functionalization of chitosan.

Another work of the same research group appeared in a study published by Petrova et al. in 2014. Herein the authors had refined the technique by successfully conducting the biopolymer-analogous transformation without the addition of any acid or base. In this optimized procedure, chitosan was simply mixed with sodium NaBES in water. During heating at 70 °C, the reaction mixture self-assembled into a physical gel as the progressively modified polymer became more hydrophilic. This novel approach in a neutral aqueous medium totally prevents O-substitution, resulting in N-SEC with a moderate DS of up to 0.55 and high yields about 81 % [51].

The suggested method represented a crucial step towards a simpler route for producing well-defined SEC. In a later study, varying the reaction parameters Petrova et al. reported the synthesis of N-SEC with a DS of up to 0.78 and up to 1.00, following a similar reaction pathway used in their previous work [52, 53]. Collectively, all reported methods for the preparation of N-SEC across different reaction conditions are presented in Table 1.

Table 1

SEC parameters depending on the reaction conditions

Molar ratio Chitosan: NaBES:HCl	Concentration of chitosan in reaction media, %	T, ˚C	Sulfur content, %	DS calculated by ^{1}H NMR data	Reference
1:1:0.25	21	70	5.06	0.31	[45]
1:1:0.5	23		4.17	0.24	
1:1:1	20		0.20	0	
1:2:0.25	23	50	5.24	0.30	
		70	6.55	0.44	
		90	6.23	0.46	
1:2:0.5	23	50	3.44	0.16	
	10	70	4.64	0.24	
	20		7.12	0.50	
	30		4.12	0.24	
1:2:0.5 (acetic acid)	20	70	6.45	0.40	
1:3:0.25	23	50	6.87	0.33	
1:3:0.5	23	50	3.28	0.16	
		70	4.86	0.30	
1:2:0	21	50	6.46	0.45	[51]
		70	7.48	0.55	
1:1:0	12	70	8.94	0.71	[52]
1:2:0	12	70	9.22	0.72	
	21	50	6.46	0.45	
		70	7.48	0.55	
1:3:0	12	70	9.66	0.78 (the DS was unchanged after 48 h)	
		90	9.32	0.70	
1:4:0	12	70	8.92	0.68	
1:5:0	8	70	9.01	0.70	
1:2:0	12	70	ns	1.0 (reaction was carried out for 12 h)	[53]

The data presented in Table 1 demonstrates that DS in the N-2-sulfoethylation of chitosan with NaBES in a gel phase was significantly influenced by the reaction parameters. The molar ratio of chitosan to NaBES and the amount of acid used for gel formation proved to be the most critical factors. An increase in the NaBES excess up to a 1:2-1:3 ratio enhanced the DS, whereas a further increase in the molar ratio did not result in higher DS. Notably, the presence of hydrochloric acid was essential for physical gel formation but exerted a pronounced negative effect on substitution efficiency; excess HCl (e.g., 1:1:1 ratio) completely suppressed the reaction (DS = 0), whereas reactions performed with minimal or no HCl afforded the highest DS values. Replacement of HCl with acetic acid had negligible impact on the DS, offering a safer alternative for gel preparation while maintaining comparable efficiency. The optimal chitosan concentration in the reaction medium was found to be approximately 12-20 %, consistent with a pronounced gel effect that maximizes local reagent concentration and minimizes diffusion limitations. The reaction temperature of 70 °C provided the highest DS, whereas lower temperatures (50 °C) halved the DS and higher temperatures (90 °C) yielded only slight or no additional benefit. This behavior is most readily explained by the onset of competing side-reactions of the alkylating agent NaBES that becomes kinetically significant above 70 °C. In aqueous media NaBES can undergo both hydrolysis to the inactive 2-hydroxyethanesulfonate and elimination of HBr to vinylsulfonate. Both conversions reduce the effective concentration of the S_N2-active reagent intended to interact with chitosan amino groups. Under the mildly acidic conditions used in several of the entries, a secondary contribution from limited acid-catalyzed scission of the polysaccharide backbone cannot be excluded, although the thermal sensitivity of the reagent itself turns out the primary limitation. Consequently, 70 °C represents the practical optimum that maximizes the rate of the desired N-alkylation while minimizing reagent loss.

The reaction time had limited influence on the outcome: most experiments were conducted for 24 h, a DS of 1.0 was achieved in one case after only 12 h, and prolongation of the reaction up to 48 h did not lead to any further increase in DS. These findings demonstrate that careful control of reaction conditions is crucial for achieving high degrees of N-substitution in SEC.

In contrast to the regioselective gel-phase protocols proposed by Pestov's group, earlier established N, O-sulfoethylation protocols considered heterogeneous conditions with NaCES in alkaline organic media. Owing to the high crystallinity and limited reactivity of chitosan, a pretreatment step was essential to disrupt intermolecular hydrogen bonds and expose the reactive sites.

In another study by Petrova et al., the biopolymer was pretreated by swelling in water for 5 days or through ultrasonication, followed by reaction of the swollen chitosan with excess NaCES in 85 % 2-propanol in the presence of NaOH (typical molar ratios chitosan:NaCES:NaOH = 1:6:6 or 1:6:9) under a nitrogen atmosphere at 80 °C for 3 h. Products were purified by dialysis and freeze-dried. The pretreatment increased the DS, improved water solubility at higher DS, and reduced intrinsic viscosity due to bulky substituents and partial degradation. This less selective route still enabled practical access to water-soluble SEC with tunable DS [37].

Gabriel and Heinze conducted a comparative study on the synthesis of SEC using two distinct reagents: NaVS in an alkaline IPA slurry (heterogeneous) and NaBES under acidic aqueous conditions (homogeneous). For the NaVS route, the authors modified the reagent stoichiometry (chitosan:NaVS:NaOH = 1:4:4) and reaction conditions (stirring for 1 h at room temperature followed by 5 h at 80 °C) relative to earlier protocols (e.g., a 1:6:6 ratio and a single 3 h step at 80 °C) [37]. A pivotal finding of this work was the exclusive formation of O-substituted chitosan at the C-3 and C-6 positions. Thus, it was demonstrated that quantitative conversion of NaCES to NaVS does not occur fully under the alkaline conditions. Residual NaCES therefore coexists with NaVS and reacts with chitosan predominantly via an S_N2 (Williamson-type) pathway, which favors N-substitution at the more nucleophilic amino groups. In contrast, pure NaVS under heterogeneous alkaline conditions (isopropanol/NaOH) promotes chemoselective O-substitution at the C-3 and C-6 hydroxyl groups. This distinction accounts for the mixed N, O-substitution patterns reported in earlier NaCES-based protocols and for the exclusively O-substituted products obtained when NaVS itself is used. In the same study, the NaBES protocol was also modified; chitosan was suspended in water (3 % gel concentration) under nitrogen, acidified with concentrated HCl for 10 minutes, and then reacted with NaBES at 70 °C for 24 hours [39].

Subsequent investigations generally aimed to refine the existing methodologies.

Another study was directed towards process purification facilitation when Bolshakov et al. developed a streamlined protocol employing a 1:2 molar ratio of chitosan to sodium NaBES. The reagents were mixed in their dry state, hydrated, and heated at 70 °C for 24 hours with periodic agitation. Following the addition of a

NaOH solution, the reaction mass was cooled, stirred intensively for 10 hours, and then shaken for 15 hours. The product was isolated by precipitation in acetone and dried at 40-50 °C. The principal advancement of this method was the simplification of the purification stage, effectively eliminating the laborious Soxhlet extraction required in earlier procedures [54].

More recently, Heise et al. revised the dual-reagent strategy, investigating the sulfoethylation of chitosan with both NaVS and NaBES under alkaline pH. Diverging from prior protocols, the NaVS reaction was conducted without IPA or a nitrogen atmosphere, which resulted in a comparatively lower DS of 0.69. Conversely, the NaBES reaction, performed in IPA under alkaline conditions, achieved a higher DS of 1.05. Notably, both synthetic pathways predominantly yielded O-substitution at the C-6 position [35].

In summary, the collective work of Pestov and Petrova established foundational protocols for synthesizing N-SEC with DS varying from 0.2 to 1. Subsequently, iterative modifications by other researchers, building upon both these methods and the earlier work of Nud'ga for O, N-substituted derivatives, have progressively steered the field towards the selective synthesis of O-SEC.

Overall, the synthetic routes for chitosan sulfoethylation can be summarized as presented in Figure 2.

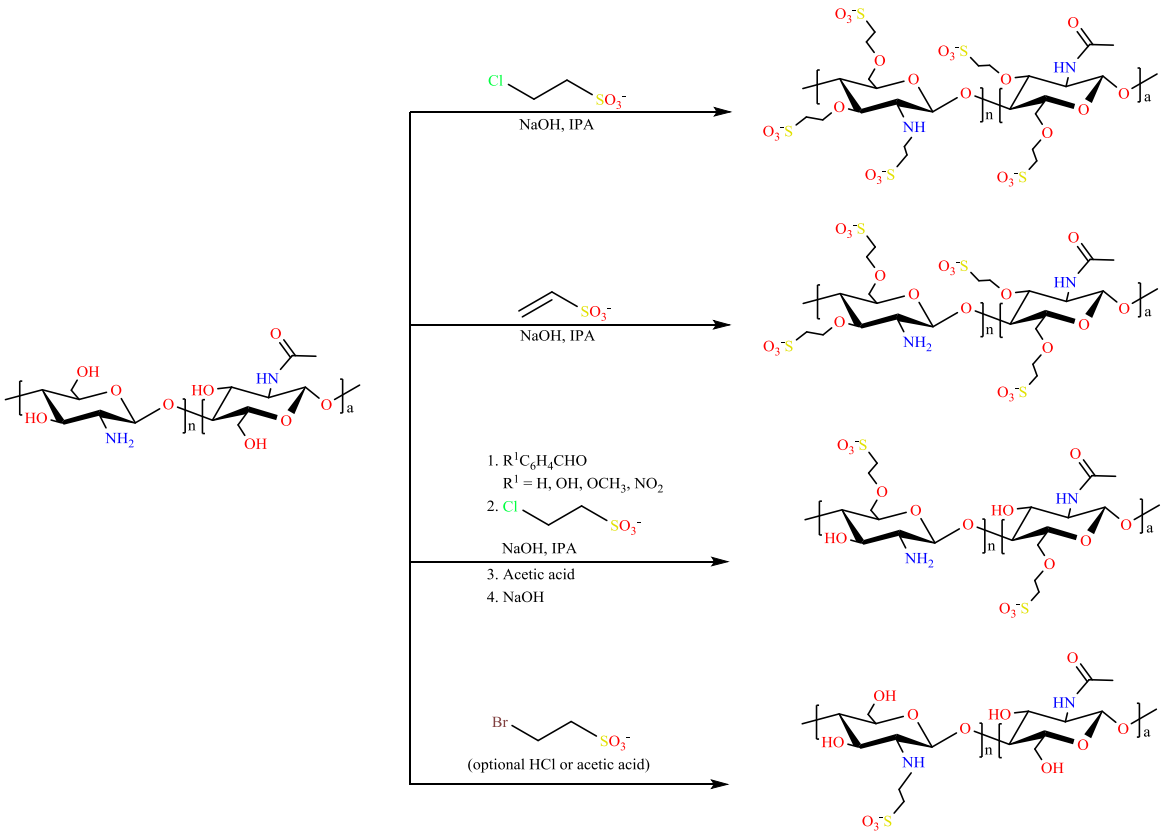

Figure 2. Synthetic routes of sulfoethyl chitosan

The DS of SEC is governed by several reaction parameters, including reagent, reagent ratio, reaction medium, temperature, reaction time, and pretreatment of the starting polymer. Early studies demonstrated that increasing the molar ratio of sulfoethylation reagent generally increases sulfur incorporation and, consequently, DS. However, excessively high reagent ratios may adversely affect the physicochemical properties of the final product.

So far, chemical approaches to synthesize SEC are various and well-studied. But still sulfoethylation of chitosan remains a laboratory-scale technology without market distribution.

Considering the reasons for that one would find that the synthesis of SEC traditionally relies on high-cost sulfoethylating agents. From an economic perspective, sodium NaCES is substantially more cost-effective than NaBES, but its lower reactivity and tendency to form NaVS in situ under alkaline conditions may limit the achievable DS [39]. This trade-off between reagent cost, reactivity, and substitution selectivity must be carefully considered when designing a scalable and economically viable synthesis route. Also, purification procedure typically involves precipitation with large volumes of organic solvents either ethanol or

acetone, followed by exhaustive dialysis, which contributes to a high E-factor [39]. Overall, the precursor costs, synthesis yield, and the amounts of chitosan and reagents turn out to be the key challenges for both economic and environmental sustainability [55]. This means that future research should prioritize the development and adaptation of greener methodologies for SEC production with systematic evaluation, to enable truly scalable and environmentally responsible manufacturing.

3.2 Characterization

Comprehensive physicochemical characterization of any biopolymer is a prerequisite for establishing reliable structure-property correlations and ensuring batch-to-batch reproducibility in both synthetic and applicative contexts. Analytical protocols must consider multiple hierarchical levels of structural organization, including primary structure, molar mass characteristics, and conformational behavior in solution, all of which govern macroscopic properties such as rheology, complexation ability, and bioactivity. In the case of SEC, the introduction of anionic sulfoethyl groups further complicates the analytical landscape: the presence of strong acid sulfonate moieties not only enhances polyelectrolyte character and modulates the overall charge density but also introduces additional variables, such as the position of substitution (O-, N- or mixed substitution), the relative distribution along the polymer chain, and the resulting changes in the hydrophile–lipophile balance. Moreover, the charged nature of the derivative makes its solution properties highly sensitive to ionic strength, pH, and counterion type, necessitating analytical strategies capable of distinguishing between substitution-derived effects and those arising from purely conformational or associative phenomena. Consequently, a rigorously designed analytical framework for SEC must integrate complementary orthogonal techniques that address both covalent structural features and non-covalent dynamic behavior, thereby enabling unambiguous interpretation of its functional performance.

3.2.1 Sulfoethylation Confirmation and Degree of Substitution

The proton magnetic resonance analysis is a typical procedure for structure investigation but one of the key methods to determine the DS. Its accurate determination is essential for rationalizing SEC data, since DS directly affects the polymer's hydrodynamic radius and its interaction with the stationary phase. Petrova et al. suggested the formula for calculating the DS from 1H NMR spectra represented by equation (1) [51]

$$DS = \frac{m + 2d}{m + d + a}, \quad (1).$$

However, we suggest that the degree of acetylation (DA) of chitosan shall be considered, so the formula version of this expression that additionally accounts for this will be described by the equation (2):

$$DS = \left(\frac{m + 2d}{m + d + a} \right) \times (1 - DA), \quad (2)$$

where *m* — the mole fraction of monosulfoethylated glucosamine units, *d* — the mole fraction of disulfoethylated glucosamine units, *a* — the mole fraction of glucosamine units, *DA* — degree of acetylation. *m*, *d*, and *a* values were calculated using integral intensities of the corresponding signals in ^{1}H NMR spectrum.

The spectrum also reveals the structure of the biopolymer reflecting its modification type. For N-SEC the typical ^{1}H NMR spectrum can be described as (D_2O/DCl), δ, ppm: 2.08 (CH_3), 3.23 (H 2 $GlcNH_2$), 3.35 ($NHCH_2CH_2$), 3.44–4.10 (H 2,3,4,5,6 $NHCH_2CH_2$), 4.62 (H 1 GlcNHAc), 4.94 (H 1 $GlcNH_2$), 5.06 (H 1 $GlcNHCH_2CH_2$), 5.12 (H 1 $GlcN(CH_2CH_2SO_3H)2$) [51], while O-SEC shows the overlapping NMR pattern in the H-1 region as indicating mainly free amino groups with a small amount of N-monosubstituted SEC [37].

Another independent approach to investigate and cross-validate the DS values obtained from ^{1}H NMR is C, H, N, S elemental analysis. It is typically used to characterize the DS using the equation represented by equation (3):

$$DS = \frac{\omega(S) \times M(N)}{\omega(N) \times M(S)} \times 100\%, \quad (3)$$

where ω*(S)* and ω*(N)* are the mass fractions and *M(S)* and *M(N)* are the atomic weights of sulfur and nitrogen, respectively [37].

This method is particularly advantageous for SEC analysis due to the fixed nitrogen content per repeating polysaccharide unit (one N atom per glucosamine ring), while the sulfur content scales linearly with the number of introduced sulfoethyl groups.

However, the elemental analysis critically depends on the sample's purity. The often underestimated concern is that any nitrogen- or sulfur-containing impurities including residual unreacted reagents, inorganic salts, solvents, or by-products will distort the elemental composition data and lead to an incorrect DS value. This problem is particularly acute in polysaccharide chemistry, where the high molecular weight and macromolecular nature of the polymer make it hard to remove low-molecular-weight contaminants completely [56]. The removal of low-molecular-weight impurities from SEC samples is typically achieved by exhaustive dialysis against deionized water followed by lyophilization. This approach was employed by Gabriel and Heinze [39] in their chemoselective sulfoethylation study, where the reaction product was purified by dialysis to remove residual NaVS and other by-products prior to characterization. Similarly, Petrova et al. [53] utilized ethanol precipitation and extensive washing to purify N-SEC after synthesis, ensuring removal of unreacted NaBES before analysis for DS calculation.

Consequently, following a proper sample preparation the calculated DS reflects the average number of substituents per monomer unit, providing a bulk compositional parameter that complements the site-specific information available from NMR.

Covalently bound sulfonates can be successfully detected by Fourier transform Infrared spectroscopy (FT-IR). While investigating the FT-IR spectrum one should consider the background of the characteristic chitosan bands — broad N-H and O-H stretching (≈3376 cm^{-1}), C-H stretching (≈2881 cm^{-1}), amide I (≈1652 cm^{-1}), and C-O/C-C vibrations (≈1067 cm^{-1}) while for SEC new intense absorption bands appear in the regions of 1159-1164 cm^{-1} and 1040-1043 cm^{-1}, corresponding to the asymmetric and symmetric S=O stretching vibrations of the sulfonate group. Additional characteristic bands at approximately 740-744 cm^{-1} and 594 cm^{-1} are attributed to C-S and C-SO_3 stretching vibrations, respectively [45, 51, 54].

The position and shape of these bands, together with changes in the amino/hydroxyl regions, allow differentiation of the substitution patterns. In O-substituted chitosan, the band with a maximum at 1530 cm^{-1} is particularly prominent as a complex band arising from the overlap of amide II (1550-1560 cm^{-1}) and protonated amino group (1560-1520 cm^{-1}) contributions [37, 39].

Complementary Raman spectroscopy provides further structural insight, revealing new bands at 745 cm^{-1} (S–C stretching) and 1044 cm^{-1} (symmetric SO_3^- stretching), along with enhanced CH_2-related vibrations (2940 cm^{-1} ν_{sym}/a_{sym}, 1410 cm^{-1} δ, 806 cm^{-1} ρ) due to the introduced ethylene spacer. Importantly, the intensity of these sulfoethyl-specific bands increases proportionally with the DS, offering a convenient qualitative tool for monitoring the extent of modification [35]. These combined vibrational data corroborate the substitution patterns established by NMR and elemental analysis.

Overall, key analysis of SEC can be structured as represented in Figure 3.

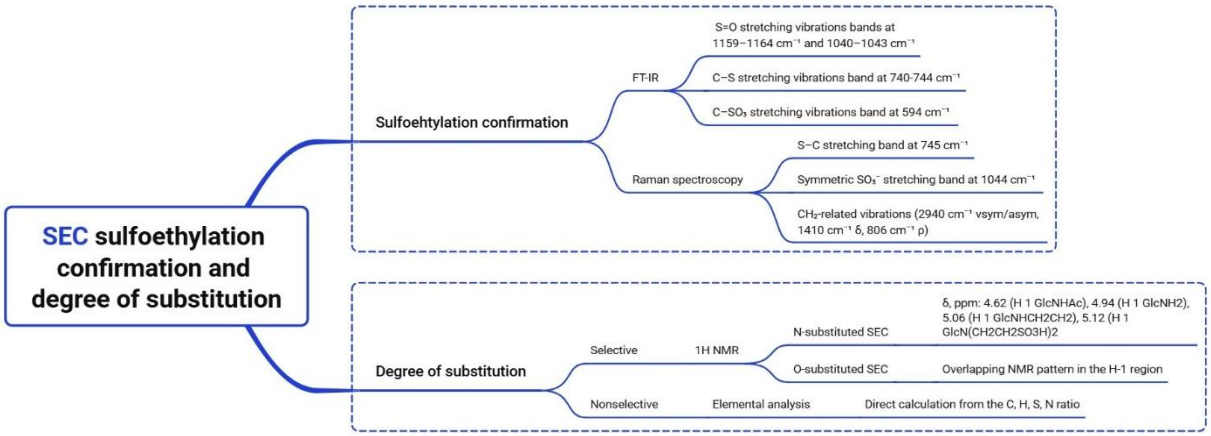

Figure 3. Sulfoethylation confirmation and degree of substitution of SEC

3.2.2 Molecular Structure

X-ray diffraction analysis of SEC films cast from 2 % acetic acid solutions, which resulted in protonated amino groups and sulfonate groups predominantly in the anionic form, initially balanced by acetate and

residual sodium counter-ions, revealed significant changes in the supramolecular structure compared to unmodified chitosan. The native chitosan film exhibited a characteristic reflection at 2θ = 20-22°, typical of its semi-crystalline structure. On the contrary, introduction of sulfoethyl groups led to progressive amorphization of the polymer, manifested as weakening or broadening of the main reflection and the appearance of a diffuse halo at 20-23°. This effect became more pronounced with increasing DS. Additionally, new reflections appeared (e.g., at 13° for hydrated chitosan polymorph in SEC with DS = 0.45 and at 16.5° for anhydrous polymorph in aged SEC with DS = 0.94), indicating the presence of different crystalline modifications. Notably, SEC films gradually lost solubility in 2 % acetic acid and water upon storage (partially after 3 months, completely after 6 months), in contrast to much higher stability of chitosan films. The observed structuration during aging is attributed to the formation of intra- and intermolecular ionic crosslinks involving the sulfonate and amino groups, which enhances the ordering of the polymer matrix over time [37]. It should be noted that the crystalline/amorphous character of SEC is expected to differ substantially if the polymer is examined in the pure sodium-salt form, the fully protonated (acid) form, or after exchange with multivalent cations (e.g., Ca^{2+}), because ionic cross-linking by such cations can further rigidify or reorganize the network.

Increasing DS substantially modifies the supramolecular organization of N-SEC in solution. The intrinsic viscosity decreases continuously with increasing substitution, reflecting a reduction in hydrodynamic volume and molecular chain expansion. For example, intrinsic viscosity decreased from approximately 7.7 dL/g for native chitosan to about 1.5 dL/g for highly substituted derivatives. Simultaneously, the average aggregate size decreased markedly as DS increased.

At the same time dynamic light scattering measurements showed that the hydrodynamic radius of polymer aggregates decreased from approximately 242 nm at DS ≈ 0.94 to about 82 nm at DS ≈ 1.30 in alkaline solution. In addition to size reduction, aggregate morphology changes from predominantly spherical structures to more elongated aggregates depending on both DS and solvent composition. These observations indicate that sulfoethyl substitution weakens intermolecular associations while promoting more compact and solvent-dependent molecular assemblies.

The increasing sulfoethylation also alters the optical anisotropy of the polymer. Molecular hydrodynamics and optical methods in shear flow have been employed to study the conformational and supramolecular behavior of SEC in dilute solutions. Measurements of reduced viscosity showed linear concentration dependences, allowing reliable determination of intrinsic viscosity values using the Huggins equation and confirming the absence of noticeable polyelectrolyte effects under the studied conditions. Flow birefringence (Maxwell effect) was directly proportional to the velocity gradient, indicating that the solutions were molecularly dispersed. Significant differences were observed in the optical shear coefficient ([n]/[η]) between chitosan and its sulfoethylated derivatives. While unmodified chitosan exhibited positive birefringence, SEC displayed strong negative birefringence. This sign inversion suggests that in SEC aggregates the axis of highest polarizability is oriented perpendicular to the longest geometrical axis of the particle, pointing to a highly ordered supramolecular organization driven by short-range intermolecular interactions (van der Waals, hydrophobic, and hydrogen bonding). These findings highlight that sulfoethylation induces substantial changes in the orientational and conformational characteristics of chitosan macromolecules in solution [37].

3.2.3 Molecular Weight Determination

The introduction of bulky sulfoethyl groups as well as the reaction conditions such as temperature, acidity of the reaction media and process duration, can lead to depolymerization of the polymer chain, which substantially affects the physicochemical and biological activity of SEC discussed further. Nevertheless, molecular-weight analysis is required for proper interpretation of the physicochemical and biological properties of the synthesized biopolymer. Several methods have been developed and readapted for SEC.

3.2.3.1 Capillary Viscometry

For native chitosan, capillary viscometry has historically been the most widely employed indirect method for molecular weight (MW) estimation, relying on the Mark-Kuhn-Houwink (MKH) relationship [57]. For chitosan derivatives, however, this approach becomes fundamentally invalid without prior determination of new MKH constants, because chemical modification drastically alters chain conformation and hydrodynamic volume. Studies on sulfated chitosan derivatives have demonstrated that viscosimetry yields MW values that are not comparable with results from absolute methods [58]. The determination of molecular weight for sulfated chitosan based on constants established for heparin has been recognized as incorrect, while ap-

plying the Kasaai equation, originally derived for native chitosan, to its derivatives introduces substantial errors. The fundamental principle articulated for native chitosan applies equally to SEC: the MKH equation relies on constants (K and α) specific to a given polymer-solvent-temperature system, reflecting the unique hydrodynamic volume and chain conformation of the unmodified polymer in that solvent. Introduction of sulfoethyl groups inevitably changes chain stiffness, solvation, excluded volume and polyelectrolyte behavior, rendering literature constants for native chitosan inapplicable.

3.2.3.2 Size-Exclusion Chromatography

Aqueous size-exclusion chromatography is one of the key methods for MW determination of SEC [35]. However, several specific challenges emerge when analyzing chitosan derivatives. Firstly, the refractive index increment $\frac{dn}{dc}$ for derivatives can differ substantially from that of native chitosan. While expected $\frac{dn}{dc}$ values for related polysaccharides fall within 0.136-0.176 mL/g, sulfated derivatives require experimental determination of this parameter on a case-by-case basis [59]. The dependence of $\frac{dn}{dc}$ on DS, ionic strength, and pH must be carefully characterized. Failure to use the correct $\frac{dn}{dc}$ value introduces large errors in the calculated MW. This is because the optical constant of the light-scattering detector (often denoted K_{LS}) contains the term $\left(\frac{dn}{dc}\right)^2$, consequently, the light-scattering signal itself scales with $\left(\frac{dn}{dc}\right)^2$. An inaccurate $\frac{dn}{dc}$ therefore propagates directly and quadratically into the molecular-weight result.

Secondly, column calibration using polymer standards (e.g., dextrans or pullulans) introduces uncertainties comparable to those encountered for native chitosan. The conformational disparity between SEC and neutral polysaccharide standards remains a fundamental limitation. Even when using universal calibration procedures, the scatter in reported MKH constants for chitosan derivatives poses a significant challenge [60]. Next, the polyelectrolyte nature of SEC demands careful optimization of mobile phase conditions. Sufficient ionic strength is required to suppress electrostatic chain expansion and obtain stable, well-defined hydrodynamic volumes. However, the presence of both cationic (amino) and anionic (sulfonate) groups may create complex charge-shielding requirements that are not fully addressed by simple salt addition.

3.2.3.3 Light Scattering Techniques

Static light scattering (SLS) can provide absolute weight-average molecular-weight information, whereas dynamic light scattering (DLS) provides hydrodynamic size and aggregation information through measurement of translational diffusion. Similarly to native chitosan, these two techniques offer significant advantages for SEC analysis. For N-SEC with DS ≈ 0.5-0.7, light scattering has been applied to determine MW and radius of gyration in solution, enabling conformational characterization [37]. However, being recognized as a critical limitation for native chitosan, the extreme sensitivity of light scattering to aggregates is equally problematic for SEC [61]. Rigorous sample preparation, including filtration and use of DLS to deconvolute contributions from aggregates and individual macromolecules, remains imperative. The presence of aggregates in SLS is revealed by concave Zimm (or Berry) plots; however, linear dependences may still be observed for samples with bimodal distributions, requiring more advanced or combined analysis with size-exclusion chromatography. The dn/dc for SEC must be measured under the same solvent and temperature conditions used for scattering experiments since it strongly depends on DS, pH, ionic strength, and potentially on the presence of heavy metal impurities.

3.2.3.4 Analytical Ultracentrifugation

The matrix-free method that requires no calibration against polymer standards, analytical ultracentrifugation (AUC) remains the "gold standard" for absolute MW determination of chitosan and its derivatives [62]. For sulfoethylated chitosan, AUC offers particular value in cases where other methods yield inconsistent results due to aggregation or polyelectrolyte effects. Implementation of this method allows the characterization of complex formation including polyelectrolyte complexes with other charged polymers, which is especially relevant for SEC, given its application in drug delivery and biomedical contexts. Sedimentation equilibrium provides absolute MW independent of molecular shape, while sedimentation velocity offers insights into conformation through the sedimentation coefficient [63]. For SEC, sedimentation coefficients and intrinsic viscosities can be combined to construct hydrodynamic parameter-MW relationships,

similarly to the MKH equation, as demonstrated for other chitosan derivatives. Recent advances in multi-wavelength detection add an orthogonal spectral dimension to conventional hydrodynamic characterization. However, as for native chitosan, AUC of SEC is labor-intensive, requires expensive instrumentation and highly trained operators, and is generally limited to specialized applications or as a confirmatory reference method.

3.2.3.5 Gel Electrophoresis

An emerging and promising approach for rapid analysis of chitosan derivatives is agarose gel electrophoresis [64]. The electrophoretic mobility of charged macromolecules in agarose gels is governed by three principal factors: molecular weight, degree of substitution (charge density), and degree of deacetylation. For SEC, electrophoretic mobility differs from native chitosan, making this method suitable for monitoring modification reactions and estimating DS. A key advantage of electrophoresis is the ability to screen large numbers of samples rapidly with minimal material consumption and without expensive instrumentation [65]. However, the method remains semi-quantitative and requires calibration using well-characterized samples, as inherent polydispersity produces diffuse bands rather than sharp zones. As with native chitosan, the lack of narrow-disperse SEC standards necessitates calibration with heterologous polymers, introducing uncertainty due to differences in charge density and hydrodynamic properties. Nevertheless, for comparative analyses within a single experimental run, electrophoresis offers significant practical utility, which is useful when the MW changes during storage or hydrolytic degradation.

Summarizing the MW estimation approaches, it becomes clear that the aggregation remains a persistent challenge for SEC analysis and may be even more complex compared to native chitosan [37]. The introduction of sulfoethyl groups introduces additional anionic centers which can promote the formation of zwitterionic structures or intramolecular ion pairs. This significantly complicates the solution behavior of the biopolymer and consequently, the analytical determination of its MW [66]. The balance of electrostatic repulsions, hydrophobic interactions (from residual acetyl groups), and hydrogen bonding in SEC differs markedly from that of native chitosan, affecting chain conformation, hydrodynamic volume, and aggregation propensity.

3.2.4 Thermal Stability

Thermogravimetric analysis demonstrates that SEC has only a minor influence on the thermal degradation profile of N-chitosan. All derivatives exhibit similar decomposition behavior regardless of DS, indicating that the DS has little effect on the degradation mechanism. The first weight loss observed between approximately 50 and 110 °C corresponds to evaporation of physically adsorbed and bound water. The principal degradation stage occurs between 210 and 300 °C and involves decomposition of the polysaccharide backbone together with cleavage of sulfoethyl substituents, releasing water, sulfur dioxide, carbon dioxide, and small amounts of acetic acid originating from residual acetyl groups. At higher temperatures, up to approximately 500 °C, further degradation produces ethylene and ammonia. Although increasing DS does not significantly change the thermal degradation pattern, SEC generally exhibits lower thermal stability than native chitosan, with decomposition beginning at approximately 200 °C due to the presence of thermally less stable sulfoethyl groups [51, 52].

Taken together, these analytical parameters provide a basis for relating SEC structure to its physicochemical properties and potential applications.

4 Sulfoethyl Chitosan Applications

The unique combination of water solubility, negative surface charge, and biomimicry of natural sulfated polysaccharides has opened diverse application domains for SEC. In drug delivery, nanoparticles based on SEC have been explored as carriers for positively charged therapeutic agents, exploiting electrostatic interactions for sustained release. While several studies have demonstrated the utility of chitosan-based nanoparticles and nanogels in this context, dedicated investigations specifically employing sulfoethyl chitosan remain limited and warrant further exploration [20, 67-69]. SEC has also been examined for its anticoagulant properties. In particular, sulfoethyl chitosan and SECS-capped silver nanoparticles have been shown to inhibit factor Xa and exhibit heparin-like activity [35]. Anticoagulant activity has likewise been reported for sulfated chitosan [70].

A thorough assessment of any novel biomaterial requires systematic evaluation of its interactions with biological systems. The available data for SEC allows several clear trends to be identified.

Most reported studies on sulfoethyl- or closely related sulfonated chitosan derivatives and its N-acetylated precursor chitin indicate low-to-moderate cytotoxicity. Work on O, N-SEC implanted in animal models noted the absence of significant local toxicity [54]. At the same time latest findings of Samokhin et al. revealed the potential of SEC-based gels for bacterial delivery in the gastrointestinal tract with no toxic effect on fibroblast cell cultures in vitro. Moreover, when administered to mice, no adverse reactions, neither behavioral nor allergic were observed in the animals [71]. Moreover, sulfoethylated chitin and chitin-glucan complex (SE-C and SE-CG respectively) both protect plasmid DNA and mammalian cells against oxidative damage. In the DNA-topology assay, SE-CG suppresses Fe^{2+}-induced single-strand breaks by chelating ferrous ions, yet it can enhance H_2O_2-mediated nicking under certain conditions [72]. In V79 hamster lung cells, 24 h pre-incubation with SE-G (150-750 μg mL^{-1}) significantly reduces both H_2O_2-generated strand breaks and FPG-sensitive oxidized purines produced by visible-light-excited methylene blue [73]. The same SE-CG preparation is antimutagenic in the Ames assay against 9-aminoacridine, sodium azide and MNNG [74]. Remarkably, the revealed protective effects are observed at lower DS values than those typically required for carboxymethyl derivatives, underscoring the advantage of the strongly acidic sulfoethyl group.

SEC exhibits good hemocompatibility according to Heise et al. The permanent negative charge of the sulfonate groups electrostatically repels the negatively charged erythrocyte membrane. In plasma coagulation assays the polymer prolongs activated partial thromboplastin time. Low-molecular-weight SEC and its silver-core nanoparticles have been shown to inhibit factor Xa and to prolong both activated partial thromboplastin time and prothrombin time [35]. Anticoagulant activity of SEC is the most thoroughly documented biological property of the biopolymer and is driven by its structural analogy to heparin. Although SEC lacks the precise pentasaccharide sequence of heparin, its sulfonate groups enable electrostatic interactions with coagulation factors. In vitro assays consistently show DS- and concentration-dependent prolongation of aPTT (and often PT). Later study demonstrated that both neat low-molecular-weight sulfoethyl chitosan and the corresponding silver-core nanoparticles inhibit factor Xa and markedly prolong clotting times [35]. However, unlike heparin, the structure-activity relationship for SEC appears in a simpler manner: higher DS generally correlates with stronger activity.

Unmodified chitosan shows broad-spectrum antimicrobial activity mainly through its protonated amino groups, which disrupt microbial membranes [75], and is readily degraded by lysozyme via recognition of N-acetylglucosamine sequences [76]. Sulfated chitosan derivatives often display reduced or even absent antibacterial activity compared with the parent biopolymer [77] and show altered (frequently slower or pattern-dependent) lysozyme-mediated degradation [32]. Although it requires a systemic investigation, SEC is expected to behave similarly: diminished antimicrobial activity and slower or modified biodegradation relative to unmodified chitosan. Once confirmed, the reduced degradability may be useful for long-term implants but less suitable for rapidly clearing systems. Direct experimental data on both properties for sulfoethyl chitosan remain limited.

The influence of the pattern of deacetylation on the functional properties of chitosan has been well established [78, 79]. For SEC a structural complexity arises from the pattern of sulfoethylation, which can similarly modulate the polymer's physicochemical and biological behavior.

Furthermore, the properties of SEC are not solely determined by the overall degree of substitution but also by the regio-selectivity of the modification. Substitution at the amino groups (N-SEC) versus hydroxyl groups (O-SEC) yields derivatives with fundamentally different characteristics.

Monosubstituted N-SEC units retain a secondary amino group that remains protonatable, while N, N-disulfoethylated units contain a tertiary nitrogen. In both cases a strongly acidic sulfoethyl moiety is introduced in close proximity to the nitrogen. This architecture creates a chelating, amphoteric ligand environment that is particularly effective for selective metal-ion binding. Cross-linked N-SEC resins exhibit high affinity and selectivity toward Ag^{+} and Cu^{2+} in multicomponent solutions containing other transition and alkaline-earth metals, making them attractive as sorbents for the recovery or pre-concentration of these ions from industrial or analytical matrices [53].

O-sulfoethyl chitosan derivative preserves the primary amino groups of the original chitosan while placing the anionic sulfoethyl substituents exclusively on the hydroxyl positions. The retained primary amines maintain the classical cationic character of chitosan under acidic conditions and enable classical amine-mediated interactions (electrostatic complexation, Schiff-base chemistry, or coordination). At the same time the permanently anionic sulfoethyl groups improve water solubility and introduce polyampholytic behavior [39]. Consequently, O-SEC is well suited for the formation of polyelectrolyte complexes with polycations,

the fabrication of multilayer membranes, and applications that benefit from a high density of free primary amines (e.g., enzyme immobilization or mucoadhesive formulations).

Mixed O, N-SEC combines both substitution patterns and typically reaches higher overall degrees of substitution. The resulting materials display enhanced water solubility across a broader pH range, pronounced ampholytic character, and the ability to form both intra- and intermolecular ionic cross-links upon drying. These features have been exploited in several biomedical contexts: as templates and stabilizing agents for silver nanoparticles that exhibit anticoagulant activity (particularly inhibition of factor Xa), and as components of polyelectrolyte-complex membranes and films whose aggregation behavior and hydrodynamic properties can be tuned by the degree of substitution [35, 37]. The simultaneous presence of primary and secondary amines together with sulfonate groups also makes mixed O, N-SEC a versatile platform for subsequent dual functionalization or for constructing hierarchical materials with spatially differentiated charge densities.

In summary, the choice among O-, N-, and O, N-regioisomers of sulfoethyl chitosan is not merely a synthetic detail but a rational design parameter. N-SEC is preferred when selective metal chelation is required; O-SEC is advantageous when free primary amines and controlled polyelectrolyte complexation are needed; and mixed O, N-SEC offers the broadest solubility window and the most versatile platform for biomedical and nanoparticle applications. Precise control of regioselectivity therefore enables the tailoring of sulfoethyl chitosan derivatives to specific end-use requirements.

Beyond these biological properties, several practical applications of SEC have been disclosed in patent. The suggested approach was aimed to focus on the direct use of the biopolymer in the inventions and resulted only in several patent applications worldwide, which strongly correlate with the functional properties of SEC mainly governed by its molecular architecture, which combines the rigid, hydrophilic backbone of chitosan with bulky anionic sulfoethyl substituents.

Such a unique structure imparts two major characteristics: a pronounced polyelectrolyte behavior arising from the presence of strong acid sulfonate groups, and excellent water solubility across a wide pH range, overcoming the main limitation of the native chitosan insolubility in neutral and alkaline media. However, these two features also strongly depend on the DS of the biopolymer. Sulfoethyl substituent is strongly hydrophilic, which affects even chitin making it fully water-soluble at DS ≈ 0.3 [80]. Thus, the presence of N-acetyl groups does not preclude solubility once a modest density of $–SO_3^-$ groups is introduced.

Similarly, for chitosan, increasing DS progressively decreases the basicity of the amino groups in SEC. The electron-withdrawing sulfoethyl substituents exert a negative inductive effect, reducing the electron density on the amino nitrogen and consequently lowering its proton affinity. Potentiometric titration studies consistently demonstrated a decrease in the dissociation constants of amino groups along with DS growth. Sulfoethylation has important consequences for both ion exchange and coordination properties because the reduced Lewis basicity weakens the stability of metal complexes formed through amino nitrogen atoms while simultaneously altering the balance between electrostatic and coordination interactions, which allows considering SEC as a promising biosorbent with tunable properties [52, 53, 81].

However, the influence of DS on sorption behavior is more complex than a simple increase or decrease in adsorption capacity. In general, increasing substitution of the amino groups hydrogen atoms by sulfoethyl residues reduces the overall sorption capacity towards numerous transition metal ions due to the lower amino-group basicity that weakens possible coordination interactions. Consequently, dynamic exchange capacities for Cu(II) and Ag(I) decreased with increasing DS, while stability constants of their complexes with the biopolymer became progressively smaller [52, 81].

Despite this anticipating a negative effect, higher DS markedly improved sorption selectivity. Increasing sulfoethyl content shifts the optimum sorption pH toward more acidic values and enhances discrimination between the metal ions, which are chemically similar. For example, derivatives with the DS around 0.5 exhibit significantly greater selectivity towards Ag(I) over Cu(II) than less substituted SEC samples. This behavior had been attributed to several complementary factors, including decreased amino-group basicity, participation of sulfonate oxygen atoms in mixed-ligand coordination, formation of chelate structures involving both amino and sulfonate groups, and the appearance of disulfoethylated glucosamine units at higher substitution levels. It has been proposed that since Ag(I) is a soft Lewis acid, reduction of amino-group basicity favors the formation of relatively more stable silver complexes, resulting in higher Ag/Cu selectivity [51, 81].

This result underlines the importance of the acetylation degree of chitosan. Previously it has been reported that electron-beam cross-linked SE-CG resins adsorb Cu(II), Ni(II), Co(II) and Zn(II) from mixed

solutions at pH 6.5 with a total capacity of 0.319 mmol g^{-1} — higher than the parent chitin-glucan (0.205 mmol g^{-1}) [82]. Selectivity follows the order Co(II) < Ni(II)<Cu(II)>Zn(II). The sulfonate groups act primarily by ion exchange rather than by strong five-membered chelate formation, explaining the modest capacity relative to carboxymethyl analogues. In contrast, N-SEC of comparable DS exhibits higher Cu(II)/Ag(I) selectivity because the free amino groups that remain after partial N-substitution participate in coordination [52, 81, 83].

Similar trends have been reported for SEC biosorption towards noble metal ions. Increasing DS enhanced the sorption selectivity of SEC towards Pd(II) relative to Pt(IV), while simultaneously shifting the optimum recovery conditions toward less acidic solutions. In contrast, sorption of perrhenate ions decreases with increasing DS because of steric hindrance and reduced amino-group basicity lower the number of effective anion-exchange sites. Therefore, the effect of sulfoethyl substitution strongly influenced the adsorption mechanism of a particular metal species. Overall, increasing DS decreases the absolute adsorption capacity for many coordination-controlled systems but substantially improves metal-ion selectivity, making highly substituted SEC particularly attractive for selective separation and analytical applications [83, 84].

The foregoing trends were successfully used as a key feature for the representative analytical application: the use of crosslinked N‑SEC with a DS of 0.5 as a solid-phase extraction sorbent for copper preconcentration in environmental water analysis, which has been patented by Ural Federal University named after the first President of Russia B.N. Yeltsin under the IPC classification G01N 21/63, which refers to systems or processes for investigating or analyzing materials using light, specifically where the material being investigated is optically excited [85]. In this method, the SEC-based material was packed into a cartridge, through which the water sample is percolated at a flow rate of 1.0-2.0 mL/min while copper ions were quantitatively retained on biosorbent. The coexisting metal ions were extracted by no more than 10 % reaching 15 % for Iron ions. Subsequent elution with 0.1 mol/L nitric acid yielded a copper-enriched eluate almost free of interfering matrix components, enabling sensitive and interference-free determination by atomic spectroscopy. The remarkable selectivity of N‑SEC observed in the work along with the natural origin of the biosorbent ensures the additional advantage in terms of environmental safety, distinguishing this approach from conventional methods that employ synthetic resins or hazardous organic reagents

The DS also governs the solubility of N-SEC. Introduction of sulfoethyl groups progressively converts chitosan from a weakly acidic polymer into a polyampholytic material with enhanced hydration and reduced intermolecular interactions. At relatively low substitution levels with DS below 0.45, N-SEC remains soluble only in dilute acidic media, similarly to unmodified chitosan. However, when the DS reaches 0.94 or higher, the biopolymer becomes readily soluble in water as well as in both acids (2 % acetic acid) and alkalies (2 % NaOH). This behavior originates from the increasing contribution of negatively charged sulfonate groups, which compensate the protonated amino groups and suppress extensive interchain hydrogen bonding. Nevertheless, the substitution pattern also plays an important role. While O-SEC dissolves only under strongly acidic (pH < 5) or strongly alkaline (pH > 13) conditions, the N-SEC remains soluble throughout the entire pH range because of its polyampholytic character [37, 39].

Logically the water-soluble compositions would require the use of N-substituted chitosan derivative.

The application scope of SEC further encompasses the textile industry under the classification C11D3/001 referring to the softening compositions in terms of textile, where it has been developed as an effective soil-release additive for washing agents. Herein Henkel AG and Co KGaA suggested the innovation addressed to cleaning cotton and cotton–polyester blends, which dominate modern textiles. By introducing N‑SEC with the DS = 0.52 into model detergent formulations containing surfactants (alkylbenzene sulfonate, sodium lauryl ether sulfate, fatty alcohol ethoxylate, fatty acid salt), builders, chelating agent, and auxiliary components afforded a substantial improvement in fatty stain removal on cotton and cotton‑polyester blend fabrics, whereas similarly introduced N, O‑carboxymethyl chitosan additive provided no significant benefit over the base composition. This finding highlights that exclusive N‑substitution is advantageous for soil-release performance and further illustrates the technological versatility of sulfoethyl chitosan [86].

At the same time, it has been demonstrated that highly substituted chitosan may undergo structural evolution during storage. Although freshly prepared films from SEC with DS = 0.94 were soluble over a broad pH range, prolonged storage results in complete loss of solubility while maintaining substantial swelling ability. This behavior has been attributed to the gradual formation of ionic crosslinks between oppositely charged amino and sulfonate groups during dehydration, producing physically crosslinked networks with

reduced solubility but preserved water uptake that should be considered within the studies and product development and storage [37, 83].

Another important property of SEC stipulating its functional performance in diverse applications that has been mentioned is its swelling behavior. Swelling itself reflects the complex interplay between the biopolymer chains caused by electrostatic repulsion among charged sulfonate groups, counterion distribution, and the osmotic pressure generated within the biopolymer network.

In this regard it also should be considered that sulfoethylation progressively disrupts the ordered crystalline structure of chitosan. The bulky sulfoethyl substituents interfere with intermolecular hydrogen bonding, resulting in partial amorphization of the polymer matrix. The reduced crystallinity enhances water penetration into the polymer network and consequently increases its swelling capacity. Even relatively low-substituted samples with the DS about 0.45 demonstrate significantly greater swelling than unmodified chitosan, consistent with the increased amorphous character of the material [37, 83].

Consequently, a thorough understanding of the structure-swelling relationship is essential for rational design and predictive use of this derivative in hydrated environments

The swelling behavior of SEC films in physiological saline solution was significantly influenced by the DS and storage time. Films were cast from 2 % acetic acid and subsequently treated with ammonia in ethanol to deprotonate the amino groups. Introduction of sulfoethyl groups markedly increased the swelling degree even at a relatively low DS = 0.45, which is attributed to the amorphization of the polymer matrix caused by the bulky substituents [37].

Further increase in swelling ratio can be reached by a widely introduced cross-linking approach. However, compared with the extensive literature addressing the influence of the DS, the effect of the degree of cross-linking on the physicochemical and sorption properties of SEC has received very limited attention. Up-to-date, only one systematic study has evaluated the influence of cross-linking density on SEC using glutaraldehyde cross-linked N-SEC with a fixed DS of 0.5. Increasing the degree of cross-linking resulted in a progressive decrease in both the moisture-content coefficient and the static exchange capacity toward hydroxide ions, reflecting reduced swelling and the consumption of amino groups during cross-link formation. Despite the lower number of accessible amino groups, the sorption selectivity toward Ag(I) over Cu(II) increased with increasing cross-linking density, particularly at pH 6.0-7.0 which had been attributed this behavior to the reduced availability of primary amino groups for coordination and the preferential stabilization of Ag(I) complexes through cooperative interactions involving the remaining amino groups and neighboring sulfonate functionalities. Consequently, a higher degree of cross-linking improved sorbent selectivity at the expense of exchange capacity and water uptake, highlighting cross-linking as an additional parameter for tuning SEC performance in selective metal-ion separation [51, 87].

Following the described strategy another solution in the field of preserving or maintaining viable microorganisms under the classification C12N 1/04 has been proposed by Novosibirsk State Technical University of Russia.

The cross-linking approach of SEC was involved in cryogel formation and further applied for bacterial stabilization. In this context, cross-linking with glutaraldehyde (GA) was conducted under subzero conditions resulting into an interconnected 15-50 μm macroporous structure that exhibited a swelling degree of 500-700 wt.% and porosity of 10-50 wt.%, which was found structurally optimal for bacterial entrapment. The cross-linking reaction consumed a significant part of free amino groups, further reducing the antimicrobial activity of SEC thus creating a bacteria-friendly environment. The cryogel effectively stabilized E. faecium L3, E. faecalis, B. subtilis, and E. coli over 12 months at both 4 °C and 22 °C, maintaining high bacterial titers (10^6-10^9 CFU/mL) without additional cooling making it also economically beneficial [88].

Considering the latest patent, it is important to acknowledge that GA is proven to exhibit cytotoxicity due to the residual unreacted aldehyde groups that can potentially leach from the cross-linked matrix. Moreover, the cross-linking reaction with GA may yield products containing oligomeric GA chains, further complicating toxicity assessment [89, 90]. Nevertheless, several factors mitigate this concern in the context of cryogel fabrication for bacterial stabilization and biomedical applications. Firstly, cryotechnological approach and high reactivity of GA, result in stable cryogels which can be obtained at remarkably low cross-linker concentrations, thereby reducing the cytotoxic burden [91]. Secondly, the application is primarily intended for ex vivo microbial preservation rather than direct implantation or systemic administration, which substantially lowers the toxicological risk. In this regard, the use of GA cross-linked biopolymers are well-established and legally accepted in various industrial biotechnological applications.

Nonetheless, for biomedical or food-contact applications where long-term biocompatibility is emergent, the alternative cross-linking strategies should be involved. The versatility and tunability of chitosan hydrogels through various cross-linking mechanisms has been represented by numerous publications. As a direct substituent for GA, a naturally occurring genipin (Gp) exhibits low cytotoxicity and high biocompatibility [92]. Besides that, the natural origin and low toxicity make Gp increasingly preferred for biomedical applications, the structure of chitosan cross-linked products turn out to be unpredictable due to competing cross-linking steps and the polymerization of Gp into grafted oligomeric chains [93]. Similarly, diepoxy compounds, such as ethylene glycol diglycidyl ether, present an advantage: although they are cytotoxic, the unreacted epoxy rings undergo hydrolysis upon contact with water, yielding non-toxic products, thereby eliminating the need for rigorous removal of residual cross-linker [94]. Another naturally occurring cross-linker, citric acid, is a generally recognized as safe compound, that has been widely explored as a non-toxic cross-linking agent for chitosan-based materials, forming ester linkages between carboxyl groups and hydroxyl groups of the polymer backbone under mild conditions [95].

Beyond covalent cross-linking, physical cross-linking strategies offer a route to materials that entirely avoid potentially toxic chemical reagents. Physical cross-linking relies on reversible non-covalent interactions such as ionic complexation, hydrogen bonding, hydrophobic interactions, and electrostatic associations to form stable hydrogel networks [96]. In these cases, the structure and interactions in both covalently and ionically cross-linked chitosan hydrogels are fundamentally different. The ionic cross-linking offers gentler conditions and greater biocompatibility, while covalent cross-linking provides superior mechanical strength. Recent advances have enabled the fabrication of injectable self-healing hydrogels that combine the reversibility of physically cross-linked networks with the mechanical robustness of covalently cross-linked materials [97]. Furthermore, stimuli-responsive chitosan hydrogels capable of responding to pH, temperature, and other physiological triggers have been extensively explored, with physical cross-linking playing a key role in enabling such responsiveness [98].

In summary, while GA remains a cost-effective and widely accepted cross-linker for ex vivo applications such as bacterial stabilization, the choice of cross-linking strategy should be carefully tailored to the intended implementation route. The greener alternatives, such as Gp, diepoxy compounds, citric acid or physical cross-linking are particularly attractive for applications requiring stringent biocompatibility, such as drug delivery, wound healing, and tissue engineering [99].

Despite its remarkable history covering more than fifty years of research, the patent portfolio for SEC appeared remarkably modest. These isolated examples, however, stand in sharp contrast to the thousands of patents granted for other chitosan derivatives, which highlights that the translation of this fundamental knowledge into intellectual property has been conspicuously slow in this area. Several factors may contribute to this patent gap including a more complicated synthesis route of SEC, which may limit its adoption by industrial players, and the market trajectories tending to application mainly of the native chitosan or its carboxymethylated derivative.

However, the current gap can be evaluated not as an abandoned frontier but a green field requiring a proactive patent strategy, encouraging researchers and innovators for new attempts and efforts for SEC implementation in everyday life.

5 Conclusions and Future Perspectives

This critical review provides a comprehensive overview of sulfoethyl chitosan (SEC), covering its synthesis, characterization, physicochemical, biological properties, current applications and future perspectives. Regioselective synthetic routes enable N-, O-, and mixed O, N-substituted derivatives with controlled degrees of substitution. The choice of reagent and reaction conditions, whether NaBES in acidic gel-phase for N-selectivity or NaVS under alkaline conditions for O-substitution, determines the regioselectivity and, consequently, the physicochemical and biological behavior of the resulting product. Characterization of SEC presents specific challenges especially for elemental analysis and molecular weight determination. Elemental analysis provides a bulk estimate of DS, provided that the sample is rigorously purified, whereas ^{1}H NMR provides site-specific structural information and is more suitable for distinguishing N- and O-substitution patterns. The presence of residual reagents, inorganic salts, or by-products can distort elemental analysis data, leading to incorrect DS values, thus requiring purification for reliable data. The purification affects analytical accuracy and influences biological properties since the residual reagents may affect cytotoxicity, hemocompatibility, and antimicrobial activity. The biological properties of SEC include anticoagulant activi-

ty, hemocompatibility, cytotoxicity, slight antimicrobial effects and bacterial stabilization capacity and are governed by the degree of substitution and substitution pattern. Comparative analysis with SEC precursors, such as chitin and chitin‑glucan complexes, reveals distinct structure–activity trends.

Despite its demonstrated versatility, SEC has been translated into only a handful of patented applications. These include selective solid‑phase extraction of copper from environmental waters, anticoagulant coatings, and macroporous cryogels for bacterial stabilization. The limited patent portfolio indicates that SEC remains an underexploited biopolymer with substantial space for intellectual property development. To systematically guide future research and industrial translation, Table 2 presents a structured gap analysis. For each identified gap, we propose specific future research directions and outline the potential impact of their achievement, providing an actionable framework for researchers, industrial partners, and funding agencies.

Table 2

SEC research gap analysis

	Knowledge Gap	Future Direction	Potential Impact
Synthesis and characterization	Lack of standardized purification procedures for SEC compromises DS determination by elemental analysis	Develop and mandate rigorous purification prior to analysis, and cross-validate the elemental analysis data with ^{1}H NMR spectra corrected for the DA.	Accurate and reliable DS determination
	Structural characterization often remains incomplete, no O- vs. N-substitution ratio is determined	Mandate combined NMR and FT-IR analysis for routine characterization, report DS, DA, substitution pattern, and MW as minimal dataset	Improved understanding of structure–property relationships and rational design of SEC for specific applications
	Lack of validated analytical methods for residual reagent quantification in SEC samples	Develop and validate liquid, gas or ion chromatography methods for quantitative determination of residual sulfoethylating agents and by-products	Improved quality control most important for biomedical applications and regulatory acceptance
	No systematic study on the stability of SEC solutions and solid-state SEC under different storage conditions	Conduct accelerated stability studies, monitor DS, MW, and solubility over time, establish shelf-life and storage recommendations	Reliable product quality over time and regulatory compliance
Biomedical and biological evaluation	SEC's potential immunomodulatory activity performed by other sulfated polysaccharides, has not been explored	Evaluate SEC's effect on macrophage polarization, cytokine secretion, and complement activation	Identification of immunomodulatory applications and possible synergy
	Antimicrobial activity of SEC against clinically relevant pathogens, including antibiotic-resistant strains, has not been systematically studied	Perform standardized antimicrobial susceptibility testing (MIC, MBC) against Gram-positive, Gram-negative, and fungal pathogens; evaluate potential synergy with conventional antibiotics and biopolymers	Identification of potential antimicrobial applications
	No data on SEC's interaction with cell membranes	Perform cellular uptake studies using fluorescently labeled SEC, investigate endocytosis pathways, evaluate intracellular trafficking and localization	Understanding of SEC's cellular interactions, safety assessment
Application-specific gaps	Limited systematic comparison with established commercial sulphated materials	Benchmark SEC against heparin (anticoagulant) and commercial biosorbents (metal recovery) under standardized conditions	Identification of competitive advantages and niches
	Biomedical applications of SEC remain underexplored: lack systematic evaluation on drug delivery systems and pharmaceutical excipient	Systematically develop SEC-based drug delivery platforms including nanoparticles, hydrogels, polyelectrolyte complexes also as mucoadhesive formulations	Expansion of SEC application portfolio, high-value biomedical products

	Potential of SEC for environmental remediation beyond metal sorption (e.g., dye removal, oil spill cleanup, PFAS adsorption) remains unexplored	Evaluate SEC-based biosorbents for removal of various pollutants and compare with commercial solutions	Expansion into the environmental market, sustainable remediation solutions, circular economy applications
Scaling-up and industrialization	SEC remains significantly underpatented compared to other chitosan derivatives	Prioritize patent gaps and fulfill those providing a competitive media in this field	Established IP position attractive for industry and future commercialization
	No established cost structure for SEC production	Perform comprehensive techno-economic analysis across the reported synthetic routes, identify cost drivers among raw materials and reagents, purification, energy and compare with competing chitosan derivatives and commercial alternatives.	Attraction of industrial investment by the evidence-based selection of the most economically viable synthesis route
	Lack of standardized quality control protocols for industrial-grade SEC	Develop and validate quality control protocols for DS, MW, purity, residual reagents, and endotoxin levels; establish specifications for different application grades (pharmaceutical, food, environmental, industrial)	Regulatory compliance and customer confidence
	SEC remains a laboratory-scale technology without market distribution, no pilot-scale data available	Conduct pilot-scale studies (10-100 L reactors), assess batch consistency and scalability different synthetic approaches, propose the optimized process parameters for large-scale production considering personnel and environmental safety	Lowering the scaling-up risks, demonstration of manufacturing feasibility
	No defined manufacturing process for SEC and SEC-based products	Establish good manufacturing practice (GMP) guidelines for SEC and SEC-based products with protocols optimized for end-use applications	Regulatory acceptance for biomedical and pharmaceutical products

Addressing these gaps will accelerate the transition of SEC from a laboratory derivative to a commercially viable biopolymer for medical, food, and environmental applications. With focused attention on these priorities, SEC has potential to establish itself as a sustainable and functional material in the global biopolymer market.

Funding

This research was supported by the Ministry of Education and Science of the Russian Federation throughout the "Priority-2030" program at Novosibirsk State Technical University (project No. SP-3 Zh-5/1).

Declaration of Generative AI and AI-Assisted Technologies in the Manuscript Preparation Process

During the preparation of this work, the author(s) used ChatGPT-4o to assist in creating the graphical layout and illustrative concepts for the chemical modification of chitosan and its functional outcomes in Figure 1. After using this tool, the authors thoroughly reviewed and edited the content. All chemical structures were manually cross-checked and verified for scientific accuracy. The authors take full responsibility for the ultimate content of the publication.

*Author Information**

**The authors' names are presented in the following order: First Name, Middle Name and Last Name*

Ksenia Sergeievna Bedritskikh (*corresponding author*) — 2nd year PhD student, Faculty of Natural Sciences, Novosibirsk State University, 1 Pirogova str., 630090, Novosibirsk, Russia and Junior Research Fellow, Faculty of Physical Engineering, Novosibirsk State Technical University, 20 Prospekt K. Marksa, 630073, Novosibirsk, Russia; *e-mail:* k.bedri.16@gmail.com; https://orcid.org/0009-0007-1409-3761

Arsalan Saeidi — 2nd year PhD student, Faculty of Natural Sciences, Novosibirsk State University, 1 Pirogova str., 630090, Novosibirsk, Russia and Junior Research Fellow, Faculty of Physical Engineering, Novosibirsk State Technical University, 20 Prospekt K. Marksa, 630073, Novosibirsk, Russia; *e-mail:* saeidi@corp.nstu.ru; https://orcid.org/0009-0006-2395-5127

Anna Evgenievna Ivanova — 2nd year student, Faculty of Physical Engineering, Novosibirsk State Technical University, 20 Prospekt K. Marksa, 630073, Novosibirsk, Russia; *e-mail:* utapak2006@gmail.com; https://orcid.org/0009-0008-7565-7054

Alexander Viktorovich Pestov — PhD in Chemistry, Research Fellow, I.Ya. Postovsky Institute of Organic Synthesis, Ural Branch of the Russian Academy of Sciences, 22 Sofya Kovalevskaya St., 620990, Yekaterinburg, Russia; *e-mail:* pestov@ios.uran.ru; https://orcid.org/0000-0002-4270-3041

Ekaterina Anatolievna Litvinova — PhD in Biology, Research Fellow, Faculty of Physical Engineering, Novosibirsk State Technical University, 20 Prospekt K. Marksa, 630073, Novosibirsk, Russia; *e-mail:* e.litvinova@corp.nstu.ru; https://orcid.org/0000-0001-6398-7154

Aleksandr Alekseyevich Drannikov — PhD in Pharmacy, Junior Research Fellow, Faculty of Physical Engineering, Novosibirsk State Technical University, 20 Prospekt K. Marksa, 630073, Novosibirsk, Russia; *e-mail:* drannikov@corp.nstu.ru; https://orcid.org/0000-0002-4839-1667.

Author Contributions

The manuscript was written through contributions of all authors. All authors have given approval to the final version of the manuscript. CRediT: **Ksenia S. Bedritskikh** data curation, investigation, writing-original draft, writing-review & editing; **Arsalan Saeidi** data curation, investigation, visualization, writing-original draft, writing-review & editing; **Anna E. Ivanova** investigation, formal analysis; **Alexandr V. Pestov** writing-review & editing; **Ekaterina A. Litvinova** funding acquisition, writing-original draft; **Aleksandr A. Drannikov** conceptualization, supervision, visualization, writing-original draft, writing-review & editing.

References

1 El-Saadony, M. T., Saad, A. M., Alkafaas, S. S., Dladla, M., Ghosh, S., Elkafas, S. S., Hafez, W., Ezzat, S. M., Khedr, S. A., Hussien, A. M., Fahmy, M. A., Elesawi, I. E., Salem, H. M., Mohammed, D. M., Abd El-Mageed, T. A., Ahmed, A. E., Mosa, W. F. A., El-Tarabily, M. K., AbuQamar, S. F., & El-Tarabily, K. A. (2025). Chitosan, derivatives, and its nanoparticles: Preparation, physicochemical properties, biological activities, and biomedical applications–A comprehensive review. *International Journal of Biological Macromolecules*, *313*, 142832. https://doi.org/10.1016/j.ijbiomac.2025.142832

2 Sharkawy, A., Barreiro, M. F., & Rodrigues, A. E. (2020). Chitosan-based Pickering emulsions and their applications: A review. *Carbohydrate Polymers*, *250*, 116885. https://doi.org/10.1016/j.carbpol.2020.116885

3 Dambuza, A., Mokolokolo, P. P., Makhatha, M. E., & Sibeko, M. A. (2025). Pharmacological and biological efficacy of chitosan-based materials. *International Journal of Molecular Sciences*, *26*(21), 10735. https://doi.org/10.3390/ijms262110735

4 Gao, Y., & Wu, Y. (2022). Recent advances of chitosan-based nanoparticles for biomedical and biotechnological applications. *International Journal of Biological Macromolecules*, *203*, 379–388. https://doi.org/10.1016/j.ijbiomac.2022.01.162

5 Karimlar, S., Pirbalouti, A. G., Teymuori, Z., Moslehishad, M., & Hamidi-Esfahani, Z. (2026). Applications of Chitosan, an Eco-Friendly Biopolymer in Agricultural Systems, Herbal Products, and Functional Foods: A Review. *Food Science & Nutrition*, *14*(1), e71367. https://doi.org/10.1002/fsn3.71367

6 Suryani, S., Chaerunisaa, A. Y., Joni, I. M., Ruslin, R., Aspadiah, V., Anton, A., Sartinah, A., & Ramadhan, L. O. A. N. (2024). The chemical modification to improve solubility of chitosan and its derivatives application, preparation method, toxicity as a nanoparticles. *Nanotechnology, Science and Applications*, 41–57. https://doi.org/10.2147/NSA.S450026

7 Qin, C., Li, H., Xiao, Q., Liu, Y., Zhu, J., & Du, Y. (2006). Water-solubility of chitosan and its antimicrobial activity. *Carbohydrate polymers*, *63*(3), 367–374. https://doi.org/10.1016/j.carbpol.2005.09.023

8 Argilashki, D., & Uzunova, Y. (2026). Enhancing drug delivery through chemical modification of chitosan: A review. *Pharmacia*, *73*, 1–14. https://doi.org/10.3897/pharmacia.73.e180564

9 Zamruddin, N. D., Salleh, K. M., & Mutalib, H. A. A. (2026). Chemical Modification of Chitosan for Enhanced Environmental Applications. In *Biopolymers from Plant Origin for Environmental Sustainability* (pp. 307–332). Cham: Springer Nature Switzerland. https://doi.org/10.1007/978-3-032-16034-8_13

10 Argüelles-Monal, W. M., Lizardi-Mendoza, J., Fernández-Quiroz, D., Recillas-Mota, M. T., & Montiel-Herrera, M. (2018). Chitosan derivatives: introducing new functionalities with a controlled molecular architecture for innovative materials. *Polymers*, *10*(3), 342. https://doi.org/10.3390/polym10030342

11 Zhang, J., Xia, W., Liu, P., Cheng, Q., Tahirou, T., Gu, W., & Li, B. (2010). Chitosan modification and pharmaceutical/biomedical applications. *Marine drugs*, *8*(7), 1962-1987. https://doi.org/10.3390/md8071962

12 Szabová, J., Mravec, F., Mokhtari, M., Le Borgne, R., Kalina, M., & Berret, J. F. (2023). N, N, N-Trimethyl chitosan as a permeation enhancer for inhalation drug delivery: Interaction with a model pulmonary surfactant. *International Journal of Biological Macromolecules*, *239*, 124235. https://doi.org/10.1016/j.ijbiomac.2023.124235

13 Nagy, V., Snorradóttir, B. S., Lauzon, H. L., & Másson, M. (2024). Design of experiments optimization of N, N, N-trimethyl chitosan synthesis using N, N-diisopropylethylamine base. *Carbohydrate Research*, *545*, 109289. https://doi.org/10.1016/j.carres.2024.109289

14 Borsagli, F. G. M., Mansur, A. A., Chagas, P., Oliveira, L. C., & Mansur, H. S. (2015). O-carboxymethyl functionalization of chitosan: complexation and adsorption of Cd (II) and Cr (VI) as heavy metal pollutant ions. *Reactive and Functional Polymers*, *97*, 37–47. https://doi.org/10.1016/j.reactfunctpolym.2015.10.005

15 Chen, L., Tian, Z., & Du, Y. (2004). Synthesis and pH sensitivity of carboxymethyl chitosan-based polyampholyte hydrogels for protein carrier matrices. *Biomaterials*, *25*(17), 3725–3732. https://doi.org/10.1016/j.biomaterials.2003.09.100

16 Jayakumar, R., Prabaharan, M., Nair, S. V., Tokura, S., Tamura, H., & Selvamurugan, N. (2010). Novel carboxymethyl derivatives of chitin and chitosan materials and their biomedical applications. *Progress in Materials Science*, *55*(7), 675–709.https://doi.org/10.1016/j.pmatsci.2010.03.001

17 Dubovskaia, P. I., Saeidi, A., Pronchenko, A. A., Drannikova, A. I., Lukoyanov, I. A., Aripova, F. K., Savenko, M. E., Veretennikova, E. A., Pestov, A. V., Litvinova, E. A. & Drannikov, A. A. (2025). Gel-Phase Synthesis and pH-Sensitive Swelling-Structure Relationships of N-Carboxyethylchitosan. *Eurasian Journal of Chemistry*, *30*(2 (118)), 19–33. https://doi.org/10.31489/2959-0663/2-25-6

18 Bernkop-Schnürch, A., Hornof, M., & Guggi, D. (2004). Thiolated chitosans. *European Journal of Pharmaceutics and Biopharmaceutics*, *57*(1), 9–17. https://doi.org/10.1016/S0939-6411(03)00147-4

19 Wang, W., Meng, Q., Li, Q., Liu, J., Zhou, M., Jin, Z., & Zhao, K. (2020). Chitosan derivatives and their application in biomedicine. *International journal of molecular sciences*, *21*(2), 487. https://doi.org/10.3390/ijms21020487

20 Alfinaikh, R. S., Alamry, K. A., & Hussein, M. A. (2025). Sustainable and biocompatible hybrid materials-based sulfated polysaccharides for biomedical applications: a review. *RSC advances*, *15*(6), 4708–4767. https://doi.org/10.1039/d4ra07277d

21 Jiao, G., Yu, G., Zhang, J., & Ewart, H. S. (2011). Chemical structures and bioactivities of sulfated polysaccharides from marine algae. *Marine drugs*, *9*(2), 196–223. https://doi.org/10.3390/md9020196

22 Yermak, I. M., Mischchenko, N. P., Davydova, V. N., Glazunov, V. P., Tarbeeva, D. V., Kravchenko, A. O., Pimenova., E. A. & Sorokina, I. V. (2017). Carrageenans-sulfated polysaccharides from red seaweeds as matrices for the inclusion of echinochrome. *Marine Drugs*, *15*(11), 337. https://doi.org/10.3390/md15110337

23 Pereira, L., & Valado, A. (2025). Beyond Nutrition: The Therapeutic Promise of Seaweed-Derived Polysaccharides Against Bacterial and Viral Threats. *Marine Drugs*, *23*(10), 407. https://doi.org/10.3390/md23100407

24 Nikitina, M., Kochkina, N., Arinina, M., Kulichikhin, V., & Terekhova, I. (2023). β-cyclodextrin modified hydrogels of kappa-carrageenan for methotrexate delivery. *Pharmaceutics*, *15*(9), 2244. https://doi.org/10.3390/pharmaceutics15092244

25 Mikami, T., & Kitagawa, H. (2017). Sulfated glycosaminoglycans: their distinct roles in stem cell biology. *Glycoconjugate Journal*, *34*(6), 725–735. https://doi.org/10.1007/s10719-016-9732-9

26 Esposito, F., Vessella, G., Sinquin, C., Traboni, S., Iadonisi, A., Colliec-Jouault, S., Zykwinska, A. & Bedini, E. (2022). Glycosaminoglycan-like sulfated polysaccharides from Vibrio diabolicus bacterium: Semi-synthesis and characterization. *Carbohydrate polymers*, *283*, 119054. https://doi.org/10.1016/j.carbpol.2021.119054

27 Feng, Q., Lin, S., Zhang, K., Dong, C., Wu, T., Huang, H., Xiaohui, Y.,.Zhang, L., Gang, L. & Bian, L. (2017). Sulfated hyaluronic acid hydrogels with retarded degradation and enhanced growth factor retention promote hMSC chondrogenesis and articular cartilage integrity with reduced hypertrophy. *Acta biomaterialia*, *53*, 329–342. https://doi.org/10.1016/j.actbio.2017.02.015

28 Wang, X., Hadi, M. K., Niu, J., Zhou, Q., & Ran, F. (2023). Anticoagulant macromolecules. *Macromolecules*, *56*(12), 4387–4430. https://doi.org/10.1021/acs.macromol.2c02501

29 Liu, J., & Pedersen, L. C. (2007). Anticoagulant heparan sulfate: structural specificity and biosynthesis. *Applied microbiology and biotechnology*, *74*(2), 263–272. https://doi.org/10.1007/s00253-006-0722-x

30 Jabeen, F., Ahmad, R., Mir, S., Awwad, N. S., & Ibrahium, H. A. (2025). Carrageenan: structure, properties and applications with special emphasis on food science. *RSC advances*, *15*(27), 22035–22062. https://doi.org/10.1039/d5ra03296b

31 Steiger, B. G., & Wilson, L. D. (2020). Modular chitosan-based adsorbents for tunable uptake of sulfate from water. *International journal of molecular sciences*, *21*(19), 7130. https://doi.org/10.3390/ijms21197130

32 Aguanell, A., Del Pozo, M. L., Pérez-Martín, C., Pontes, G., Bastida, A., Fernández-Mayoralas, A., García-Junceda, E., & Revuelta, J. (2022). Chitosan sulfate-lysozyme hybrid hydrogels as platforms with fine-tuned degradability and sustained inherent antibiotic and antioxidant activities. *Carbohydrate polymers*, *291*, 119611. https://doi.org/10.1016/j.carbpol.2022.119611

33 Karlybaeva, B. P., Berdimbetova, G. E., & Boymirzaev, A. S. (2023). Synthesis and characteristics of sulfated chitosan based on chitin/chitosan from artemia parthenogenetica cysts. *Kimya Problemleri*, *21*(3), 242–250.

34 Zargar, V., Asghari, M., & Dashti, A. (2015). A review on chitin and chitosan polymers: structure, chemistry, solubility, derivatives, and applications. *ChemBioEng reviews*, *2*(3), 204–226. https://doi.org/10.1002/cben.201400025

35 Heise, K., Hobisch, M., Sacarescu, L., Maver, U., Hobisch, J., Reichelt, T., Sega, M., Fischer, S., & Spirk, S. (2018). Low-molecular-weight sulfonated chitosan as template for anticoagulant nanoparticles. *International journal of nanomedicine*, 4881–4894. https://doi.org/10.2147/IJN.S172230

36 Suwan, J., Zhang, Z., Li, B., Vongchan, P., Meepowpan, P., Zhang, F., Mousa, S. A., Mousa, S., Premanode, B., Kongtawelert, P., & Linhardt, R. J. (2009). Sulfonation of papain-treated chitosan and its mechanism for anticoagulant activity. *Carbohydrate research*, *344*(10), 1190–1196. https://doi.org/10.1016/j.carres.2009.04.016

37 Petrova, V. A., Chernyakov, D. D., Moskalenko, Y. E., Gasilova, E. R., Strelina, I. A., Okatova, O. V., Baklagina, Y. G., Vlasova, E.N. & Skorik, Y. A. (2017). O, N-(2-sulfoethyl) chitosan: Synthesis and properties of solutions and films. *Carbohydrate polymers*, *157*, 866–874. https://doi.org/10.1016/j.carbpol.2016.10.058

38 Tsai, H. S., Wang, Y. Z., Lin, J. J., & Lien, W. F. (2010). Preparation and properties of sulfopropyl chitosan derivatives with various sulfonation degree. *Journal of Applied Polymer Science*, *116*(3), 1686–1693. https://doi.org/10.1002/APP.31689

39 Gabriel, L., & Heinze, T. (2020). Structure design of polysaccharides–Chemoselective sulfoethylation of chitosan. *European Polymer Journal*, *140*, 109978. https://doi.org/10.1016/j.eurpolymj.2020.109978

40 Nud'ga, L. A., Plisko, E. A., & Danilov, S. N. (1974). *Zhurnal Prikladnoi Khimii*, 47(4), 872–875.

41 Muzzarelli, R. A. (1992). Modified chitosans carrying sulfonic acid groups. *Carbohydrate polymers*, *19*(4), 231–236. https://doi.org/10.1016/0144-8617(92)90074-Z

42 Plisko, E. A., Nud'ga, L. A., & Danilov, S. N. (1977). Chitin and its chemical transformations. *Russian Chemical Reviews*, *46*(8), 764–774. https://doi.org/10.1070/rc1977v046n08abeh002171

43 Nud'ga, L. A., Plisko, E. A., & Danilov, S. N. (1973). *Zhurnal Obshc. Khimii*, 43, 2752.

44 Nud'ga, L. A., Petrova, V. A., Ben'kovich, A. E. A., & Petropavlovskii, G. A. (2001). Comparative study of reactivity of cellulose, chitosan, and chitin-glucan complex in sulfoethylation. *Russian Journal of Applied Chemistry*, *74*(1), 145–148. https://doi.org/10.1023/A:1012776807384

45 Pestov, A. V., Petrova, Y. S., Bukharova, A. V., Neudachina, L. K., Koryakova, O. V., Matochkina, E. G., Kodess, M. I., & Yatluk, Y. G. (2013). Synthesis in a gel and sorption properties of N-2-sulfoethyl chitosan. *Russian journal of applied chemistry*, *86*(2), 269–272. https://doi.org/10.1134/S1070427213020225

46 An, N. T., Dong, N. T., & Le Dung, P. (2009). Water-soluble N-carboxymethylchitosan derivatives: Preparation, characteristics and its application. *Carbohydrate Polymers*, *75*(3), 489–497. https://doi.org/10.1016/j.carbpol.2008.08.017

47 Skorik, Y. A., Gomes, C. A., Vasconcelos, M. T. S., & Yatluk, Y. G. (2003). N-(2-Carboxyethyl) chitosans: regioselective synthesis, characterisation and protolytic equilibria. *Carbohydrate Research*, *338*(3), 271–276. https://doi.org/10.1016/s0008-6215(02)00432-9

48 Desbrieres, J., & Babak, V. G. (2008). Interfacial properties of amphiphilic systems on the basis of natural polymers—chitin derivatives. *Russian Journal of General Chemistry*, *78*(11), 2230–2238. https://doi.org/10.1134/S1070363208110443

49 Muzzarelli, R. A. (1988). Carboxymethylated chitins and chitosans. *Carbohydrate polymers*, *8*(1), 1–21. https://doi.org/10.1016/0144-8617(88)90032-X

50 Aranaz, I., Alcántara, A. R., Civera, M. C., Arias, C., Elorza, B., Heras Caballero, A., & Acosta, N. (2021). Chitosan: An overview of its properties and applications. *Polymers*, *13*(19), 3256. https://doi.org/10.3390/polym13193256

51 Petrova, Y. S., Bukharova, A. V., Neudachina, L. K., Adamova, L. V., Koryakova, O. V., & Pestov, A. V. (2014). Chemical properties of N-2-Sulfoethylchitosan with a medium degree of substitution. *Polymer Science Series B*, *56*(4), 487–493. https://doi.org/10.1134/S1560090414040083

52 Petrova, Y. S., Neudachina, L. K., Mekhaev, A. V., & Pestov, A. V. (2014). Simple synthesis and chelation capacity of N-(2-sulfoethyl) chitosan, a taurine derivative. *Carbohydrate polymers*, *112*, 462–468. http://dx.doi.org/10.1016/j.carbpol.2014.06.028

53 Petrova, Y. S., Pestov, A. V., Usoltseva, M. K., & Neudachina, L. K. (2015). Selective adsorption of silver (I) ions over copper (II) ions on a sulfoethyl derivative of chitosan. *Journal of hazardous materials*, *299*, 696–701. http://dx.doi.org/10.1016/j.jhazmat.2015.08.001

54 Bolshakov, I. N., Gornostaev, L. M., Fominykh, O. I., & Svetlakov, A. V. (2022). Synthesis, chemical and biomedical aspects of the use of sulfated chitosan. *Polymers*, *14*(16), 3431. https://doi.org/10.3390/polym14163431

55 Shetranjiwalla, S., & Ononiwu, A. (2025). Identifying barriers to scaled-up production and commercialization of chitin and chitosan using green technologies: A review and quantitative green chemistry assessment. *International Journal of Biological Macromolecules*, *305*, 141062. https://doi.org/10.1016/j.ijbiomac.2025.141062

56 Wang, T., Kusumi, K., Zhu, L., Mei, L., Manabe, A., Asghari, M., Samani, B. H., Yamamoto, T. & Kanda, H. (2024). Removal of acetyl-rich impurities from chitosan using liquefied dimethyl ether. *International Journal of Biological Macromolecules*, *280*, 136381. https://doi.org/10.1016/j.ijbiomac.2024.136381

57 Kasaai, M. R. (2007). Calculation of Mark–Houwink–Sakurada (MHS) equation viscometric constants for chitosan in any solvent–temperature system using experimental reported viscometric constants data. *Carbohydrate polymers*, *68*(3), 477–488. https://doi.org/10.1016/j.carbpol.2006.11.006

58 Knight, B. M., Mondal, R., Han, N., Pietra, N. F., Hall, B. A., Edgar, K. J., Welborn, V.V., Madsen, L.A., Yoreo, J.J.D. & Dove, P. M. (2024). Kinetics of calcite nucleation onto sulfated chitosan derivatives and implications for water–polysaccharide interactions during crystallization of sparingly soluble salts. *Crystal Growth & Design*, *24*(15), 6338. https://doi.org/10.1021/acs.cgd.4c00602

59 Caltabiano, A. M., Foley, J. P., & Striegel, A. M. (2018). Aqueous size-exclusion chromatography of polyelectrolytes on reversed-phase and hydrophilic interaction chromatography columns. Journal of Chromatography A, 1532, 161–174. https://doi.org/10.1016/j.chroma.2017.12.007

60 Nguyen, S., Winnik, F. M., & Buschmann, M. D. (2009). Improved reproducibility in the determination of the molecular weight of chitosan by analytical size exclusion chromatography. *Carbohydrate polymers*, *75*(3), 528–533. https://doi.org/10.1016/j.carbpol.2008.08.013

61 Wu, C., Zhou, S., & Wang, W. (1995). A dynamic laser light-scattering study of chitosan in aqueous solution. *Biopolymers: Original Research on Biomolecules*, *35*(4), 385–392. https://doi.org/10.1002/bip.360350406

62 Fee, M., Errington, N., Jumel, K., Illum, L., Smith, A., & Harding, S. E. (2003). Correlation of SEC/MALLS with ultracentrifuge and viscometric data for chitosans. *European Biophysics Journal*, *32*(5), 457–464. https://doi.org/10.1007/s00249-003-0317-8

63 Errington, N., Harding, S. E., Vårum, K. M., & Illum, L. (1993). Hydrodynamic characterization of chitosans varying in degree of acetylation. *International Journal of Biological Macromolecules*, *15*(2), 113–117. https://doi.org/10.1016/0141-8130(93)90008-A

64 Konovalova, M., Shagdarova, B. T., Zubov, V., & Svirshchevskaya, E. (2019). Express analysis of chitosan and its derivatives by gel electrophoresis. *Progress on Chemistry and Application of Chitin and its Derivatives*, *24*, 84–95. https://doi.org/10.15259/PCACD.24.007

65 Lootsik, M. D., Manko, N. O., Bilyy, R. O., Lutsyk, M. M., & Stoika, R. S. (2022). Analysis of chitosan molecular weight profile by electrophoresis in a porosity step gradient polyacrylamide gel. *The Ukrainian Biochemical Journal*, *94*(2), 76–84. https://doi.org/10.15407/ubj94.02.076

66 Yanagisawa, M., Kato, Y., Yoshida, Y., & Isogai, A. (2006). SEC-MALS study on aggregates of chitosan molecules in aqueous solvents: Influence of residual N-acetyl groups. *Carbohydrate polymers*, *66*(2), 192–198. https://doi.org/10.1016/j.carbpol.2006.03.008

67 Arpa, M. D., & Akbuğa, F. J. (2025). Chitosan-based nanogels in modern drug delivery: Focus on protein and gene applications. *Gels*, *11*(9), 735. https://doi.org/10.3390/gels11090735

68 Hou, Y., Hu, J., Park, H., & Lee, M. (2012). Chitosan-based nanoparticles as a sustained protein release carrier for tissue engineering applications. *Journal of Biomedical Materials Research Part A*, *100*(4), 939–947. https://doi.org/10.1002/jbm.a.34031

69 Saputra, H. A. (2025). Chitosan and its biomedical applications: A review. *Next Materials*, *9*, 101270. https://doi.org/10.1016/j.nxmate.2025.101270

70 Sajith, M. P., Pitchai, A., Ramasamy, P., & Sajith Jr, M. P. (2024). Anticoagulant protective effects of sulfated chitosan derived from the internal bone of spineless cuttlefish (Sepiella inermis). *Cureus*, *16*(7). https://doi.org/10.7759/cureus.64558

71 Samokhin, A., Korel, A., Blinova, E., Pestov, A., Kalmykova, G., Akulova, N., Betz, V., Tkachenko, V., & Litvinova, E. (2023). Delivery of B. subtilis into animal intestine using chitosan-derived bioresorbable gel carrier: preliminary results. *Gels*, *9*(2), 120. https://doi.org/10.3390/gels9020120

72 Kogan, G., Rauko, P., & Machová, E. (2003). Fungal chitin–glucan derivatives exert protective or damaging activity on plasmid DNA. *Carbohydrate research*, *338*(9), 931–935. https://doi.org/10.1016/S0008-6215(03)00041-7

73 Slameňová, D., Lábaj, J., Križková, L., Kogan, G., Šandula, J., Bresgen, N., & Eckl, P. (2003). Protective effects of fungal (1→ 3)-β-D-glucan derivatives against oxidative DNA lesions in V79 hamster lung cells. *Cancer Letters*, *198*(2), 153–160. https://doi.org/10.1016/S0304-3835(03)00336-7

74 Čipák, L., Miadoková, E., Dingová, H., Kogan, G., Novotný, L., & Rauko, P. (2001). Comparative DNA protectivity and antimutagenicity studies using DNA-topology and Ames assays. *Toxicology in vitro*, *15*(6), 677–681. https://doi.org/10.1016/S0887-2333(01)00080-7

75 Matica, M. A., Aachmann, F. L., Tøndervik, A., Sletta, H., & Ostafe, V. (2019). Chitosan as a wound dressing starting material: Antimicrobial properties and mode of action. *International journal of molecular sciences*, *20*(23), 5889. https://doi.org/10.3390/ijms20235889

76 Ren, D., Yi, H., Wang, W., & Ma, X. (2005). The enzymatic degradation and swelling properties of chitosan matrices with different degrees of N-acetylation. *Carbohydrate Research*, *340*(15), 2403–2410. https://doi.org/10.1016/j.carres.2005.07.022

77 Pires, N. R., Cunha, P. L., Maciel, J. S., Angelim, A. L., Melo, V. M., de Paula, R. C., & Feitosa, J. P. (2013). Sulfated chitosan as tear substitute with no antimicrobial activity. *Carbohydrate polymers*, *91*(1), 92–99. https://doi.org/10.1016/j.carbpol.2012.08.011

78 Zubareva, A. A., Gasilova, E. R., Poshina, D. N., & Skorik, Y. A. (2026). Molecular weight of chitosan: From structural complexity to analytical reliability. *Carbohydrate Polymers*, 125348. https://doi.org/10.1016/j.carbpol.2026.125348

79 Kurita, K. (2001). Controlled functionalization of the polysaccharide chitin. *Progress in polymer science*, *26*(9), 1921–1971. https://doi.org/10.1016/S0079-6700(01)00007-7

80 Šandula, J., Kogan, G., Kačuráková, M., & Machová, E. (1999). Microbial (1→ 3)-β-d-glucans, their preparation, physicochemical characterization and immunomodulatory activity. Carbohydrate polymers, 38(3), 247–253. https://doi.org/10.1016/S0144-8617(98)00099-X

81 Petrova, Y. S., & Neudachina, L. K. (2014). Complexing properties of N-2-sulfoethyl chitosans. *Russian Journal of Inorganic Chemistry*, *59*(8), 907–911. https://doi.org/10.1134/S0036023614080166

82 Skorik, Y. A., Pestov, A. V., & Yatluk, Y. G. (2010). Evaluation of various chitin-glucan derivatives from Aspergillus niger as transition metal adsorbents. *Bioresource technology*, *101*(6), 1769–1775. https://doi.org/10.1016/j.biortech.2009.10.033

83 Petrova, Y. S., Neudachina, L. K., Oseeva, M. Y., & Pestov, A. V. (2018). Effect of Complex-Former Ion Concentration on the Selectivity of Metal Ion Sorption on Cross-Linked N-2-Sulfoethylchitosan. *Russian Journal of Inorganic Chemistry*, *63*(3), 400-405. https://doi.org/10.1134/S003602361803018X

84 Evdokimova, O. V., Pestov, A. V., Pechishcheva, N. V., & Shunyaev, K. Y. (2016). Preparation of sorbents based on chitosan and its sulfoethyl derivative for sorption of perrhenate ions. *Russian Journal of Applied Chemistry*, *89*(8), 1377–1382. https://doi.org/10.1134/S1070427216080267

85 Petrova, Y. S., Neudachina, L. K., & Pestov, A. V. (2013). *Method of identifying copper in natural and potable water* (Patent No. RU 2532922 C1) Russian Federation Federal Service for Intellectual Property [in Russian]. https://new.fips.ru/Archive/PAT/2014FULL/2014.11.20/DOC/RUNWC1/000/000/002/532/922/DOCUMENT.PDF

86 Kropf, C., Gebert-Schwarzwaelder, A., Junkes, C., Falenski, L., Heinze, T., & Gabriel, L. (2022). *Chitosan derivatives as soil release agents* (Patent No. US 12570928 B2). U.S. Patent and Trademark Office. https://www.uni-jena.de/iomc25-en/36/patents

87 Petrova, Y. S., Pestov, A. V., Alifkhanova, L. M. K., & Neudachina, L. K. (2015). Effect of the degree of cross-linking of N-2-sulfoethylchitosan on the sorption selectivity of copper (II) and silver (I). *Russian Journal of Applied Chemistry*, *88*(9), 1434–1439. https://doi.org/10.1134/S1070427215090086

88 Korel, A. V., Drannikov, A. A., Pestov, A. V., Gribchenko, I. B., Goncharova, E. P., Samokhin, A. S., Aripova, F. K., Bets, V. D., Bogdanova, K. Y., Litvinova, E. A., Bedritskikh, K. S., & Pronchenko, A. A. (2026). *Sulfoethyl chitosan cryogel, method for producing sulfoethyl chitosan cryogel and its use for stabilizing bacteria* (Patent No. RU 2863024 C1). Russian Federation Federal Service for Intellectual Property [in Russian]. https://www1.fips.ru/ofpstorage/Doc/IZPM/RUNWC1/000/000/002/863/024/%D0 %98 %D0 %97-02863024-00001/document.pdf

89 Pinto, R. V., Gomes, P. S., Fernandes, M. H., Costa, M. E., & Almeida, M. M. (2020). Glutaraldehyde-crosslinking chitosan scaffolds reinforced with calcium phosphate spray-dried granules for bone tissue applications. *Materials Science and Engineering: C*, *109*, 110557. https://doi.org/10.1016/j.msec.2019.110557

90 Wegrzynowska-Drzymalska, K., Grebicka, P., Mlynarczyk, D. T., Chelminiak-Dudkiewicz, D., Kaczmarek, H., Goslinski, T., & Ziegler-Borowska, M. (2020). Crosslinking of chitosan with dialdehyde chitosan as a new approach for biomedical applications. *Materials*, *13*(15), 3413. https://doi.org/10.3390/ma13153413

91 Nikonorov, V. V., Ivanov, R. V., Kil'Deeva, N. R., Bulatnikova, L. N., & Lozinskii, V. I. (2010). Synthesis and characteristics of cryogels of chitosan crosslinked by glutaric aldehyde. *Polymer Science Series A*, *52*(8), 828–834. https://doi.org/10.1134/S0965545X10080092

92 Ye, J., Fu, S., Zhou, S., Li, M., Li, K., Sun, W., & Zhai, Y. (2020). Advances in hydrogels based on dynamic covalent bonding and prospects for its biomedical application. *European Polymer Journal*, *139*, 110024. https://doi.org/10.1016/j.eurpolymj.2020.110024

93 Kil'deeva, N. R., Kasatkina, M. A., & Mikhailov, S. N. (2017). Peculiarities of obtaining biocompatible films based on chitosan cross linked by genipin. *Polymer Science, Series D*, *10*(2), 189–193. https://doi.org/10.1134/S1995421217020095

94 Kildeeva, N. R., Privar, Y. O., & Bratskaya, S. Y. (2025). Crosslinking agents in the targeted design of chitosan-based materials. *Colloid Journal*, *87*(6), 875–902. https://doi.org/10.7868/S3034543X25060094

95 Tian, B., Hua, S., Tian, Y., & Liu, J. (2020). Chemical and physical chitosan hydrogels as prospective carriers for drug delivery: A review. *Journal of Materials Chemistry B*, *8*(44), 10050-10064. https://doi.org/10.1039/D0TB01869D

96 Tian, B., & Liu, J. (2023). Smart stimuli-responsive chitosan hydrogel for drug delivery: A review. *International Journal of Biological Macromolecules*, *235*, 123902. https://doi.org/10.1016/j.ijbiomac.2023.123902

97 Tsai, C. C., Chandel, A. K. S., Mitsuhashi, K., Fujiyabu, T., Inagaki, N. F., & Ito, T. (2024). Injectable, shear-thinning, self-healing, and self-cross-linkable benzaldehyde-conjugated chitosan hydrogels as a tissue adhesive. *Biomacromolecules*, *25*(2), 1084–1095. https://doi.org/10.1021/acs.biomac.3c01117

98 Sharmin, N., Rosnes, J. T., Prabhu, L., Böcker, U., & Sivertsvik, M. (2022). Effect of citric acid cross linking on the mechanical, rheological and barrier properties of chitosan. *Molecules*, *27*(16), 5118. https://doi.org/10.3390/molecules27165118

99 Berger, J., Reist, M., Mayer, J. M., Felt, O., Peppas, N. A., & Gurny, R. J. E. J. O. P. (2004). Structure and interactions in covalently and ionically crosslinked chitosan hydrogels for biomedical applications. *European journal of pharmaceutics and biopharmaceutics*, *57*(1), 19–34. https://doi.org/10.1016/S0939-6411(03)00161-9

How to Cite: Akojwar, N.S., Yenorkar, N.Y., Dondulkar, A.O., Ganeshpurkar, A., Behera, B., & Prasad, S.K. (2026). Analytical Characterization and Molecular Interaction Study of Quercetin-Loaded Transferosomes. *Eurasian Journal of Chemistry, 31, 3(123), 38–52.* https://doi.org/10.31489/2959-0663/3-26-2

PHYSICAL AND ANALYTICAL CHEMISTRY

Article

Received: 29 April 2026 | Revised: 30 July 2026 |
Accepted: 3 August 2026 | Published online: 27 August 2026

UDC 543.544+ 547.97

https://doi.org/10.31489/2959-0663/3-26-2

Natasha S. Akojwar[1], Nikhil Y. Yenorkar[1], Ayusha O. Dondulkar[1], Ankit Ganeshpurkar[2], Beauty Behera[3], Satyendra K. Prasad[1*]

[1]*Department of Pharmaceutical Sciences, Rashtrasant Tukadoji Maharaj Nagpur University, Nagpur, Maharashtra, India*
[2]*Department of Pharmaceutical Sciences, Dr. Harisingh Gour Vishwavidyalaya (A Central University), Sagar, Madhya Pradesh, India*
[3]*Department of Pharmaceutics, Delhi Pharmaceutical Sciences and Research University, New Delhi, India*
*(*Corresponding author's e-mail: skprasad.rs.phe@itbhu.ac.in)*

Analytical Characterization and Molecular Interaction Study of Quercetin-Loaded Transferosomes

Quercetin is a bioactive flavonoid that has potent anti-inflammatory activity. Its topical applications are limited due to poor solubility and permeability. The present study aims to develop and characterize quercetin-loaded transferosomes and to establish a validated RP-HPLC method for its quantification. Molecular docking studies revealed favourable binding of quercetin with key inflammatory targets. This included NF-kB (-8.66 kcal/mol), IgE (-7.22 kcal/mol), and TSLP (-6.54 kcal/mol). An RP-HPLC method was developed using C18 column with the mobile phase of acetonitrile and 0.3 % OPA (50:50 v/v). The method showed good linearity over the range of 20-120 µg/mL (R = 0.998). The retention time of quercetin was 4.303 min. Validation parameters demonstrated accuracy (99.89-100.11 %), precision (RSD <2 %), and sensitivity with LOD and LOQ of 0.57 µg/mL and 1.69 µg/mL, respectively. Transferosomes prepared using the thin-film hydration method exhibited a mean particle size of 190.4±1.6 nm, PDI of 0.324, and zeta potential of -22.4 mV. The entrapment efficiency was found to be 86.24 ± 1.61 %. FTIR, DSC, and SEM confirmed successful drug incorporation and vesicle formation. The transferosome exhibited sustained release (93.6 ± 0.9 % at 24 h) and Korsmeyer-Peppas kinetics. Hence, the developed system represents a promising platform for transferosome-loaded quercetin assessment.

Keywords: quercetin, transferosomes, drug delivery, molecular docking, RP-HPLC, method validation, anti-inflammatory activity, skin disorders

1 Introduction

Quercetin is a naturally occurring flavonoid widely distributed in fruits and vegetables [1]. It is known for its anti-oxidant, anti-inflammatory, and immunomodulatory properties. Due to these activities, quercetin has attracted considerable interest for applications in inflammatory skin conditions. However, its practical use is limited by poor aqueous solubility, low stability, and inadequate skin permeability [2]. Topical delivery offers a direct and non-invasive route for the management of localized skin disorders. However, effective delivery of poorly soluble compounds like quercetin through the skin remains a challenge. The stratum corneum works as a strong barrier, restricting drug permeation and reducing therapeutic efficiency. Therefore, there is a need for carrier systems that can improve drug solubility and enhance skin permeation.

Transferosomes are ultra-deformable vesicular systems composed of phospholipids and edge activators [3]. These vesicles could easily pass through the narrow pores of the skin due to their flexible membrane structure. The presence of surfactants destabilizes the lipid bilayer, allowing the vesicles to deform without

© 2026 The Authors. This is an open access article under the CC BY-NC-ND license (http://creativecommons.org/licenses/by-nc-nd/4.0/)

losing integrity. This property makes transferosomes suitable carriers for transdermal and topical drug delivery [4].

In addition to formulation development, understanding molecular interactions between drug molecules and biological targets is important. Molecular docking provides insight into binding affinity and interaction patterns, supporting the potential biological activity of the compound [5]. Furthermore, reliable analytical methods are required for accurate quantification of the drug during formulation and evaluation [6]. Although several studies have reported quercetin-loaded transferosomal formulations for topical and transdermal delivery, these investigations have primarily focused on formulation development and biological evaluation. In most of these studies, drug quantification has been performed using UV spectrophotometric methods. However, a formulation-specific HPLC method validated in accordance with ICH guidelines for quantitative estimation of quercetin encapsulated within transferosomes has not been adequately reported. Such a method offers reliable quantification with high specificity in the presence of formulation excipients and supports routine analytical evaluation of transferosomal formulations [6]. Therefore, the present study integrates formulation development, physicochemical characterization, validated RP-HPLC method development, and molecular docking to provide a thorough analytical and formulation approach for quercetin-loaded transferosomes.

2 Experimental

2.1 Materials

Quercetin was obtained from Xi'an Herb Bio-tech Co. Ltd (Xi'an City, China). Phospholipon ® 90G was procured from Lipoid (Ludwigshafen, Germany). Edge activator (Tween 80) was purchased from Sigma-Aldrich (USA). Chloroform, methanol, and acetone were obtained from HiMedia Laboratories (Mumbai, India). HPLC-grade methanol, acetonitrile, and water were used for chromatographic analysis (Sisco Research Laboratories Pvt. Ltd., Mumbai, India). Double-distilled water was prepared in-house and used throughout the study. All other chemicals and reagents used were of analytical grade and utilized without further purification.

2.2 *Methods*

2.2.1 In silico Molecular Docking Analysis

Molecular docking analysis was performed using Schrödinger Maestro software (Ver. 13.3) with default parameters to investigate the binding affinity and interaction profile of quercetin, hydrocortisone, and tacrolimus with selected protein targets relevant to inflammatory pathways. Hydrocortisone and tacrolimus were selected as reference drugs because they are widely used in the clinical management of localized skin disorders [7]. The two-dimensional (2D) structure of quercetin was retrieved from PubChem. The X-ray crystal structures of target proteins, including human IgE-Fc bound to its high-affinity receptor FC Epsilon RI (PDB: 2Y7Q), the NF-kB crystal structure of a higher-order complex of p50 (PDB: 3GUT), and TSLP, the pro-inflammatory cytokine (PDB: 5J11) were obtained from the RCSB PDB (Protein Data Bank: https://www.rcsb.org/). Protein structures were selected based on high resolution and acceptable R-free values [8]. Protein preparation (bond-order assignment, water-molecule removal, hydrogen-atom addition, etc.) was performed using the Protein Preparation Wizard in Maestro. Missing residues were corrected, followed by restrained energy minimization. Ligand preparation was performed using LigPrep, and the structures were energy minimized to generate the most stable conformers. A receptor grid was generated by defining the active site region using site-mapping. Using the Glide module, docking simulations were conducted. Selection of optimal binding poses was done based on docking scores and interaction analyses. Protein-ligand interactions were studied using Maestro visualization tools.

2.2.2 HPLC Method Development and Validation

Instrument Set-up Parameters and Run Conditions

A PDA-coupled RP-HPLC system (Shimadzu DGU-20A5R, Kyoto, Japan) with a C-18 column (Shim-Pack Solar 4.6 I.D.×250 mm, 5 µm) was utilized to quantify quercetin. The instrument included a Model LC-20AD binary pump, SIL-20AC HT autosampler with LabSolutions software, CTO-10AS column oven, SPD-M40 detector photodiode array (PDA), and a degassing unit model no. DGU-20A5R. The detection wavelength was set at 369 nm. The mobile phase was made up of ACN and 0.3 % (v/v) o-phosphoric acid (OPA) in water in the ratio 50:50, delivered in isocratic mode at a flow rate of 1.0 mL/min. Before use, the solvents were passed through a membrane filter (pore size:0.45 µm) and degassing was done by sonication. The column temperature was maintained at 25°C. The runtime was kept to confirm complete elution of the analyte,

and the injection volume was set to 10 µL. All chromatographic analyzes were carried out under optimized conditions to achieve adequate resolution and peak symmetry [9, 10].

Preparation and Dilution of Analytes

The preparation of quercetin stock was done by precisely weighing an appropriate amount of the drug and dissolving it using methanol to get a sample of 1000 µg/mL concentration. Suitable serial dilution was done for the stock in order to prepare various working standard solutions. The various sample solutions were made by dissolving a precisely measured amount of the transferosomal formulation in methanol, followed by sonication to ensure complete extraction of the drug. Before use, the samples were passed through a membrane filter (pore size:0.45 µm). Appropriate dilutions were made with methanol to bring the concentration within the linearity range of the method [11].

2.2.3 Method Validation

The developed RP-HPLC method was validated in accordance with ICH guidelines with respect to linearity, accuracy, precision, sensitivity, specificity, robustness, and ruggedness [12]. Linearity was assessed by analysing several quercetin standard solutions at different concentrations. Calibration curves were generated from plots of peak area and concentration. The correlation coefficient (R2) was thus determined. Different concentration levels (e.g., 80%, 100%, and 120%) were made for accuracy studies, and the percentage recovery was calculated. Intra-day and interday precision were evaluated. The results were expressed as percentage relative standard deviation (%RSD). Using the curve slope in addition to the standard deviation of response, the limit of detection and limit of quantification values were calculated. To ensure the absence of interference at the retention time of quercetin, both blank and sample solutions were assessed. Robustness of the method was studied by making deliberate small changes in study conditions, including flow rate, constituents of the mobile phase, and wavelength, and observing their effect on the results. Ruggedness was determined by performing the analysis under different conditions, such as different analysts and instruments and evaluating the consistency of the results. System suitability was assessed by repeated injection of standard quercetin solution (n=6) under optimized conditions. Parameters such as retention time, theoretical plate count, tailing factor, and peak area reproducibility were evaluated to ensure adequate performance of the chromatographic system [13].

2.3 Preparation of Quercetin-loaded Transferosomes

Quercetin-loaded transferosomes (QCT-TF) were prepared using the thin film hydration method [14]. Briefly, 120 mg of Phospholipid (Phospholipon 90G) and 20mg of Tween 80 (lipid-to-edge activator ratio of 6:1 w/w) were dissolved in a chloroform-methanol mixture (2:1 v/v). Quercetin (10% w/w of total lipid) was added to the same organic phase. Under vacuum, the solvent was evaporated in a rotary evaporator (REMI Equipment Pvt. Ltd., India) at 40 °C and 100 rpm. This led to the formation of a thin film on the round-bottom flask, which was further dried overnight. The dried film was hydrated with 10 mL of phosphate-buffered saline (PBS, pH = 6.0) under continuous stirring. This resulted in the formation of multilamellar vesicles. The sample was then probe sonicated for three cycles of 5s each to reduce vesicle size and improve uniformity. The prepared transferosomes were stored under refrigeration until further use [15].

2.4 Characterization of Transferosomes

*2.4.1 Dynamic Light Scattering (DLS) Studie*s

The DLS principle was used to determine transferosome size, zeta potential, and homogeneity/ PDI (Horiba, Kyoto, Japan). Samples were appropriately diluted with distilled water before analysis. Measurements were carried out at room temperature, and each sample was analyzed in triplicate [16].

2.4.2 Scanning Electron Microscopy

For analysis of the surface architecture of the prepared transferosomes, scanning electron microscopy was performed (Leo Supra, Germany). Samples were placed on a suitable stub and allowed to dry. A thin film of palladium was coated on dried samples to improve their conductivity. The samples were then observed under the microscope to evaluate vesicle shape, surface characteristics, and structural integrity [17].

2.4.3 Molecular Analysis Using ATR-FTIR and DSC

The molecular compatibility and solid-state characteristics of quercetin in the optimised transferosomal formulation were investigated using Attenuated Total Reflectance-Fourier Transform Infrared (ATR-FTIR) and Differential Scanning Calorimetry (DSC) [4]. Comparative analyses were performed using pure quercetin, Phospholipon® 90G and thequercetin-loaded transferosomes to evaluate potential drug-excipient

interactions, changes in the characteristic functional groups, and alterations in the physical state of quercetin following encapsulation.

FTIR analysis was carried out using an ATR-FTIR spectrophotometer (Shimatzu Corporation, Kyoto, Japan). The spectra of all samples were recorded over the wavenumber range of 4000- 400 cm^{-1} at a spectral resolution of 4 cm^{-1} with 32 scans per sample. The characteristic absorption bands were compared to assess molecular compatibility and confirm successful incorporation of quercetin into the transferosomal vesicles.

Thermal analysis was performed using a Differential Scanning Calorimeter (DSC, Mettler Toledo, Switzerland). Approximately 5mg of each sample was weighed into standard aluminium pans and hermetically sealed, while an empty sealed aluminium pan served as the reference. The samples were heated from 40 to 450 °C at a heating rate of 10 °C/min under a nitrogen purge of 50 mL/min. The obtained thermograms were comparatively analyzed to evaluate changes in the melting behaviour and thermal transitions of quercetin following encapsulation within the transferosomal system.

2.4.4 Drug Entrapment

Entrapment efficiency (*EE*, %) of quercetin in transferosomes was tested by ultracentrifugation. The transferosomal dispersion was centrifuged at high speed to separate the free drug from the entrapped drug. The supernatant containing unentrapped quercetin was collected and analyzed using the developed HPLC method [18]. The total quantity of entrapped drug was calculated by deducting the free-form drug from the total drug added. All the experiments were performed in triplicate, and results were expressed as mean ± SD. Entrapment efficiency (*EE*, %) was computed using the following equation:

$$EE = \left(\frac{\text{Total drug} - \text{Free drug}}{\text{Total drug}} \right) \times 100\,\%$$

2.4.5 In vitro Drug Release and Release Kinetics Studies

The in vitro release was carried out using a six-station Franz diffusion cell apparatus (Orchid Scientific & Innovative India Pvt. Ltd., India) with a receptor compartment capacity of 12 mL and an effective diffusion area of approximately 1.77 cm^2. A pre-soaked dialysis membrane (LA395, Dialysis membrane-110 AV; HiMedia Laboratories, Mumbai, India) was mounted between the donor and receptor compartments [6]. The receptor compartment was filled with phosphate-buffered saline (PBS, pH 7.4) and maintained at 37 ± 0.5°C under continuous magnetic stirring at 100 rpm. An accurately measured quantity of the transferosomal dispersion equivalent to 10 mg of quercetin was placed in the donor compartment. At predetermined time intervals (0.5, 1, 2, 3, 4, 5, 6, 10, 12, and 24 h), 2 mL aliquots were withdrawn from the receptor compartment. This was immediately replaced with an equal volume of fresh pre-warmed release medium to maintain constant volume and sink conditions. The collected samples were filtered through a 0.45 µm membrane filter and analysed using the validated RP-HPLC method described previously. Drug release from a plain quercetin suspension equivalent to 10 mg of quercetin in PBS (pH 7.4) was evaluated under identical experimental conditions for comparison. All experiments were performed in triplicate, and results were expressed as mean ± SD. To investigate the release mechanism, the cumulative drug release data were fitted to zero-order, first-order, Higuchi, and Korsmeyer-Peppas kinetic models. The corresponding correlation coefficients (R^2) were determined. The model showing the highest R^2 value was considered to best describe the release kinetics, while the release exponent (n) obtained from the Korsmeyer-Peppas model was used to predict the mechanism of drug release [15].

2.5 Statistical Analysis

All experiments were executed thrice, and the outcomes are discussed as mean ± standard deviation (SD) and relative standard deviation (RSD). GraphPad Prism version 8.0.2 (GraphPad Software Inc., San Diego, CA, USA) was used to apply statistics to the results. Differences between experimental groups were analyzed using two-way ANOVA, followed by Tukey's multiple comparisons test. A value of $p<0.05$ was considered statistically significant.

3 Results and Discussion

3.1 Molecular Docking Analysis

Molecular docking was carried out to evaluate the binding affinity and interaction characteristics of quercetin against clinically established anti-inflammatory agents, hydrocortisone and tacrolimus. Docking was done towards selected protein targets involved in inflammatory pathways. This included NF-kB (PDB

ID: 3GUT), TSLP (PDB ID: 5J11), and IgE (PDB ID: 2Y7Q). The calculated binding energies (**Table 1**) indicate that quercetin exhibits favourable binding across all targets with a clear preference for NF-kB. Quercetin showed the highest binding affinity toward NF-kB (-8.66 kcal/mol), followed by IgE (-7.22 kcal/mol) and TSLP (-6.542 kcal/mol). The more negative binding energy for NF-kB suggests a thermodynamically more stable complex arising from optimal complementarity between the ligands pharmacophoric features and the binding pocket [19,20]. Hydrocortisone exhibited binding energies of -6.54, -5.26, and -6.54 kcal/mol, and tacrolimus showed binding energies of -6.34, -5.29, and -6.34 kcal/mol against NF-kB, TSLP, and IgE, respectively. The comparatively lower binding energies of quercetin suggest stronger stability towards these inflammatory mediators than the reference drugs under applied docking conditions (Supplementary **Figures S1-S6**).

Table 1

Binding energy values of quercetin with selected protein targets

S. No	Ligand/Drug	Protein/Receptor	Docking score, kcal/mol
1.	**Quercetin**	**NF-kB (PDB ID: 3GUT)**	-8.66
2.	**Quercetin**	**TSLP (PDB ID: 5J11)**	-6.54
3.	**Quercetin**	**IgE (PDB ID: 2Y7Q)**	-7.22
4.	**Tacrolimus**	**NF-kB (PDB ID: 3GUT)**	-6.54
5.	**Tacrolimus**	**TSLP (PDB ID: 5J11)**	-5.26
6.	**Tacrolimus**	**IgE (PDB ID: 2Y7Q)**	-6.54
7.	**Hydrocortisone**	**NF-kB (PDB ID: 3GUT)**	-6.34
8.	**Hydrocortisone**	**TSLP (PDB ID: 5J11)**	-5.29
9.	**Hydrocortisone**	**IgE (PDB ID: 2Y7Q)**	-6.34

3.1.1 Binding Interaction Profile

The chemical structure of quercetin is presented in **Figure 1A**. The 3D and 2D interaction maps (**Figure 1**) reveal that quercetin engages in a network of hydrogen bonding and hydrophobic interactions owing to its polyphenolic scaffold. In NF-kB (**Figure 1a and d**), quercetin establishes multiple hydrogen bonds through its phenolic hydroxyl groups with polar and charged residues. These include lysine, glutamine, and arginine. The aromatic rings of quercetin were also involved in hydrophobic interactions with surrounding residues. This led to a stable conformation. The presence of multiple interaction points supports the higher binding affinity observed for this target. In comparison, both hydrocortisone and tacrolimus also interacted through hydrogen bonding and hydrophobic interactions but exhibited fewer favourable contacts, resulting in comparatively lower binding affinities.

For TSLP (**Figure 1b and e**), quercetin showed moderate binding affinity. The interaction profile indicated hydrogen-bonding interactions involving hydroxyl groups with residues such as serine and threonine. This was along with hydrophobic contacts with leucine and isoleucine residues. Although stable interactions were observed, the number and strength of interactions were comparatively lower than those seen with NF-kB. This might explain the reduced binding energy. The reference compounds formed stable interactions with residues including Ser68, Arg153, Thr77, and Asn85, although their scores remained lower.

In IgE (**Figure 1c and f**), quercetin demonstrated good binding affinity with a combination of hydrogen bonding and hydrophobic interactions. The hydroxyl groups participated in hydrogen bonding with polar residues. The planar aromatic structure facilitated hydrophobic interactions within the binding pocket. These interactions contribute to the stability of the ligand-protein complex. The interaction network is sufficient to stabilize the complex, but it appears less extensive than that observed for NF-kB. Although hydrocortisone and tacrolimus occupied the same binding pocket and established hydrogen bond residues such as Pro12, Ser93 and Glu95, their interaction networks were comparatively less extensive than those observed for quercetin [21].

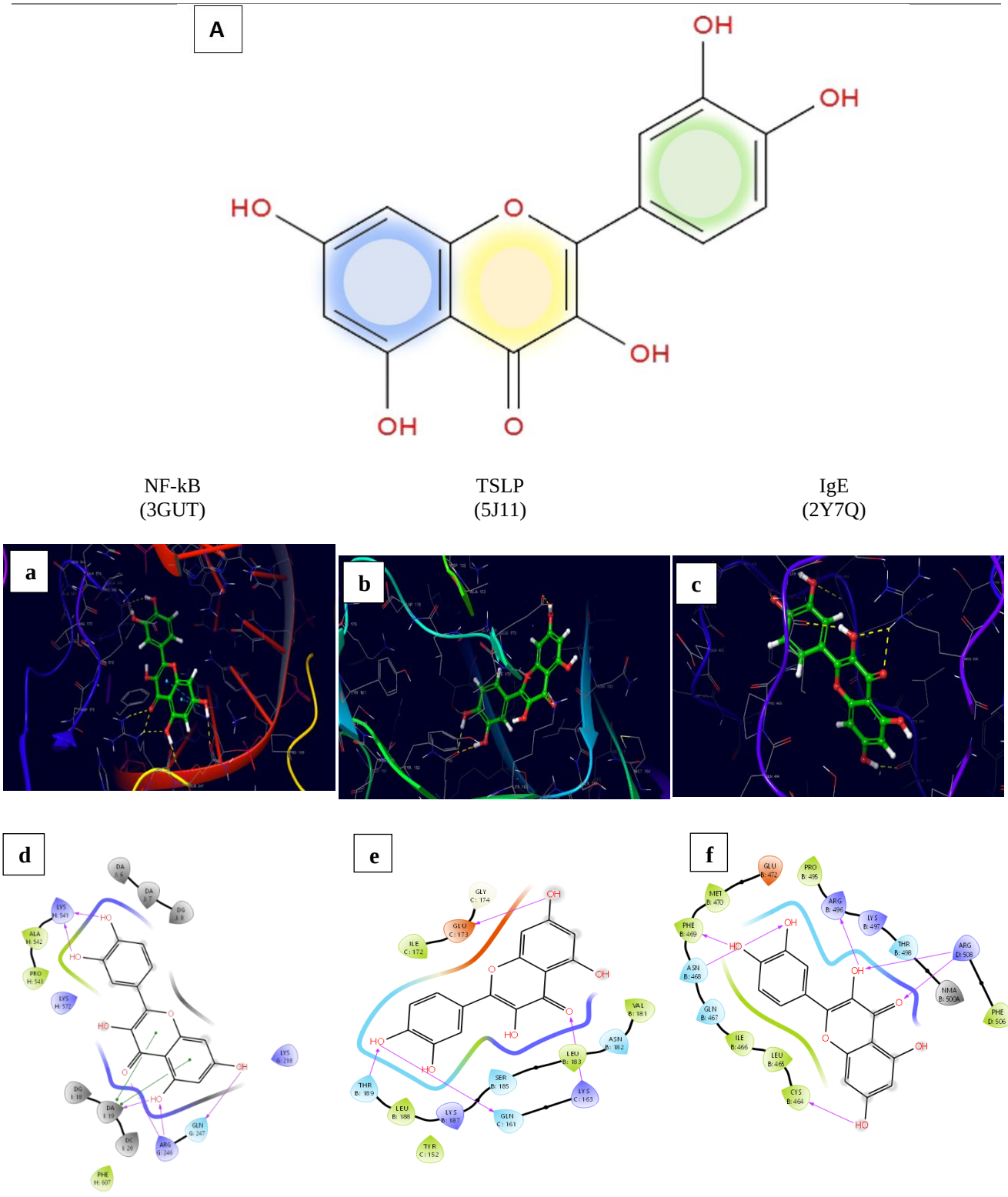

Figure 1 Structural representation and molecular docking interactions of quercetin with selected protein targets. The 2D chemical structure highlighting its functional groups is shown at the top (A). Molecular docking poses of quercetin within the active sites of (a) NF-kB (PDB ID: 3GUT), (b) TSLP (PDB ID: 5J11), and (c) IgE (PDB ID: 2Y7Q) are presented as 3D interaction views. Corresponding 2D ligand-protein interaction diagrams are shown in (d-f), illustrating hydrogen bonding and hydrophobic contacts between quercetin and key amino acid residues.

3.1.2 Pharmacophoric Considerations

The binding behaviour of quercetin could be rationalized based on its structural features. The phenolic hydroxyl groups (-OH) act as key hydrogen bond donors and acceptors, enabling strong polar interactions with amino acid residues. The carbonyl (C=O) serves as an additional hydrogen bond acceptor, enhancing interaction versatility. Due to its planar, aromatic nature, the molecule engages in hydrophobic and pi-pi stacking interactions. This facilitates stable accommodation within hydrophobic regions of the protein pocket. This combination of hydrogen bonding capacity and hydrophobic surface area represents a favourable pharmacophoric profile for interaction with protein targets involved in inflammatory signalling [22].

3.2 HPLC Method Development

3.2.1 Optimization of HPLC Method

The chromatographic conditions for the quantitative estimation of quercetin were systematically optimized to achieve adequate peak resolution, symmetry, and reproducibility. Several preliminary trials were performed. This included varying the mobile phase composition, solvent ratios, and chromatographic parameters. Initially, different ratios of aqueous phase (0.3% orthophosphoric acid) and organic phase (acetonitrile) were investigated. The mobile phase composition was systematically varied from 10:90 to 90:10 (v/v) in incremental ratios to achieve optimal separation. At higher aqueous compositions (>60%), quercetin exhibited increased retention with broadened and asymmetric peaks. This indicated strong interaction with the stationary phase. Conversely, higher organic content (>70% acetonitrile) resulted in rapid elution with poor peak resolution and reduced sensitivity. Optimization trials revealed that a 50:50 (v/v) ratio of 0.3% OPA (A) and acetonitrile (B) provided the most favourable chromatographic performance (**Figure 2**). Under these conditions, quercetin demonstrated a sharp and symmetrical peak with optimal retention.

3.2.2 Chromatographic Performance

Under the optimized conditions (mobile phase A:B = 50:50, flow rate 1.0 mL/min, injection volume 10µL, detection wavelength 369 nm), quercetin eluted at a retention time of 4.303 min (**Figure 2**). The peak was symmetrical and free from interference, indicating high specificity of the method. The chromatographic system exhibited excellent column efficiency, as evidenced by a theoretical plate count of 5941, which is significantly above the acceptable limit (>2000). This indicates efficient mass transfer and minimal band broadening during separation. Peak symmetry was evaluated using the tailing factor, which was found to be 0.887, indicating minimal peak distortion within the acceptance criteria.

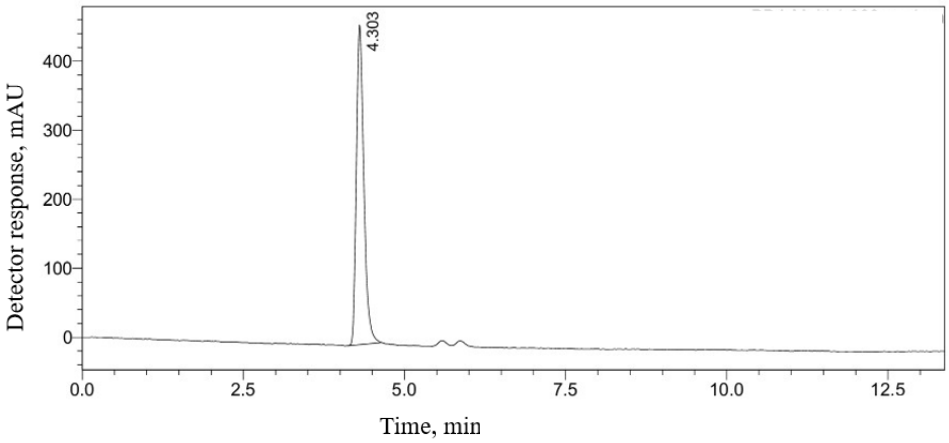

Figure 2. RP-HPLC chromatogram of quercetin under optimized conditions (0.3% OPA: ACN, 50:50 v/v), showing a sharp peak at 4.303 min with good peak symmetry and resolution. Chromatographic separation was achieved on a C18 column at a flow rate of 1.0 mL/min with detection at 369 nm

3.2.3 System Suitability and Method Reliability

The parameters for system suitability were evaluated prior to analysis to confirm the adequate working of the system under optimized conditions. A standard solution of quercetin was injected repeatedly (n=6), and key parameters, including retention time, theoretical plate count, tailing factor, and peak area consistency, were assessed. The chromatographic system produced a distinct and symmetrical peak for quercetin at a

retention time of 4.303 ± 0.01 min. Theoretical plate count was found to be 5941 ± 122, indicating satisfactory column efficiency, while the tailing factor (0.887 ± 0.03) confirmed acceptable peak symmetry. The consistency in retention time and peak area across replicate injections demonstrated stable system performance. These results show that the system was appropriate for subsequent method validation and quantitative analysis.

3.3 HPLC Method Validation

Method Validation of the optimized chromatographic conditions was done by following the ICH-guidelines. It was evaluated to ensure its suitability for analytical applications. The method was evaluated for key validation parameters indicating linearity, accuracy, precision, sensitivity, specificity, robustness, and ruggedness. Each parameter was assessed using appropriate experimental procedures under optimized chromatographic conditions. The results obtained were analyzed to confirm the reliability, consistency, and analytical performance of the method for the intended purpose [23].

3.3.1 Linearity and Range

The linearity of the developed RP-HPLC method for quercetin was evaluated over a concentration range of 20-120 µg/mL. Calibration standards were prepared at six concentration levels and analyzed under optimized chromatographic conditions. A strong linear relationship was observed between peak area and concentration, as depicted in the calibration curve (Figure 3). The regression equation was found to be:

$$y = 37567\,x - 15333\,.$$

The correlation coefficient (R^2) was found to be 0.998, indicating good linearity across the selected range. The linear response confirms that the process is fit for the quantitative assessment of quercetin within the studied concentration range. The corresponding calibration curve is provided in Supplementary **Figure S7**.

3.3.2 Sensitivity

The slope of the calibration curve and the standard deviation of the responses were used to determine the LOD and LOQ. Using the slope obtained from the regression equation (S= 37567) and considering the typical standard deviation of the response derived from calibration data, the LOD and LOQ were calculated as:

$$LOD = \frac{3.3\,x\,SD}{S}$$

$$LOQ = \frac{10\,x\,SD}{S}$$

The calculated LOD of 0.57 µg/mL and LOQ of 1.69 µg/mL directs method is sensitive enough to detect and quantify low concentrations of quercetin. Specifically, the low LOQ supports its application in routine analysis demanding high precision.

3.3.3 Accuracy

The developed RP-HPLC method's accuracy was evaluated using the standard addition technique at three concentration levels (80%, 100%, and 120%). Each level was analyzed in triplicate to assess the recovery of quercetin in the presence of the formulation matrix. The percentage recovery values obtained at all three levels ranged from 99.28 % to 100.96 % (**Table 2**).

Table 2

Accuracy data of quercetin determined by RP-HPLC using the standard addition method at 80%, 100%, and 120 % (n=3), expressed as mean % recovery ± SD and %RSD

S. No	Level, %	Amount added, µg/mL	Amount found, µg/mL	Recovery, %	Mean Recovery ± SD, %	RSD, %
1	80	80.0	79.42	99.28	99.89 ± 0.59	0.59
2		80.0	80.36	100.45		
3		80.0	79.95	99.94		
4	100	100.0	99.10	99.10	99.99 ± 0.86	0.86
5		100.0	100.82	100.82		
6		100.0	100.05	100.05		
7	120	120.0	118.96	99.13	100.11 ± 0.92	0.92
8		120.0	121.15	100.96		
9		120.0	120.28	100.23		

This indicates that the method is capable of accurately quantifying quercetin without interference from excipients present in the Transferosomal system. The %RSD values for all levels were observed to be less than 2%. The recovery values confirm the absence of significant matrix effects. This indicates that the method is both accurate and reliable for quantitative estimation of quercetin in the developed formulation.

3.3.4 Precision

The precision of the developed RP-HPLC method was evaluated in terms of intra-day (repeatability) and inter-day (intermediate precision) at three concentration levels. Each concentration was analyzed in triplicate under the same experimental conditions. For intra-day precision, the % RSD values were found to be 0.73, 0.77, and 0.76 % for 80, 100, and 120 µg/mL, respectively (**Table 3**). Similarly, inter-day precision showed %RSD values of 1.04, 0.98, and 0.94 % for the same concentrations. The observed %RSD values for both intra-day and inter-day studies were well below the acceptable limit of 2 %.

Table 3

Intraday and interday precision data for quercetin determined by RP-HPLC at 80, 100, and 120 µg/mL (n=3), expressed as mean % recovery ± SD and RSD

S. No	Concentration, µg/mL	Intraday Precision		Interday precision	
		Peak Area (Mean ± SD)	RSD, %	Peak Area (Mean ± SD)	RSD, %
1	80	2985911± 21850	0.73	2978450 ± 31200	1.04
2	100	3732389 ± 28950	0.77	3725600 ± 36800	0.98
3	120	4478867 ± 34200	0.76	4470200 ± 41950	0.94

3.3.5 Robustness

The robustness of the proposed method was investigated by deliberately applying slight changes to important parameters in chromatography (flow rate, mobile phase ratio, and detection wavelength). The influence of these variations on chromatographic responses such as retention time, peak area, tailing factor, and theoretical plate count was carefully analyzed. In all tested conditions, the RSD values for peak area remained below 2%, and the system suitability criteria were consistently met. These results indicate that the method maintains its performance even when minor adjustments are introduced (**Table 4**).

Table 4

Robustness evaluation of the RP-HPLC method under small deliberate variations in the chromatographic conditions, including Flow rate (mL/min), Mobile phase (OPA: ACN), and wavelength (nm)

Parameter	Condition	Retention time, min	RSD, %	Tailing factor	Theoretical plates
Flow rate, mL/min)	0.9 mL/min	5.82	0.88	1.21	5120
	1.0 mL/min	4.303	0.77	1.18	5941
	1.1 mL/min	3.965	0.95	1.23	5058
Mobile phase (OPA: ACN)	48:52	4.120	0.83	1.25	5190
	50:50	4.303	0.77	1.17	5283
	52:48	5.633	0.91	1.22	5210
Wavelength, nm	367	4.307	0.94	1.16	5220
	369	4.303	0.77	1.17	5285
	371	4.311	0.82	1.15	5175

3.3.6 Ruggedness

The method's ruggedness was evaluated by performing the analysis under varying conditions such as different analysts and on different days. The effect of these variations on chromatographic parameters was assessed. This included peak area, retention time (RT), and system suitability parameters. The RSD values obtained under all tested conditions were found to be less than 2%. The outcomes suggest that the method is rugged and reproducible irrespective of analysts or day-to-day experimental differences.

3.3.7 Specificity

The method's specificity was evaluated by analysing blank, standard, and sample solutions to assess potential interference from excipients and formulation components. The chromatograms obtained for the Transferosomal formulation showed no co-eluting peaks or interfering signals at the retention time of quercetin. A well-defined, sharp, and symmetrical peak was observed at the optimized retention time, indicating efficient chromatographic separation. The absence of interference from phospholipids, surfactants, or other excipients present in the Transferosomal system confirms that the method is highly specific for the detection and quantification of the drug. The validated RP-HPLC method demonstrated satisfactory analytical performance with respect to linearity, accuracy, precision, specificity, robustness and ruggedness. This supports its suitability for routine quantitative analysis and quality control of the developed transferosomal formulation.

3.4 Transferosome Evaluation

3.4.1 Dynamic Light Scattering (DLS) Studies

The particle size distribution of the optimized quercetin-loaded transferosome was determined using dynamic light scattering. The vesicles exhibited a mean particle size of 190.4 ± 1.6nm, indicating formation of nanosized carriers suitable for topical delivery (**Figure 3 a)**. The size is considered optimal for enhanced skin permeation. This is because nanoscale vesicles have the ability to efficiently traverse the stratum corneum. The obtained size falls within the range reported for previously developed quercetin-loaded transferosomal systems [6]. Minor differences in particle size among studies may be attributed to variations in phospholipid composition, edge activator concentration, drug-to-lipid ratio, and processing conditions as well as intended route of administration. The polydispersity index (PDI) values below 0.5 are generally indicative of uniform dispersion. Here, the PDI was found to be 0.324, suggesting a moderately narrow size distribution and acceptable homogeneity. This value is comparable with those reported by Pandit et al. [15] (0.333). The zeta potential was recorded as -22.4 mV (Figure 3 b). This reflects a stable colloidal system. The negative zeta potential observed in the present study is consistent with previously reported quercetin-loaded transferosomal systems [6, 15]. The negative surface charge may be attributed to the presence of phospholipids and edge activators. They contribute to the constant motion of the vesicles, thereby reducing aggregation via electrostatic repulsion [24].

3.4.2 Morphological Analysis (SEM)

The surface morphology of the optimized Transferosomal formulation was examined using scanning electron microscopy (SEM), as shown in **Figure 3 c**. The micrograph revealed the presence of a distinct vesicular structure with spherical morphology. The vesicles appeared well-formed with smooth surfaces and defined boundaries. The slightly deformed morphology is characteristic of ultra-flexible lipid-based carriers like transferosomes. The absence of crystalline drug deposits or sharp-edge particulates in the micrographs suggests that quercetin is well loaded [25, 26].

3.4.3 Molecular Analysis Using ATR-FTIR and DSC

The FTIR spectra of pure quercetin, Phospholipon® 90G, and the optimised quercetin-loaded transferosomes are presented in **Figure 3d**. Pure quercetin exhibited characteristic adsorption bands corresponding to the O-H stretching vibration (3275 cm^{-1}), aromatic C=C stretching (1605-1508 cm^{-1}), C=O stretching (1662 cm^{-1}), and C-O stretching vibrations within the 1310-1080 cm^{-1} region, confirming the identity of the drug. Phospholipon® 90G displayed its characteristic lipid peaks, including C-H stretching vibrations at 2917 and 2850 cm^{-1}, ester carbonyl (C=O) stretching at 1735 cm^{-1}, and phosphate-associated vibrations in the 1236-1061 cm^{-1} region [27, 28]. The FTIR spectrum of the optimised transferosomal formulation retained the characteristic adsorption bands of both quercetin and the phospholipid, with slight reductions in intensity and minor shifts in selected peaks. Importantly, no new adsorption bands or disappearance of characteristic functional groups were observed. This indicates the absence of chemical interactions between quercetin and the formulation excipients during transferosome preparation. These findings suggest that quercetin remained chemically stable following encapsulation and was successfully incorporated within the vesicles.

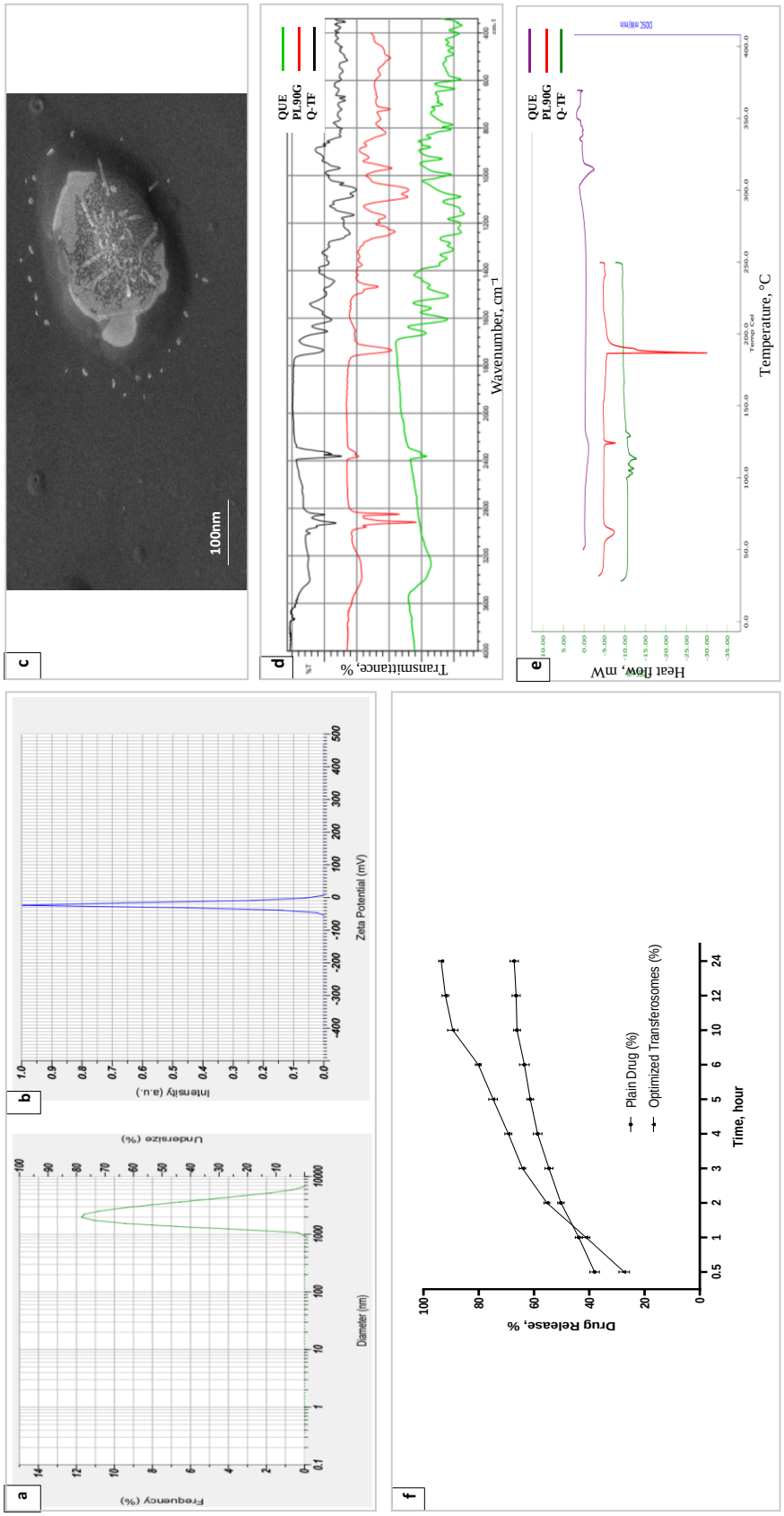

Figure 3 Physicochemical characterization of quercetin-loaded transferosomes: (a) particle size distribution, (b) zeta potential, (c) scanning electron microscopy (SEM) micrograph, (d) Fourier transform infrared (FTIR-ATR) spectra, (e) differential scanning calorimetry (DSC) thermograms, and (f) in vitro cumulative drug release profile.

The DSC thermograms of pure quercetin, Phospholipon® 90G, and the transferosomal formulation are shown in **Figure 3e**. Pure quercetin exhibited a distinct sharp endothermic peak at approximately 314^{o}C. This corresponds to its melting point and confirms its crystalline nature. In contrast, Phospholipon® 90G showed a characteristic endothermic transition around 187^{o}C. This represents the thermal behaviour of phospholipids. The DSC thermogram of the transferosome showed the absence of the characteristic melting endotherm of crystalline quercetin, while the thermal transitions associated with the lipid matrix remained evident [29]. The disappearance of the quercetin melting peak indicates that the drug was no longer present in its crystalline state but was molecularly dispersed or entrapped within transferosomes. Also, no additional thermal events indicative of drug degradation or incompatibility were observed.

3.4.4 Entrapment Efficiency

The entrapment efficiency (EE, %) of quercetin within the Transferosomal vesicles was determined using a previously developed and validated RP-HPLC method. Following ultracentrifugation, the supernatant containing unentrapped drug was collected. It was then quantified at 369nm under optimized chromatographic conditions. The entrapment efficiency was found to be 86.24 ± 1.61 %, indicating incorporation of quercetin into the lipid bilayer. The high entrapment could be attributed to the lipophilic nature of quercetin [30, 31]. The high entrapment efficiency achieved in the present study is comparable with values reported for quercetin-loaded transferosomes in the literature. Differences in drug loading and encapsulation efficiency may be influenced by lipid concentration, drug-to-lipid ratio, and preparation methodology [4,6,15].

3.4.5 In vitro Drug Release

The cumulative in vitro release profiles of plain quercetin and the optimised quercetin-loaded transferosomes are presented in **Figure 3f**. The plain drug exhibited a relatively rapid initial release, with approximately 38.1 ± 1.7% released within the first 30 min. This was followed by a gradual plateau, reaching 67.2 ± 1.5% cumulative release after 24 h. The limited release of the plain drug could be attributed to the poor aqueous solubility of quercetin. In contrast, the transferosomal formulation exhibited a characteristic biphasic release profile consisting of an initial burst release followed by a sustained release phase. Approximately 27.4 ± 1.9% of quercetin was released within the first 30 min, increasing to 80.2 ± 1.1% after 6 h. The cumulative drug release reached 93.6 ± 0.9% after 24 h, which was significantly higher than that observed for the plain drug ($p<0.05$). The reduced initial burst release from the transferosomes indicates efficient encapsulation of quercetin within the phospholipid bilayer. The subsequent sustained release could be attributed to the gradual diffusion of the drug through the hydrated lipid membrane. The incorporation of Tween 80 as an edge activator likely enhanced membrane flexibility and permeability. This facilitates controlled drug diffusion while maintaining vesicular integrity. In addition, the nanosized vesicles provide a large surface area that promotes efficient interaction with the release medium and improves drug dissolution [32].

3.4.6 Release kinetics

The release data were fitted to various kinetic models to investigate the mechanism of drug release from the developed transferosomes. Among the evaluated models, the Korsmeyer-Peppas model exhibited the highest correlation coefficient (R^2 =0.980), indicating that this model best describes the release behaviour of quercetin from the transferosomal system. The Higuchi model also demonstrated a good correlation (R^2 =0.923), suggesting that diffusion through the hydrated phospholipid matrix plays a significant role in drug release. The calculated release exponent (n=0.41) indicates Fickian diffusion. This demonstrates that quercetin release is primarily governed by concentration-driven diffusion from the lipid bilayer rather than by erosion or structural relaxation of the vesicles. The comparatively lower R^2 values obtained for the zero-order (0.611) and first-order (0.807) models further support that the release does not follow constant rate kinetics but is predominantly diffusion-controlled [33].

4 Conclusions

The present study successfully established and validated a robust RP-HPLC method for the quantitative assessment of quercetin. The analytical method demonstrated excellent linearity, accuracy, precision, and specificity, confirming its suitability for routine analysis. The optimized transferosomes exhibited nanoscale particle size, moderate polydispersity, and a negatively charged surface. FTIR and DSC analyses confirmed the compatibility and suggested successful incorporation of the drug. High entrapment efficiency confirmed effective incorporation of the drug within the vesicular system. Morphological analysis further supported the formation of deformable lipid vesicles. Additionally, molecular docking studies provided preliminary mech-

anistic insights into the interaction of quercetin with key inflammatory targets. The formulation exhibited sustained drug release over 24 h with release kinetics best described by the Korsmeyer-Peppas model. In conclusion, the study offers a promising strategy for enhanced topical delivery of quercetin that warrants further *ex vivo* and pre-clinical evaluations.

Supporting Information

The Supporting Information is available free at https://ejc.buketov.edu.kz/ejc/article/view/740/416

Funding

The authors wish to sincerely acknowledge the financial assistance provided by DST-PURSE, Government of India. This work is supported by PAIR network of SAKSHAM funded by ANRF (Anusandhan National Research Foundation), India, through grant ANRF/PAIR/ 2025/000018/PAIR, administered and mentored by IIT Indore.

*Author Information**

**The authors' names are presented in the following order: First Name, Middle Name and Last Name*

Natasha Sudhir Akojwar - DST-PURSE fellow and Ph.D. Research Scholar, Department of Pharmaceutical Sciences, Rashtrasant Tukadoji Maharaj Nagpur University, 440033, Nagpur, Maharashtra, India; e-mail: natasha.akojwar@gmail.com, https://orcid.org/0009-0000-3010-3754

Nikhil Yadavrao Yenorkar - Ph.D. Research Scholar, Department of Pharmaceutical Sciences, Rashtrasant Tukadoji Maharaj Nagpur University, 440033, Nagpur, Maharashtra, India; e-mail: nikhilyenorkar23@gmail.com, https://orcid.org/0000-0003-0660-5652

Ayusha Omprakash Dondulkar - Ph.D. Research Scholar, Department of Pharmaceutical Sciences, Rashtrasant Tukadoji Maharaj Nagpur University, 440033, Nagpur, Maharashtra, India; e-mail: ayushadondulkar155@gmail.com, https://orcid.org/0000-0002-3544-4248

Ankit Ganeshpurkar - Assistant Professor, Department of Pharmaceutical Sciences, Dr. Harisingh Gour Vishwavidyalaya (A Central University), 470003, Sagar, Madhya Pradesh, India; e-mail: ankitganeshpurkar@gmail.com, https://orcid.org/0000-0002-2029-3424

Beauty Behera - Assistant Professor, Department of Pharmaceutics, Delhi Pharmaceutical Sciences and Research University, 110017, New Delhi, India; e-mail: beauty.behera@dpsru.edu.in, https://orcid.org/0000-0003-3756-0741

Satyendra Kuldip Prasad (*corresponding author*) - Assistant Professor, Department of Pharmaceutical Sciences, Rashtrasant Tukadoji Maharaj Nagpur University, 440033, Nagpur, Maharashtra, India; e-mail: skprasad.itbhu@gmail.com, skprasad.rs.phe@itbhu.ac.in, https://orcid.org/0000-0002-4762-9733

Author Contributions

The manuscript was written through contributions of all authors. All authors have given approval to the final version of the manuscript. CRediT: **Natasha Sudhir Akojwar** data curation, investigation, methodology, validation, visualization, writing-review & editing**; Nikhil Yadavrao Yenorkar** data curation, formal analysis, visualization**; Ayusha Omprakash Dondulkar** data curation, formal analysis, visualization**; Ankit Ganeshpurkar** data curation, investigation, visualization, writing-review & editing **Beauty Behera** data curation, formal analysis, resources, supervision; **Satyendra Kuldip Prasad** conceptualization, data curation, formal analysis, funding acquisition, resources, supervision, validation, writing-original draft, writing-review & editing.

Conflict of interest

The authors declare no conflict of interest.

Declaration

The authors declare that the AI-assisted tools were used only for language refinement and grammatical editing of the manuscript and not for data generation or analysis.

References

1 Shabir, I., Kumar Pandey, V., Shams, R., Dar, A. H., Dash, K. K., Khan, S. A., ... & Pandiselvam, R. (2022). Promising bioactive properties of quercetin for potential food applications and health benefits: A review. *Frontiers in nutrition*, *9*, 999752. https://doi.org/10.3389/fnut.2022.999752

2 Tomou, E. M., Papakyriakopoulou, P., Saitani, E. M., Valsami, G., Pippa, N., & Skaltsa, H. (2023). Recent advances in nanoformulations for quercetin delivery. *Pharmaceutics*, *15*(6), 1656. 10.3390/pharmaceutics15061656

3 Simrah, Hafeez, A., Usmani, S. A., & Izhar, M. P. (2024). Transfersome, an ultra-deformable lipid-based drug nanocarrier: an updated review with therapeutic applications. *Naunyn-Schmiedeberg's Archives of Pharmacology*, *397*(2), 639-673. 10.1007/s00210-023-02670-8

4 Mali, A. J., Kakade, S., Khardekar, A., Ganeshpurkar, A., & Kumari, A. (2025). Development of novel emulgel comprising quercetin-loaded transferosomes and thuja oil for enhanced anti-inflammatory efficacy. *Next Nanotechnology*, *8*, 100246. https://doi.org/10.1016/j.nxnano.2025.100246

5 Sabarathinam, S. (2024). Unraveling the therapeutic potential of quercetin and quercetin-3-O-glucuronide in Alzheimer's disease through network pharmacology, molecular docking, and dynamic simulations. *Scientific Reports*, *14*(1), 14852. https://doi.org/10.1038/s41598-024-61779-9

6 Elkomy, M. H., Zaki, R. M., Alsaidan, O. A., Elmowafy, M., Zafar, A., Shalaby, K., Abdelgawad, M. A., Abd El-Hack, M. E., & Mahgoub, S. A. (2023). Intranasal nanotransferosomal gel for quercetin brain targeting: I. Optimization, characterization, brain localization, and cytotoxic studies. *Pharmaceutics*, *15*(7), 1805. https://doi.org/10.3390/pharmaceutics15071805

7 Chen, X., Shen, Q., Zhou, R., Lin, Y., Zhou, T., Chen, K., ... & Yang, A. (2026). Screening of active constituents in camellia oil against atopic dermatitis via molecular docking and experimental validation: elucidation of the underlying molecular mechanism: X. Chen et al. *Inflammopharmacology*, 1-14. 10.1007/s10787-026-02118-4

8 Suleman, M., Moltrasio, C., Tricarico, P. M., Marzano, A. V., & Crovella, S. (2024). Natural compounds targeting thymic stromal lymphopoietin (TSLP): a promising therapeutic strategy for atopic dermatitis. *Biomolecules*, *14*(12), 1521. https://doi.org/10.3390/biom14121521

9 Ang, L. F., Yam, M. F., Fung, Y. T. T., Kiang, P. K., & Darwin, Y. (2014). HPLC method for simultaneous quantitative detection of quercetin and curcuminoids in traditional chinese medicines. *Journal of pharmacopuncture*, *17*(4), 36. 10.3831/KPI.2014.17.035

10 Mustafa, A. M., Abouelenein, D., Angeloni, S., Maggi, F., Navarini, L., Sagratini, G., ... & Caprioli, G. (2022). A new HPLC-MS/MS method for the simultaneous determination of quercetin and its derivatives in green coffee beans. *Foods*, *11*(19), 3033. https://doi.org/10.3390/foods11193033

11 Khursheed, R., Wadhwa, S., Kumar, B., Gulati, M., Gupta, S., Chaitanya, M. V. N. L., ... & Singh, S. K. (2022). Development and validation of RP-HPLC based bioanalytical method for simultaneous estimation of curcumin and quercetin in rat's plasma. *South African Journal of Botany*, *149*, 870-877. 10.1016/j.sajb.2021.12.009

12 Li, L., Cheng, J., Lu, F., Du, Y., Xie, Y., Zhou, C., ... & Feng, Y. (2023). Optimized HPLC extraction method of quercetin and berberine based on response surface analysis. *RSC advances*, *13*(42), 29427-29437. 10.1039/d3ra04384c

13 Mansour, F. R., Abdallah, I. A., Bedair, A., & Hamed, M. (2025). Analytical methods for the determination of quercetin and quercetin glycosides in pharmaceuticals and biological samples. *Critical Reviews in Analytical Chemistry*, *55*(1), 187-212. 10.1080/10408347.2023.2269421

14 Karnam, S., Jindal, A. B., & Paul, A. T. (2024). Quality by design-based optimization of teriflunomide and quercetin combinational topical transferosomes for the treatment of rheumatoid arthritis. *International Journal of Pharmaceutics*, *666*, 124829. 10.1016/j.ijpharm.2024.124829

15 Pandit, A. P., Omase, S. B., & Mute, V. M. (2020). A chitosan film containing quercetin-loaded transfersomes for treatment of secondary osteoporosis. *Drug delivery and translational research*, *10*(5), 1495-1506. 10.1007/s13346-020-00708-5

16 Nayak, S., Karmakar, A., Shinde, S., & Kumar, L. (2026). Development of Diclofenac Acid Encapsulated Transferosomal gel with Enhanced Antioxidant and Anti-Inflammatory Activities for the Management of Musculoskeletal Pain. *AAPS PharmSciTech*, *27*(1), 68. 10.1208/s12249-025-03276-4

17 Rasheed, M. S., Ansari, S. F., & Shahzadi, I. (2022). Formulation, characterization of glucosamine loaded transfersomes and in vivo evaluation using papain induced arthritis model. *Scientific Reports*, *12*(1), 19813. https://doi.org/10.1038/s41598-022-23103-1

18 Xing, H., Yang, Y., Zhao, Z., Lv, K., Shao, Y., Zhang, Z., & Ma, D. (2026). Transfersomes with core and surface-loaded NF-κB p65 siRNA for enhanced transdermal transfection and effective treatment of psoriasis. *BMEMat*, e70084. https://doi.org/10.1002/bmm2.70084

19 Chen, H., Lu, C., Liu, H., Wang, M., Zhao, H., Yan, Y., & Han, L. (2017). Quercetin ameliorates imiquimod-induced psoriasis-like skin inflammation in mice via the NF-κB pathway. *International immunopharmacology*, *48*, 110-117. 10.1016/j.intimp.2017.04.022

20 Beken, B., Serttas, R., Yazicioglu, M., Turkekul, K., & Erdogan, S. (2020). Quercetin improves inflammation, oxidative stress, and impaired wound healing in atopic dermatitis model of human keratinocytes. *Pediatric allergy, immunology, and pulmonology*, *33*(2), 69-79. https://doi.org/10.1089/ped.2019.1137

21 Lin, C. F., Leu, Y. L., Al-Suwayeh, S. A., Ku, M. C., Hwang, T. L., & Fang, J. Y. (2012). Anti-inflammatory activity and percutaneous absorption of quercetin and its polymethoxylated compound and glycosides: The relationships to chemical structures. *European Journal of Pharmaceutical Sciences*, *47*(5), 857-864. 10.1016/j.ejps.2012.04.024

22 Srivastava, A. K., Srivastava, S., Kumar, V., Ghosh, S., Yadav, S., Malik, R., ... & Prasad, R. (2024). Identification and mechanistic exploration of structural and conformational dynamics of NF-kB inhibitors: rationale insights from in silico and in vitro studies. *Journal of Biomolecular Structure and Dynamics*, *42*(3), 1485-1505. https://doi.org/10.1080/07391102.2023.2200490

23 Sarkar, M., Khandavilli, S., & Panchagnula, R. (2006). Development and validation of RP-HPLC and ultraviolet spectrophotometric methods of analysis for the quantitative estimation of antiretroviral drugs in pharmaceutical dosage forms. *Journal of Chromatography B*, *830*(2), 349-354. 10.1016/j.jchromb.2005.11.014

24 Wu, T. H., Yen, F. L., Lin, L. T., Tsai, T. R., Lin, C. C., & Cham, T. M. (2008). Preparation, physicochemical characterization, and antioxidant effects of quercetin nanoparticles. *International journal of pharmaceutics*, *346*(1-2), 160-168. https://doi.org/10.1016/j.ijpharm.2007.06.036

25 Sahu, A. N., & Mohapatra, D. (2021). Nanovesicular transferosomes for the topical delivery of plant bioactives. *Nanomedicine*, *16*(28), 2491-2495. 10.2217/nnm-2021-0316

26 Zhang, Z. J., & Michniak-Kohn, B. (2020). Flavosomes, novel deformable liposomes for the co-delivery of anti-inflammatory compounds to skin. *International journal of pharmaceutics*, *585*, 119500. https://doi.org/10.1016/j.ijpharm.2020.119500

27 Geara, D., Fayad, S., Chebil, L., & Harb, W. (2026). Molecular interactions of quercetin in menthol-based type V deep eutectic solvents: An integrated FTIR spectroscopy and molecular dynamics study. *Journal of Molecular Liquids*, *457*, 129714. https://doi.org/10.1016/j.molliq.2026.129714

28 Pawlikowska-Pawlęga, B., Dziubińska, H., Król, E., Trębacz, K., Jarosz-Wilkołazka, A., Paduch, R., Gawron, A., & Gruszecki, W. I. (2014). Characteristics of quercetin interactions with liposomal and vacuolar membranes. Biochimica et Biophysica Acta (BBA)-Biomembranes, 1838(1), 254–265. http://dx.doi.org/10.1016/j.bbamem.2013.08.014

29 Anwer, M. K., Al-Mansoor, M. A., Jamil, S., Al-Shdefat, R., Ansari, M. N., & Shakeel, F. (2016). Development and evaluation of PLGA polymer based nanoparticles of quercetin. *International Journal of Biological Macromolecules*, *92*, 213–219. https://doi.org/10.1016/j.ijbiomac.2016.07.025

30 Zhang, Y., Yang, Y., Tang, K., Hu, X., & Zou, G. (2008). Physicochemical characterization and antioxidant activity of quercetin-loaded chitosan nanoparticles. *Journal of Applied Polymer Science*, *107*(2), 891-897. 10.1002/app.26402

31 Carvalho, D., Jesus, Â., Pinho, C., Oliveira, R. F., Moreira, F., & Oliveira, A. I. (2023). Validation of an HPLC-DAD method for quercetin quantification in nanoparticles. *Pharmaceuticals*, *16*(12), 1736. https://doi.org/10.3390/ph16121736

32 Milutinov, J., Krstonošić, V., Ćirin, D., Hadnađev, M., Đanić, M., & Pavlović, N. (2025). Development and evaluation of quercetin topical emulgels: Physicochemical and rheological properties, stability and sun protective potential. *Journal of Molecular Liquids*, *417*, 126568. https://doi.org/10.1016/j.molliq.2024.126568

33 Rosita, N., Ambarwati, N., Erawati, T., & Hariyadi, D. M. (2022). Characterization and in vitro release of inhalation quercetin solid lipid microparticles: Effect of lipid. *Journal of Advanced Pharmaceutical Technology & Research*, *13*(1), 11–17. https://doi.org/10.4103/japtr.japtr_108_21

How to Cite: Muslimova, I.B., Khairusheva, A.B., Izbassar, K.A., Bekbol, Zh.A., Lissovskaya, L.I. & Korolkov, I.V. (2026). Surface-Enhanced Raman Detection of Low-Concentration Methylene Blue Using Nanoparticles Functionalized with 12-Mercaptododecanoic Acid. *Eurasian Journal of Chemistry, 31, 3(123), 53–65.* https://doi.org/10.31489/2959-0663/3-26-4

Article

Received: 20 May 2026 | Revised: 12 August 2026 |
Accepted: 20 August 2026 | Published online: 28 August 2026

UDC 544.42+519.242.7

https://doi.org/10.31489/2959-0663/3-26-4

Indira B. Muslimova[1*], Ainur B. Khairusheva[2], Kairat A. Izbassar[2], Zhangali A. Bekbol[2], Lana I. Lissovskaya[1,2], Ilya V. Korolkov[1,2]

[1]*Institute of Nuclear Physics ARKAE, Almaty, Kazakhstan*
[2]*L.N. Gumilyov Eurasian National University, Astana, Kazakhstan*
*(*Corresponding author's e-mail: i.muslimova@inp.kz)*

Surface-Enhanced Raman Detection of Low-Concentration Methylene Blue Using Nanoparticles Functionalized with 12-Mercaptododecanoic Acid

The development of sensitive and magnetically recoverable SERS substrates is of interest for the detection of organic pollutants at low concentrations. In this study, Fe_3O_4-CA@Au-12-MDA nanoparticles were synthesized for use as a SERS substrate in the detection of methylene blue dye within a concentration range of 10^{-2}-10^{-7} M. The Fe_3O_4 magnetic nanoparticles were modified with citric acid, followed by gold deposition and surface functionalization with 12-mercapto-dodecanoic acid. The stepwise modification of the nanoparticles was confirmed by FTIR, SEM-EDX and XRD, which revealed the presence of Au and organic functional groups whilst preserving the crystalline structure of Fe_3O_4. The Fe_3O_4-CA@Au-12-MDA-based SERS substrate exhibited signal enhancement compared to conventional Raman spectroscopy. For the characteristic bands at 1623 and 1396 cm^{-1}, the approximate EF values reached 0.11×10^5 and 0.15×10^5, respectively, corresponding to 5.95- and 5.40 times signal enhancement. The estimated LOD values calculated using the 3σ criterion were 4.05×10^{-8} and 5.97×10^{-8} M for the respective bands. The calibration curves demonstrated good linearity with R^2 values of 0.94-0.99 for SERS measurements. The results obtained demonstrate the potential of Fe_3O_4-CA@Au-12-MDA nanoparticles a magnetic SERS platform for the detection of low concentrations of organic dyes.

Keywords: SERS, detection, methylene blue, gold nanoparticles, functionalization, 12-mercaptododecanoic acid, magnetic nanoparticles, Fe_3O_4, Raman spectroscopy, limit of detection.

Introduction

Detection of organic dye molecules at low concentrations is of great importance for environmental monitoring, industrial process control, and analytical chemistry. Synthetic dyes are widely used in various industries, including textile, pharmaceutical, and chemical manufacturing, resulting in their frequent release into aquatic ecosystems. Even at low concentrations, these compounds may persist in the environment and serve as indicators of anthropogenic pollution [1–3].

Among various analytical methods Surface-Enhanced Raman Scattering (SERS) has attracted considerable attention due to its ability to provide highly sensitive and molecule-specific detection through vibrational «fingerprint» signals [4, 5]. Compared with conventional analytical techniques, SERS offers rapid analysis with minimal sample preparation and low operational costs, making it a promising tool for trace detection of organic compounds. Typically, SERS detection involves substrate fabrication, analyte deposition (drop-casting or solution mixing), and signal calibration based on characteristic Raman bands of the target molecule [6–11].

Methylene blue (MB) is widely used as a model analyte in SERS studies due to its well-defined Raman spectrum, chemical stability, and strong affinity toward metallic surfaces [8, 9, 12]. In ecology applications, MB is commonly employed as a model pollutant for evaluating water purification processes and monitoring degradation efficiency in photocatalytic and oxidation systems [13, 14]. Beyond environmental analysis, SERS-based detection of MB has also been investigated in food safety applications, including the analysis of dye residues in biological tissues, as well as in the development of ultrasensitive sensing platforms based on advanced nanomaterials [15–17]. Therefore, reliable detection of methylene blue at low concentrations is not only of analytical interest but also important for evaluating the signal enhancement efficiency of newly developed nanostructured Raman substrates [18, 19].

Over the past decade, various nanostructured materials have been investigated as SERS substrates. Among them, noble metal-based systems, including gold and silver nanoparticles [15, 16], nanorods, and

© 2026 The Authors. This is an open access article under the CC BY-NC-ND license (http://creativecommons.org/licenses/by-nc-nd/4.0/)

nanoporous films [20], are the most widely used due to their strong plasmonic properties. In addition, hybrid structures such as metal-semiconductor composites [21–23] including, Au/Cu_2O и Ag/ZnO systems, as well as porous and three-dimensional architectures based on graphene foams, silicon photonic crystals, and nanowires, have demonstrated enhanced sensitivity owing to the increased density of electromagnetic «hot spots» [23–25]. More recently, emerging materials such as two-dimensional MXenes and MoS-based heterostructures [26, 27], together with flexible polymeric and paper-based substrates [17, 28], have further expanded the practical applicability of SERS-platforms.

These developments have enabled progressively lower detection limits. For example, silver nanowire-based substrates demonstrated detection capabilities down to 10^{-16} M [29], whereas various hybrid and porous systems typically operate within the range 10^{-9}-10^{-12} M [24, 30]. Other platforms, including paper-based substrates and metal oxide composites, generally achieve detection limits in the ranges 10^{-8}-10^{-10} M [17, 22]. Despite these advances, a trade-off often exists between sensitivity, reproducibility, structural complexity, and fabrication simplicity. Advanced architectures, including three-dimensional and lithographically patterned nanostructures, provide high structural precision and reproducibility but frequently require technologically complex fabrication procedures [31, 32].

In recent years, FeO-based and Fe_3O_4/Au hybrid nanostructures have attracted attention as magnetic SERS substrates due to the combination of magnetic properties and plasmonic signal enhancement [33–36]. Several studies demonstrated successful SERS detection of rhodamine dyes and other probe molecules using Fe_3O_4-containing composites and Fe_3O_4/Au systems. For example, Fe_3O_4@Au NPs have superior SERS sensitivity for rhodamine and crystal violet with a detection limit of 10^{-7} M [34], magnetically assembled Fe_3O_4@SiO_2@Au structures enabled ultrasensitive detection of rhodamine B and methylene blue down to 1 fM, while Fe_3O_4/Au liquid SERS systems demonstrated enhancement factors (EF) in the range of 10^4-10^7 depending on Au:Fe_3O_4 ratio and external magnetic field conditions[36]. In addition to substrate design, analyte adsorption efficiency plays a critical role in SERS performance. Interactions between target molecules and the substrate surface directly influence signal intensity, particularly at low concentrations [37, 38]. However, insufficient surface affinity remains a limiting factor for reliable detection in many nanoparticle-based systems. Detailed analyses describing the influence of analyte orientation, surface chemistry, and concentration on SERS intensity have been reported previously [39–41]. To address these challenges, surface functionalization strategies aimed at improving analyte localization and signal reproducibility are increasingly being explored [42]. In this context, thiol- and carboxyl-containing ligands represent a promising approach due to their affinity toward metallic surfaces and their ability to introduce functional groups promoting interactions with target molecules [43–46].

In this work, magnetic Fe_3O_4 nanoparticles were functionalized with citric acid followed by gold deposition and subsequent surface modification with 12-mercaptododecanoic acid (12-MDA) to obtain a magnetic SERS-substrate for MB detection. The presence of Au nanostructures and surface carboxyl groups contributed to enhanced Raman signal intensity and improved localization of methylene blue molecules in SERS-regions. The developed substrate enabled MB detection in the concentration range of 10^{-2}-10^{-7} M using a simple nanoparticle-based approach.

Experimental

Reagents: isopropyl alcohol, iron(II) chloride tetrahydrate, iron(III) chloride hexahydrate, hydrogen tetrachloroaurate(III) trihydrate, 12-mercaptododecanoic acid (12-MDA) were purchased from Sigma-Aldrich. Sodium hydroxide, hydrochloric acid (HCl), citric acid (CA), sodium citrate, ammonia, and ethanol were of analytical grade. Deionized water (18.2 MΩ) was prepared using the Akvilon-D 301 (Akvilon JSC, Podolsk, Russian Federation) system.

Preparation of Fe_3O_4-CA@Au nanoparticles was carried out according to the procedure reported in our previous work [47]. The modification scheme is presented in Figure 1.

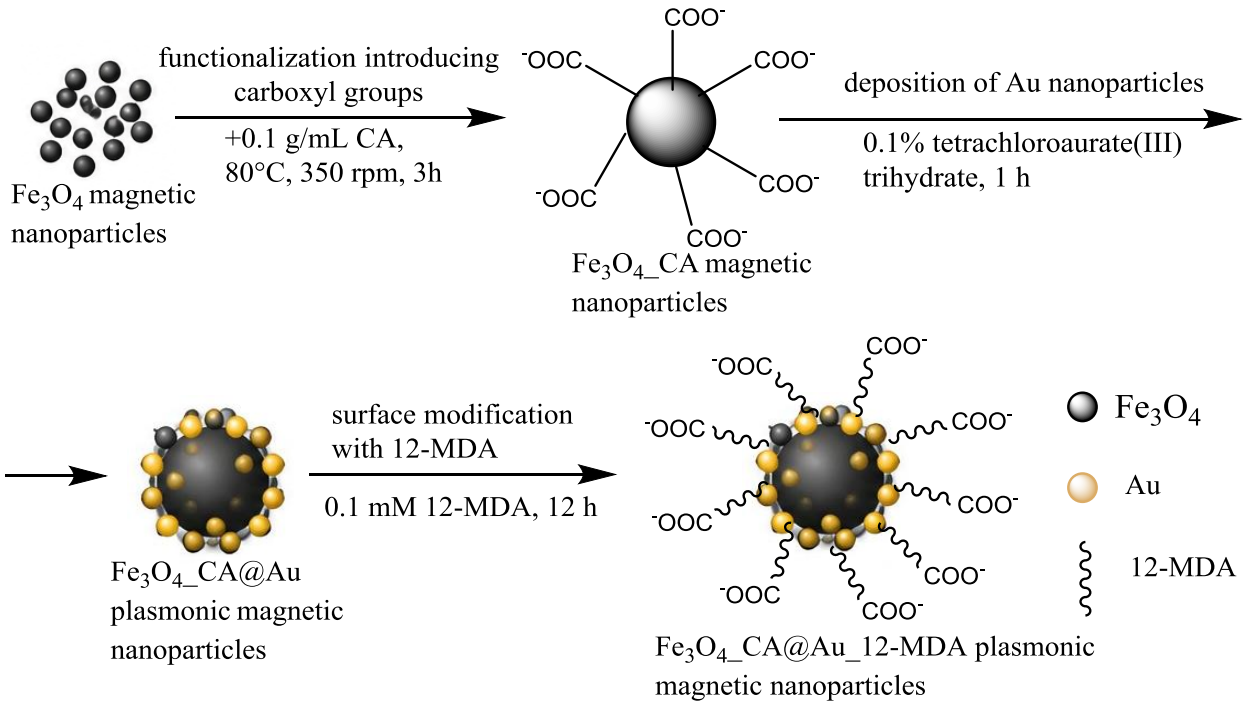

Figure 1. Schematic illustration of the preparation of Fe_3O_4-CA@Au 12-MDA nanoparticles

Preparation of Magnetite Fe_3O_4 Nanoparticles

Fe_3O_4 nanoparticles were synthesized by chemical co-precipitation from aqueous solutions of iron(II) chloride tetrahydrate $FeCl_2{\cdot}4H_2O$ (9.95 g) and iron(III) chloride hexahydrate $FeCl_3{\cdot}6H_2O$ (27.05 g) at a molar ratio of Fe^{3+}:Fe^{2+}=2:1. The synthesis was carried out in acidic medium by adding 11.8 mL of 35 % hydrochloric acid to prevent premature hydrolysis and oxidation of ions Fe^{2+}. The reaction mixture was prepared in 100 mL of deionized water and gradually heated to 60 ºC, under continuous blending. Nanoparticle precipitation was achieved by adding aqueous ammonia solution under intensive stirring until alkaline conditions were reached without heating. After reaching alkaline pH, the reaction mixture was heated at 80-85 ºC for 2 h under argon atmosphere. Under these conditions, intermediate iron hydroxide species formed and subsequently transformed into magnetite.

The obtained magnetic nanoparticles were separated using an external magnet and repeatedly washed with deionized water 5-6 times until neutral pH to remove residual ions and by-products. The nanoparticles were additionally washed with ethanol and dried at 60 ºC for 1h.

Citric Acid Functionalization of Magnetite Fe_3O_4 Nanoparticles and Subsequent Gold Deposition

At the first stage, 2 g Fe_3O_4 nanoparticles were dispersed in 50 mL of deionized water for 15 min using ultrasonication (operating frequency 20-25 kHz, 80 % amplitude, ultrasonic power 900 W). The dispersed nanoparticles were then added to an aqueous citric acid solution 0.1 g/mL and blended at 80 ºC and 350 rpm for 3 h. During this process, citric acid is adsorbed onto the Fe_3O_4 surface through coordination of its carboxylate groups with surface Fe sites. This surface functionalization preserves the crystal structure of magnetite while exposing free carboxyl groups that improve colloidal stability and provide anchoring sites for subsequent gold deposition. As a result, the Fe_3O_4 surface was functionalized with citrate molecules, exposing terminal carboxyl groups that facilitate the adsorption of Au^{3+} ions and subsequent gold deposition.

After modification, the nanoparticles were separated using a magnet, thoroughly washed with deionized water 3-5 times, and air-dried. Subsequently, 1 g of citric acid-modified nanoparticles was dispersed in 0.1 % aqueous solution of hydrogen tetrachloroaurate(III) trihydrate, where Au^{3+} ions interacted with functional groups on the nanoparticle surface.

Reduction of gold ions was performed by adding sodium citrate under heating at 60-70 ºC followed by aging of the reaction mixture for several hours. As a result, nanoparticles Fe_3O_4-CA@Au were formed. The obtained composite particles were separated magnetically, washed with diluted hydrochloric acid and deionized water to remove unbound components, and dried at 60 °C.

Modification of Nanoparticles Fe_3O_4-CA@Au with 12-MDA.

The obtained nanoparticles 0.1 g Fe_3O_4-CA@Au were surface-modified using 12-MDA. For this purpose, the nanoparticles were dispersed in a 0.1 mM 12-MDA, solution prepared in isopropanol (IPA) and stirred at room temperature for 12 h. After completion of the reaction, the nanoparticles were separated using an external magnetic field and repeatedly washed with IPA to remove unbound ligand molecules and residual reagents. As a result, organically modified Fe_3O_4-CA@Au 12-MDA nanoparticles containing surface carboxyl groups were obtained.

Characterization of Samples

Characterization of the obtained nanoparticles was performed at each modification stage: Fe_3O_4, Fe_3O_4-CA@Au и Fe_3O_4-CA@Au-12-MDA. The presence of functional groups on the nanoparticle surface was investigated using Fourier-transform infrared spectroscopy (FTIR) on an InfraLUM FT-08 spectrometer (Lumex, Russia).

The phase composition of the samples was analyzed by X-ray diffraction (XRD) using a SmartLab diffractometer (Rigaku Corporation, Japan).

Morphology and microstructure of the nanoparticles were studied by scanning electron microscopy (SEM), while elemental composition at different modification stages was determined using energy-dispersive X-ray spectroscopy (EDX) on a Hitachi TM 3030 instrument (Hitachi, Japan).

SERS Detection

The obtained Fe_3O_4-CA@Au 12-MDA nanoparticles were used for detection of the model dye MB using an EnSpectr R532 Enhanced Spectrometry. The detection scheme is presented in Figure 2. Silicon substrates were used for deposition of both the dye and nanoparticles. Raman spectra were recorded in the range of 2000-1000 cm^{-1} using laser power values of 28-32, an exposure time of 2000, and 25 scans. Each measurement was performed in triplicate. The calibration curves were constructed using the mean intensity values, and the error bars represent the standard deviation of three independent measurements. The dye concentration range was

10^{-2}–10^{-7} M. The main calibration peaks corresponded to signals at 1625 and 1396 cm^{-1} associated with aromatic vibrations of MB. For the EF calculation, the concentrations of MB used for the SERS and conventional Raman measurements were C_{SERS} =10^{-7} M and C_{Raman} =10^{-2} M, respectively. The SERS enhancement factor (EF) was calculated according to Equation (1):

$$EF = \frac{I_{SERS} / C_{SERS}}{I_{Raman} / C_{Raman}} \quad (1)$$

where I_{SERS} and I_{Raman} — the intensities of characteristic bands in SERS and conventional Raman spectra, respectively, C_{SERS} and C_{Raman} — are the corresponding analyte concentrations. Physically, this concentration-normalized ratio provides an estimate of the Raman signal enhancement relative to the analyte concentration and is primarily associated with the electromagnetic enhancement mechanism arising from localized surface plasmon resonance (LSPR) in the Au-containing nanostructures. Since the exact number of molecules contributing to the SERS signal and the effective surface area of the SERS-active regions were not independently determined, this approach provides an approximate, order-of-magnitude estimation of the EF rather than an absolute value. Therefore, the calculated EF values are used primarily for comparative evaluation of the SERS enhancement performance of the developed substrate.

The limit of detection (LOD) was estimated using the 3σ criterion according to Equation (2):

$$LOD = \frac{3\sigma}{S} \quad (2)$$

where σ — is the standard deviation of three independent measurements at the lowest experimentally tested MB concentration (10^{-7} M), S — is the slope of the corresponding calibration curve. The LOD was estimated separately for the characteristic MB bands at 1623 cm^{-1} and 1396 cm^{-1}.

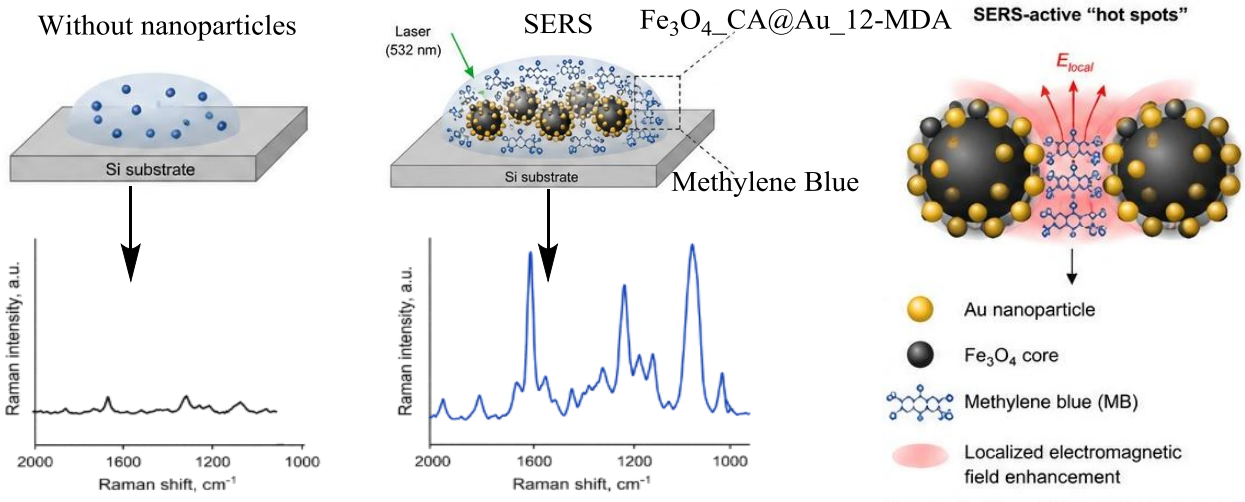

Figure 2. Application of nanoparticles Fe_3O_4-CA@Au 12-MDA as a SERS-substrate for low-concentration detection of MB

Results and Discussion

Nanoparticles before and after modification were investigated by FTIR, SEM-EDX and XRD to evaluate changes in structure, composition, and morphology during the formation of the SERS-substrate.

FTIR analysis was used to confirm modification of Fe_3O_4 nanoparticles with citric acid, subsequent gold deposition, and surface functionalization with 12-MDA. The spectra are presented in Figure 3. FTIR spectra of pristine nanoparticles Fe_3O_4 exhibited characteristic bands corresponding to vibrations Fe-O at 532 cm^{-1}, as well Fe-OH at region 3000-3600 cm^{-1}. In the spectra of samples Fe_3O_4-CA@Au COO^- group vibrations appeared at 1540 cm^{-1} and 1600 cm^{-1} and at region 2500-3600 $см^{-1}$ -OH groups. For Fe_3O_4-CA@Au-12-MDA additional peaks corresponding to C=O groups at 1700 cm^{-1}, as well as symmetric and asymmetric -CH stretching vibrations of the long-chain hydrocarbon fragment of 12-MDA at 2845 cm^{-1} and 2912 cm^{-1}.

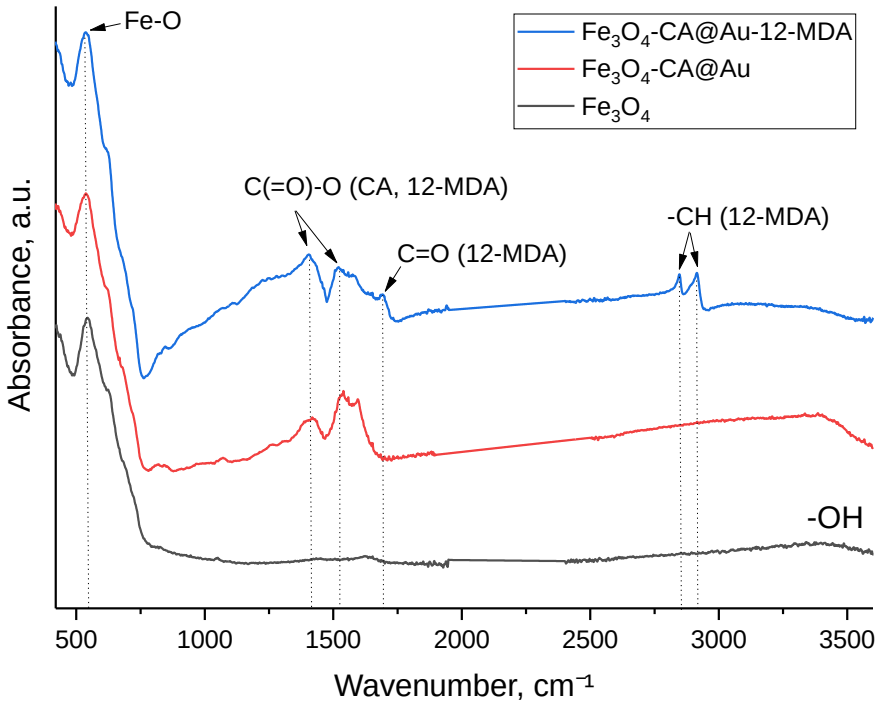

Figures 3. FTIR spectra of nanoparticles before and after modification

XRD analysis was performed to confirm the formation of the magnetic Fe_3O_4 phase and evaluate changes in crystal structure after surface modification and gold deposition. The phase composition of nanoparticles at different modification stages was investigated by X-ray diffraction (Figure 4). Pristine nanoparticles Fe_3O_4 nanoparticles exhibited characteristic diffraction peaks at 2Θ values of 30.2º, 35.5º, 43.2º, 57.1º, 62.7º and 74.2º, corresponding to the (220), (311), (400), (511), (440) and (533) crystallographic planes of magnetite Fe_3O_4, respectively, and these results are in good agreement with literature data and confirm the formation of the cubic spinel structure of magnetite [48]. After gold deposition onto nanoparticles Fe_3O_4-CA@Au additional diffraction peaks appeared at 2Θ values of 38.2º, 44.4º, 64.6º, 77.7º and 81.8º, corresponding to the (111), (200), (220), (311) and (222), planes of metallic gold with a face-centered cubic structure. The appearance of these reflections confirms successful formation of the gold shell on the surface of magnetic nanoparticles.

For samples Fe_3O_4-CA@Au-12-MDA the positions of the main diffraction peaks corresponding to magnetite and gold remained unchanged, while their intensities slightly decreased due to organic surface modification. Nevertheless, these results indicate preservation of the crystal structure of the composite nanoparticles. Furthermore, the absence of additional crystalline phases confirms the high purity of the obtained composite nanoparticles and successful stepwise surface modification without structural degradation during functionalization.

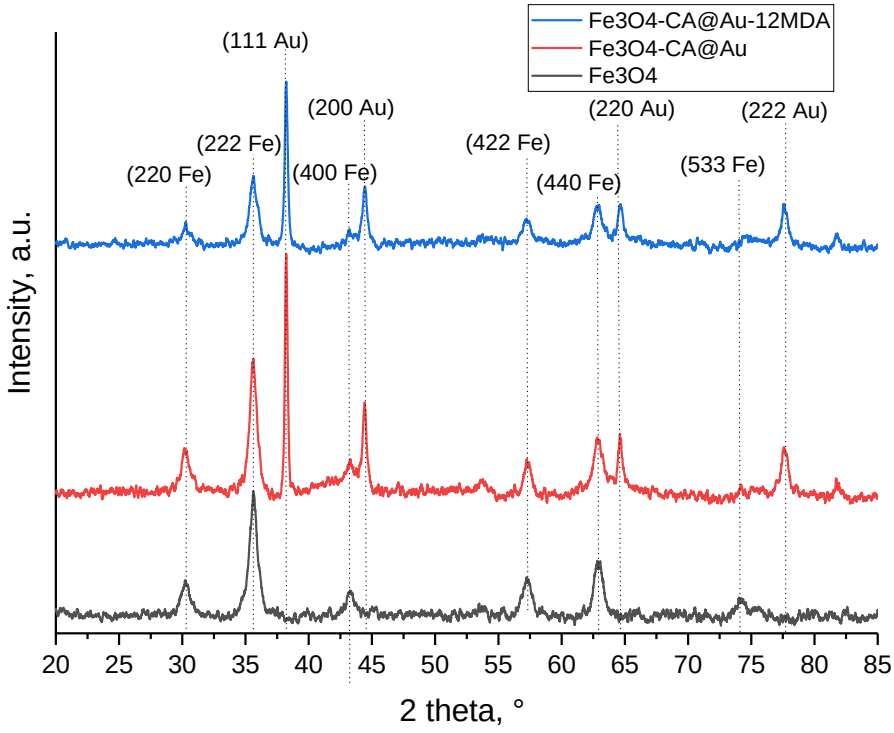

Figure 4. XRD-diffractogram of nanoparticles before and after modification

According to SEM-EDX analysis, the morphology and elemental composition of the obtained nanoparticles were investigated at different modification stages (Figure 5). Pristine nanoparticles Fe_3O_4 exhibited agglomerated irregular-shaped particles. Elemental mapping demonstrated a uniform distribution of Fe and O throughout the particles, while quantitative EDX analysis showed the presence of Fe (76.5 wt %) and O (23.5 wt %). After citric acid functionalization and gold deposition, the surface of Fe_3O_4-CA@Au nanoparticles became rougher, and EDX analysis confirmed the presence of Au (1.2 wt%) and C (14.6 wt %) together with Fe (78.1 wt %) and O (5.4 wt %). A weak sulfur signal (0.7 wt%) was detected in the intermediate Fe_3O_4-CA@Au sample. Considering that no S-containing reagents were used at this stage, this low-intensity signal is most likely attributable to the detection limit of EDX and/or background contamination. Following 12-MDA modification, sulfur (2.2 wt %) was additionally detected in Fe_3O_4-CA@Au-12-MDA samples, while the carbon content increased to 18.5 wt % (Fe 55.8 wt %, O 20 wt %, Au 3.5 wt %), indicating suc-

cessful surface functionalization with thiol-containing ligands. The quantitative elemental compositions of the nanoparticles at different modification stages are summarized in Table S1. It should be noted that the resolution of the obtained images does not allow accurate determination of the nanoparticle size. Nevertheless, the nanoparticles and their gold coating were synthesized using a previously developed method [47], while the successful formation of the obtained nanostructures was additionally confirmed by XRD analysis. The average particle sizes of Fe_3O_4 (21.2 nm) and Fe_3O_4-CA@Au (29.6 nm) reported in [47] were determined by TEM and are cited here for comparison. The increase in the average particle size reported in [47] was attributed to gold deposition on the Fe_3O_4 nanoparticles. It should be noted that the resolution of the SEM images obtained in the present study does not allow reliable determination of the individual nanoparticle size or direct visualization of an Au shell around individual Fe_3O_4 nanoparticles.

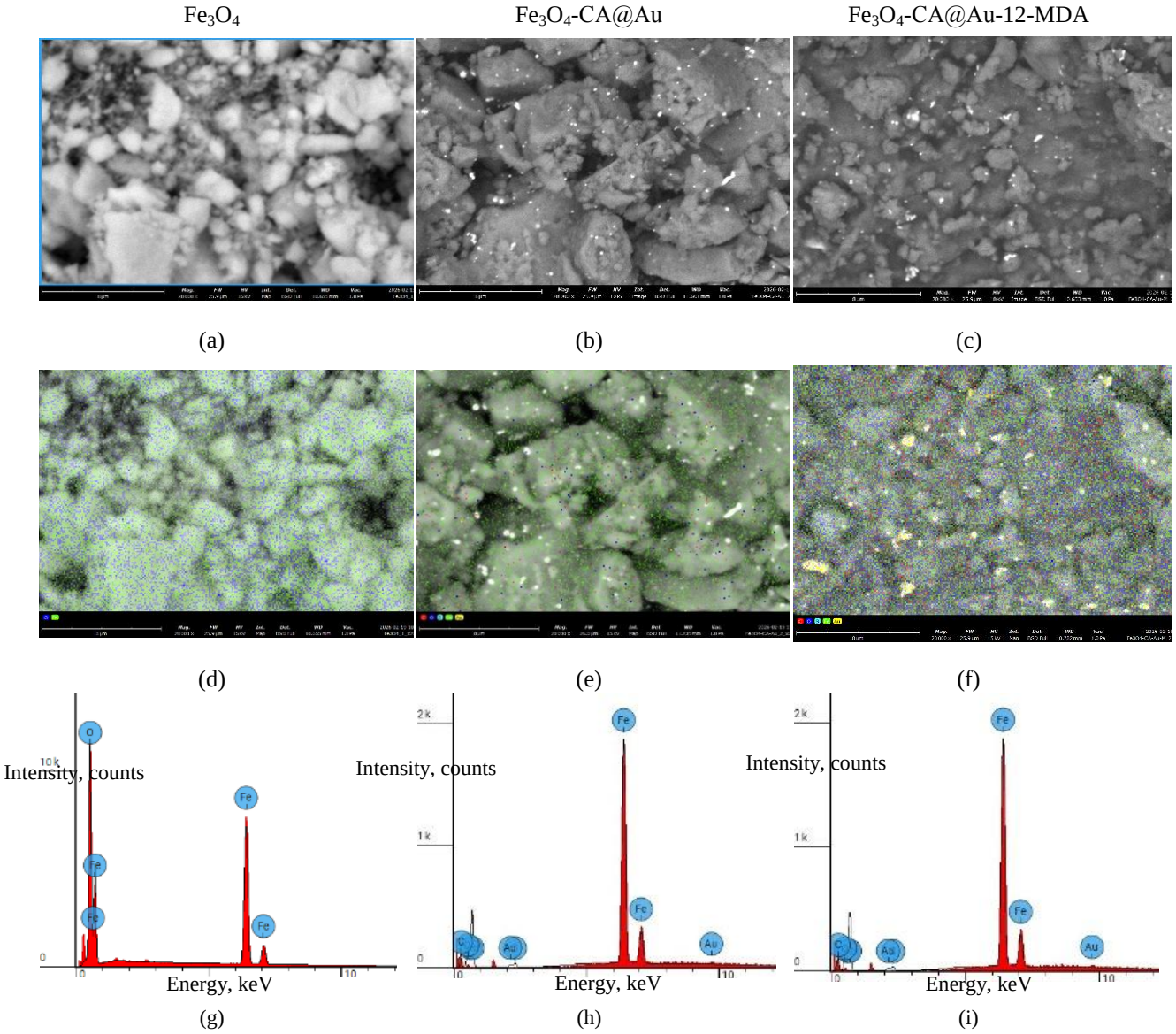

Figure 5. SEM images (a, b, c), EDX elemental mapping (d, e, f), and EDX spectra (g, h, i) of nanoparticles before and after modification

The FTIR, SEM-EDX and XRD results confirmed successful stepwise modification of Fe_3O_4, nanoparticles, gold deposition, and subsequent surface functionalization with 12-MDA. The presence of Au, preservation of the Fe_3O_4 crystal structure, and the introduction of surface carboxyl groups enabled the obtained Fe_3O_4-CA@Au-12-MDA nanoparticles to be used as a SERS-magnetic substrate for methylene blue detection in the concentration range of 10^{-2}-10^{-7} M.

Figure 6 presents Raman spectra of MB recorded without a SERS substrate and in the presence of nanoparticles Fe_3O_4-CA@Au-12-MDA. For samples without nanoparticles, the Raman signal intensity was significantly lower compared with spectra recorded in the presence of nanoparticles, while concentrations of 10^{-7} M were not detected due to the low sensitivity of conventional Raman spectroscopy.

In the presence of Fe_3O_4-CA@Au-12-MDA nanoparticles, substantial enhancement of the MB signal was observed, particularly for the characteristic bands centered at approximately 1620-1628 cm^{-1} and 1392-1400 cm^{-1}, corresponding to aromatic C=C and C-N vibrations, respectively. Compared with the conventional Raman spectrum, a slight shift of the aromatic C=C band was observed in the SERS spectra. This behavior may be associated with the adsorption of MB molecules onto the functionalized Au surface, leading to changes in the local molecular environment and adsorption geometry. Even at concentrations as low as 10^{-7}, characteristic MB bands, including the shifted aromatic C=C band, remained detectable in the presence of the SERS substrate. The intensity of the SERS signal depended on the selected recording area (Figure 7). Characteristic MB peaks were predominantly observed in localized SERS-active regions «hot spots formed in areas of nanoparticle agglomeration (Figure 7b). In regions without pronounced aggregation, the signal intensity was significantly lower or absent. To account for the variability associated with the non-uniform distribution of nanoparticle aggregates, SERS measurements were performed in triplicate. The variability of the SERS response was evaluated using the standard deviation of three independent measurements, which is presented as error bars in the calibration curves (Figure 8). An additional advantage of Fe_3O_4-CA@Au-12-MDA nanoparticles is their magnetic nature, which promoted localization of the analyte droplet without significant spreading across the surface and, consequently, concentration of MB molecules in plasmonically active regions. This likely contributed to enhancement of the local electromagnetic field within nanogaps between closely spaced metallic nanoparticles and increased intensity of the recorded signal.

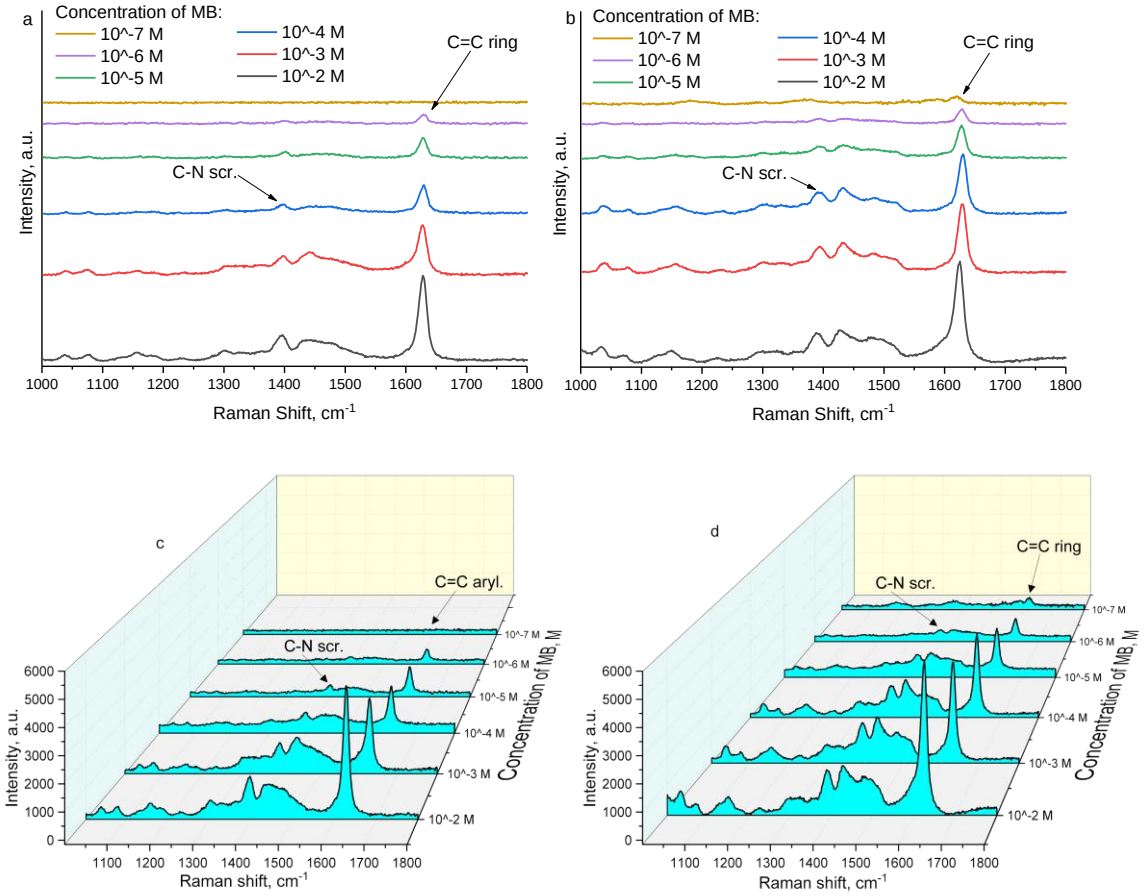

Figure 6. Raman spectra of MB in the concentration range of 10^{-2}-10^{-7} M recorded without a SERS substrate (a, c) and in the presence of a Fe_3O_4-CA@Au-12-MDA -based SERS substrate (b, d)

a b

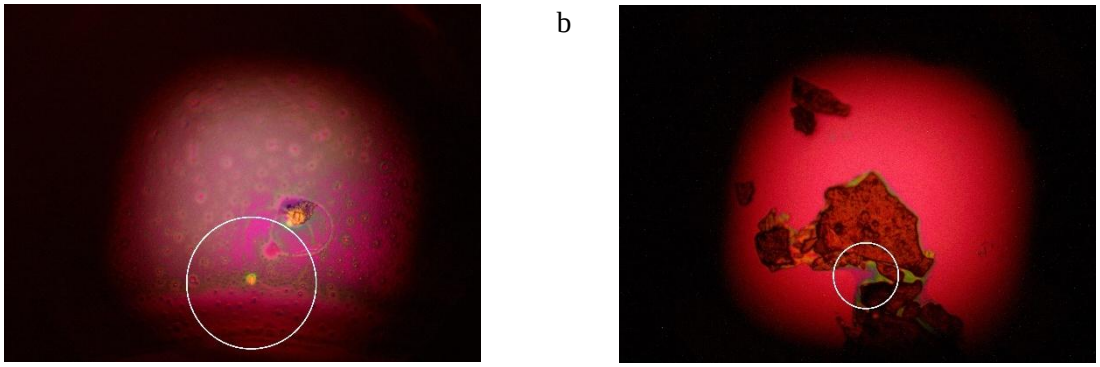

Figure 7. Optical micrographs of regions used for SERS spectrum acquisition of MB on the surface of Fe_3O_4-CA@Au-12-MDA nanoparticles: (a) region without pronounced nanoparticle agglomeration; (b) localized SERS «hot spot» region with nanoparticle agglomeration and dye accumulation

Table 1 and Figure 8 present the analytical parameters and calibration curves for MB detection using conventional Raman spectroscopy and SERS with nanoparticles Fe_3O_4-CA@Au-12-MDA. Calibration curves were constructed based on the intensities of the characteristic MB bands at 1396 и 1623 cm^{-1} in the concentration range of 10^{-2}-10^{-7} M. The calibration data represent the mean values of three independent measurements, with the corresponding standard deviations shown as error bars in Figure 8.

The developed SERS substrate enabled experimental detection of methylene blue down to 10^{-7} M and exhibited good quantitative performance, with R^2 values ranging from 0.98 to 0.99. The LOD values calculated using the 3σ criterion were 4.05×10^{-8} M and 5.97×10^{-8} M for the bands at 1623 and 1396 cm^{-1}, respectively. Thus, 10^{-7} M represents the lowest MB concentration experimentally tested and detected in this study, whereas the calculated values represent the estimated detection limits. The EF for the bands at 1623 and 1396 cm^{-1} were 0.11×10^5 and 0.15×10^5, respectively. These values were calculated by comparing the SERS response at 10^{-7} M MB with the conventional Raman response at 10^{-2} M MB, taking into account the five-order-of-magnitude difference in analyte concentration. The corresponding Raman signal intensity increases were 5.95- and 5.40 times, respectively. Since the exact number of molecules contributing to the SERS signal and the effective surface area of the SERS-active regions were not independently determined, the calculated EF values should be regarded as approximate, order-of-magnitude estimates and are used primarily for comparative evaluation of the developed SERS substrate.

A comparison with previously reported SERS substrates for MB detection is presented in Table 1. The estimated LOD values obtained for Fe_3O_4-CA@Au-12-MDA (4.05×10^{-8} and 5.97×10^{-8} M for the bands at 1623 and 1396 cm^{-1}, respectively) were lower than those reported for the Au@MUA substrate (1.9×10^6-2.3×10^6 M). As expected, Ag-based substrates exhibited considerably higher EF because of the stronger localized surface plasmon resonance of silver nanostructures. Compared with the Au@MUA substrate, the developed Fe_3O_4-CA@Au-12-MDA nanoparticles showed approximately threefold higher EF values 0.11-0.15×10^5 versus 0.4×10^4, while maintaining excellent calibration linearity (R^2 = 0.98-0.99). Although the difference cannot be attributed solely to the replacement of MUA with 12-MDA, since the nanoparticle architecture also differs, the combination of the Fe_3O_4 magnetic core, Au shell, and 12-MDA surface functionalization provides efficient SERS activity together with the practical advantage of magnetic separation and substrate recovery.

Table 1

Comparison of the analytical characteristics of previously reported SERS substrates for methylene blue detection

Sample	Peaks, cm^{-1}	LOD, M	EF	SERS-signal increase, fold	R^2	Ref.
Raman-spectra	1623		1	-	0.94	This work
SERS Fe_3O_4-CA@Au-12-MDA	1623	4.05×10^{-8}	0.11×10^5	5.95	0.98	
Raman-spectra	1396		1	-	0.97	
SERS Fe_3O_4-CA@Au-12-MDA	1396	5.97×10^{-8}	0.15×10^5	5.4	0.99	
MWCNTs-Ag	1395, 1621		4.68×10^6	-	0.99	[49]
Au@MUA	1400, 1625	1.9×10^6-2.3×10^6	0.4×10^4	-	0.93-0.95	[46]

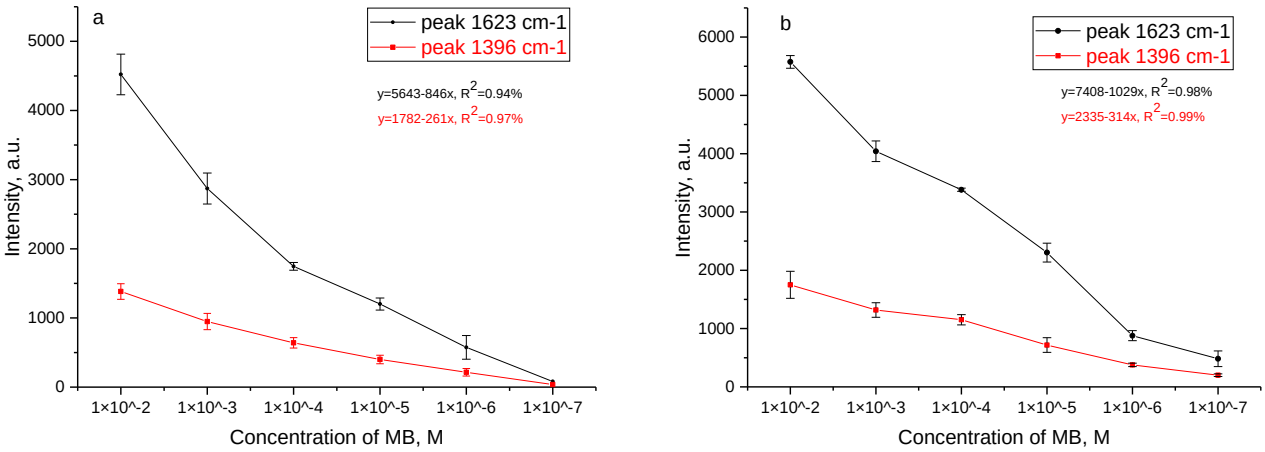

Figure 8. Calibration curves of methylene blue obtained using conventional Raman spectroscopy and SERS Fe_3O_4-CA@Au-12MDA substrates

Conclusions

In this work, Fe_3O_4-CA@Au-12-MDA nanoparticles were obtained for use as a magnetic SERS substrate for MB detection. Stepwise nanoparticle modification was confirmed by FTIR, SEM-EDX and XRD analyses. The obtained results demonstrated preservation of the Fe_3O_4 crystal structure after gold deposition and subsequent organic modification, as well as the presence of Au and carboxyl-containing groups on the nanoparticle surface.

The use of nanoparticles Fe_3O_4-CA@Au-12-MDA as a SERS substrate resulted in enhanced MB signal intensity compared with conventional Raman spectroscopy. The most intense signals were recorded in localized SERS «hot spots» regions associated with nanoparticle agglomeration. The obtained SERS substrates experimental detection of characteristic methylene blue bands in the concentration range of 10^{-2}-10^{-7} M. The estimated LOD values calculated using the 3σ criterion were 4.05×10^{-8} M and 5.97×10^{-8} M for the bands at 1623 and 1396 cm^{-1}, respectively. For the bands at 1623 and 1396 cm^{-1} the approximate EF values were 0.11×10^5 and 0.15×10^5, respectively. In addition, the Raman signal intensities increased by factors of 5.95 and 5.4 respectively, compared with conventional Raman spectroscopy. The constructed calibration curves demonstrated good linearity with R^2 values of 0.98-0.99.

Thus, the obtained Fe_3O_4-CA@Au-12-MDA nanoparticles represent a promising magnetic SERS-platform for detection of low concentrations of organic dye molecules.

Data Availability Statement

The data supporting the findings of this study are available within the article and deposited in Figshare at: https://doi.org/10.6084/m9.figshare.33292149. Further data are available from the corresponding author upon reasonable request.

Funding

This research was funded by the Science Committee of the Ministry of Science and Higher Education of the Republic of Kazakhstan (Grant No. AP23486127, BR28713053).

*Author Information**

**The authors' names are presented in the following order: First Name, Middle Name and Last Name*

Indira Bazarbayevna Muslimova (*corresponding author*) — PhD, Senior Researcher, Technological laboratory of track-etched membranes, Astana branch of the RSE «Institute of nuclear physics» of the Agency of the Republic of Kazakhstan for Atomic Energy, Abylay Khan Avenue, 2/1, 010009, Astana, Kazakhstan; *e-mail: i.muslimova@inp.kz*; https://orcid.org/0000-0002-0923-5506

Ainur Berikkyzy Khairusheva — Master's student, L.N. Gumilyov Eurasian National University, Satpayev street, 2, 010008, Astana, Kazakhstan; e-mail: *ainurkhairusheva@gmail.com*; https://orcid.org/0009-0009-1968-5189

Kairat Aslanbekuly Izbassar — Master's student, L.N. Gumilyov Eurasian National University, Satpayev street, 2, 010008, Astana, Kazakhstan; e-mail: *kaira.kim31@gmail.com*; https://orcid.org/0009-0007-2368-2189

Zhangali Akhmetkaliuly Bekbol — Master's student, L.N. Gumilyov Eurasian National University, Satpayev street, 2, 010008, Astana, Kazakhstan; e-mail: *zhangali.bekbol@mail.ru;* https://orcid.org/0000-0002-8703-0874

Lana Igorevna Lissovskaya — Master of Natural Sciences, Engineer of the Technological laboratory of track-etched membranes, Astana branch of the RSE «Institute of nuclear physics» of the Agency of the Republic of Kazakhstan for Atomic Energy, Abylay Khan Avenue, 2/1, 010009, Astana, Kazakhstan; *e-mail: l.lissovskaya@inp.kz*; https://orcid.org/0000-0002-3894-6366

Ilya Vladimirovich Korolkov — PhD, Leading Researcher, Technological laboratory of track-etched membranes, Astana branch of the RSE «Institute of nuclear physics» of the Agency of the Republic of Kazakhstan for Atomic Energy, Abylay Khan Avenue, 2/1, 010009, Astana, Kazakhstan; *e-mail: i.korolkov@inp.kz*; https://orcid.org/0000-0002-0766-2803

Author Contributions

The manuscript was written through contributions of all authors. All authors have given approval to the final version of the manuscript. CRediT: **Indira Bazarbayevna Muslimova** data curation, investigation, validation, formal analysis, visualization, writing-review, writing-original draft & editing; **Ainur Berikkyzy Khairusheva** methodology, formal analysis; **Kairat Aslanbekuly Izbassar** formal analysis, validation; **Zhangali Akhmetkaliuly Bekbol** formal analysis, validation; **Lana Igorevna Lissovskaya** formal analysis, validation; **Ilya Vladimirovich Korolkov** conceptualization, methodology, supervision, writing-review & editing

Declaration of Generative AI and AI-Assisted Technologies in the Writing Process

During the preparation of this work, the authors used ChatGPT for language editing and grammar improvement of the manuscript. After using this service, the authors carefully reviewed and edited the content and take full responsibility for the final version of the publication.

Conflicts of Interest

The authors declare no conflict of interest.

References

1 Hayat, M., Shah, A., Hakeem, M. K., Irfan, M., Haleem, A., Khan, S. B., & Shah, I. (2022). A designed miniature sensor for the trace level detection and degradation studies of the toxic dye Rhodamine B. *RSC Advances*, *12*(25), 15658–15669. https://doi.org/10.1039/D2RA01722A

2 Koohkan, R., Kaykhaii, M., Sasani, M., & Paull, B. (2020). Fabrication of a Smartphone-Based Spectrophotometer and Its Application in Monitoring Concentrations of Organic Dyes. *ACS Omega*, *5*(48), 31450–31455. https://doi.org/10.1021/ACSOMEGA.0C05123

3 Han, C., Wang, Z., Cui, J., Liu, S., Yang, L., Fu, Y., Zhu, B., & Guo, C. (2025). Rapid Quantitative Detection of Dye Concentration in Pt/TiO2 Photocatalytic System Based on RGB Sensing. *Sensors*, *25*(10), 3195. https://doi.org/10.3390/S25103195

4 Wang, C., Weng, G., Li, J., Zhu, J., & Zhao, J. (2024). A review of SERS coupled microfluidic platforms: From configurations to applications. *Analytica Chimica Acta*, *1296*, 342291. https://doi.org/10.1016/j.aca.2024.342291

5 Chen, B., & Qiu, X. (2025). Surface-Enhanced Raman Scattering (SERS) for exosome detection. *Clinica Chimica Acta*, *568*, 120148. https://doi.org/10.1016/j.cca.2025.120148

6 Pérez-Jiménez, A. I., Lyu, D., Lu, Z., Liu, G., & Ren, B. (2020). Surface-enhanced Raman spectroscopy: benefits, trade-offs and future developments. *Chemical Science*, *11*(18), 4563–4577. https://doi.org/10.1039/D0SC00809E

7 Fan, M., Andrade, G. F. S., & Brolo, A. G. (2020). A review on recent advances in the applications of surface-enhanced Raman scattering in analytical chemistry. *Analytica Chimica Acta*, *1097*, 1–29. https://doi.org/10.1016/J.ACA.2019.11.049

8 Langer, J., de Aberasturi, D. J., Aizpurua, J., Alvarez-Puebla, R. A., Auguié, B., Baumberg, J. J., Bazan, G. C., Bell, S. E. J., Boisen, A., Brolo, A. G., Choo, J., Cialla-May, D., Deckert, V., Fabris, L., Faulds, K., Javier García de Abajo, F., Goodacre, R., Graham, D., Haes, A. J., Liz-Marzán, L. M. (2020). Present and Future of Surface-Enhanced Raman Scattering. *ACS Nano*, *14*(1), 28–117. https://doi.org/10.1021/ACSNANO.9B04224

9 Pilot, R., Signorini, R., Durante, C., Orian, L., Bhamidipati, M., & Fabris, L. (2019). A Review on Surface-Enhanced Raman Scattering. *Biosensors*, *9*(2), 57. https://doi.org/10.3390/BIOS9020057

10 Zhang, Q., Chai, Y., Li, X., Wang, Z., Zhang, X., Effah, C. Y., Ding, L., & Wu, Y. (2026). Surface-enhanced Raman spectroscopy for protein detection: Challenges and countermeasures. *Talanta*, *298*, 128901. https://doi.org/10.1016/j.talanta.2025.128901

11 Lin, S., Nie, Z., Xing, Y., Wang, R., & Yu, F. (2026). SERS detection and antibacterial treatment of bacterial infections. *Coordination Chemistry Reviews*, *546*, 217079. https://doi.org/10.1016/j.ccr.2025.217079

12 Rathod, J., Byram, C., Kanaka, R. K., Bharati, M. S. S., Banerjee, D., Akkanaboina, M., & Soma, V. R. (2022). Hybrid Surface-Enhanced Raman Scattering Substrates for the Trace Detection of Ammonium Nitrate, Thiram, and Nile Blue. *ACS Omega*, *7*(18), 15969–15981. https://doi.org/10.1021/ACSOMEGA.2C01095

13 Anastasopoulos, J. A., Soto Beobide, A., Manikas, A. C., & Voyiatzis, G. A. (2017). Quantitative surface-enhanced resonance Raman scattering analysis of methylene blue using silver colloid. *Journal of Raman Spectroscopy*, *48*(12), 1762–1770. https://doi.org/10.1002/JRS.5233

14 Nguyen, T. Van, Vu, C. D., Pham, T. B., Pham, V. H., Bui, H., Vu, T. H. H., & Pham, V. H. (2021). Detection of Ultra-Low Concentration of Methylene Blue by Porous Silicon Photonic Crystals Covered With Silver Nanoparticles as Efficient Sers Substrate. *Communications in Physics*, *31*(4), 381. https://doi.org/10.15625/0868-3166/15927

15 Li, C., Huang, Y., Lai, K., Rasco, B. A., & Fan, Y. (2016). Analysis of trace methylene blue in fish muscles using ultra-sensitive surface-enhanced Raman spectroscopy. *Food Control*, *65*, 99–105. https://doi.org/10.1016/J.FOODCONT.2016.01.017

16 Xu, T., Wang, X., Huang, Y., Lai, K., & Fan, Y. (2019). Rapid detection of trace methylene blue and malachite green in four fish tissues by ultra-sensitive surface-enhanced Raman spectroscopy coated with gold nanorods. *Food Control*, *106*, 106720. https://doi.org/10.1016/J.FOODCONT.2019.106720

17 Yang, G., Fang, X., Jia, Q., Gu, H., Li, Y., Han, C., & Qu, L. L. (2020). Fabrication of paper-based SERS substrates by spraying silver and gold nanoparticles for SERS determination of malachite green, methylene blue, and crystal violet in fish. *Microchimica Acta*, *187*(5), 310. https://doi.org/10.1007/S00604-020-04262-2

18 Schiavi, S., Taglietti, A., Magni, A., Galinetto, P., & Albini, B. (2025). Increasing SERS performance of silver nanoparticles with nanometric coating of polydopamine: A novel approach for methylene blue detection. *Applied Surface Science*, *687*, 162223. https://doi.org/10.1016/J.APSUSC.2024.162223

19 Tayyaba, N., Zago, S., Giura, A., Fiore, G., Ribotta, L., Scaglione, F., & Rizzi, P. (2025). Nanoporous Copper Films via Dynamic Hydrogen Bubbling: A Promising SERS Substrate for Sensitive Detection of Methylene Blue. *Nanomaterials*, *15*(12), 945. https://doi.org/10.3390/NANO15120945

20 Huh, Y., & Ryu, S. (2025). Ultra-Effective Methylene Blue Detection by Nanoporous Gold for Surface-Enhanced Raman Spectroscopy. *Electronic Materials Letters*, *21*(2), 260–267. https://doi.org/10.1007/S13391-024-00541-9

21 Pham, T. T. H., Vu, X. H., Dien, N. D., Trang, T. T., Chi, T. T. K., Phuong, P. H., & Nghia, N. T. (2022). Ag nanoparticles on ZnO nanoplates as a hybrid SERS-active substrate for trace detection of methylene blue. *RSC Advances*, *12*(13), 7850–7863. https://doi.org/10.1039/D2RA00620K

22 Zamora-Peredo, L., García-Ramirez, J. I., García-Velasco, A. C., Hernández-Torres, J., García-González, L., Bizarro, M., & Báez-Rodríguez, A. (2021). Influence of Ag Photodeposition Conditions over SERS Intensity of Ag/ZnO Microspheres for Nanomolar Detection of Methylene Blue. *Nanomaterials*, *11*(12), 3414. https://doi.org/10.3390/NANO11123414

23 Yang, J., Chen, B., Peng, J., Huang, B., Deng, W., Xie, W., & Luo, Z. (2021). Preparation of CuO Nanowires/Ag Composite Substrate and Study on SERS Activity. *Plasmonics*, *16*(4), 1059–1070. https://doi.org/10.1007/S11468-020-01358-6

24 Ren, S., Fu, J., Liu, G., Zhang, H., Wang, B., & Yu, J. (2025). Ultrasensitive detection of methylene blue by surface-enhanced Raman scattering (SERS) with Ag nanoparticle-decorated magnetic CoNi layered double hydroxides. *Analytical Methods*, *17*(5), 1010–1020. https://doi.org/10.1039/D4AY01841A

25 Srichan, C., Ekpanyapong, M., Horprathum, M., Eiamchai, P., Nuntawong, N., Phokharatkul, D., Danvirutai, P., Bohez, E., Wisitsoraat, A., & Tuantranont, A. (2016). Highly-Sensitive Surface-Enhanced Raman Spectroscopy (SERS)-based Chemical Sensor using 3D Graphene Foam Decorated with Silver Nanoparticles as SERS substrate. *Scientific Reports*, *6*(1), 23733. https://doi.org/10.1038/srep23733

26 Peng, Y., Cai, P., Yang, L., Liu, Y., Zhu, L., Zhang, Q., Liu, J., Huang, Z., & Yang, Y. (2020). Theoretical and Experimental Studies of Ti3C2 MXene for Surface-Enhanced Raman Spectroscopy-Based Sensing. *ACS Omega*, *5*(41), 26486–26496. https://doi.org/10.1021/ACSOMEGA.0C03009

27 Wei, H., Liu, X., Cui, Y., Li, L., Liu, Y., Ma, Y., Li, H., & Xu, Q. (2025). Gold nanobipyramids/MXene@PVDF membrane material for SERS detection and sensitive determination of fluorescent dyes. *Spectrochimica Acta Part A: Molecular and Biomolecular Spectroscopy*, *334*, 125944. https://doi.org/10.1016/J.SAA.2025.125944

28 Sharma, S., Kumar, R., & Yadav, R. M. (2024). Polyacrylonitrile as a versatile matrix for gold nanoparticle-based SERS substrates. *Nanoscale Advances*, *6*(4), 1065–1073. https://doi.org/10.1039/D3NA01112G

29 Horta, I., Neto, N. F. A., Kito, L. T., Miranda, F., Thim, G., Pereira, A. L. de J., & Pessoa, R. (2025). Ultra-Trace Monitoring of Methylene Blue Degradation via AgNW-Based SERS: Toward Sustainable Advanced Oxidation Water Treatment. *Sustainability*, *17*(10), 4448. https://doi.org/10.3390/SU17104448

30 Quan, Y., Su, R., Yang, S., Chen, L., Wei, M., Liu, H., Yang, J., Gao, M., & Li, B. (2021). In-situ surface-enhanced Raman scattering based on MTi20 nanoflowers: Monitoring and degradation of contaminants. *Journal of Hazardous Materials*, *412*, 125209. https://doi.org/10.1016/J.JHAZMAT.2021.125209

31 Guselnikova, O., Lim, H., Kim, H. J., Kim, S. H., Gorbunova, A., Eguchi, M., Postnikov, P., Nakanishi, T., Asahi, T., Na, J., & Yamauchi, Y. (2022). New Trends in Nanoarchitectured SERS Substrates: Nanospaces, 2D Materials, and Organic Heterostructures. *Small*, *18*(25), 2107182. https://doi.org/10.1002/SMLL.202107182

32 Srivastava, K., Le-The, H., Lozeman, J. J. A., van den Berg, A., van der Stam, W., & Odijk, M. (2024). Prospects of nano-lithographic tools for the fabrication of surface-enhanced Raman spectroscopy (SERS) substrates. *Micro and Nano Engineering*, *23*, 100267. https://doi.org/10.1016/J.MNE.2024.100267

33 Du, J., Xu, J., Sun, Z., & Jing, C. (2016). Au nanoparticles grafted on Fe3O4 as effective SERS substrates for label-free detection of the 16 EPA priority polycyclic aromatic hydrocarbons. *Analytica Chimica Acta*, *915*, 81–89. https://doi.org/10.1016/J.ACA.2016.02.009

34 Li, F., Yu, Z., Zhao, L., & Xue, T. (2016). Synthesis and application of homogeneous Fe3O4 core/Au shell nanoparticles with strong SERS effect. *RSC Advances*, *6*(13), 10352–10357. https://doi.org/10.1039/C5RA27875A

35 He, J., Song, G., Wang, X., Zhou, L., & Li, J. (2022). Multifunctional magnetic Fe3O4/GO/Ag composite microspheres for SERS detection and catalytic degradation of methylene blue and ciprofloxacin. *Journal of Alloys and Compounds*, *893*, 162226. https://doi.org/10.1016/J.JALLCOM.2021.162226

36 Hu, F., Lin, H., Zhang, Z., Liao, F., Shao, M., Lifshitz, Y., & Lee, S. T. (2014). Smart Liquid SERS Substrates based on Fe3O4/Au Nanoparticles with Reversibly Tunable Enhancement Factor for Practical Quantitative Detection. *Scientific Reports*, *4*(1), 7204. https://doi.org/10.1038/srep07204

37 Ha Anh, N., Quan Doan, M., Xuan Dinh, N., Quang Huy, T., Quang Tri, D., & Le, A. T. (2022). Gold nanoparticles-based SERS nanosensor for thiram and chloramphenicol monitoring in food samples: Insight into effects of analyte molecular structure on their sensing performance and signal enhancement. *Applied Surface Science*, *584*, 152555. https://doi.org/10.1016/J.APSUSC.2022.152555

38 Vo Huu, T., Tran Nhat, V. T., Xuan, M. N., Thi Ngoc, H. N., Hoang, L. N., Anh, T. D., Huu, K. N., & Le Vu Tuan, H. (2025). Synergistic enhancement of EM and CM in Ag/AZO thin films for high-performance SERS detection of R6G and methylparaben. *RSC Advances*, *15*(19), 14604–14619. https://doi.org/10.1039/D5RA01381J

39 Scher, K. M. R., Wang, Z., Nair, A., Wu, Y., Bartoli, M., Rovere, M., Tagliaferro, A., Rangan, S., Wang, L., & Fabris, L. (2022). Concentration and Surface Chemistry Dependent Analyte Orientation on Nanoparticle Surfaces. *The Journal of Physical Chemistry C*, *126*(38), 16499–16513. https://doi.org/10.1021/ACS.JPCC.2C05007

40 Liu, X., Ye, Z., Xiang, Q., Xu, Z., Yue, W., Li, C., Xu, Y., Wang, L., Cao, X., & Zhang, J. (2023). Boosting electromagnetic enhancement for detection of non-adsorbing analytes on semiconductor SERS substrates. *Chem*, *9*(6), 1464–1476. https://doi.org/10.1016/j.chempr.2023.01.017

41 Liu, C. Y., Cheng, H. W., Lai, M. Y., Tsai, H. M., Liang, M. Y., Biring, S., & Liu, S. W. (2024). Analyte-induced SERS hot spots for dramatically improving the ability to distinguish different concentrations of chemical solutions. *Journal of the Taiwan Institute of Chemical Engineers*, *165*, 105769. https://doi.org/10.1016/J.JTICE.2024.105769

42 Sun, F., Galvan, D. D., Jain, P., & Yu, Q. (2017). Multi-functional, thiophenol-based surface chemistry for surface-enhanced Raman spectroscopy. *Chemical Communications*, *53*(33), 4550–4561. https://doi.org/10.1039/C7CC01577A

43 Renata, S., Verma, N., Tu, Z., Pan, R. L., Hofmann, M., & Lin, C. H. (2021). Development of a tri-functional nanoprobe for background-free sers detection of sialic acid on the cell surface. *Chemosensors*, *9*(5), 92. https://doi.org/10.3390/CHEMOSENSORS9050092

44 Raveendran, J., & Docoslis, A. (2021). Detection and quantification of toxicants in food and water using Ag–Au core-shell fractal SERS nanostructures and multivariate analysis. *Talanta*, *231*, 122383. https://doi.org/10.1016/J.TALANTA.2021.122383

45 Chandran, L., Mohan, A., & Gopchandran, K. G. (2025). Mercaptoundecanoic acid functionalized gold nanoparticles as SERS substrate for the sensing of 6-thioguanine molecules. *Next Research*, *2*(1), 100130. https://doi.org/10.1016/J.NEXRES.2025.100130

46 Khairusheva, A.B., & Korolkov, I.V. (2026). Synthesis and surface functionalization of gold microtubes for SERS detection of dyes. *RSC Advances*, *16*(24), 22204–22215. https://doi.org/10.1039/D6RA01224H

47 Bekbol, Z. A., Izbasar, K. A., Zaboronok, A., Lissovskaya, L. I., Yang, H., Pihosh, Y., Ishikawa, E., Shakirzyanov, R. I., & Korolkov, I. V. (2025). Carborane-Containing Iron Oxide@Gold Nanoparticles for Potential Application in Neutron Capture Therapy. *Nanomaterials*, *15*(16), 1243. https://doi.org/10.3390/nano15161243

48 Ama, O. M., Aigbe, U. O., Anku, W. W., Osibote, O. A., & Pal, K. (2022). Degradation of Methylene Blue Dye and Bisphenol-A Using Expanded Graphene-Polypyrrole-Magnetite Nanocomposite. *Topics in Catalysis*, *65*(19–20), 1745–1754. https://doi.org/10.1007/S11244-022-01626-1

49 Dinh, N. X., Huy, T. Q., Van Vu, L., Tam, L. T., & Le, A. T. (2016). Multiwalled carbon nanotubes/silver nanocomposite as effective SERS platform for detection of methylene blue dye in water. *Journal of Science: Advanced Materials and Devices*, *1*(1), 84–89. https://doi.org/10.1016/J.JSAMD.2016.04.007

How to Cite: Al-Abbasi, A., Sida, H., Matter, H., & Massoud, F. (2026). Experimental and Theoretical Evaluation of Pentoxifylline as a Sustainable Corrosion Inhibitor for Medium Carbon Steel in HCl. *Eurasian Journal of Chemistry, 31, 3(123), 66–85.* https://doi.org/10.31489/2959-0663/3-26-15

Article

Received: 11 June 2026 | Revised: 18 August 2026 |
Accepted: 24 August 2026 | Published online: 2 September 2026

UDC 544.65:544.18:547.857.4

https://doi.org/10.31489/2959-0663/3-26-15

Aisha Al-Abbasi[1]*, Hussan Sida[2], Hamdy Matter[3], Fatima Massoud[4]

[1]*Chemistry Department, Faculty of Science, Sebha University, Sebha, Libya*
[2]*Scientific Research Consultation Center, Sebha University, Sebha, Libya*
[3]*Chemistry Department, Faculty of Science, Benghazi University, Benghazi, Libya*
[4]*Chemical Engineering Department, Faculty of Engineering, Sebha University, Libya*
(**Corresponding author's e-mail: ais.alabbasi@sebhau.edu.ly*)

Experimental and Theoretical Evaluation of Pentoxifylline as a Sustainable Corrosion Inhibitor for Medium Carbon Steel in HCl

This study aims to evaluate pentoxifylline (PTF), a pharmaceutical drug, as a sustainable green corrosion inhibitor for medium carbon steel in a 0.2 M HCl environment, addressing the critical need for non-toxic industrial alternatives. Experimental investigations were conducted using gravimetric weight loss measurements, hydrogen evolution tests, and electrochemical Tafel polarization across a temperature range of 293.15 to 313.15 K. Theoretical analyses, including Density Functional Theory (DFT) and Monte Carlo simulations, were further employed to explore molecular reactivity and adsorption behavior on the Fe (110) surface. The results revealed that inhibition efficiency increases with PTF concentration, reaching a maximum of 90.0 % at 500 ppm and 293.15 K. Thermodynamic parameters indicated that the process follows the Langmuir isotherm through a spontaneous physical adsorption mechanism. Electrochemical data confirmed that PTF acts as a mixed-type inhibitor, effectively suppressing both anodic metal dissolution and cathodic hydrogen evolution. Furthermore, the addition of iodide ions demonstrated a significant synergistic effect, enhancing the protective capacity to 99.4 %. In conclusion, PTF serves as a highly effective eco-friendly alternative for steel protection. Future research is recommended to investigate the long-term stability of PTF under dynamic industrial flow conditions.

*Keywords: g*reen inhibitor, corrosion inhibitor, adsorption, pentoxifylline, medium carbon steel, HCl, adsorption isotherms, Tafel polarization, Langmuir isotherm, DFT calculations.

1 Introduction

Corrosion is one of the most critical concerns for metal and industrial material. It is caused by a slow chemical or electrochemical reaction between material and the environment [1]. This phenomenon is the root cause of severe erosion in many metallic systems and industries. Rusting can take place on metals, polymers, and even ceramics. In aqueous solutions, corrosion is predominantly a result of electrochemical processes, in different times scale due to electrons exchange between metal surface and electrolyte solution. Corrosion induced economic loss is incredibly colossal and estimated to be trillion dollars on an annual basis across the globe [2, 3]. Apart from economic impact, it can also bring about environmental and health consequences, especially if metal containers are used to hold food, water, or pharmaceutical products.

Steel is the most commonly used material in high pressure industrial application because of its availability at low cost, high mechanical strength and ease of fabrication. They are widely utilized in the oil and gas fields, tank farms, pipelines, heat exchangers and chemical processing plants [4]. On the other hand, steel surfaces are extremely susceptible to corrosion in contact with acidic solutions. Acidic media are widely employed in industrial processes including acid cleaning, pickling, descaling, and oil well acidizing [5]. In this type of system, H^+ and dissolved O_2 are also good corrosion promoters, and they are active in high-temperature water environments. Hence, the steel surface protection in acidic media is still a challenging issue.

Numerous techniques have been evolved to mitigate corrosion damage. Such methods are protective coatings, cathodic protection, anodic protection, and the addition of corrosion inhibitors [6]. Corrosion inhibitors are one of the most feasible and cost-effective methods to combat corrosion, particularly in acidic media, of these methods. Corrosion inhibitors decreases the solubility of metal either by adsorbing at the metal surface forming a film or by modifying electrochemical reactions at the interface [7]. Organic com-

© 2026 The Authors. This is an open access article under the CC BY-NC-ND license (http://creativecommons.org/licenses/by-nc-nd/4.0/

pounds having heteroatoms such as N, O, S and P are reported to have good inhibition properties as these atoms are able to interact with the metal surface by their lone pair of electrons and π-electrons [7-15].

Although a lot of synthetic inhibitors are of high efficiency, some of them are toxic, costly and have environmental hazards. Therefore, due to the toxicity of some of the inhibitors used, recent efforts have been directed towards the synthesis of non-toxic, greener inhibitors. Due to their non-toxic nature and biodegradability, natural products and pharmaceuticals have been widely considered for application as green corrosion inhibitors for metals. Expired drugs are highly promising products since they can be considered as candidates for reuse rather than being disposed as waste [16-19]. Numerous pharmaceutical molecules have aromatic rings and heteroatoms that increase their propensity to adsorb on metal surfaces, and can be investigated for potential use in corrosion inhibition [20, 21]. However, a critical review of the existing literature reveals a significant gap in the detailed atomistic understanding of how hexadentate drug molecules like Pentoxifylline interact with the Fe (110) surface, particularly when combined with inorganic synergistic ions in HCl media. Most existing studies focus on macroscopic experimental observations without providing a rigorous theoretical correlation to justify their industrial efficacy.

To address these limitations, the present study offers a novel, multi-faceted evaluation that bridges the gap between experimental performance and theoretical molecular dynamics. In this investigation, hexadentate pentoxifylline (PTF) was adopted as the inhibitor for the corrosion of medium carbon steel in 0.2 M HCl. The adsorption and inhibition properties of PTF were investigated through weight loss studies, hydrogen evolution, electrochemical methods and quantum chemical calculations. Moreover, the effect of iodide ions as synergist on the inhibitive performance of PTF was also investigated. The novelty and scientific contribution of this work lie in the precise integration of high-level Density Functional Theory (DFT) and Monte Carlo simulations on the Fe (110) surface to elucidate the electronic donor-acceptor mechanisms of PTF, providing new insights into sustainable and highly efficient multi-component corrosion protection systems that have not been fully explored in previous literature.

2 Experimental

2.1 Materials

Pentoxifylline (400 mg tablets) was a gift from Santa Farma, Turkey. The medium carbon steel samples were procured from Libyan Steel Factory, Libya. Elemental composition of the steel was C (0.33 %), Si (0.17 %), Mn (0.72 %), P (0.013 %), S (0.002 %), and Fe (98.765 %). For the weight loss test, the steel was cut mechanically into cylindrical pieces having the dimensions of 4 cm in length and 1 cm in diameter. Surface were polished with SiC abrasive papers (400–1200 grit size). After polishing, the test samples were rinsed with ethanol and acetone, air-dried and kept in desiccators to protect from moisture prior to utilization. A stock solution of hydrochloric acid (5.0 N) was prepared from commercial HCl (37 %) and standardized against sodium carbonate solution. The necessary concentration of 0.2 M HCl was prepared by dilution with deionized water. A stock solution of pentoxifylline inhibitor (1000 ppm) was prepared and the various concentrations viz., 50 to 500 ppm were tested in the study.

2.2 Instrumentation

The experimental procedures, including gravimetric measurements and hydrogen evolution tests, were conducted at the Chemistry Department, Faculty of Science, Sebha University, Libya. The weight loss experiments were performed using a precision analytical balance (Ohaus, Ga110-Made in West Germany). A thermostatic water bath to maintain constant temperatures (Clifton Bata-England). Electrochemical measurements, including potentiodynamic Tafel polarization, were carried out using a Potentiostat, manufactured by ACM Instruments (field model). The medium carbon steel was sourced from the Libyan Steel Factory, Libya. For the computational modeling, Density Functional Theory (DFT) and Monte Carlo simulations were executed at the Scientific Research Consultation Center, Sebha University, using the BIOVIA Materials Studio software (version 5.5) developed by Accelrys (now BIOVIA, USA).

2.3 Gravimetric Estimations

For the weight loss test, the steel was precisely cut into cylindrical pieces (4 cm length, 1 cm diameter) using a lathe machine. The cutting process was performed under continuous liquid cooling to prevent thermal overheating and minimize mechanical induced stresses on the steel specimens. This ensures that the metallurgical properties of the medium carbon steel remain unchanged during preparation. Subsequently, the surfaces were polished with SiC abrasive papers (400–1200 grit size) to remove any residual surface irregularities. After polishing, the test samples were rinsed with ethanol and acetone, air-dried and kept in desicca-

tors to protect from moisture prior to utilization. The pre-weighed medium carbon steel samples were fully immersed in 50 mL of various concentrations of inhibitors from 50 to 500 ppm. The tests were performed in a thermostatically water bath at various temperatures. At the end of the Soaking time, the steel samples were taken out, cleaned and dried then weighed once more. The values of weight loss were calculated by subtracting the final weight of the samples from the initial weight. Each experiment was performed in triplicate for reproducibility. Corrosion rate (CR) in mmy is calculated using Equation (1) [22, 23]:

$$\mathrm{CR}\left(\mathrm{mmy}\right) = \frac{8.76\times10^{4}W}{\mathrm{At}D} \tag{1}$$

From the corrosion rate data, the inhibition efficiency (% Inh) and the surface coverage (θ) were calculated with help of the following equations (2) and (3).

$$I\% = \left(1 - \frac{CR_{inh}}{CR_0}\right)\times100 \tag{2}$$

$$\theta = \left(1 - \frac{CR_{inh}}{CR_0}\right) \tag{3}$$

where CR_0 is the corrosion rate without and CR_{inh} is the corrosion rate with the inhibitor.

2.4 Hydrogen Evolution Tests

Hydrogen evolution experiments were carried out in a closed flask assembled to an inverted burette via a plastic tube [24]. The flask was filled with 0.2 M HCl solution, PTF inhibitor was also therein, as well as none. The system was kept at 303.15 K by a thermostatic water bath. The volume of released hydrogen gas was recorded every 2 min for 60 min. The experiments were performed with and without 200ppm PTF as well as iodide ion as a synergistic additive. Hydrogen evolution rate (Hr) was calculated using Equation (4).

$$\mathrm{H_r} = \left(\mathrm{V_2} - \mathrm{V_1}\right)/\left(\mathrm{t_2} - \mathrm{t_1}\right) \tag{4}$$

where V_1 and V_2 are the volumes of hydrogen observed at times t_1 and t_2, respectively. The volume of hydrogen was plotted against the immersion time, and the slope of the resulted straight line was the corrosion rate. The inhibition efficiency was calculated from the Equation (5) [25]:

$$\mathrm{Inh\%} = \left[1\left(H_0 / \mathrm{H}_{inh}\right)\right]\times100 \tag{5}$$

where H_0 and Hinh are the rates of hydrogen evolution in the absence and presence of inhibitor respectively.

2.5 Tafel Polarization Tests

The electrochemical cell contained a working electrode– a suitable electrode for the solution being studied, Ag/AgCl reference electrode, and carbon rod as counter electrode. The potentiodynamic polarization experiments were performed by sweeping the potential from −500 mV versus the open circuit potential (OCP) to +500 mV vs. OCP at a scan rate of 1 $\mathrm{mVs^{-1}}$. The working electrode was made by insulating all sides but one exposed face joined by a copper wire. Prior to each run, the surface of the steel was polished with different sized abrasive papers (60-1200 grit). The measurements were made at room temperature with a 1000 mL capacity open electrochemical cell in 0.2 M HCl solution with and without 500 ppm of PTF inhibitor.

2.6. Computational Details

2.6.1. Molecular Reactivity and Molecular Dynamics

The density functional theory calculations were carried out with Materials Studio software via the $\mathrm{DMol^3}$ module (version 5.5). To ensure scientific validity and reproducibility, all calculations were performed using the Double Numerical plus Polarization (DNP) basis set. The calculations were conducted in the gas phase to investigate the intrinsic molecular reactivity of PTF, following the standard methodology widely adopted in established corrosion inhibition research. This approach ensures that the electronic descriptors (HOMO, LUMO, etc.) represent the inherent donor-acceptor capacity of the molecule without the shielding effects of a dielectric medium, allowing for direct comparison with literature data. Geometry optimizations were carried out with high-precision convergence criteria (1.0×10^{-5} Ha for energy and 0.002 Ha/Å for force) to ensure that the stationary structures represent true energy minima, consistent with stable configurations reported in previous studies using similar functionals. calculations were performed at the level of the generalized gradient approximation (GGA) within the BLYP exchange correlation functional [26, 27].

The frontier molecular orbitals, HOMO and LUMO, are also considered in order to study the adsorption characteristics of the organic compounds on the metal surface. Based on Koopman's theorem, the HOMO and the LUMO energies were utilized to calculate the values of the ionization potential and the electron affinity [28-30].

$$\Delta E = E_{LUMO} - E_{HOMO} \quad (6)$$

$$I = -E_{HOMO} \quad (7)$$

$$A = -E_{LUMO} \quad (8)$$

Other quantum chemical descriptors like electronegativity (χ), hardness (η), and softness (σ) of the inhibitor molecule are given by Pearson [30].

$$\chi = \frac{I + A}{2} \quad (9)$$

$$\eta = \frac{I - A}{2} \quad (10)$$

$$\sigma = \frac{1}{\eta} \quad (11)$$

The fraction of electrons transferred (ΔN), and electrophilicity index (ω) were also derived as follows [31]:

$$\Delta N = \frac{\chi_{Fe} - \chi_{inh}}{2(\eta_{Fe} + \eta_{inh})} \quad (12)$$

Using a theoretical value, $\chi_{Fe} = 7eV$ and the value of $\eta_{Fe} = 0$ eV for iron according to Pearson's electronegativity scale[22]. The electrophilicity index (ω) has been defined as [32-34]:

$$\Delta\omega = \frac{\chi^2}{2\eta} \quad (13)$$

2.6.2 Monte Carlo Simulations

Monte Carlo simulations were carried out to study the adsorption of PTF molecules on Fe (110) surface using the Adsorption Locator module within the Materials Studio software package, as it is specifically designed for identifying low-energy adsorption configurations. The Forcite module was utilized only for the initial geometry optimization of the inhibitor and the metal surface. The calculations were performed with the COMPASS force field (Condensed-phase Optimized Molecular Potentials for Atomistic Simulation Studies) [35, 36]. The Fe surface was cut along the (110) plane and modeled as a supercell with dimensions of 12 Å × 12 Å, which provides sufficient surface area to host a single PTF molecule while minimizing periodic self-interaction artifacts. A vacuum thickness of 15 Å was used to suppress the spurious interactions between periodic images along the z-axis. While the simulations were conducted in a vacuum to establish a fundamental baseline for the intrinsic binding energy, this gas-phase approximation effectively identifies the preferred molecular orientation on the iron lattice. The adsorption search was performed using the Metropolis Monte Carlo algorithm within the NVT statistical ensemble (constant number of particles, volume, and temperature) at 298.15 K. The simulation consisted of a total of 1,000,000 Monte Carlo steps, including 100,000 equilibration cycles followed by 900,000 production/sampling cycles to sample the identification of the global energy minimum. For non-bonded interactions, a cutoff distance of 12.5 Å was applied, utilizing the Ewald summation method for electrostatic interactions and the atom-based method for van der Waals interactions.

3 Results and Discussion

3.1 Mass Loss Approach

3.1.1 The Inhibition Properties of Pentoxifylline Drugs

The Inhibition Properties of Pentoxifylline Drugs Table 1 and Figure 1 illustrate the results for the estimated corrosion rate (mmy) and inhibition efficiency (Inh%) of medium carbon steel in 0.2 M HCl solution in the presence and absence of various doses of PTF inhibitor (100–500 ppm). The results demonstrate that the corrosion rate of medium carbon steel was significantly reduced after the addition of PTF compared with that in the blank solution. As shown in Figure 1, the corrosion rates decreased stepwise with increasing in-

hibitor concentration. This behavior implies that PTF molecules successfully inhibit the dissolution of steel in HCl medium through adsorption onto the steel surface [37].

Table 1

Corrosion rates (C.R., mmy) for HCl (0.2 M) induced medium carbon steel dissolution with and without inhibitor at different temperatures.

Inhibitor Conc., ppm	293.15 k		303.15 k		313.15 k	
	C.R., mmy	Inh., %	C.R., mmy	Inh., %	C.R., mmy	Inh., %
0	11.416	-	21.2600	-	59.682	-
100	2.7366	76.0278	6.1120	71.2512	7.466	43.1941
200	1.7693	84.5011	4.8609	77.1357	5.135	62.7341
300	1.5292	86.6039	4.4890	78.8851	4.461	67.7512
400	1.1824	89.6426	3.5538	83.2840	4.21	69.0759
500	1.1404	90.0099	3.1573	85.1492	5.515	69.6574

The data presented in Table 1 also indicates that temperature has a positive impact on the rate of corrosion. The efficiency of inhibition became less at several temperatures ranging between 293.15 and 313.15 K. This may be due to the fact that the corrosion reaction was accelerated under high temperature. Moreover, the rise in temperature might result in the desorption of PTF from the steel surface and disclosure of more metal atoms to the acidic solution by destruction of the protective layer. The maximum inhibition efficiency achieved by PTF (90.0 %) is notably higher than the 84.9 % efficiency reported by Popović for expired metformin, suggesting that PTF's hexadentate structure provides more extensive surface coverage on the steel substrate [38].

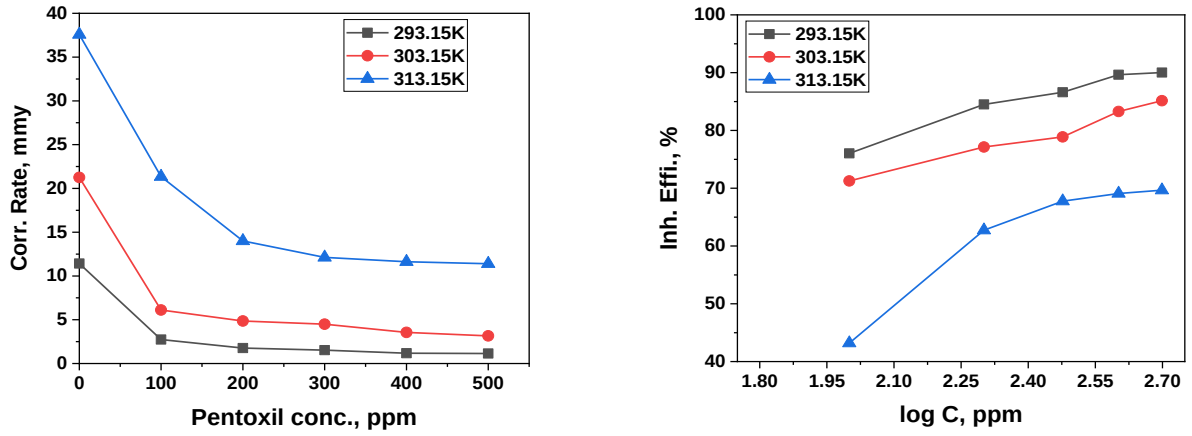

Figure 1. Corrosion rate (A) and inhibition efficiency (B) of PTF at different concentrations

3.1.2 Thermodynamic Parameters of the Corrosion Inhibition

Figure 2 presents the inhibition efficiency of PTF on the medium carbon steel surface as a function of changing temperature. The results show that the inhibition efficiency decreased with the temperature, indicating that the protective film of PTF molecules is unstable at high temperatures [39]. In contrast to the findings of Mahmood, where inhibition efficiency showed a slight increase with temperature, PTF exhibits a decrease, which confirms the predominantly physical nature of its adsorption compared to the chemisorptive behavior of p-bromopiperazinylbenzene [40].

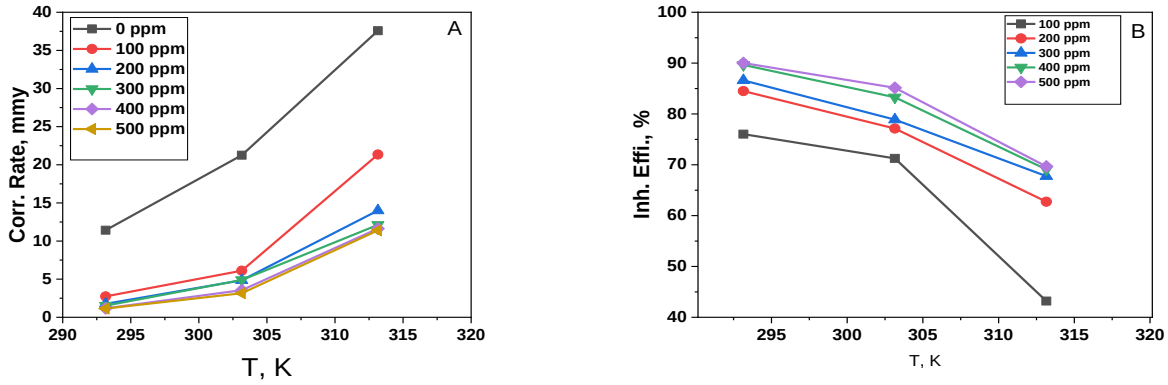

Figure 2. Corrosion rate (A), and efficiency of inhibition (B), at different temperatures

The activation parameters of the corrosion are needed to better understanding the mechanism of inhibition. The temperature dependence of the corrosion rate was analyzed in terms of the Arrhenius equation [41-43]:

$$\ln R = \ln A - \frac{\Delta E_a^*}{\mathcal{R}T} \quad (14)$$

where R is the universal gas constant, ΔE_a^* is the apparent activation energy and A is the Arrhenius pre-exponential factor. The Arrhenius plots are given in Figure 3. In all plots, perfect or close to unity, (R^2: 0.998-1.000), liner Arrhenius behaviour was confirmed. Energy of activation calculations and are said to be derived from the slopes of these plots. Thermodynamic parameters were also calculated through the transition-state equation [43-45]:

$$\ln\left(\frac{R}{T}\right) = \left[\ln\frac{\mathcal{R}}{N^O h} + \frac{\Delta S_a^*}{\mathcal{R}}\right] - \frac{\Delta H_a^*}{\mathcal{R}T} \quad (15)$$

where h is Planck's constant, N is Avogadro's number, ΔS_a^* is the activation entropy and ΔH_a^* a is the activation enthalpy. The changes in free energy of activation for thermal decomposition, ΔG_a^*, were also determined. The values of enthalpy of activation ($\sqrt{\Delta H_a^*}$) and entropy of activation ($\sqrt{\Delta S_a^*}$), which are shown in Table 2, were calculated using the slope and intercept of the curves.

$$\Delta G_a^* = \Delta H_a^* - T\Delta S_a^* \quad (16)$$

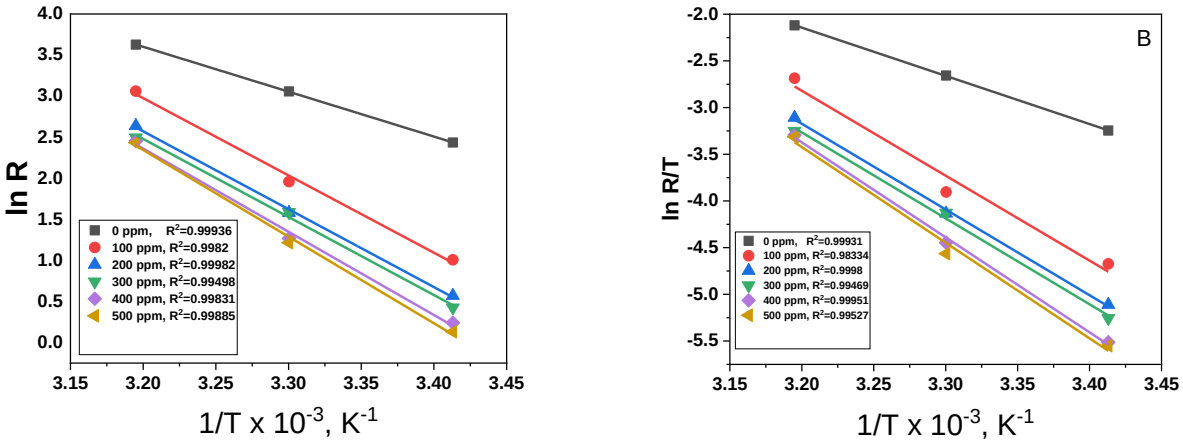

Figure 3. Arrhenius (A) and transition state (B) plots for the corrosion of medium carbon steel in 0.2 M HCl in the absence and presence of PTF

Table 2 provides the calculated thermodynamic parameters, including the activation energy (ΔE_a^*), enthalpy (ΔH_a^*), and entropy ΔS_a^*, which were derived from the Arrhenius and transition-state plots shown in Figure 3 [46-48].

Table 2

Values of the thermodynamic constants for the dissolution of medium carbon steel in the absence and presence of PTF in 0.2 M HCl

Inhibitor Conc., ppm	ΔE_a^*, KJ·mol^{-1}	ΔH_a^*, KJ·mol^{-1}	ΔS_a^*, J·mol^{-1}K^{-1}	ΔG_a^*, KJ·mol^{-1}		
				293.15, K	303.15, K	313.15, K
0	45.477	42.958	-77.969	65.815	66.594	67.374
100	78.178	75.66	21.001	69.504	69.294	69.084
200	78.902	76.383	20.378	70.409	70.206	70.002
300	79.004	76.486	19.696	70.712	70.515	70.318
400	87.147	84.628	45.087	71.411	70.960	70.509
500	87.721	85.202	46.525	71.563	71.098	70.633

The thermodynamic shown in Table 2 indicated that all energies of activation were positive, which is evidence of corrosion process endothermic nature. The activation energy was raised in the presence of the inhibitor as compared to the blank solution, denoting that the inhibitor forms a barrier through those acts as the energy barrier that hinders the dissolution of steel. The increase in active energy also implies that inhibition effectiveness may reduce at higher temperatures due to less adsorption of inhibitor molecules onto surface of medium carbon steel [43].

The enthalpy values, Table 2, were found to increase with the concentration of inhibitor. The positive enthalpy values suggest that the inhibition is an endothermic process and the dissolution of steel is more retarded in the presence of high concentrations of PTF [43, 44]. In contrast, after addition of the inhibitor, the entropy values were more negative. This behavior indicates that the activated complex in the corrosion reaction is more ordered than the reactants [21]. The calculated ΔG_a^* values are also presented in Table 2. Positive value was obtained for the blank solution, while negative values were found for the inhibited systems. The increase in value showed that the inhibition reaction is feasible and the transition state became stable as temperature increased [39]. Moreover, the free energy of activation decreased with increasing inhibitor concentration from 50 to 200 ppm, which could be related to the development of the activated complex too being less stable. But, the value of the free energy increased again at 300 — 400 ppm, which was attributed to the generation of a more stable activated complex on the surface of steel [39]. The observed increase in activation energy (ΔE_a^*) upon the addition of PTF (from 45.4 to 87.7 kJ/mol) is consistent with the findings of Malki, who reported a similar upward trend in ΔE_a^* values (from 21.0 to 40.46 kJ/mol), confirming the formation of a physical barrier that restricts the corrosion process [49].

3.1.3 Synergistic Effect

Table 3 and Figure 4 present the corrosion rate and inhibition efficiency values at 303.15 K, demonstrating the synergistic effect between iodide ions and PTF molecules [27 ،28]. Furthermore, Table 4 and Figure 5 show the impact of fixed potassium iodide (KI) concentration on the inhibitory performance of varying PTF concentrations [29 ،30]. The S_I values in these tables indicate strong synergistic behavior between iodide ions and PTF molecules.

Table 3

Corrosion rate and inhibition efficiency at 303 K in the presence of KI and PTF

KI conc., ppm	0, ppm PTF		200, ppm PTF		
	C.R., mmy	Inh, %	C.R., mmy	Inh, %	SI
0	21.260	-	4.861	77.136	-
50	17.626	17.094	2.069	90.269	1.948
100	15.773	25.811	1.934	90.903	1.865
150	14.310	32.693	1.869	91.210	1.751
200	12.617	40.655	1.620	92.380	1.781

The inhibition efficiency increased dramatically with the addition of iodide ions as shown in Table 3. The maximum protection was achieved at 200 ppm KI with inhibition efficiency 92.38 % in presence of 200 ppm PTF. The decrease in the corrosion rate proves the presence of a synergistic effect between iodide ions and PTF molecules. This can be related to the fact that the iodide ions can promote the steel surface adsorption of inhibitor molecules. Iodide ions are much more strongly adsorbed due to their big ionic size and high polarizability. Their adsorption promotes the interaction of PTF molecules with the metal surface, so that a denser protective film is formed [50, 51]. Our synergistic PTF/Iodide system (99.4 %) demonstrates superior performance compared to the dual-inhibitor compositions evaluated by Tsygankova, such as the Drotaverine/KCNS mixture which reached 98.0 % efficiency [52].

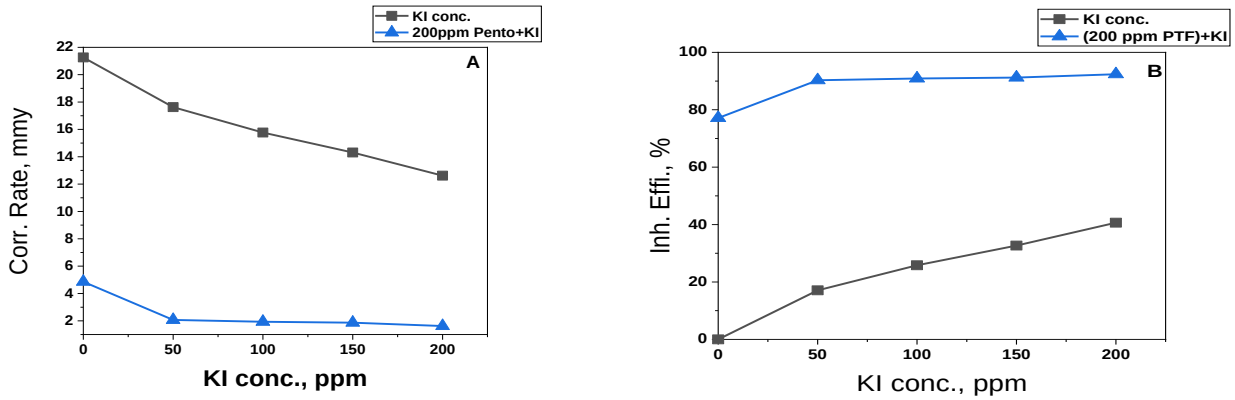

Figure 4. Corrosion rate (A) and inhibition efficiency (B) as a function of KI concentration in the presence of PTF at 303.15 K

These findings also reveal that the corrosion rate continuously decreases with raising KI content. Under dual PTF and KI presence the rate of corrosion was even lower than that in the solutions containing only potassium iodide. This is attributed to the fact that progressively adsorption of PTF molecules enhances the coverage and protective oil film on the steel substrate. Similarly, the inhibition efficiency increased as the KI concentration increased. Furthermore, the inhibitory effectiveness in the binary system of KI + PTF was superior to that of PTF alone, indicating a synergistic positive effect of the iodide ions. A concentration of KI of 150 ppm was chosen to investigate more the inhibition performance of the medium carbon steel in acidic medium containing variable concentrations of PTF at fixed KI concentration. The corrosion rates and subsequent inhibitor efficiencies calculated are presented in Table 4 and Figure 5.

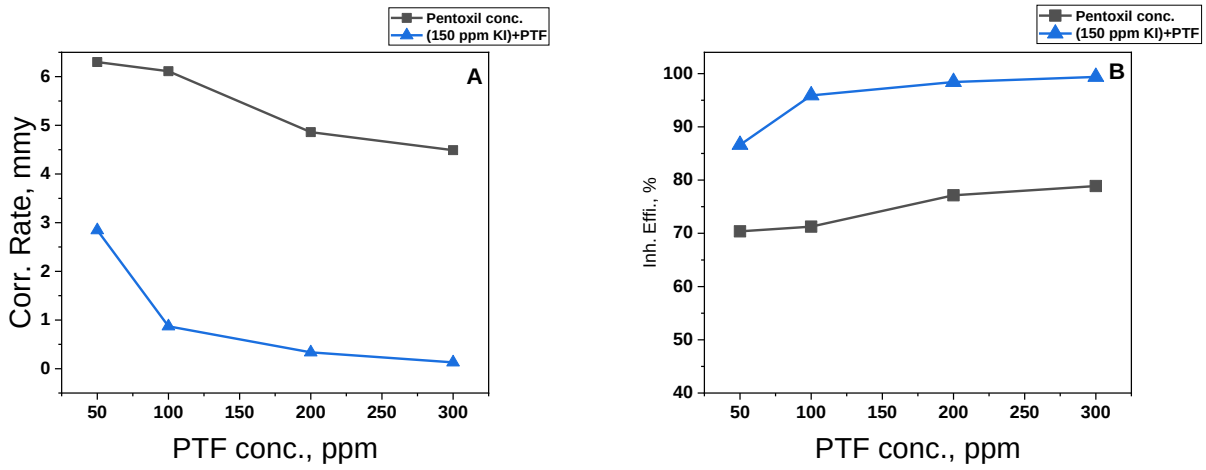

Figure 5. Corrosion rate and inhibition efficiency in the presence of PTF, with a fixed concentration of KI at 303.15 K

Table 4

Corrosion rate and inhibition efficiency in the presence of PTF, with a fixed concentration of KI at 303.15 K

PTF conc., ppm	0, ppm KI		150, ppm KI		
	C.R., mmy	Inh, %	C.R., mmy	Inh, %	SI
50 ppm	6.300	70.367	2.846	86.614	1.490
100 ppm	6.112	71.251	0.871	95.902	4.721
200 ppm	4.861	77.136	0.337	98.416	9.715
300 ppm	4.489	78.885	0.130	99.387	23.169

In acidic medium, the corrosion of steel surface produces positively charged metal ions [51]. In these circumstances, PTF molecules may be adsorbed on the steel surface [53-55]. Meanwhile, iodide ions can also be readily adsorbed by electrostatic attraction since it is negatively charged and the metallic cation are positively charged [51]. Iodide ion adsorption decreases the rate of corrosion and the number of delocalized active sites on the surface of steel. Iodide ions significantly enhance the adsorption of PTF molecules on the steel surface and assist in the formation of a strong anti-corrosive film on steel. When the KI concentration was about 150 ppm, the co-adsorption process was the most effective with an inhibition efficiency of 99.3866 % in the presence of 300 ppm PTF.

The synergism influence between PTF and iodide ions was estimated by the synergistic parameter (SI), which is defined as follows [57-55]:

$$SI = \left(1 - I_{1+2}\right) / \left(1 - I'_{1+2}\right) \quad (18)$$

Here I_1 and I_2 are the inhibition efficiency of iodide ions and PTF respectively, and I'_{1+2} is the inhibition efficiency for the presence of KI and PTF together. Interpretation The S_I values indicate synergistic effects for values exceeding unity in the reverse for less than unity [51, 58, 59]. The case with iodide ions and PTF also has the highest values of S_I listed in Tables 3 and 4, indicating very strong synergistic behaviour between iodide ions and PTF molecules in that particular situation.

3.1.4 Adsorption Isotherms

Figure 6 displays the linearity of the experimental values fitted to the Langmuir, El-Awady, Temkin, and Freundlich adsorption isotherm models. Table 5 lists the calculated adsorption parameters, including the equilibrium constant (K_{ads}) and the standard free energy of adsorption (ΔG^{o}_{ads}), derived from these models.

In general, adsorption of organic molecules on a metal surface is the process where already adsorbed water molecules on the steel surface are displaced by the organic molecules in the solution phase. Inhibitor molecules must interact intensely with the metal surface for the adsorption to be successful. These interactions can be of an electrostatic nature and/or by a covalent bonding between the chemisorbed species and the metal surface atoms. Hence, to achieve a better approximation to the adsorption behaviour of the PTF molecule on the medium carbon steel, we considered in this study a number of different adsorption isotherm models. The surface coverage (θ) values obtained from the mass loss technique were used in this analysis. Langmuir, El-Awady, Temkin and Freundlich adsorption isotherms were investigated and thermodynamic parameters of adsorption were calculated, too.

From the examined adsorption models, the Langmuir adsorption model was the most appropriate for the experimental data with the highest values of correlation coefficient (R^2). The Langmuir adsorption model was tested by plotting C/θ as a function of the inhibitor concentration (C), and the data are shown in Figure 6.

$$\frac{C}{\theta} = \frac{1}{K_{ads}} + C \quad (19)$$

where K_{ads} is the equilibrium constant for adsorption. Straight lines with slopes close to unity and the intercepts were $1/K_{ads}$ at all the temperatures studied. The lines high linearity suggest that the PTF molecules on medium carbon steel surface have been the Langmuir isotherm. The values of K_{ads} and ΔG_{ads} calculated are given in Table 5.

Also, the El-Awady isotherm of adsorption was tested by applying Eq. (20). Linear relationships were obtained when $\log(\theta/1-\theta)$ was plotted versus log C as shown in Figure 6. The values of the correlation R^2 were good indicating that fitting of the experimental data were acceptable. The calculated y, 1/y, K_{ads}, and ΔG_{ads} values are reported in Table 5.

$$\log\frac{\theta}{1-\theta} = \frac{1}{y}\log K_{ads} + y\log C \tag{19}$$

The linearized version of the Freundlich equation was used to analyses the adsorption isotherm Freundlich isotherm was also verified by applying the equation in linearized form. Straight lines were obtained when we plot log θ against log C. Their slopes and intercepts are 1/n and log K_{ads}, respectively.

$$\log\theta = \log K_{ads} + \frac{1}{n}\log C \tag{20}$$

The parameter n is an empirical parameter that is related to adsorption properties. In general, as 1/n was between 0 and 1, adsorption process is favorable, when n is near to or less than unity, then the adsorption is unfavorable [60]. The Temkin adsorption isotherm was further employed by Eq. (22). The plots of θ against ln C were linear (Fig 6). The slope and intercept were equal to 1/ *f* and (1/ *f* ln K_{ads}), respectively.

$$\theta = \frac{1}{f}\ln c + \frac{1}{f}\ln K_{ads} \tag{22}$$

The standard free energy of adsorption was determined by the following equation (23) [61]:

$$\Delta G^{o}_{ads} = RT\ln\left(55.5\,K_{ads}\right) \tag{24}$$

where R is the gas constant, T is the absolute temperature and 55.5 is the molar concentration of water in solution. The determined adsorption parameters are listed in Table 5 [37].

The adsorption details for the PTF inhibition of medium carbon steel corrosion in HCl solution are given in Table 5. The values of correlation coefficients for all models were found to be high (R^2 > 0.90), indicating that the experimental data were well fitted by all investigated adsorption models. The superior fit of the Langmuir isotherm (R^2 = 0.999) for PTF adsorption is in full agreement with recent studies by Malki and Abdel-Hameed [49], validating the formation of a stable, protective monolayer of pharmaceutical molecules on the steel surface. However, the Langmuir adsorption isotherm achieved the maximum R^2 values that were close to 0.999 and confirmed that this isotherm best represents the adsorption of PTF molecules on the surface of the medium carbon steel in the medium of hydrochloric acid. The calculated K_{ads} values for the process under study were less than unity, indicating that the adsorption is predominantly physical and that that the PTF molecules and the steel surface are associated via physical forces [37]. This behaviour is very favourable for a protective adsorbed layer formation via electrostatic interaction.

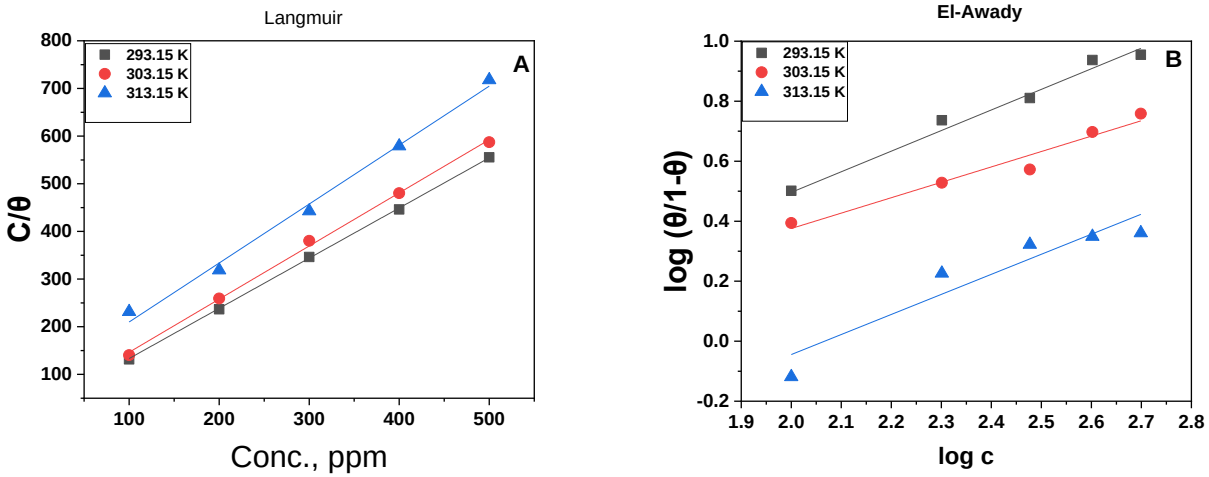

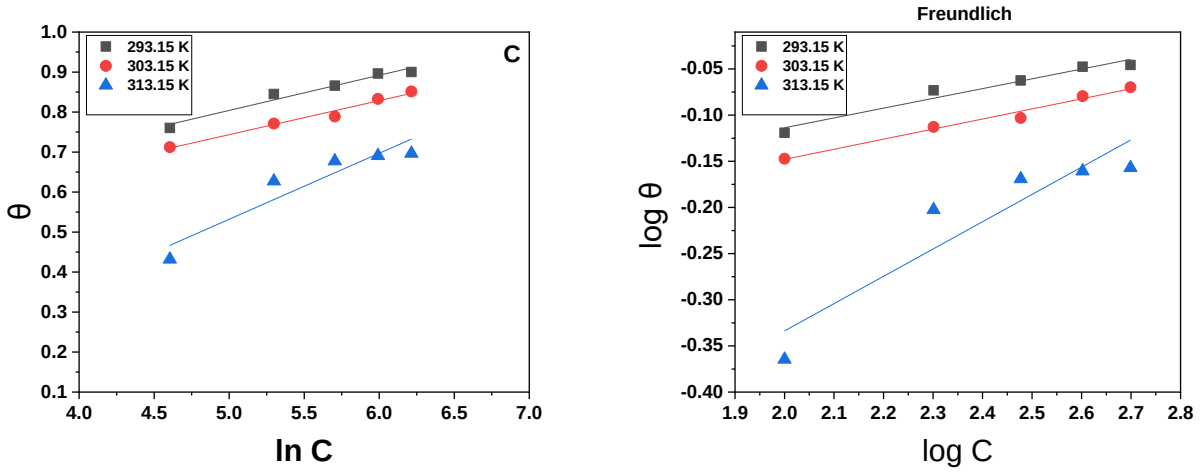

Figure 6. Linearity of the experimental values to the Langmuir (A), El-Awady (B), Temkin (C) and Freundlich (D) fractional productivity adsorption isotherm

Table 5

Adsorption parameters(K_{ads} and ΔG_{ads}) from Langmuir El-Awady and Freundlich isotherm curves at 298 K

	Parameters	293.15, K	303.15, K	313.15, K
Langmuir	K_{ads}	0.038	0.0285	0.0113
	$\Delta G_{ads,}$ KJ·mol^{-1}	-1.908	-1.157	-1.166
Freundlich	K_{ads}	0.473	0.430	0.119
	$\Delta G_{ads,}$ KJ·mol^{-1}	-20.575	-19.549	-5.649
	1/n	0.1059	0.1092	0.2957
El-Awady	K_{ads}	0.155	0.229	0.036
	$\Delta G_{ads,}$ KJ·mol^{-1}	-5.245	-6.408	-1.281
	1/y	1.512	1.964	1.448
	y	0.661	0.509	0.691
Temkin	K_{ads}	63.209	42.093	0.170
	$\Delta G_{ads,}$ KJ·mol^{-1}	-19.893	-19.547	-5.837
	f	11.377	11.751	-6.061
	α	-5.688	-5.875	-3.030

The Temkin adsorption curves for the linear behavior are shown in Figure 6, which reveals that Temkin isotherm can also be used to represent the PTF adsorption. The negative values of α and f imply that attractive interactions exist between the adsorbed PTF molecules on the steel surface.

The El-Awady adsorption model fitting is also shown in Figure 6 and the derived values of y and 1/y are presented in Table 5. The resulting 1/y values imply that a singe PTF molecule covers two active sites on the medium carbon steel surface, which in turn leads to effective surface coverage and enhanced inhibition performance.

The Freundlich adsorption curves are depicted in Figure 6. The calculated 1/n- values fulfil the criteria $0 < 1/n < 1$ which indicates that PTF molecules easily adsorbs on the RS surface [62].

The ΔG_{ads} values calculated at various T are also given in Table 5. The PTF adsorption free energy ΔG_{ads} were all negative and less than −40 kJ/mol, which implied adsorption of the PTF molecules were spontaneous. These findings also confirm that PTF molecules have been adsorbed on the metal surface by electrostatic force between the inhibitor molecules and metal surface, which means that the inhibition process is dominantly governed by physisorption [37].

3.2. Hydrogen Evolution Measurements

Figure 7 illustrates the volume of evolved hydrogen gas as a function of immersion time for medium carbon steel dissolution in 0.2 M HCl, comparing the blank solution with those containing PTF and potassium iodide. Table 6 summarizes the corrosion rates and inhibition efficiencies calculated from these hydrogen evolution measurements.

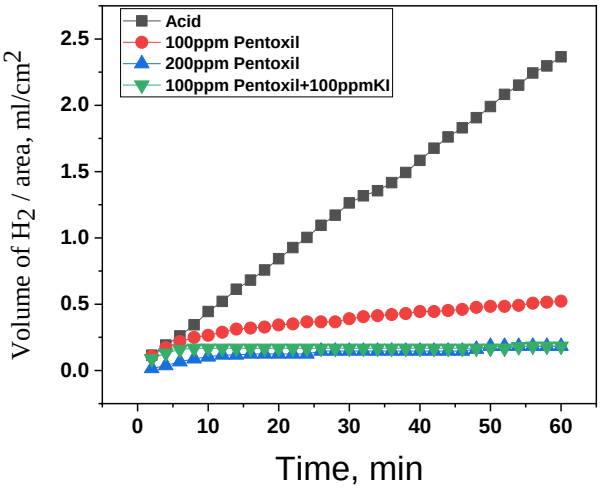

Figure 7. Volume of evolved hydrogen as a function of time for medium carbon steel dissolution in in 0. 2 M HCl with and without PTF and potassium iodide

The volume of evolved hydrogen gas was found to be increased continuously with the increase of immersion time. This is known since hydrogen evolution is a by-product of the corrosion reaction in the acid solution. The hydrogen evolution rate, however, showed an evident decrease when PTF molecules were introduced. The results obtained suggest that a rise in the concentration of PTF is inversely proportional to the amount of produced hydrogen gas. This decrease indicates the surface coverage, and all the above data confirms that I inhibits the corrosion process via adsorption onto the steel surface. Adsorbed inhibitor molecules can create a protective film at the interface of metal and acidic solution that protects the metal from corrosion and also restricts the hydrogen evolution rate. Inhibition efficiency values, based on hydrogen evolution measurement, are presented in Table 6.

Table 6

Corrosion rate and inhibition efficiency of PTFs from hydrogen evolution

Solutions	C.R., $mL \cdot cm^{-2} \cdot min^{-1}$	Inh, %
Acid conc., 0.2, M	0.0388	0
100, ppm PTF	0.0057	85.3093
200, ppm PTF	0.0021	94.5876
100, ppm PTF + 100, ppm KI	0.0005	98.5689

The results showed a continuous increase in the volume of evolved hydrogen gas with increasing immersion time. This behaviour is expected because hydrogen evolution accompanies the corrosion reaction in acidic solution. However, the hydrogen evolution rate decreased noticeably after the addition of PTF molecules. The obtained data indicate that increasing PTF concentration reduces the amount of generated hydrogen gas. This reduction confirms that the inhibitor suppresses the corrosion reaction through adsorption on the steel surface. The adsorbed inhibitor molecules form a protective layer that isolates the metal from the acidic environment and decreases the rate of hydrogen evolution. The marked reduction in hydrogen evolution observed with PTF aligns with the results of Tsygankova, who demonstrated that expired pharmaceutical molecules successfully retard the cathodic hydrogen gas generation in acidic media [52].

PTF molecules adsorb on the surface of the medium carbon steel at the metal/solution interface, inhibiting the dissolution of the steel in HCl solution and hence decreasing the cathodic hydrogen evolution reaction [25]. The inhibitor's molecular structure and its capacity to adsorb on the steel surface are directly associated with the inhibitory properties. Furthermore, the results reveal that the corrosion rate is decreased remarkably in the dual action of PTF and potassium iodide. Inhibitor molecules are adsorbed on the steel surface and organized to serve as a thin, protective layer, which significantly inhibit metal dissolution and hydrogen production.

3.3. Electrochemical Tafel Polarization Tests

Electrochemical polarization studies were conducted to determine the efficiency of PTF as an inhibitor and to gain further insights into the mechanism of inhibition and the durability of the adsorbed inhibitor film on the medium carbon steel surface for an extended time of 22 h immersion. Figure 8 shows the potentiodynamic polarization curves of the medium carbon steel in 0.2 M HCl with and without 500 ppm of PTF inhibitor. As observed in the Figure, the curves with and without the inhibitor appear closely aligned, reflecting the moderate nature of the inhibition effect under these conditions.

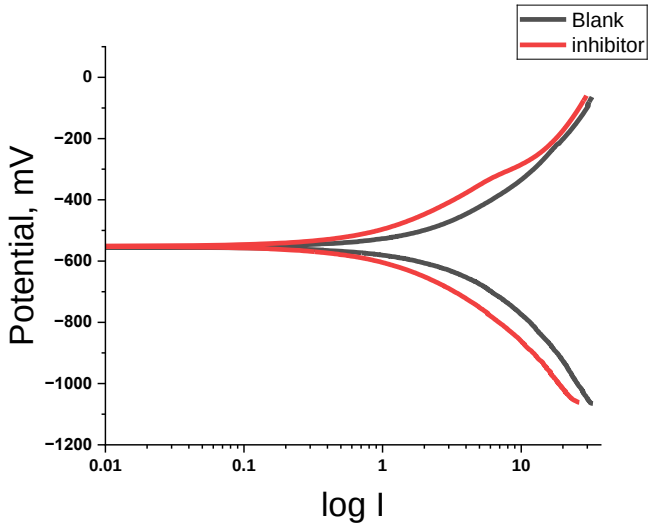

Figure 8. Potodynamical polarization curves of the medium carbon steel in 0.2 M HCl with and without PTF inhibitor

The electrochemical parameters derived from these curves, including corrosion current density (*Icorr*) and linear polarization resistance (LPR), are presented in Table 7. The results indicate a measurable reduction in the corrosion current density (*Icorr*) from 1.3418 mA/cm² for the blank solution to 1.0188 mA/cm² for the inhibited solution. This corresponds to a calculated inhibition efficiency of approximately 24 % and a corresponding increase in linear polarization resistance (LPR) from 19.441 to 25.605 Ohm.cm².

Table 7

Parameters of the electrochemical polarization of the medium carbon steel in 0.2 M HCl with and without 500 ppm of the PTF inhibitor

	LPR, Ohm·cm²	Rest Potential, mV	Area, cm²	*Icorr*, mA/cm²	C.R., mmy
BLANK	19.441	-564.31	0.837	1.3418	15.551
500, PPM	25.605	-560.67	0.837	1.0188	11.807

The slight displacement at the anodic and cathodic ends suggests that PTF acts as a mixed-type inhibitor, though its capacity to suppress the metal dissolution and hydrogen evolution reactions is limited at room temperature after prolonged immersion. The classification of PTF as a mixed-type inhibitor in this study is consistent with the observations of Popović, confirming that most pharmaceutical-based green inhibitors suppress both anodic and cathodic reactions simultaneously [38].

3.4 Computational Studies

3.4.1 Molecular Reactivity

Quantum chemical calculations and molecular dynamics simulation were performed to study inhibition properties of PTF molecules on medium carbon steel corrosion. Various quantum chemical parameters including E_{HOMO}, E_{LUMO}, $\Delta E_{(HOMO-LUMO)}$, electronegativity, softness, hardness, electrophilicity, nucleophilicity and electron affinity were discussed to predict the adsorption property as well as inhibition efficiency of the inhibitor molecules. The chemical reactivity of PTF was investigated by means of frontier molecular orbitals HOMO and LUMO [63]. Co-existence of O, N and π-electron system also increases the inhibitor molecules adsorption capacity on the surface of steel.

Figure 9 presents the optimized molecular structures and the HOMO and LUMO density distributions for the PTF inhibitor molecule. Table 9 provides the calculated quantum chemical descriptors, such as energy gap (ΔE), electronegativity (χ), and fraction of electrons transferred (ΔN). Additionally, Table 10 and Figure 11 detail the results of the Monte Carlo simulations, showing the most stable adsorption configurations of PTF on the Fe (110) surface [52 ،53].

The optimized structures of molecules and HOMO and LUMO distributions of the studied inhibitor are presented in Figure 9.

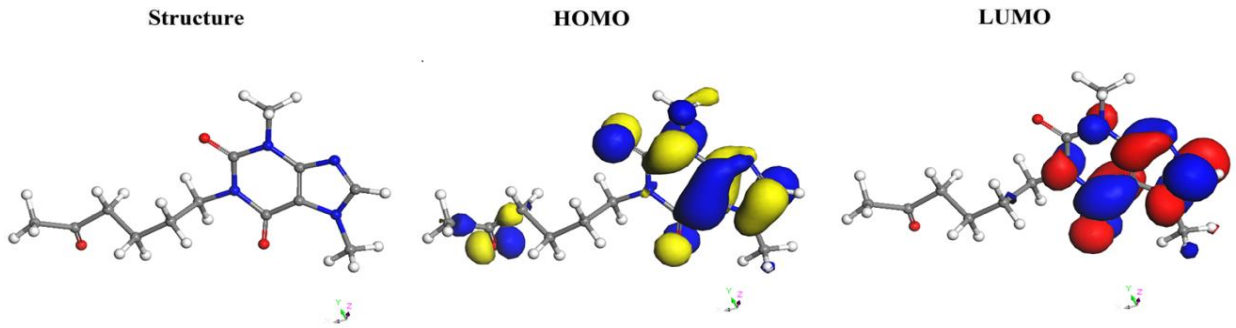

Figure 9. The obtained molecular structure, HOMO and LUMO of the neutral inhibitor molecules using the DFT

Table 8

The net atomic charges of investigated molecule calculated by Mulliken

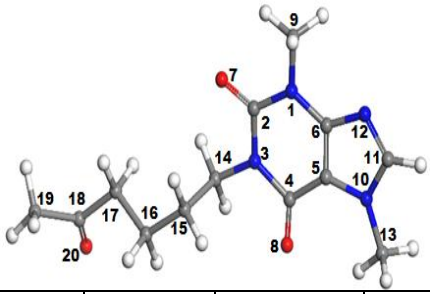

Atom numbering	Mulliken Charge	Atom numbering	Mulliken Charge
N(1)	-0.331	C(11)	-0.057
C(2)	0.558	N(12)	-0.303
N(3)	-0.376	C(13)	0.011
C(4)	0.403	C(14)	-0.082
C(5)	0.126	C(15)	-0.1
C(6)	0.291	C(16)	-0.097
O(7)	-0.499	C(17)	-0.155
O(8)	-0.509	C(18)	0.367
C(9)	0.084	C(19)	-0.208
N(10)	-0.313	O(20)	-0.4

The HOMO density was mainly localized around the oxygen and nitrogen atoms in the PTF molecule and these sites may act as electron donor to the metal surface. On the other hand, the LUMO was pentagonal-shaped and located over two fused heterocyclic π-bond regions. The findings indicate that electron transfer from PTF molecules to the unoccupied *d* orbitals of Fe atoms can be accompanied by a back-donation between the metal surface and the anti-bonding of the inhibitor molecules. Because high electron density, Oxygen and Nitrogen atoms are considered as active adsorption centers. The adsorption active sites of the inhibitor molecules were also identified by Mulliken population analysis. The calculated Mulliken charges of atoms for PTF are listed in Table 8. The identification of nitrogen and oxygen heteroatoms as primary active centers in PTF correlates effectively with the findings of Malki, whose research on quinazolinone derivatives also highlighted these atoms as the key donors for interaction with the iron surface [49].

The result indicated that oxygen atoms, nitrogen atoms and some carbon atoms have negative charge densities, which can provide electrons to the surface of the iron. The atomic charge distribution reveals valuable information on the reactive centres for adsorption. Atoms with higher negative charges can have an enhanced interaction with the empty orbitals of the metal surface [64], this promote the adsorption of inhibitor molecules.

Another critical parameter affecting molecule reactivity and adsorption on metal surfaces is the energy difference between HOMO and LUMO orbitals, ΔE(HOMO-LUMO) [28]. The binding energy was −177.025 eV and the band gap for PTF was 3.477 eV which are given in Table 9. The adsorption of these compounds is also favored by the relatively large negative binding energies which produced stable inhibitor molecules with dominant physical interaction.

Table 9

Calculated quantum chemical parameters for the PTF inhibitor

Theoretical parameters	Value
HOMO, ev	-5.677
LUMO, ev	-2.230
$\Delta E = E_{LUMO} — E_{HOMO}$, eV	3.477
Ionisation, ev	5.677
Affinity, ev	2.23
Electronegativity (χ), eV	3.9535
Hardness (η), ev	1.7385
Softness (σ)	0.5752
Electrons transferred fraction (Δn)	0.87619
Electrophilicity (ω)	4.4953
Binding energy, eV	-177.025

The value of PTFs electronegativity (χ = 3.9535 eV) is also tabulated in Table 9. Electronegativity corresponds to the propensity of molecules to accept that is own electrons [34, 65]. In general, low electronegativity values in metals have been linked to higher inhibition efficacy [66]. The fraction of transferred electrons (ΔN) is also an important quantum quantity. When ΔN is below 3. 6, electrons transfer from the molecule to the metal surface [67]. The computed ΔN value for PTF was 0.87619 eV, suggesting that an electron transfer between inhibitor molecule and steel surface is success and nearly equal to one electron [68].

The electrophylic,ω, can be used as a useful descriptor for molecular reactivity. Species with small electrophilicity values are strong nucleophiles while species with large values of ω are electrophiles. The determined electrophilicity for PTF is 4.4953 eV, which suggest the inhibitor molecule is electrophilic. Moreover, the small magnitude of ionization energy value (I = 5.677 eV) indicates high reactivity of molecule [69], leading to better inhibition efficiency.

Chemical hardness/softness are also useful quantum chemical variables [70]. In general, the smaller the hardness and the higher the softness the better the inhibitors [71]. Calculated value of hardness (η = 1.7385 eV) and softness (σ = 0.5752 eV) of PTF is furnished in Table 9. The bigger hardness with respect to the softness has the physical meaning that the molecule has a rather hard nature.

3.4.2 Monte Carlo Simulation

Molecular dynamics simulation is an excellent modern method to investigate the interaction between inhibitors and metal surface. This study focuses on the use of Monte Carlo simulation to analyse the adsorption of PTF molecules on an Fe (110) surface. In the simulation, a number of key parameters of adsorption are obtained, i.e. the total energy, the adsorption energy, the rigid adsorption energy, and the deformation energy. The parallel orientation of PTF on the Fe(110) surface identified in our Monte Carlo simulations correlates effectively with the configurations reported by Malki for quinazolinone derivatives, proving that such a flat alignment optimizes the interaction of nitrogen and oxygen heteroatoms with the iron lattice [49]. Adsorption energy is the sum of rigid adsorption energy and deformation energy and in the case of adsorption on a steel surface is given in kcal/mol [69, 72, 73]. The adsorption energies for the various adsorption positions of PTF molecules on the Fe (110) surface and with those from Monte Carlo simulation are listed in Table 10. The most stable adsorption configuration is displayed in Figure 10.

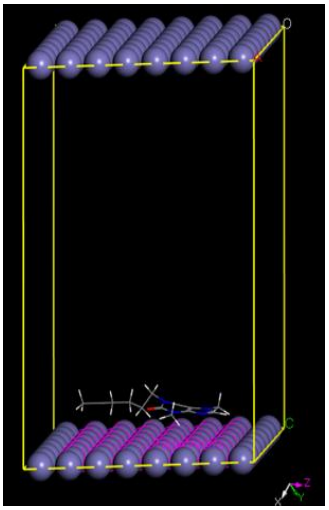

Figure 10. The polymers and descriptors for the lowest adsorption configurations (structure 9) of PTF on the Fe (110) surface obtained by the Monte Carlo simulation.

The parameter (dE_{ads}/dN_i) listed in Table 10 represents the adsorption energy of the steel–adsorbate system after removal of one adsorbate component. The results obtained verify that the chosen adsorption arrangement is the most stable low-energy adsorption configuration for PTF molecules on the surface of Fe (110). The net adsorption energy values were all negative which implied the attraction between inhibitor molecules and the metal is dominated by van der waals forces. In Figure 10, schematic adsorption configurations of single PTF molecules along different directions with the Fe (110) surface are also presented. This Figure shows the most stable equilibrium adsorption structure and the strong interaction between the inhibitor molecules and the metal surface.

Table 10

Outputs and descriptors of the various PTF adsorption configuration structures on Fe (110) calculated by the MC adsorption simulation.

Structures	Total energy, kcal/mol	Adsorption energy, kcal/mol	Rigid adsorption energy, kcal/mol	Deformation energy, kcal/mol	dE_{ad}/d_{Ni}
1	-255.796	-123.463	-128.86	5.399	-123.463
2	-254.715	-122.382	-128.55	6.168	-122.382
3	-254.413	-122.081	-127.522	5.441	-122.081
4	-254.203	-121.87	-127.248	5.378	-121.87
5	-253.928	-121.595	-127.234	5.64	-121.595
6	-253.719	-121.386	-127.2195	5.833	-121.386
7	-253.328	-120.995	-126.679	5.684	-120.995
8	-252.77	-120.437	-125.889	5.452	-120.437
9	-251.428	-119.095	-126.225	7.1296	-119.095

Similarly, in [71] the implication was that planar inhibitor molecules are adsorbed parallel to the metal surface, where electron donation and back-donation, between the inhibitor molecules and metallic surface, dominate the adsorption process [69]. On the other hand, non-planar inhibitor molecules typically exhibit different adsorption behaviour, and for such molecules a straightforward correlation between inhibition efficiency and hardness values can be found.

4 Conclusions

This study establishes pentoxifylline (PTF) as a highly effective and sustainable green corrosion inhibitor for medium carbon steel in 0.2 M HCl, achieving a maximum inhibition efficiency of approximately 90 % at 20 °C and 500 ppm. Experimental investigations reveal that the inhibition mechanism is driven by spontaneous physical adsorption following the Langmuir isotherm, with efficiency decreasing at higher temperatures due to the thermal desorption of the drug film from the steel surface. A significant lesson learned is the potent synergistic effect achieved by combining PTF with iodide ions, which facilitates a more resilient adsorption layer and drastically enhances the protective capacity. These findings are further validated by DFT calculations and Monte Carlo simulations, which identify nitrogen and oxygen heteroatoms as the primary electron-donating centers interacting with the Fe (110) surface. Ultimately, the research confirms that repurposing pharmaceutical molecules offers a non-toxic, cost-effective, and industrially viable strategy for eco-friendly corrosion mitigation.

*Author Information**

**The authors' names are presented in the following order: First Name, Middle Name and Last Name*

Aisha Al-Abbasi (*corresponding author*) — Professor, Candidate of Chemical Sciences, Chemistry Department, Faculty of Science, Sebha University, 071, Sebha, Libya; e-mail: ais.alabbasi@sebhau.edu.ly; https://orcid.org/0000-0002-6082-9246

Hussan Sida — Master Student of Chemical Sciences, Scientific Research Consultation Center, Sebha University, 071, Sebha, Libya; e-mail: hu.sida@sebhau.edu.ly

Hamdy Matter — Associate Professor, Chemistry Department, Faculty of Science, Benghazi University, 061, Benghazi, Libya; e-mail: hamdy.matter@gmail.com, https://orcid.org/0000-0003-3966-566X

Fatima Massoud — Master Student of Chemical Engineering, Chemical Engineering Department, Faculty of Engineering, Sebha University, 071, Sebha, Libya; e-mail: Fati.barka@sebhau.edu.ly

Author Contributions

The manuscript was written through contributions of all authors. All authors have given approval to the final version of the manuscript. CRediT: **Aisha Al-Abbasi:** conceptualization, supervision, methodology, investigation, data curation, validation, writing-original draft, writing-review & editing, and project administration; **Hussan Sida:** investigation, data curation, methodology, visualization, and formal analysis; **Hamdy Matter:** investigation, methodology, and formal analysis related to the electrochemical polarization experiments, as well as interpretation of the electrochemical results; **Fatima Massoud:** investigation and data collection related to the electrochemical polarization experiments.

Acknowledgements

The authors would like to thank the Chemistry Department and Sebha University for providing the laboratory facilities required to carry out this work.

References

1 Al-Abbasi, A. & Sida, H. (2024). Colorimetric evaluation of the corrosion rate of steel in acidic media in the presence of pentoxifylline drug and KI. *Int. J. Corros. Scale Inhib.*, *13*(2), 995-1011. https://doi.org/10.17675/2305-6894-2024-13-2-19

2 Ekeocha, C., Ikenna, O., Etim, I. -I., & Oguzie, E. (2023). Review of forms of corrosion and mitigation techniques: A visual guide. *African Scientific Reports*, 117. https://doi.org/10.46481/asr.2023.2.3.117

3 Al-abbasi, A., Zirik, R., Ahwidi, H., & Massoud, F. (2025). Corrosion Mitigation of Medium Carbon Steel in HCl Solution Using Ficus Carica Leaf Extract: Mass Loss Technique. *Journal of Pure & Applied Sciences 24*(3), 105-109. https://doi.org/10.51984/jopas.v24i3.4199

4 Kumar, N., Anunay, P., Kumar, S., Meena, L. K., & Singh, D. (2026). An overview on emerging green organic corrosion inhibitors: sustainable solution for oil and gas industrial applications. *RSC Advances*, *16*(5), 3909-3948. https://doi.org/10.1039/D5RA08166A

5 Abbas, A., Adesina, A. Y., & Suleiman, R. K. (2023). Influence of Organic Acids and Related Organic Compounds on Corrosion Behavior of Stainless Steel—A Critical Review. Metals, 13(8), 1479. https://doi.org/10.3390/met13081479

6 Dalmora, G. P. V., Borges Filho, E. P., Maraschin Conterato, A. A., Roso, W. S., Pereira, C. E., & Dettmer, A. (2025). Methods of corrosion prevention for steel in marine environments: A review. *Results in Surfaces and Interfaces*, *18*, 100430. https://doi.org/https://doi.org/10.1016/j.rsurfi.2025.100430

7 Khaled, K. F. & Hackerman, N. (2003). Investigation of the inhibitive effect of ortho-substituted anilines on corrosion of iron in 1 M HCl solutions. *Electrochimica Acta*, *48*(19), 2715-2723. https://doi.org/http://dx.doi.org/10.1016/S0013-4686(03)00318-9

8 Bahrami, M. J., Hosseini, S. M. A., & Pilvar, P. (2010). Experimental and theoretical investigation of organic compounds as inhibitors for mild steel corrosion in sulfuric acid medium. *Corros Sci*, *52*. https://doi.org/10.1016/j.corsci.2010.04.024

9 Goulart, C. M., Esteves-Souza, A., Martinez-Huitle, C. A., Rodrigues, C. J. F., Maciel, M. A. M., & Echevarria, A. (2012). Experimental and theoretical evaluation of semicarbazones and thiosemicarbazones as organic corrosion inhibitors. *Corrosion Science*, *67*, 281-291. https://doi.org/http://dx.doi.org/10.1016/j.corsci.2012.10.029

10 Suliman, M. S., & Al-abbasi, A. (2007). The synergistic effect of halide ions and organic nitrogen containing compounds on the inhibition of mild steel corrosion in hydrochloric acid solution. In *Proceedings of the 6th Libyan Corrosion Conference* (Vol. 6). Tripoli, Libya

11 Yadav, M., Kumar, S., Sinha, R. R., Bahadur, I., & Ebenso, E. E. (2015). New pyrimidine derivatives as efficient organic inhibitors on mild steel corrosion in acidic medium: Electrochemical, SEM, EDX, AFM and DFT studies. *Journal of Molecular Liquids*, *211*, 135-145. http://dx.doi.org/10.1016/j.molliq.2015.06.063

12 Al-abbasi, A. A., Mohamed Tahir, M. I., & Kassim, M. B. (2012). N-(Pyrrolidin-1-ylcarbothioyl)benzamide. *Acta Crystallographica Section E*, *68*(1), o201. https://doi.org/doi:10.1107/S1600536811053694

13 Al-abbasi, A. & Kassim, M. (2011). 1-Ethyl-1-methyl-3-(2-nitrobenzoyl)thiourea. *Acta Crystallographica Section E*, *67*(7), o1840. https://doi.org/doi:10.1107/S1600536811024652

14 Al-abbasi, A., Tan, S., & Kassim, M. (2010). 1-Benzoyl-3-(4-hydroxyphenyl)thiourea. *Acta Crystallographica Section E*, *66*(12), o3181. https://doi.org/doi:10.1107/S1600536810045988

15 Belkher, N. A., Al-abbas, A.A., & Zidan, M. (2019). Potentiometric Studies on Stability Constant of the Complexes of SomeEssential Transition Metal Ions with L-Valine. *Journal of Pure & Applied Science 13*(3), 59-63. https://doi.org/10.51984/jopas.v18i3.240

16 Al-abbasi, A., and Shana, I. (2021). Corrosion Inhibition of Mild Steel in Acidic Media by Expired Carbimazole Drug. *Journal of Pure & Applied Sciences*, *20*(2), 176–180. https://doi.org/10.51984/jopas.v20i2.1646

17 AL-abbassi, A., Taher, G., Matrood, E., Dnkm, A., Sallh, A., Izrik, R., & Suliman, M. (2020). Study of the Behavior of Sodium Diclofenac Expired Drug as an Corrosion Inhibitor of Iron in Sulfuric Acid Using UV-VIS Spectrophotometry. International Journal of Scientific Research in Science, Engineering and Technology, 233–242. Internet Archive. https://doi.org/10.32628/ijsrset207248

18 Khalifa, S., AL-abbassi, A., Suliman, M. (2018). Adsorption and Corrosion Inhibition of Mild Steel in Acidic Media by Expired Pharmaceutical Drug. *Journal of Pure & Applied Sciences*, *17*, 1-6. https://doi.org/10.51984/jopas.v17i4.414

19 Al-abbasi, A., Alqasim, Z. A., Rahuma, F., & Mona, H. (2024). Corrosion Inhibition of Reinforced Steel in 3.5 % Sodium Chloride using Expired Pentoxifylline Drug: A Mass Loss Study. *International Science and Technology Journal*, *2*, 1-21. https://doi.org/www.doi.org/10.62341/ISTJ

20 Gece, G. k. (2011). Drugs: A review of promising novel corrosion inhibitors. *Corrosion Science*, *53*(12), 3873-3898. https://doi.org/http://dx.doi.org/10.1016/j.corsci.2011.08.006

21 Njoku, C. N., Maduoma, T. U., Emori, W., Odey, R. E., Unimke, B. M., Yakubu, E., Anorondu, C. C., Udunwa, D. I., Njoku, O. C., & Oyoh, K. B. (2023). Natural and synthetic drugs as eco-friendly and sustainable corrosion inhibitors for metals: a review. Pigment &Amp; Resin Technology, 53(6), 1074–1087. https://doi.org/10.1108/prt-07-2023-0063

22 AL-Abbasi, A. (2006). *Study of corrosion inhibition kinetics of steel by using some organic compounds* [Master's thesis, Sebha University. Sebha University Repository.

23 Al-abbasi, A. S. M., & Milad, A. (2017). The synergistic effects of iodide ions on the corrosion inhibition of mild steel in H2SO4 using phenyl benzoylthiourea. In *Proceedings of the 1st International Conference on Science and Technology*. Sebha, Libya

24 Hazazi, O. A., & Abdallah, M. (2013). Prazole Compounds as Inhibitors for Corrosion of Aluminum in Hydrochloric acid. International Journal of Electrochemical Science, 8(6), 8138–8152. https://doi.org/10.1016/s1452-3981(23)12874-4

25 Elsaeed, S. M., El Tamany, E. S. H., Ashour, H., Zaki, E. G., Khamis, E. A., & El Nagy, H. A. (2018). Corrosion and hydrogen evolution rate control for X-65 carbon steel based on chitosan polymeric ionic liquids: experimental and quantum chemical studies. *RSC Advances*, *8*(66), 37891-37904. https://doi.org/10.1039/C8RA05444D

26 Becke, A. D. (1988). Density-functional exchange-energy approximation with correct asymptotic behavior. Physical Review A, 38(6), 3098–3100. https://doi.org/10.1103/physreva.38.3098

27 Lee, C., Yang, W., & Parr, R. G. (1988). Development of the Colle-Salvetti correlation-energy formula into a functional of the electron density. *Physical Review B, 37*(2), 785. https://doi.org/10.1103/physrevb.37.785

28 Kara, Y. S., Sagdinc, S. G., & Esme, A. (2012). Theoretical study on the relationship between the molecular structure and corrosion inhibition efficiency of long alkyl side chain acetamide and isoxazolidine derivatives. *Protection of Metals and Physical Chemistry of Surfaces*, *48*(6), 710-721. https://doi.org/10.1134/s2070205112060056

29 Sastri, V. S. & Perumareddi, J. R. (1994). Selection of Corrosion Inhibitors for Use in Sour Media. *CORROSION*, *50*(6), 432-437. https://doi.org/doi:10.5006/1.3293521

30 Pearson, R. G. (1988). Absolute electronegativity and hardness: application to inorganic chemistry. *Inorganic Chemistry*, *27*(4), 734-740. https://doi.org/10.1021/ic00277a030

31 Martinez, S. (2003). Inhibitory mechanism of mimosa tannin using molecular modeling and substitutional adsorption isotherms. *Materials Chemistry and Physics*, *77*(1), 97-102. http://dx.doi.org/10.1016/S0254-0584(01)00569-7

32 Khalil, N. (2003). Quantum chemical approach of corrosion inhibition. *Electrochim Acta*, *48*. https://doi.org/10.1016/s0013-4686(03)00307-4

33 Gece, G. (2008). The use of quantum chemical methods in corrosion inhibitor studies. *Corros Sci*, *50*. https://doi.org/10.1016/j.corsci.2008.08.043

34 Parr, R. G., Szentpály, L. V., & Liu, S. (1999). Electrophilicity index. *Journal of the American Chemical Society*, *121*(9), 1922-1924.

35 Khaled, K. F. & El-Maghraby, A. (2010). Experimental, Monte Carlo and molecular dynamics simulations to investigate corrosion inhibition of mild steel in hydrochloric acid solutions. *Arabian Journal of Chemistry*, *7*(3), 319-326. http://dx.doi.org/10.1016/j.arabjc.2010.11.005

36 Musa, A. Y., Jalgham, R. T. T., & Mohamad, A. B. (2011). Molecular dynamic and quantum chemical calculations for phthalazine derivatives as corrosion inhibitors of mild steel in 1 M HCl. *Corrosion Science*, *56*, 176-183. http://dx.doi.org/10.1016/j.corsci.2011.12.005

37 Akinbulumo, O. A., Odejobi, O. J., & Odekanle, E. L. (2020). Thermodynamics and adsorption study of the corrosion inhibition of mild steel by Euphorbia heterophylla L. extract in 1.5 M HCl. *Results in Materials*, *5*, 100074. https://doi.org/10.1016/j.rinma.2020.100074

38 Popović, A. S., Aligayev, A., Trajković, D. V., Jovanović, G., Rakočević, L., & Grgur, B. N. (2026). Coupled experimental and theoretical investigation of an antidiabetic drug as a green corrosion inhibitor for low-carbon steel in acidic media. *Journal of Electroanalytical Chemistry*, *1011*, 120076. https://doi.org/10.1016/j.jelechem.2026.120076

39 Abdul Rahiman, A. F. S. & Sethumanickam, S. (2017). Corrosion inhibition, adsorption and thermodynamic properties of poly(vinyl alcohol-cysteine) in molar HCl. *Arabian Journal of Chemistry*, *10*, S3358-S3366. https://doi.org/10.1016/j.arabjc.2014.01.016

40 Mahmood, A. *et al.* (2025). Corrosion inhibition of steel in acidic solution using p-bromopiperazinylbenzene: Experimental and DFT calculations. *International Journal of Corrosion and Scale Inhibition*, *14*, 706-729. https://doi.org/10.17675/2305-6894-2025-14-2-15

41 Kumar Shukla S., Tanwer, S. (2021). Evaluation of Corrosion inhibition properties of pharmaceutically active compound Cefotaxime sodium on mild steel surface in sulfuric acid medium. Journal of the Turkish Chemical Society Section A: Chemistry, 8(4), 1099–1110. https://doi.org/10.18596/jotcsa.972325

42 Umoren, S. A., Solomon, M. M., Udosoro, I. I., & Udoh, A. P. (2010). Synergistic and antagonistic effects between halide ions and carboxymethyl cellulose for the corrosion inhibition of mild steel in sulphuric acid solution. *Cellulose*, *17*(3), 635-648. https://doi.org/10.1007/s10570-010-9409-7

43 Schorr, M., & Yahalom, J. (1972). The significance of the energy of activation for the dissolution reaction of metal in acids. Corrosion Science, 12(11), 867–868. https://doi.org/10.1016/s0010-938x(72)80015-5

44 Ebenso, E. E., & Obot, I. B. (2010). Inhibitive Properties, Thermodynamic Characterization and Quantum Chemical Studies of Secnidazole on Mild Steel Corrosion in Acidic Medium. International Journal of Electrochemical Science, 5(12), 2012–2035. https://doi.org/10.1016/s1452-3981(23)15402-2

45 Ebenso, E. E. (2003). Synergistic effect of halide ions on the corrosion inhibition of aluminium in H2SO4 using 2-acetylphenothiazine. *Materials Chemistry and Physics*, *79*(1), 58-70. https://doi.org/10.1016/S0254-0584(02)00446-7

46 Deyab, M. A., & El-Rehim, S. S. A. (2014). Effect of succinic acid on carbon steel corrosion in produced water of crude oil. Journal of the Taiwan Institute of Chemical Engineers, 45(3), 1065–1072. https://doi.org/10.1016/j.jtice.2013.09.004

47 Deyab, M. A. (2015). Egyptian licorice extract as a green corrosion inhibitor for copper in hydrochloric acid solution. Journal of Industrial and Engineering Chemistry, 22, 384–389. https://doi.org/10.1016/j.jiec.2014.07.036

48 Obot, B., Obi-Egbedi, N. O., & Umoren, S. A. (2009). Experimental and theoretical investigation of clotrimazole as corrosion inhibitor for aluminium in hydrochloric acid and effect of iodide ion addition. *Der Pharma Chemica*, *1*(1), 151-166.

49 Hashim, N. M., Rahim, A. A., Osman, H., & Raja, P. B. (2012). Quinazolinone compounds as corrosion inhibitors for mild steel in sulfuric acid medium. Chemical Engineering Communications, 199(6), 751–766. https://doi.org/10.1080/00986445.2011.617801

50 Abdel Hameed, R., Essa, A., Mohamed, D., Abdallah, M., Aljohani, M., Al-Mhyawi, S., Soluman, M., & Arafa, E. (2021). Evaluation of Expired Augmentine Drugs as Corrosion Inhiitor for Carbon Steel Alloy in 1.0 n hcl Acidic Environment Using Analytical Techniques. *Egyptian Journal of Chemistry*, *65*(4), 735-745. https://doi.org/10.21608/ejchem.2021.95853.4495

51 Feng, L., Zhang, S., Zhou, Y., Pan, R., Du, H., Liu, F., & Yang, Y. (2023). Expired Glucosamine Drugs as Green Corrosion Inhibitors for Carbon Steel in H2SO4 Solution and Synergistic Effect of Glucosamine Molecules with Iodide Ions: Combined Experimental and Theoretical Investigations. *Crystals*, 13(2), 205. https://doi.org/10.3390/cryst13020205

52 Kur'yato, L. E. T. a. V. A. (2025). Anticorrosive, antihydrogenating and bactericidal effects of a number of expired drugs. *International Journal of Corrosion and Scale Inhibition*, 14(4). https://doi.org/10.17675/2305-6894-2025-14-4-6

53 Wang, X., Yang, H., & Wang, F. (2011). An investigation of benzimidazole derivative as corrosion inhibitor for mild steel in different concentration HCl solutions. *Corrosion Science*, *53*(1), 113-121. https://doi.org/10.1016/j.corsci.2010.09.029

54 Zhang, H. -h., Gao, K., Yan, L., & Pang, X. (2017). Inhibition of the corrosion of X70 and Q235 steel in CO2-saturated brine by imidazoline-based inhibitor. *Journal of Electroanalytical Chemistry*, *791*, 83-94. https://doi.org/10.1016/j.jelechem.2017.02.046

55 Zheng, T., Liu, J., Wang, M., Liu, Q., Wang, J., Chong, Y., & Jia, G. (2022). Synergistic corrosion inhibition effects of quaternary ammonium salt cationic surfactants and thiourea on Q235 steel in sulfuric acid: Experimental and theoretical research. Corrosion Science, 199, 110199. https://doi.org/10.1016/j.corsci.2022.110199

56 Ali, S. M. & Al Lehaibi, H. A. (2016). Control of zinc corrosion in acidic media: Green fenugreek inhibitor. *Transactions of Nonferrous Metals Society of China*, *26*(11), 3034-3045. https://doi.org/10.1016/S1003-6326(16)64434-5

57 Mohamed, K. E. M., Ibrahim, O. H., El-Bedawy, M. E., & Ali, A. H. (2020). Synergistic effect of different Zn salts with sodium octanoate on the corrosion inhibition of carbon steel in cooling water. *Journal of Radiation Research and Applied Sciences*, *13*(1), 276-287. https://doi.org/10.1080/16878507.2020.1730603

58 Khadom, A. A., Abd, A. N., & Ahmed, N. A. (2022). Synergistic effect of iodide ions on the corrosion inhibition of mild steel in 1 M HCl by Cardaria Draba leaf extract. *Results in Chemistry*, *4*, 100668. https://doi.org/10.1016/j.rechem.2022.100668

59 Tang, M., Li, X., Deng, S., & Lei, R. (2021). Synergistic inhibition effect of Mikania micrantha extract with KI on steel corrosion in H2SO4 solution. *Journal of Molecular Liquids*, *344*, 117926. https://doi.org/10.1016/j.molliq.2021.117926

60 Oza, B. N., Sinha, R.S. (1982). Thermometric study of corrosion behaviour of high strength Al–Mg alloy in phosphoric acid in presence of halides. *Trans SAEST*, *17*(1), 281–285.

61 El-Awady, A. A., Abd-El-Nabey, B. A., & Aziz, S. G. (1992). Kinetic-Thermodynamic and Adsorption Isotherms Analyses for the Inhibition of the Acid Corrosion of Steel by Cyclic and Open-Chain Amines. Journal of the Electrochemical Society, 139(8), 2149–2154. https://doi.org/10.1149/1.2221193

62 Ituen, E., Akaranta, O., & James, A. (2017). Evaluation of Performance of Corrosion Inhibitors Using Adsorption Isotherm Models: An Overview. *Chemical Science International Journal*, *18*, 1-34. https://doi.org/10.9734/CSJI/2017/28976

63 Madkour, L. H. & Elshamy, I. H. (2016). Experimental and computational studies on the inhibition performances of benzimidazole and its derivatives for the corrosion of copper in nitric acid. *International Journal of Industrial Chemistry*, *7*(2), 195-221. https://doi.org/10.1007/s40090-015-0070-8

64 Yang, W. & Parr, R. G. (1985). Hardness, softness, and the fukui function in the electronic theory of metals and catalysis. *Proc Natl Acad Sci U S A*, *82*(20), 6723-6. https://doi.org/10.1073/pnas.82.20.6723

65 Chattaraj, P. K., Sarkar, U., & Roy, D. R. (2006). Electrophilicity Index. *Chemical Reviews*, *106*(6), 2065-2091. https://doi.org/10.1021/cr040109f

66 Zarrouk, A., Hammouti, B., Dafali, A., Bouachrine, M., Zarrok, H., Boukhris, S., & Al-Deyab, S. S. (2014). A theoretical study on the inhibition efficiencies of some quinoxalines as corrosion inhibitors of copper in nitric acid. *Journal of Saudi Chemical Society*, 18(5), 450–455. https://doi.org/10.1016/j.jscs.2011.09.011

67 Martinez, S., & Štagljar, I. (2003). Correlation between the molecular structure and the corrosion inhibition efficiency of chestnut tannin in acidic solutions. *Journal of Molecular Structure: THEOCHEM*, 640(1-3), 167–174. http://dx.doi.org/10.1016/j.theochem.2003.08.126

68 Lukovits, I., Kálmán, E., & Pálinkás, G. (1995). Nonlinear Group-Contribution Models of Corrosion Inhibition. *Corrosion*, 51(3), 201–205. https://doi.org/10.5006/1.3294362

69 Khaled, K. F. (2009). Experimental and atomistic simulation studies of corrosion inhibition of copper by a new benzotriazole derivative in acid medium. *Electrochimica Acta*, *54*(18), 4345-4352. http://dx.doi.org/10.1016/j.electacta.2009.03.002

70 Kaya, S. & Kaya, C. (2015). A new method for calculation of molecular hardness: A theoretical study. *Computational and Theoretical Chemistry*, *1060*, 66-70. https://doi.org/10.1016/j.comptc.2015.03.004

71 Ebenso, E. E., Isabirye, D. A., & Eddy, N. O. (2010). Adsorption and quantum chemical studies on the inhibition potentials of some thiosemicarbazides for the corrosion of mild steel in acidic medium. *Int J Mol Sci*, *11*. https://doi.org/10.3390/ijms11062473

72 Zeng, J., Zhang, J., & Gong, X. Molecular dynamics simulation of interaction between benzotriazoles and cuprous oxide crystal. *Computational and Theoretical Chemistry*, *963*(1), 110-114. http://dx.doi.org/10.1016/j.comptc.2010.10.006

73 Znini, M., Majidi, L., Bouyanzer, A., Paolini, J., Desjobert, J.M., & Costa, J., Hammouti, B. (2012). Essential oil of Salvia aucheri mesatlantica as a green inhibitor for the corrosion of steel in 0.5 M H2SO4. *Arabian Journal of Chemistry*, *5*(4), 467-474. https://doi.org/10.1016/j.arabjc.2010.09.017

How to Cite: Ahmed, A.A., & Mohammed, M.A. (2026). Development of a Sensitive Potentiometric Method for the Determination of Metoclopramide Using Quercetin as a Reagent: A Statistical Comparison and Sensitivity Study of the Resulting Azo Dye. *Eurasian Journal of Chemistry, 31, 3(123), 86–97.* https://doi.org/10.31489/2959-0663/3-26-11

Article

Received: 24 June 2026 | Revised: 28 August 2026 | Accepted: 7 September 2026 | Published online: 14 September 2026

UDC 544.42+519.242.7

https://doi.org/10.31489/2959-0663/3-26-11

Alaa A. Ahmed[1*], Maha A. Mohammed[2]

[1]*Department of Chemistry, Second Karkh Education Directorate, Ministry of Education, Baghdad, Iraq*
[2]*Department of Chemistry, College of Education for Pure Science (Ibn Al-Haitham), University of Baghdad, Baghdad, Iraq*
*(*Corresponding author's e-mail: alaa.abed1105a@ihcoedu.uobaghdad.edu.iq)*

Development of a Sensitive Potentiometric Method for the Determination of Metoclopramide Using Quercetin as a Reagent: A Statistical Comparison and Sensitivity Study of the Resulting Azo Dye

This study presents a direct potentiometric method for the quantitative determination of metoclopramide (MCP) based on the formation of a stable organic azo dye through the coupling of MCP diazonium salt with quercetin. The chromophore was monitored using a dual-platinum electrode over a concentration range of 2.0−20.0 μg·mL^{-1}, exhibiting an inverse linear relationship between the electrode potential and the logarithm of MCP concentration. The calibration equation was E = 70.517−36.276 log C (R^2 = 0.9601). Transient sensitivity analysis identified a localized near-Nernstian region at 2.0−4.0 μg·mL^{-1} with a slope of −58.90 mV per log C, whereas the overall working range exhibited a highly reproducible empirical non-Nernstian response. Information-theoretic analysis yielded a mutual information value, *I(C; E)*, of 1.89 bits, corresponding to 57 % of the theoretical maximum information capacity. Based on ten independent blank measurements (σ = 0.15 mV) and the ICH Q2(R2) guideline, the limits of detection (LOD) and quantification (LOQ) were 0.253 and 0.767 μg·mL^{-1}, respectively, with a repeatability of RSD=2.62 %. The proposed double platinum potentiometric configuration provides a rapid, simple, low-cost electroanalytical approach for the direct quantitative determination of metoclopramide.

Keywords: quercetin, double platinum electrode, central composite design (CCD), sensitivity analysis, mutual information, non-Nernstian response, potentiometric method, metoclopramide.

1 Introduction

Metoclopramide (MCP) is a potent dopamine D_2 receptor antagonist widely used to stimulate gastrointestinal motility and to treat nausea and vomiting [1]. Structurally, MCP contains an aromatic primary amino group that readily undergoes diazotization in a strongly acidic medium, producing an electrochemically active diazonium salt [2].Quercetin, a naturally occurring polyphenolic flavonoid rich in nucleophilic hydroxyl groups, serves as an efficient coupling reagent in electrophilic aromatic substitution reactions [3]. Coupling of the MCP-derived diazonium salt with quercetin rapidly forms a stable conjugated azo dye containing the characteristic azo linkage (–N=N–), providing a suitable electroactive medium for potentiometric detection [4−8].Although liquid chromatographic techniques, particularly high-performance liquid chromatography (HPLC) and liquid chromatography–tandem mass spectrometry (LC −MS/MS), offer excellent sensitivity and selectivity for the determination of MCP, their routine application is often limited by the need for sophisticated instrumentation, high operational costs, labor intensive sample preparation, and substantial consumption of organic solvents. Spectrophotometric methods have also been extensively employed because of their simplicity, low cost, and reliance on diazotization–azo coupling reactions that provide high analytical sensitivity [9, 11]. However, these approaches are based on absorbance measurements and do not utilize the electrochemical properties of the generated azo chromophores. Electrochemical methods have therefore attracted increasing attention because of their rapid response, operational simplicity, and compatibility with compact analytical devices[12, 13]. Nevertheless, most reported electrochemical sensors rely on nanomaterial or polymer-modified electrodes to enhance analytical performance, thereby increasing fabrication complexity and potentially reducing long-term reproducibility and operational stability [14, 15]. Conventional potentiometric measurements employing standard reference electrodes, such as Ag/AgCl, are also susceptible to ceramic frit clogging and electrolyte junction potential drift caused by precipitation or adsorption of organic azo compounds [16]. Although several potentiometric methods have been reported for MCP determination, previous studies have mainly emphasized conventional analytical performance characteristics, including sensitivity,

© 2026 The Authors. This is an open access article under the CC BY-NC-ND license (http://creativecommons.org/licenses/by-nc-nd/4.0/)

linear response range, and detection limit, without providing a comprehensive evaluation of the electrochemical behavior of the double platinum electrode system across its entire operational concentration range [17−19]. Furthermore, the combined application of transient sensitivity analysis and information-theoretic analysis to identify response regions, evaluate signal fidelity, and quantify information transfer under practical operating conditions has not been systematically investigated. Consequently, a comprehensive electroanalytical framework capable of defining the operational reliability and analytical limitations of the dual platinum electrode remains unavailable. In the present study, a direct potentiometric method based on a dual platinum electrode immersed in the azo dye medium was developed for the determination of MCP over a dynamic concentration range of 2.0−20.0 $\mu g \cdot mL^{-1}$ interval. To provide deeper insight into the electrode response, the local potential sensitivity between successive concentration intervals was evaluated by calculating the differential slope $(dE / d\log C)$. In addition, mutual information analysis $(I(C;E))$ was employed to quantify the concentration-dependent information contained in the potentiometric signal, thereby providing complementary information beyond that obtained from the coefficient of determination (R^2) alone [20−22]. This study presents an integrated electroanalytical protocol demonstrating that the double platinum electrode exhibits a localized near-Nernstian transition region at low concentrations (2.0–4.0 $\mu g \cdot mL^{-1}$), whereas the broader concentration range is characterized by a highly reproducible empirical non-Nernstian response, thereby defining the operational limits of reliable sensor performance for the direct quantitative determination of metoclopramide.

2 Experimental

2.1. Instrumentation

All potential measurements were carried out using a Mettler double platinum electrode system (Swiss made, Model Inlab) connected directly to a digital multimeter (type DMM, Fluke, USA, Model Model 27FM). Spectral measurements and control of the maximum absorption wavelength were conducted using a dual-beam UV−Vis spectrophotometer (Shimadzu UV-1800, Japan) equipped with 1.0 cm quartz cuvettes to determine the maximum absorption wavelength (λ_{max}) and to optimize the azo dye formation conditions using the Central Composite Design (CCD).Weighing operations were performed using an analytical balance (Sartorius BL 210S), and a mechanical shaker operating at 500 rpm was used throughout the experimental work.

2.2. Chemicals and Reagents

All chemicals and reagents were of high analytical purity. Quercetin (99.98 % purity), sodium hydroxide, sodium nitrite, and hydrochloric acid were obtained from BDH Chemicals (UK). Absolute ethanol (99.9 % purity) was obtained from Sigma-Aldrich (Germany). Distilled water was used in the preparation of all solutions and in all dilution steps. The reference standard, metoclopramide (MCP), was supplied as a pure powder by the State Company for Pharmaceutical Industries and Medical Appliances (SDI) in Samarra, Iraq.

2.3. Preparation of Standard and Working Solutions

2.3.1. Quercetin Stock Solution

A stock solution of quercetin (1000 $\mu g \cdot mL^{-1}$) was prepared by accurately weighing 0.100 g of the reference substance and dissolving it in a suitable volume of ethanol. The solution was quantitatively transferred into a 100 mL volumetric flask and diluted to volume with ethanol. Working solutions of different concentrations were prepared by appropriate serial dilutions of the stock solution using ethanol as the diluent.

2.3.2. Metoclopramide Hydrochloride (MCP) Stock Solution

A stock solution of metoclopramide hydrochloride (1000 $\mu g \cdot mL^{-1}$) was prepared by accurately weighing 0.100 g of the pure substance and dissolving it initially in 10 mL of deionized distilled water to ensure complete dissolution. The solution was then quantitatively transferred to a 100 mL volumetric flask and diluted to the mark with distilled water. Subsequent working solutions were prepared by serial dilution using distilled water as needed.

2.3.3. Preparation of Auxiliary Reagents

Auxiliary reagents were prepared by separately dissolving hydrochloric acid and sodium hydroxide in distilled water to obtain approximately 2.0 M HCl and 2.0 M NaOH solutions, respectively. Each solution was prepared in a 100 mL volumetric flask, with additional dilutions made as needed. A sodium nitrite solution (100 $\mu g \cdot mL^{-1}$) was prepared by dissolving 0.010 g of sodium nitrite in distilled water and diluting to 100

mL in a volumetric flask. Further dilutions were carried out as required. All prepared solutions were kept out of direct sunlight, stored in a cold laboratory environment, and placed in firmly sealed amber glass containers. Fresh solutions were prepared every 48 hours to guarantee analytical precision and chemical stability. Specifically, hydrochloric acid (HCl) and sodium nitrite ($NaNO_2$) serve as the essential reagents for diazotization, converting the primary aromatic amino group of MCP into the highly reactive diazonium intermediate. Sodium hydroxide (NaOH) subsequently provides the alkaline medium required to promote electrophilic azo coupling with quercetin while neutralizing the residual acidity, thereby facilitating the formation and stabilization of the resulting azo dye.

2.4. Preliminary Investigation and Determination of Maximum Absorption Wavelength (λ_{max})

The maximum absorption wavelength (λ_{max}) of the coloured azo coupling product was ascertained by preliminary investigations using the UV−Vis spectrophotometer. To create the appropriate diazonium salt, MCP was first diazotized using sodium nitrite in an acidic solution at a low temperature (0–5 ^{o}C). Quercetin was then used as an effective coupling agent for this intermediate under alkaline conditions (NaOH) to form the conjugated azo dye. Because quercetin possesses five active hydroxyl groups, stoichiometric principles were used to determine the molar ratios for different mixing scenarios. The reaction conditions were optimized experimentally using the Central Composite Design (CCD), and the absorption spectrum of the final reaction mixture showed a maximum absorption wavelength (λ_{max}) at 426 nm. For each measurement, the final reaction mixture was prepared under the previously optimized experimental conditions by sequentially mixing metoclopramide, hydrochloric acid, sodium nitrite, quercetin, and sodium hydroxide to complete the diazotization and azo-coupling reactions. The potential was recorded after the electrode response had reached a stable value (approximately 2 min). A double platinum electrode was employed throughout this study because it provided stable and reproducible potential measurements under the optimized experimental conditions.

2.5. Potentiometric Measurements

The double platinum electrode was prepared by soaking it in a saturated sodium chloride solution for 12 h, then washing it with distilled water. For connection, the dual platinum electrode was connected to the millivolt meter by connecting the blue wire to the COM port and the red wire to the voltage/resistance port (VΩ). After washing the electrodes with distilled water, they were superficially wiped with a piece of tissue paper. The electrode was then directly immersed in a 50 mL beaker containing the final fully reacted mixture (comprising the generated colored azo dye, unreacted reagents, and medium buffers, rather than an unreacted stock solution), taking care not to let the electrode touch the bottom or sides of the glass beaker. The reading was recorded after exactly 2 min. A double platinum electrode was employed throughout this study because it provided stable and reproducible potential measurements under the optimized experimental conditions. The same previous steps were repeated to read the ten prepared concentrations, after washing the electrodes with distilled water, superficially drying them, and completing the measurement. The voltage measurements were recorded for subsequent analyses.

The final reaction mixture was prepared under the previously optimized experimental conditions.

2.6. Mutual Information Analysis

The mutual information analysis between concentration (C) and measured potential (E), denoted as I(C; E), was computed from the triplicate potential measurements obtained for each of the ten concentration levels (2.0–20.0 $\mu g \cdot mL^{-1}$). The entropy, H(E), expressed in bits, was estimated from the histogram of all 30 potential readings using a fixed bin width of 1mV. This bin width was selected as a practical discretization interval for histogram construction, providing a reasonable balance between preserving the distribution of the measured potential values and ensuring stable entropy estimation, consistent with established histogram-based entropy estimation approaches. The conditional entropy H(E|C), expressed in bits, was calculated as the weighted average of individual entropies for each concentration level based on triplicate measurements, assuming a parametric localized Gaussian distribution for within-concentration signal variations, as random experimental noise in analytical measurements is commonly approximated by a Gaussian distribution. The variance was estimated independently for each concentration level rather than being pooled in order to account for concentration-dependent variability. The mutual information was then obtained using the following equation:

$$I(C;E) = H(E) - H(E/C) \quad (1)$$

The maximum possible information content for ten equally probable concentrations is $\log_2(10) = 3.32$ bits.

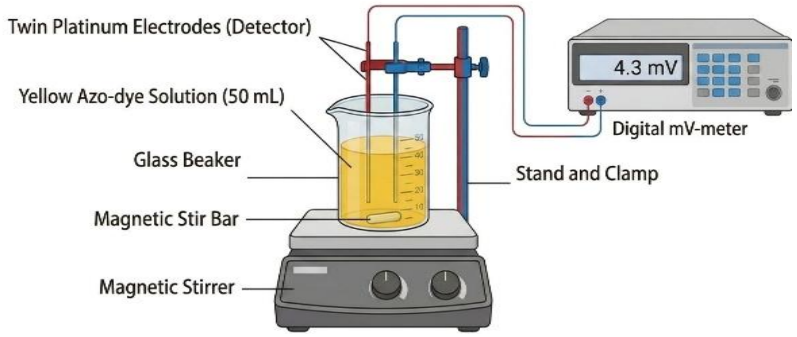

Scheme 1. Schematic of bipotentiometric cell for azo-dye stability study. Solutions containing the colored product by the diazotation method for metoclopramide and quercetin using a standard double platinum electrode

3 Results and Discussion

3.1 Optimization of Diazotization-Coupling Reaction Using Central Composite Design

A Central Composite Design (CCD)] 22], was applied to optimize the three independent variables affecting the diazotization-coupling reaction of MCP: MCP concentration (X_1, μg·mL $^{-1}$), $NaNO_2$ volume (X_2, mL), and diazotization time (X_3, min). The response was the absorbance at 426 nm. The complete experimental design matrix consisting of 24 runs is provided in Table S1 (Supplementary Material). The experimental data were fitted to a second-order polynomial (quadratic) model. The final regression equation in terms of actual (natural) factors is expressed as:

$$A = -0.123 + 0.0012X_1 + 0.045X_2 + 0.008X_3 - 0.000045X_1X_2 + 0.000011X_1X_3 - \\ -0.0028X_2X_3 - 0.0000008X_1^2 - 0.028X_2^2 - 0.00104X_3^2 \quad (2)$$

The goodness-of-fit statistics for this model are summarized in Table 1. The coefficient of determination ($R^2 = 0.973$) indicates that the model explains 97.3 % of the total variance. The adjusted R^2 (0.956) and predicted R^2 (0.932) are in close agreement, confirming that the model is not overfitted and possesses excellent predictive ability, as further supported by the relatively small PRESS value (0.0087).

Table 1

Goodness-of-fit statistics for the quadratic response surface model

Metric	Value
R^2 (Coefficient of determination)	0.9730
Adjusted R^2	0.9560
Predicted R^2	0.9320
PRESS (Predicted Residual Sum of Squares)	0.0087
CV% (Coefficient of Variation)	3.55 %
RMSE (Root Mean Square Error)	0.0198

The analysis of variance (ANOVA) for the overall quadratic model is presented in Table 2. The model F-value of 58.40, with a p-value < 0.0001, indicates that the model is highly significant. Furthermore, the lack-of-fit test yielded an F-value of 1.87 with a p-value = 0.153 ($p > 0.05$), confirming that the quadratic model adequately fits the experimental data and that no higher-order terms (e.g., cubic terms) are required. The coefficient of variation (CV = 3.55 %) and the root mean square error (RMSE = 0.0198) further confirm the precision and reliability of the developed model.

Table 2

Analysis of variance (ANOVA) for the quadratic response surface model

Source	SS	Df	MS	F-value	p-value
Model	0.2125	9	0.0236	58.40	< 0.0001
Error	0.0056	14	0.0004	-	-
Total	0.2181	23	-	-	-

To verify the underlying assumptions of regression analysis, a comprehensive residual analysis was performed, and the diagnostic plots are illustrated in Fig. 1. The normal probability plot (Fig. 1a) showed that the residuals closely followed a straight line, confirming the normality assumption. The plot of residuals versus fitted values (Fig.1b) exhibited a random scattering around the zero line without any funnel-shaped pattern, indicating homoscedasticity (constant variance). The residuals versus run order plot (Fig.1c) revealed no systematic trends or periodic oscillations, confirming the independence of the residuals. Additionally, all Cook's distance values were below 0.5, and all leverage values were below the critical threshold (2p/n = 0.83), confirming the absence of influential outliers. These diagnostic checks collectively confirm that the quadratic model is statistically valid and stable.

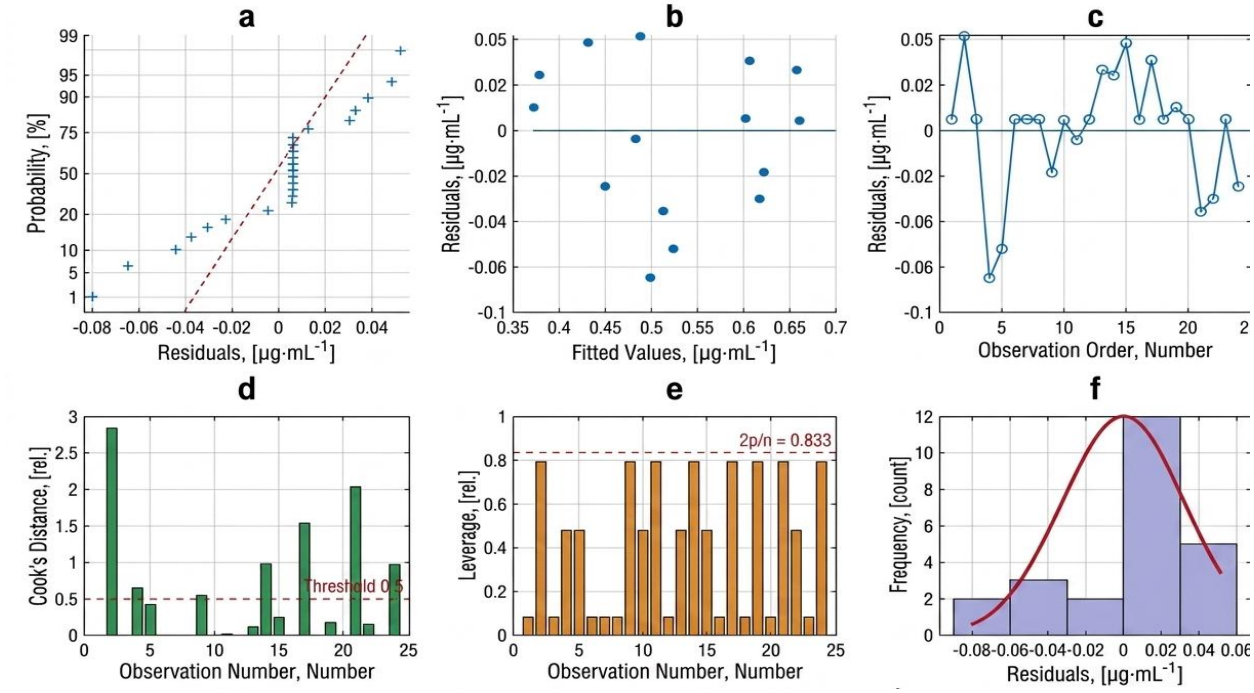

Figure 1. Diagnostic plots for residual analysis: (a) Normal probability plot, (b) residuals vs. fitted values, (c) residuals vs. run order, (d) Cook's distance and leverage

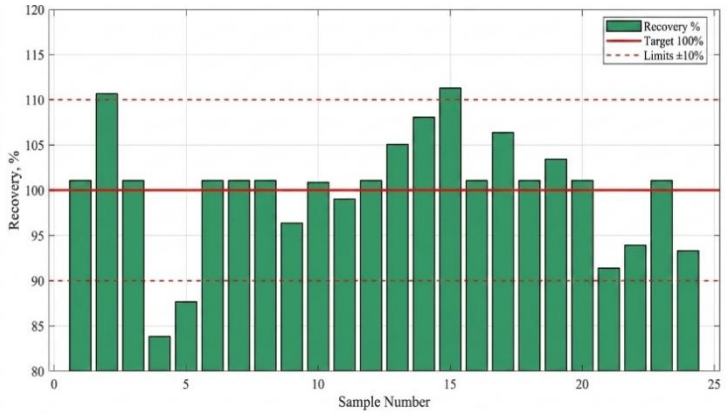

Figure 2. Accuracy and tuning for each CCD model run

To further evaluate the predictive capability and experimental reliability of the CCD model, the recovery percentages for all 24 experimental runs were calculated and are presented in Fig. 2. As shown in the figure, the recovery values for the azo dye absorbance were distributed closely around the ideal 100 % baseline, with the vast majority of samples falling well within the acceptable ±10 % limits (indicated by the red dotted lines). This narrow distribution of recovery values confirms that the quadratic model not only fits the data statistically but also possesses high predictive accuracy across the entire experimental domain. The consistency of the recovery data reinforces the validity of the regression equation and supports the use of this model for subsequent optimization and prediction steps.

The interactive effects of the three independent variables on the absorbance at 426 nm were visualized using three-dimensional response surface plots, as illustrated in Fig. 3. The figure comprises three separate surfaces: (a) at a fixed diazotization time (TD = 10 min), showing the combined effect of MCP concentration and $NaNO_2$ volume; (b) at a fixed $NaNO_2$ volume (2 mL), illustrating the interaction between MCP concentration and time; and (c) at a fixed MCP concentration (50 μg·mL^{-1}), depicting the influence of $NaNO_2$ volume and time on the absorbance. Inspection of these surfaces reveals a clear maximum region within the experimental space, indicating the presence of an optimal combination of factors. The elliptical contours observed in some surfaces suggest moderate interactions between the variables, which is consistent with the significant interaction terms (X_1X_2 and X_1X_3) identified in the ANOVA analysis (TABLE II). The highest absorbance values are concentrated around the center points of the design ($X_1 \approx 50$ μg·mL^{-1}, $X_2 \approx 2$ mL, $X_3 \approx 10$ min), which visually confirms the numerical optimization result.

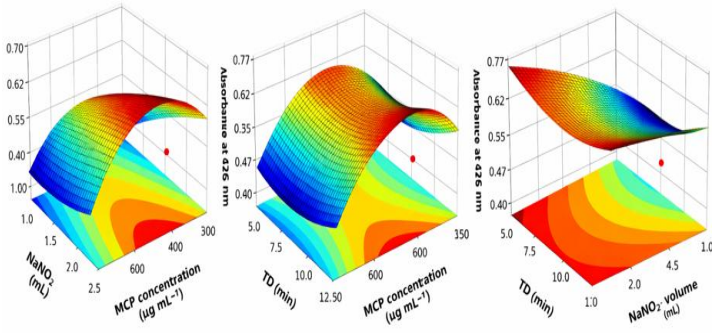

Figure 3. Response surface plots showing the effect of independent variables (X_1: MCP concentration, X_2: $NaNO_2$ volume, X_3: diazotization time) on the absorbance of the azo dye at 426 nm: (a) X_1 vs. X_2 at fixed X_3; (b) X_1 vs. X_3 at fixed X_2; (c) X_2 vs. X_3 at fixed X_1

Optimization employing central composite design (CCD) successfully identified the statistically validated conditions that maximized the absorbance response, which were determined to be X_1 = 50 μg·mL^{-1} (MCP concentration), X_2= 2 mL ($NaNO_2$ volume), and X_3= 10 min (diazotization time).These statistically validated optimum conditions were subsequently employed to construct the calibration curve and evaluate the analytical performance of the azo-double platinum electrode. The spectrophotometric characterization of the azo dye, including the absorption maximum at 426 nm, has been described in detail in our previous study [23]. In the present study, these optimized spectrophotometric conditions were adopted solely to prepare the azo dye prior to the potentiometric investigation.

3.2 Electrochemical Calibration and Analytical Validation

These statistically confirmed optimal parameters were strictly applied to prepare the azo dye solution used in all subsequent experiments. The concentration range of 2.0–20.0 μg·mL^{-1} was selected because it corresponded to the optimized concentration interval established for azo dye formation under the selected experimental conditions, thereby ensuring consistent reaction conditions throughout the potentiometric measurements. Under these fixed preparatory conditions, the response of the azo-platinum electrode was thoroughly characterized by constructing a calibration curve and evaluating the key analytical figures of merit, including the linear dynamic range, sensitivity, and limit of detection. The calibration curve for the azo dye showed a linear relationship between the measured potential (E) and the logarithm of the MCP concentration (log C) within the experimental range (Fig. 4). Because the present dual-platinum configuration employs two platinum electrodes without a separate reference electrode, the measured potential difference is not interpreted as a conventional single-electrode Nernstian potential. Accordingly, the overall experimental

slope of −36.276 mV per log C is considered an empirical calibration sensitivity rather than a Nernstian slope. Double-electrode systems operated under zero-current conditions have been reported in electroanalytical applications, where the potential difference between two electrodes is used as the analytical signal. Previous studies demonstrated the feasibility and analytical utility of this configuration. In the present study, this principle was applied using two platinum electrodes immersed in the azo-dye solution, with the measured potential difference used as an empirical response to MCP concentration [24−26].

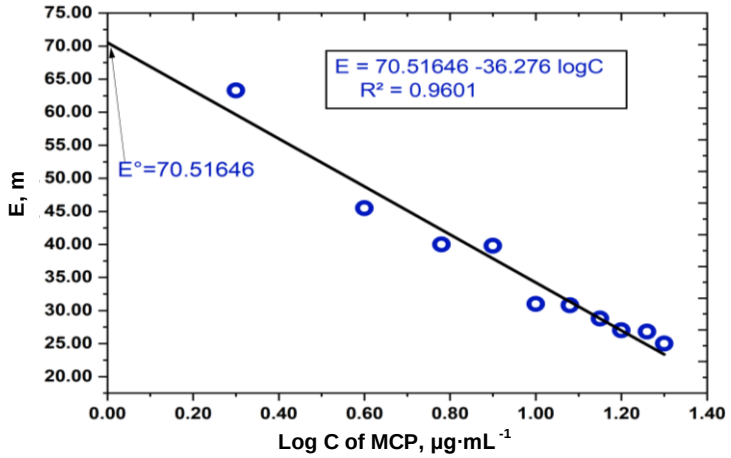

Figure 4. Calibration curve of the azo-modified platinum electrode showing the relationship between measured potential (E / mV) and logarithm of MCP concentration (µg·mL^{-1}) under optimal conditions.

The calibration data in Table 3 show a linear relationship (R^2 = 0.960, R = −0.980) with a slope of −36.276 ± 2.615 mV per log C in the concentration range of 2.0–20.0 µg·mL^{-1}. Statistical parameters confirmed the reliability of the regression: t_{calc} =13.870, F_{calc} =192.500, and RSD%=2.62 %.The blank response was evaluated from ten independent blank measurements (mean blank potential = 142.20 mV), and the corresponding standard deviation (σ = 0.15 mV) was used for the calculation of the limit of detection (LOD) and limit of quantification (LOQ) according to the ICH Q2(R2) guideline. The LOD and LOQ were 0.253 and 0.767 µg·mL^{-1}, respectively, with standard errors of slope and intercept (S_b= 2.615, S_a= 2.625), suggesting good precision. Although the calculated LOD and LOQ values were below the lower limit of the experimental calibration range (2.0 µg·mL^{-1}), these values represent statistical estimates of the detection and quantification capability and do not establish an experimentally validated linear calibration response below 2.0 µg·mL^{-1}. Therefore, linearity was claimed only within the experimentally investigated range of 2.0–20.0 µg·mL^{-1}. The mean blank potential of 142.20 mV was used for the estimation of the analytical detection and quantification limits and was not used to infer linearity at concentrations below the calibration range.

Table 3

Analytical parameters for the determination of MCP using the dual platinum electrode

No.	Parameter	Symbol	Value
1	Linear Range, µg·mL^{-1}	—	2.0 − 20.0
2	Regression Equation	—	E = 70.517−36.276 log C
3	Slope, mV per log C	B	−36.276 ± 2.615
4	Intercept, mV	A	70.517± 2.625
5	Coefficient of determination	R^2	0.9601
6	Correlation coefficient	R	−0.9798
7	Adjusted R^2	R^2_{adj}	0.9551
8	Limit of Detection, µg·mL^{-1}	LOD	0.253
9	Limit of Quantification, µg·mL^{-1}	LOQ	0.767
10	Standard error of slope	S_b	2.615
11	Standard error of intercept	S_a	2.625
12	RSD, %	RSD%	2.620 %
13	t-test statistic (slope)	t_{calc}	13.873
14	F-test statistic (regression)	F_{calc}	192.457

Table 4 shows relative error (RE%) values ranging from −39.5 % to −25.4 % over the concentration range of 12−18 μg·mL^{-1}, indicating a systematic underestimation. The RSD (%) values at metoclopramide concentrations of 12.0, 16.0 and 18.0 μg·mL^{-1} were 0.61 %, 0.71 % and 0.68 %, respectively, all below 2.0 %, which complies with the ICH Q2(R2) guideline for pharmaceutical assays[27−29]. Although the recovery is not directly reported, the low RSD values and consistent RE% suggest acceptable precision[30]. Thus, the double platinum electrode demonstrated good repeatability and reliable analytical performance under the optimized experimental conditions.

Table 4

Accuracy and Precision of the Proposed Potentiometric Method

C, μg·mL^{-1}	E_{corr}, mV	RSD, %	RE, %	A	Mean Signal ± SD, mV
12.0	−8.225	0.610	−39.500	0.500	−8.225 ± 0.050
16.0	−11.500	0.710	−25.400	0.629	−11.500 ± 0.082
18.0	−12.000	0.680	−25.800	0.606	−12.000 ± 0.082

Table 5 compares the measured and calculated electrode potentials to evaluate whether the observed deviations (ΔE) at different concentration levels exceed the threshold expected from random experimental variability. Deviations exceeding the ±2σ criterion would provide preliminary evidence of systematic effects, including possible molecular self-assembly, according to the statistical approach adopted in comparable electrochemical studies[31]. Conversely, when all absolute deviation values (|ΔE|) remain within the ±2σ interval, no statistically significant systematic deviation is detected under the present experimental conditions, and the observed differences are attributed to random experimental error. Therefore, this analysis provides a quantitative statistical basis supporting the absence of detectable self-assembly of metoclopramide within the investigated concentration range.

Table 5

Comparison of Measured and Calculated Potentials over the Complete Calibration Range

MCP Conc., μg·mL^{-1}	log C	E_{meas} Mean, mV	E_{calc}, mV	ΔE, mV	Remark
2.0	0.301	63.200	59.600	+3.600	Within 2σ
4.0	0.602	45.470	48.680	−3.210	Within 2σ
6.0	0.778	40.030	42.290	−2.260	Within 2σ
8.0	0.903	39.770	37.760	+2.010	Within 2σ
10.0	1.000	31.100	34.240	−3.140	Within 2σ
12.0	1.079	30.700	31.370	−0.670	Within 2σ
14.0	1.146	28.700	28.940	−0.240	Within 2σ
16.0	1.204	27.100	26.840	+0.260	Within 2σ
18.0	1.255	26.770	24.990	+1.780	Within 2σ
20.0	1.301	24.900	23.320	+1.580	Within 2σ

3.3 Transient Sensitivity Analysis

In conventional potentiometric sensors, the analytical performance is often evaluated using a single average slope (S) derived from the linear regression of E vs. log C, based on the Nernst equation. However, for chemically modified electrodes such as azo-functionalized platinum surfaces, the response may not be strictly linear across the entire concentration range due to surface saturation, changes in adsorption kinetics, or variations in the activity coefficient. A more rigorous approach is to calculate the local (transient) sensitivity[31] between consecutive measurement points[32,33], defined as:

$$S_i = \frac{E_{i+1} - E_i}{\log C_{i+1} - \log C_i} \tag{3}$$

where S_i represents the slope (mV per log C) for interval i. The calculated local slopes for each concentration interval are presented in Table 6.

Table 6

Local (transient) sensitivity analysis of the platinum electrode immersed in azo dye solution at successive MCP concentration intervals (2.0−20.0 μg·mL^{-1})

Terval, μg·mL^{-1}	log C range	Δlog C	ΔE, mV	Local sensitivity S_i, mV per log C
1 (2−4)	0.301−0.602	0.301	−17.73	−58.90
2 (4−6)	0.602−0.778	0.176	−5.44	−30.90
3 (6−8)	0.778−0.903	0.125	−0.26	−2.08
4 (8−10)	0.903−1.000	0.097	−8.67	−89.40
5 (10−12)	1.000−1.079	0.079	−0.40	−5.06
6 (12−14)	1.079−1.146	0.067	−2.00	−29.90
7 (14−16)	1.146−1.204	0.058	−1.60	−27.60
8 (16−18)	1.204−1.255	0.051	−0.33	−6.47
9 (18−20)	1.255−1.301	0.046	−1.87	−40.70

The theoretical Nernstian slope for a monovalent ion at 25 °C is −59.16 mV per log C. Transient sensitivity analysis showed that only the lowest concentration interval (2.0–4.0 μg·mL^{-1}) exhibited a local of −58.9 mV per log C (Fig. 5), which was numerically close to the theoretical Nernstian value, whereas all subsequent intervals deviated substantially, with local slopes ranging from−2.08 to −89.4 mV per log C. Accordingly, the overall calibration curve (E vs. log C) constructed over the concentration range of 2.0–20.0 μg·mL^{-1} yielded an average slope of −36.276 ± 2.615 mV per log C. Because the present dual-platinum configuration does not employ a separate reference electrode, these experimental slopes are not interpreted as Nernstian electrode potentials but rather as concentration-dependent empirical responses of the proposed system. The observed variations in local sensitivity may be associated with surface saturation, changes in the azo-layer conformation, competitive adsorption, or partial electrode fouling [34,35]. Because the 2.0–4.0 μg·mL^{-1} interval comprised only two experimental concentration levels, it was not treated as an independent statistically validated calibration range. Therefore, the complete concentration range (2.0–20.0 μg·mL^{-1}) was adopted for empirical calibration, whereas the transient sensitivity analysis was used only to interpret concentration dependent changes in electrode behavior.

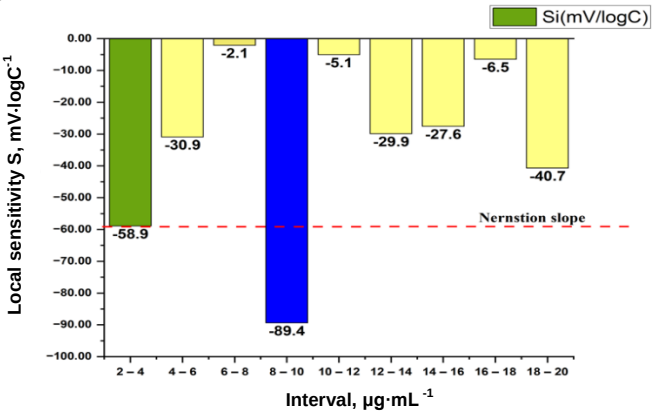

Figure 5. Local slope analysis showing perfect Nernstian fit at 2.0−4.0 μg·mL^{-1} (-58.9 mV per log C) versus severe deviations at higher concentration ranges.

3.4 Mutual Information Analysis

The calculated mutual information, I(C; E), was 1.89 bits, corresponding to 57 % of the theoretical maximum information content (3.32 bits). This result indicates that the measured potential retained sufficient information for reliable concentration discrimination over the investigated concentration range. The remaining information loss (43 %) reflects the increased within-concentration variability observed at higher concentrations, which increases the conditional entropy, $H(E/C)$, and consequently reduces the mutual information.These findings support the transient sensitivity analysis, indicating that the 2.0–4.0 μg·mL^{-1} interval represents a localized near-Nernstian response rather than an independent statistically validated calibration range.

Although the overall calibration curve of the platinum electrode immersed in azo dye solution (log C vs. E) over the concentration range of 2.0−20.0 μg·mL^{-1} gave a slope of -36.276 ± 2.615 mV per log C, which is lower than the theoretical Nernstian value (− 59.16 mV per log C), this does not indicate electrode failure. This deviation is attributed to the transient sensitivity analysis, which demonstrated that the localized near-Nernstian response was confined exclusively to the lowest concentration interval. Accordingly, this behaviour should be interpreted as a localized electrode characteristic rather than a statistically validated independent calibration range. At concentrations exceeding 6.0 μg·mL^{-1}, surface saturation and changes in the adsorption mechanism occur, leading to decreased sensitivity and fluctuations in the local slope, as shown in the Transient Sensitivity Analysis section. Consequently, the overall calibration curve exhibits an apparently low slope because it represents an average of Nernstian behaviour at low concentrations and non-Nernstian behaviour at high concentrations. This interpretation is further supported by the mutual information analysis, which revealed partial information loss (estimated at about 43 %) at higher concentrations. Although the present interpretation is supported by the transient sensitivity and mutual information analyses, complementary electrochemical techniques such as cyclic voltammetry (CV) and electrochemical impedance spectroscopy (EIS) could provide additional mechanistic insight into the origin of the observed non-Nernstian behaviour.

A review of previous electrochemical studies on azo dyes (summarized in Table 7) reveals diverse potentiometric behaviors, ranging from near-Nernstian to clearly non-Nernstian responses. The localized slope of –58.90 mV/decade observed in the present work at 2.0–4.0 μg/mL is remarkably **similar** to the theoretical Nernstian value and is **comparable** to the best near-Nernstian systems listed in Table 7, despite the overall non-Nernstian empirical behavior across the wider concentration range.

Table 7

Summary of Previous Electrochemical Studies on the Azo Dye

Main Technique	Analyte	Linear range	Slope, mV/decade	Compliance with Nernst model	Ref.
Potentiometry	Self-association of simple azo dyes	-	-	Not compliant (kinetic/thermodynamic model)	[31]
Potentiometric solid-state ion-selective sensor	Direct Red 81 (azo dye)	-5.66×10^{-6} — 1.00×10^{-2} mol.L^{-1}	−34.0	Yes (Near-Nernstian response	[36]
Potentiometric ion-selective electrode	Cu^{2+} ions	1.0×10^{-6} -1.0×10^{-2} mol.L^{-1}	29.5 ± 0.2	Yes (Nernstian response)	[37]
Electrochemical Impedance Spectroscopy (EIS)	Dopamine and paracetamol	1.0×10^{-1} – 1.0×10^{3} μmol x L^{-1}	Not available	No (chemical signal converted to electrical)	[38]
Potentiometry (transition metal complexes)	Proton-ligand and stability constants of sulfonamide azo dyes	-	-	Yes (Nernstian applied for pK_a)	[39]

4 Conclusions

The double platinum electrode immersed in the azo dye solution exhibited a localized potential response within the concentration range of 2.0–4.0 μg·mL^{-1}, where the local slope (−58.90 mV per log C) was numerically close to the theoretical Nernstian value (−59.16 mV per log C). Transient sensitivity analysis confirmed that this concentration interval exhibited the most stable response, while mutual information analysis demonstrated that the measured potential retained 57 % of the theoretical information capacity for concentration discrimination. Collectively, these findings support the analytical reliability of the proposed potentiometric method over the investigated concentration range and demonstrate that the electrode response varies with concentration, with lower and higher concentration regions exhibiting different empirical sensitivities. The proposed approach therefore provides a simple and reproducible electroanalytical method for the quantitative determination of metoclopramide under the investigated experimental conditions.

*Author Information**

**The authors' names are presented in the following order: First Name, Middle Name and Last Name*

Alaa Abdulnabi Ahmed (*corresponding author*) — PhD in Chemistry, Department of Chemistry, Second Karkh Education Directorate, Ministry of Education, 10011, Baghdad, Iraq; e-mail: alaa.abed1105a@ihcoedu.uobaghdad.edu.iq; https://orcid.org/0009-0004-0469-4457

Maha Abd Alsattar Mohammed — Assistant Professor, Department of Chemistry, College of Education for Pure Science (Ibn Al-Haitham), University of Baghdad, 10071, Baghdad, Iraq; e-mail: maha.a.m@ihcoedu.uobaghdad.edu.iq; https://orcid.org/0000-0002-4565-8135

Author Contributions

The manuscript was written through contributions of all authors. All authors have given approval to the final version of the manuscript. CRediT: **Alaa Abdulnabi Ahmed:** conceptualization, methodology, investigation, data curation, formal analysis, visualization, writing–original draft; **Maha Abd Alsattar Mohammed:** supervision, validation, methodology, writing–review & editing.

Acknowledgments

The authors would like to thank the Department of Chemistry, College of Education for Pure Science (Ibn Al-Haitham), University of Baghdad, Baghdad, Iraq, for providing laboratory facilities

References

1 Shteingolts, S. A., Davydova, V. V., Mar'yasov, M. A., Nasakin, O. E., Fayzullin, R. R., & Lodochnikova, O. A. (2020). Crystal structure of dacarbazine, metoclopramide, and acetylcholine pentacyanopropenides. Journal of Structural Chemistry, 61, 928–936. https://doi.org/10.1134/S002247662006013X

2 Flayyih, F. H., Alshirifi, A. N., & Kadem, K. J. (2025). A new spectrophotometric method for the determination of imidacloprid in real samples by diazotization-coupling reaction. *Methods and Objects of Chemical Analysis*, 20, 46–51. https://doi.org/10.17721/moca.2025.46-51

3 Aghababaei, F., & Hadidi, M. (2023). Recent advances in potential health benefits of quercetin. *Pharmaceuticals*, 16, 1020. https://doi.org/10.3390/ph16071020

4 Carrillo-Martinez, E. J., Flores-Hernández, F. Y., Salazar-Montes, A. M., Nario-Chaidez, H. F., & Hernández-Ortega, L. D. (2024). Quercetin, a flavonoid with great pharmacological capacity. *Molecules*, 29, 1000. https://doi.org/10.3390/molecules29051000

5 Rao, M. J., & Zheng, B. (2025). The role of polyphenols in abiotic stress tolerance and their antioxidant properties to scavenge reactive oxygen species and free radicals. *Antioxidants*, 14, 74. https://doi.org/10.3390/antiox14010074

6 Nazarnezhad, S., Nasiri, S. N., Gorgani, S., Aghajanloo, B., & Seyedasli, N. (2026). Quercetin-loaded biocomposites for wound healing applications: From therapeutic efficacy to delivery platforms. *Phytochemistry Reviews*, 25, 1899–1928. https://doi.org/10.1007/s11101-025-10185-8

7 Qi, W., Qi, W., Xiong, D., & Long, M. (2022). Quercetin: Its antioxidant mechanism, antibacterial properties and potential application in prevention and control of toxipathy. *Molecules*, 27, 6545. https://doi.org/10.3390/molecules27196545

8 Sinan, R. (2010). Spectrophotometric determination of metoclopramide hydrochloride in pharmaceutical tablets by diazotization-coupling method with 1-naphthol as the coupling agent. *Baghdad Science Journal*, 7, 704–712. https://doi.org/10.21123/bsj.2010.7.1.704-712

9 Barzani, H. A. H., Omer, R. A., Barzani, K. I. S., Jawhar, Z. H., & Sulaiman, S. H. (2026). Evolving methodologies for the analytical determination of metoclopramide. *Critical Reviews in Analytical Chemistry*. https://doi.org/10.1080/10408347.2025.2612234

10 Hamamoto, K., Mizuno, Y., Kato, M., Yamagishi, N., & Furuhama, K. (2013). Simple and sensitive method for measurement of metoclopramide in cattle plasma by LC-MS/MS using a multimode chromatography. *Journal of Veterinary Medical Science*, 75, 509–514. https://doi.org/10.1292/jvms.12-0220

11 Ghasemi, M., Rahmani, M., & Khajeh, M. (2024). Development of a liquid-phase microextraction method prior to HPLC analysis of quercetin in food samples. *Journal of Chromatographic Science*, 62, 390–398. https://doi.org/10.1093/chromsci/bmad028

12 Barzani, H. A. H., Omer, R. A., Barzani, K. I. S., Jawhar, Z. H., & Sulaiman, S. H. (2026). Analytical techniques for quantification of metoclopramide: A comprehensive review. *Biomedical Chromatography*, 40, e70316. https://doi.org/10.1002/bmc.70316

13 Wu, J., Liu, H., Chen, W., Ma, B., & Ju, H. (2023). Device integration of electrochemical biosensors. Nature Reviews Bioengineering, 1, 346–360. https://doi.org/10.1038/s44222-023-00032-w

14 Theyagarajan, K., & Kim, Y. J. (2023). Recent developments in the design and fabrication of electrochemical biosensors using functional materials and molecules. *Biosensors*, 13, 424. https://doi.org/10.3390/bios13040424

15 Xhanari, K., & Finšgar, M. (2023). Recent advances in the modification of electrodes for trace metal analysis: A review. *Analyst*, 148, 5805–5821. https://doi.org/10.1039/D3AN01252B

16 Jampasa, S., Khamcharoen, W., Traipop, S., Jesadabundit, W., Ozer, T., & Chailapakul, O. (2023). Recent advances on nanomaterial-modified film-electrode-based sensors: Approach to clinical purpose. *Current Opinion in Electrochemistry*, 42, 101420. https://doi.org/10.1016/j.coelec.2023.101420

17 Drużyńska, M., Lenar, N., & Paczosa-Bator, B. (2025). Advances in reference membranes for potentiometric sensing applications. *Membranes*, 15, 376. https://doi.org/10.3390/membranes15120376

18 Al-Haideri, A. A., Abdulla, N. I., & Malih, I. K. (2017). Polymeric membrane sensors for the selective determination of metoclopramide hydrochloride and their applications to pharmaceutical analysis. *Iraqi Journal of Pharmaceutical Sciences*, 21, 70–77. https://doi.org/10.31351/vol21iss1pp70-77

19 Demir, İ., Bulduk, İ., Darwish, I. A., & Enginar, H. (2024). A green approach for metoclopramide quantification in pharmaceutical products: New HPLC and spectrophotometric methods. *Scientific Reports*, 14, 8765. https://doi.org/10.1038/s41598-024-59149-6

20 Singh, R., Gupta, R., Bansal, D., Bhateria, R., & Sharma, M. (2024). A review on recent trends and future developments in electrochemical sensing. *ACS Omega*, 9, 7336–7356. https://doi.org/10.1021/acsomega.3c080

21 Rahn, K. L., Peramune, U., Zhang, T., & Anand, R. K. (2023). Label-free electrochemical methods for disease detection. *Annual Review of Analytical Chemistry*, 16, 49–69. https://doi.org/10.1146/annurev-anchem-091622-085754

22 Dorschel, C. A. (1989). LC detectors: Evaluation and practical implications of linearity. *Analytical Chemistry*, 61, 951A–958A. https://doi.org/10.1021/ac00192a001

23 Ahmed, A. A., & Mohammed, M. A. (2026). UV–visible spectrophotometric determination of metoclopramide using quercetin in pure and pharmaceutical forms. Analytical Methods in Environmental Chemistry Journal, 9, 131–141. https://doi.org/10.24200/amecj.v9.i01.1113

24 Stock, J. T. (1971). Bipotentiometric titration: Microchemical and general applications. Microchemical Journal, 16, 557–570. https://doi.org/10.1016/0026-265X(71)90049-X

25 Kirowa-Eisner, E., Golombek, G., & Ariel, M. (1968). New indicating system: Twin electrodes, at zero current. II. The choice of electrodes. *Journal of Electroanalytical Chemistry, 16*, 33–40. https://doi.org/10.1016/S0022-0728(68)80274-8

26 Kirowa-Eisner, E., & Ariel, M. (1966). New indicating system: Twin electrodes, at zero current. I. Proposed mechanism. *Journal of Electroanalytical Chemistry*, 12, 286–293. https://doi.org/10.1016/S0022-0728(96)80003-9

27 Abdulkareem, H. M., Al-Tameemi, M., Ibraheem, I. H., & Hadi, M. S. (2020). Surfactant cloud point extraction as a procedure of preconcentrating for metoclopramide determination using spectroanalytical technique. *Baghdad Science Journal*, 17, 57–64. https://doi.org/10.21123/bsj.2020.17.1.0057

28 Duesselberg, A. L. M., Weber, I. C., Zosso, Y., Salah, P., & Bao, Z. (2026). Machine learning-driven multiplexed biomarker detection with polymer-enhanced electrochemical sensors. ACS *Electrochemistry*, 2, 1444–1455. https://doi.org/10.1021/acselectrochem.6c00079

29 European Medicines Agency. (2022). ICH Q2(R2): Validation of analytical procedures. https://www.ema.europa.eu/en/ich-q2r2-validation-analytical-procedures-scientific-guideline

30 International Council for Harmonisation. (2022). ICH guideline Q2(R2): Validation of analytical procedures. *International Council for Harmonisation*.

31 Simončič, B., Špan, J., & Vesnaver, G. (1994). A study of the self-association of simple azo dyes using the potentiometric method. *Dyes and Pigments*, 26, 257–266. https://doi.org/10.1016/0143-7208(94)80041-3

32 Bakker, E., & Pretsch, E. (2007). Modern potentiometry. *Angewandte Chemie International Edition*, 46, 5660–5668. https://doi.org/10.1002/anie.200605068

33 Cammann, K. (1979). Analysis techniques using ion-selective electrodes. In Working with ion-selective electrodes (pp. 121–161). *Springer*. https://doi.org/10.1007/978-3-642-67276-7_6

34 González-Franco, J., Olmos, J., Ruiz, A., & Ortuño, J. Á. (2025). Principal component analysis of transient potential signals from ion-selective electrodes for the identification and quantification of different ions. *Chemosensors*, 13, 305. https://doi.org/10.3390/chemosensors13080305

35 Shannon, C. E. (1948). The mathematical theory of communication. *Bell System Technical Journal*, 27, 379–423. https://doi.org/10.1002/j.1538-7305.1948.tb01338.x

36 Heragy, M. O., Moustafa, A. A. M., ElZanfaly, E. S., Al-Shareef, W. A., & Saad, A. S. (2022). Miniaturized solid-state sensor for inline monitoring of the microbial biodegradation of a biohazardous textile azo dye (Direct Red-81). *Talanta Open*, 6, 100146. https://doi.org/10.1016/j.talo.2022.100146

37 Boumya, W., Achak, M., Bakasse, M., & El Mhammedi, M. A. (2020). Indirect determination of dopamine and paracetamol by electrochemical impedance spectroscopy using azo coupling reaction with oxidized 2,4-dinitrophenylhydrazine (DNPH): Application in commercial tablets. *Journal of Science: Advanced Materials and Devices*, 5, 218–225. https://doi.org/10.1016/j.jsamd.2020.04.003

38 Almansrawi, S. A., & Alrufaie, M. M. (2023). Spectrophotometric determination of sulfanilamide using oxidative coupling reaction with the presence of the peroxidase enzyme. *Egyptian Academic Journal of Biological Sciences, Section C: Physiology and Molecular Biology*, 15, 573.

39 El-Mossalamy, E. H. (2009). Potentiometric and spectroscopic studies of sulfonamide azo-dye complexes with some transition metal ions and uranium. *Portuguese Electrochimica Acta*, 27, 143–154. https://doi.org/10.4152/pea.200902143

How to Cite: Baimuratova, R.K., Bazargulov, R.N., Kleinikova, S.A., Zolotukhina, E.V., Gor'kov, K.V., Zhidkov, M.V., & Dzhardimalieva, G.I. (2026). Effect of Graphite Content on the Structural and Electrochemical Properties of MIL-88B(Fe)/Graphite Composites. *Eurasian Journal of Chemistry, 31, 3(123), 98–116.* https://doi.org/10.31489/2959-0663/3-26-5

INORGANIC CHEMISTRY

Article

Received: 20 July 2026 | Revised: 14 August 2026 |
Accepted: 19 August 2026 | Published online: 27 August 2026

UDC 546.26+544.6

https://doi.org/10.31489/2959-0663/3-26-5

Rose K. Baimuratova[1*], Ravil N. Bazargulov[1,2], Sofia A. Kleinikova[1], Ekaterina V. Zolotukhina[1], Konstantin V. Gor'kov[1], Mikhail V. Zhidkov[1], Gulzhian I. Dzhardimalieva[1,3]

[1]*Federal Research Center of Problems of Chemical Physics and Medicinal Chemistry Russian Academy of Sciences, Chernogolovka, Moscow region, Russia*
[2]*Lomonosov Moscow State University, Moscow, Russia*
[3]*Moscow Aviation Institute (National Research University), Moscow, Russia*
*(*Corresponding author's e-mail: rozab@icp.ac.ru)*

Effect of Graphite Content on the Structural and Electrochemical Properties of MIL-88B(Fe)/Graphite Composites

MIL-88B(Fe)/graphite composites are promising conductive materials for electrochemistry, combining the advantages of metal-organic frameworks and carbon. A series of composites with graphite contents from 12.5 to 75 wt.% was synthesized via in situ precipitation in aqueous medium at room temperature, using a trinuclear iron(III) oxoacetate complex as an inorganic precursor. The physicochemical characteristics were investigated by X-ray diffraction, Raman spectroscopy, SEM, TGA, nitrogen adsorption–desorption analysis, and infrared spectroscopy. An inverse linear correlation was found between the graphite content and the mass loss of the MOF composite at the first decomposition stage, attributed to dehydration. With increasing graphite weight fraction, the rate of mass loss of the composite decreases. The specific surface area nonlinearly decreases with increasing graphite content from 220 m^2/g for pristine MIL-88B(Fe) to 15.2 m^2/g for the composite with 75 wt.% graphite, while the calculated QSDFT pore diameter shifts from 4.6 nm for pure MIL-88B(Fe) to a stable 3.1 nm for the composites, indicating that graphite localizes on the outer crystal surfaces rather than penetrating the MOF pores. Electrocatalytic activity of MIL-88B(Fe) toward glucose oxidation was demonstrated by cyclic voltammetry. The results provide a physicochemical foundation for the development of electrode materials for non-enzymatic electrochemical glucose sensors based on MIL-88B(Fe) systems.

Keywords: MIL-88B(Fe), metal-organic frameworks, graphite composites, electrocatalytic activity, glucose, electrochemical sensors, in situ synthesis, porous structure

Introduction

Electrocatalysis, which accelerates electrochemical reactions at the electrode–electrolyte interface using catalysts, is widely employed in hydrogen energy applications, including fuel cells and water electrolysis systems [1–23], electrochemical energy storage devices such as batteries and supercapacitors [3], CO_2 conversion into valuable products like formate and methanol, N_2 reduction to ammonia [4–6], electrochemical wastewater treatment methods including anodic oxidation and electro–Fenton processes [7, 8], as well as in devices for metabolite monitoring, for example, for the electrocatalytic oxidation of glucose on modified electrodes [9–11]. The efficiency of electrocatalysis depends on the electrode material, which must combine high catalytic activity, good electrical conductivity, and stability under anodic polarization conditions [7].

Metal–organic frameworks (MOFs) are a class of porous coordination polymers constructed from metal ions or clusters connected by organic linkers into two- or three-dimensional structures [12]. Among iron-containing MOFs (Fe-MOFs), MIL-88B(Fe) is particularly noteworthy, as its structure consists of trimeric

© 2026 The Authors. This is an open access article under the CC BY-NC-ND license (http://creativecommons.org/licenses/by-nc-nd/4.0/)

iron oxo-clusters bridged by terephthalate ligands, forming a hexagonal framework with one-dimensional channels approximately 6–9 Å in diameter [13, 14].Owing to their developed porosity, which ensures efficient mass transport of reagents to the electrode surface, and the presence of catalytically active Fe^{3+}/Fe^{2+} centers capable of reversibly participating in redox reactions under an applied potential, iron-based MOFs are being actively explored for electrochemical applications [15]. MOFs can be used as electrode materials in batteries, serve as electrocatalysts for reactions occurring in fuel cells or electrolyzers, and also act as a basis for supercapacitor electrodes [16]. In contrast to non-porous metal nanoparticles or microparticles, where only surface atoms in contact with the electrolyte can be electrochemically active and reactions occur solely at the surface, in porous electrochemically active MOFs the utilization of metal ions can theoretically reach 100 % [16]. Ionic conductivity can be provided by the MOF itself, by the electrolyte, or by guest molecules introduced into the pores of the framework [17]. MIL-88B(Fe) belongs to the class of flexible metal-organic frameworks, which can reversibly change the unit cell volume upon adsorption/desorption of guest molecules. For the MIL-88 family, which is known for its "breathing" behavior, the volume change can reach 85–230 % depending on the nature of the linker and the type of guest molecules, while the crystal structure remains intact [18–20]. Pore tunability enables host-guest molecular recognition, which enhances the activity and selectivity of sorption, separation, and catalysis [21], and also makes these materials promising for electrochemical sensors. However, pristine MOFs suffer from low electrical conductivity, which limits their use as electrode materials [14]. A solution to this problem is the fabrication of MOF composites with complex architectures by combining them with carbon-based materials (activated carbon, carbon nanotubes (CNTs), fullerene, graphite, graphene oxide, etc.), as well as with nanoparticles or oxides of metals and non-metals [22–24]. The formation of MOF composites with graphite, carbon nanotubes, acetylene black, or reduced graphene oxide (rGO) enables the creation of a conductive network that improves electron transport from the external circuit to the catalytic centers of the MOF [25, 26]. In such systems, the carbon component not only enhances the overall conductivity but also acts as a dispersing support, preventing aggregation of MOF nanoparticles and increasing the number of available active sites, which in turn improves the electrochemical performance [27, 28] or photocatalytic activity [29]. Zhang et al. demonstrated that MIL-53(Fe)@rGO delivers a capacity of 550 $mA \cdot h\ g^{-1}$ after 100 cycles at 100 $mA \cdot h\ g^{-1}$ in lithium-ion batteries [27]. Jin et al. obtained a Fe_3O_4/C nanocomposite via post-synthetic thermal treatment of MIL-88B(Fe) at 600 °C, with the capacity increasing up to the 200th cycle (from ~800 to 928 $mA \cdot h\ g^{-1}$), which the authors attributed to an "activation process" [28]. It was shown that oxygen-functionalized CNTs reduce Fe(III) to Fe(II) and consequently increase the Fenton-like activity in the CNT@MIL-88B-Fe composite [29]. The potential of such composites in biosensors was demonstrated by Qin et al., who used a MIL-88A@NiFe-PB heterostructure with high sensitivity (1963.2 $\mu A \cdot mM^{-1}\ cm^{-2}$) for glucose detection [30].

However, most studies are based on the use of expensive carbon components (rGO, CNTs) and, as a rule, are limited to a single MOF/carbon ratio. Systematic data on the effect of graphite content on the structure and properties of MIL-88B(Fe)/graphite composites are lacking in the literature. In this regard, in the present work we investigated the effect of graphite content on the structure and physicochemical properties of MIL-88B(Fe)/graphite composites synthesized by in situ precipitation in aqueous medium. It was shown that varying the graphite weight fraction enables control not only of the conductivity but also of the specific surface area, morphology, and thermal stability, while preserving the porous structure of the MOF. For the first time, it is demonstrated that MIL-88B(Fe) exhibits electrocatalytic activity toward glucose oxidation, opening prospects for its use in non-enzymatic electrochemical sensors.

Experimental

Reagents and Materials

Iron(III) chloride hexahydrate ($FeCl_3 \cdot 6H_2O$, chemically pure), sodium acetate trihydrate ($CH_3COONa \cdot 3H_2O$, analytical grade), D-glucose (>99 %, $C_6H_{12}O_6$), cetyltrimethylammonium bromide (CTAB, $C_{19}H_{42}BrN$, analytical grade), potassium hydroxide (KOH, RusKhim, ≥90 %, analytical grade), and ethyl alcohol (95 %, pharmaceutical grade) were purchased from Ruskhim Trade Company and used without further purification. Terephthalic acid (1,4-benzenedicarboxylic acid, H_2BDC, 98 %) was supplied by Sigma-Aldrich. Fine graphite powder of grade GK-1, which according to GOST 17022-81 is intended for the production of drawing and office pencil leads (≥99.5 % of particles ≤63 μm), was used as the carbon component.

Synthesis of the inorganic precursor $[Fe_3O(OAc)_6]Cl$

The metal-organic framework MIL-88B(Fe) was obtained at room temperature according to a previously reported procedure [31]. As an inorganic precursor, the trinuclear iron(III) oxo-acetate complex $Fe_3(\mu_3\text{-}O)(CH_3COO)_6(H_2O)_3]Cl{\cdot}12H_2O$ ($[Fe_3O(OAc)_6]Cl$), was synthesized according to reaction (1) [32]:

$$3FeCl_3 + 6CH_3COONa + 4H_2O \rightarrow [Fe_3(\mu_3\text{-}O)(CH_3COO)_6(H_2O)_3]Cl + 6NaCl + 2HCl \quad (1)$$

A sample of $FeCl_3{\cdot}6H_2O$ weighing 56 g (0.21 mol) was dissolved in 70 mL of hot distilled water (55 °C) under stirring until complete dissolution. Sodium acetate trihydrate weighing 56.5 g (0.41 mol) was dissolved in 70 mL of hot distilled water (55 °C). After complete dissolution of both reagents, the iron(III) chloride solution was added dropwise to the sodium acetate solution, and the reaction mixture was thermostated at 55 °C and stirred for 120 min. After the stirring was completed, the solution was left for slow crystallization in air at room temperature for 12 h, and then kept for several additional days. The resulting orange-red crystalline precipitate was collected by filtration on a Büchner funnel, washed with a small amount of cold ethanol to remove impurities, and dried in an oven at 50 °C to constant weight. Calculated for $Fe_3(\mu_3\text{-}O)(CH_3COO)_6(H_2O)_3]Cl{\cdot}12H_2O$ (wt. %): C, 17.1; H, 5.6; Fe, 19.8; Cl, 4.2. Found (wt. %): C, 17.1±0.1; H, 5.70±0.15. IR spectroscopy (KBr, ν_{max}/cm^{-1}): 3523 ν(O–H); 2929 ν(C–H); 1601 $\nu_{as}(COO^-)$, 1520 $\nu_{as}(COO^-)$, 1444 $\nu_s(COO^-)$; 665 ν(Fe–O).

Synthesis of MIL-88B(Fe)/graphite composites

A series of MIL-88B(Fe)/graphite composites with varying graphite content was prepared by reacting the inorganic precursor $[Fe_3O(OAc)_6]Cl$ with the potassium salt of terephthalic acid under mechanical stirring (1000 rpm). Precursor masses and product yields are listed in Table 1.

Table 1

Precursor masses and yields for MIL-88B(Fe)/graphite composite synthesis

Sample	Graphite content, wt. %	m(graphite), g	m(KOH), g	m(H_2BDC), g	m($[Fe_3O(OAc)_6]Cl$), g	m(composite), g (yield %)
MIL-88B(Fe)	0	0	2.36	3.15	4.65	4.1 (91.1 %)
MIL-88B/graphite (75 wt %)	75	1.50	2.36	3.15	4.65	5.4 (90.1 %)
MIL-88B/graphite (50 wt %)	50	3.00	1.58	2.10	3.10	5.4 (90.1 %)
MIL-88B/graphite (25 wt %)	25	4.50	0.79	1.05	1.55	5.5 (92.0 %)
MIL-88B/graphite (12.5 wt %)	12.5	0.75	2.76	3.67	5.43	5.1 (84.7 %)

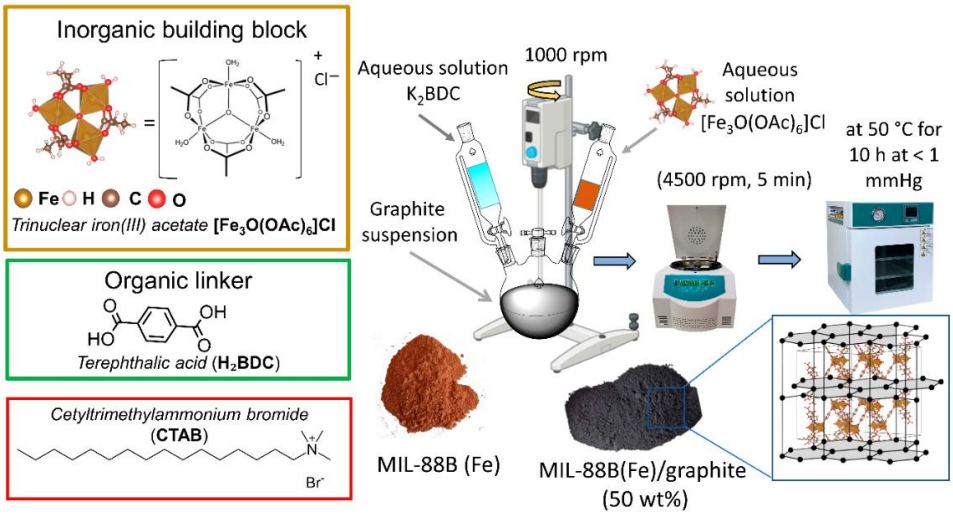

Figure 1. Schematic representation of MIL-88B(Fe)/graphite composite synthesis using the trinuclear iron(III) oxo-acetate complex

The synthesis was carried out in a 1 L three-neck round-bottom flask equipped with a mechanical overhead blade stirrer at 1000 rpm. Graphite and CTAB were first dispersed in 100 mL of water using a mechanical stirrer at 1500 rpm for 30 min at room temperature. H_2BDC was dissolved in 250 mL of water by adding

the appropriate amount of KOH. $[Fe_3O(OAc)_6]Cl$ was dissolved in 250 mL of water with heating (50–55 °C) and stirring at 250 rpm. The resulting precursor solutions were transferred to addition funnels and added dropwise to the graphite suspension over 30 min under vigorous stirring, as shown in Figure 1. The reaction mixture was stirred for 60 min at 1000 rpm. The resulting precipitate was separated by centrifugation (4500 rpm, 5 min), washed twice with water (50 mL) and ethanol (20 mL) to remove unreacted components, and dried at 50 °C in a vacuum oven for 10 h. The yields ranged from 84 to 92 % of the theoretical values (Table 1).

Characterization Methods

Carbon (C), hydrogen (H), and nitrogen (N) mass fractions in the synthesized samples were determined by combustion analysis using a Velp EMA 502 elemental analyzer (VELP Scientifica, Italy). FTIR spectra were recorded on a Bruker ALPHA spectrometer (Bruker Optik GmbH, Germany) in the range of 360–4500 cm^{-1} with a resolution of 2 cm^{-1} using KBr pellets containing 0.7 wt. % of the sample powder (32 scans). X-ray powder diffraction (XRD) patterns were collected on an Aeris Benchtop diffractometer (Malvern Panalytical, Netherlands) in Bragg–Brentano geometry with a vertical θ–θ goniometer (CuKα radiation, λ = 1.5460 Å; 2θ = 5–65°, step 0.012°). Thermogravimetric analysis (TGA) was performed on a TGA/SDTA851e thermoanalyzer (Mettler Toledo, Switzerland) in dynamic mode over 25–600 °C at a heating rate of 10 °C/min under a nitrogen atmosphere (absolute instrumental temperature accuracy ±0.5 °C, sample mass 4–6 mg, Al_2O_3 crucibles). The specific surface area, average pore radius, and pore size distribution were determined by low-temperature N_2 adsorption–desorption at 77 K on an AUTOSORB-1 analyzer (Quantachrome Instruments, USA). Samples were degassed at 120 °C for 2 h under vacuum (residual pressure $\leq 10^{-3}$ mbar) before measurement. The measurement was performed by the static volumetric method using helium for dead-volume calibration. Textural analysis and pore size distributions were evaluated using Quenched Solid Density Functional Theory (QSDFT, carbon slit-pore equilibrium model) and the t-plot method, while the Barrett–Joyner–Halenda (BJH) model was applied to characterize the general mesoporous features. Isotherm types were classified according to IUPAC 2015 recommendations. The morphology of the samples was examined by scanning electron microscopy (SEM) using an EM−30 microscope (Coxem, South Korea) at an accelerating voltage of 15 kV in secondary electron (SE) detection mode. Raman spectroscopy was performed using a Confotec® NR500 scanning confocal Raman microscope (SOL instruments, Belarus) equipped with a green laser (532 nm). The laser power of ~1.3 mW was chosen to avoid thermal degradation of the MOF. The signal accumulation time was 60 s. Spectra were recorded in the range of 100–1700 cm^{-1}, which covers the characteristic vibrational modes of both the graphite matrix and the MOF. The morphology and distribution of MOF particles within the graphite matrix were studied using an Optelics Hybrid confocal laser microscope (Lasertec Corp., Japan) equipped with planar apochromatic objectives (50× and 100× magnification).Quantitative particle size analysis was performed using ImageJ software [33] from bright-field optical micrographs.

Electrochemical Measurements

Electrochemical measurements were carried out using an Autolab PGSTAT 101 potentiostat (Metrohm-Autolab, Netherlands) and screen-printed three-electrode (SPE) test strips (Elta Ltd., Zelenograd, Russia). The three-electrode system comprised a graphite counter electrode, a custom Ag/AgCl reference electrode, and a graphite working electrode modified with a MOF or a composite. The reference electrode was prepared by electrooxidizing silver in 1 M NaCl at 1.6 V for 20 s. The potential of the resulting Ag/AgCl, Cl^- electrode in 0.15 M NaCl was 0.278 V vs. the standard hydrogen electrode (SHE). All potentials herein are given vs. this reference electrode. The working electrode was modified by applying a drop of a suspension of the studied MOF in 0.1 M acetate buffer (pH 5.5). For the electrochemical studies, a 100 μL aliquot of a solution was applied onto the test strip. Cyclic voltammograms were recorded at a scan rate of 0.02 V/s. Chronoamperometric data were recorded at an applied constant potential of 0.5 V.

Results and Discussion

Synthesis of MIL-88B(Fe)/Graphite Composites

The MIL-88B(Fe)/graphite composites were synthesized by in situ precipitation of the MOF onto graphite surfaces in an aqueous medium at room temperature to nucleate and grow directly on the graphite surface, ensuring intimate interfacial MOF–graphite contact and, consequently, efficient electron transport between the two components. The advantages of the proposed method over known approaches are: (i) use of a trinuclear acetate precursor with defined coordination geometry instead of $FeCl_3$ enables targeted formation

of the framework structure with the required network topology, implementing a "rational design" strategy [31, 34]; (ii) the aqueous medium eliminates the use of toxic dimethylformamide (DMF), traditionally employed in MIL-88B(Fe) synthesis [13]; and (iii) room temperature reduces energy consumption and simplifies scale-up. To improve the wettability of the graphite surface with water, prevent sedimentation of graphite particles, and ensure uniform distribution of graphite throughout the composite volume, cetyltrimethylammonium bromide (CTAB), a cationic surfactant, was introduced into the reaction mixture during the synthesis. It is known that the addition of CTAB reduces the interfacial tension at the graphite–water interface [35], which prevents aggregation of hydrophobic particles and allows a homogeneous suspension to be obtained, which is necessary for uniform MOF deposition onto the graphite surface.

Elemental Composition

CHNO elemental analysis results for individual components and synthesized samples are presented in Table 2. The actual graphite content in each sample was calculated from elemental analysis, noting that the total carbon content in the composite ($C_{composite}$) equals the sum of contributions from graphite and from the MOF:

$$C_{\text{composite}} = x \cdot C_{\text{graphite}} + (1 - x) \cdot C_{\text{MOF}} \quad (2),$$

where x is the graphite mass fraction; $(1 - x)$ is the MIL-88B(Fe) mass fraction. Therefore:

$$x = \frac{C_{composite} - C_{MOF}}{C_{graphite} - C_{MOF}} \times 100\% \quad (3)$$

where $C_{composite}$, C_{MOF}, and $C_{graphite}$ are the carbon contents in the composite, in MIL-88B(Fe), and in pristine graphite, respectively, determined by CHNO elemental analysis.

Table 2

Elemental analysis results of MIL-88B(Fe)/graphite composites

Sample	C, wt %	H, wt %	O, wt %	Graphite content, wt %
Graphite	98.2 ± 0.9	0.12 ± 0.05	2.47 ± 0.23	-
$[Fe_3O(OAc)_6]Cl$	17.12 ± 0.13	5.7 ± 0.2	29 ± 1	-
MIL–88B(Fe)	38.1 ± 0.3	2.6 ± 0.1	31.5 ± 0.5	0
MIL-88B(Fe)/graphite (12.5 wt %)	43.06 ± 0.91	3.1 ± 0.1	32.38 ± 0.35	8.3 ± 1.5
MIL-88B(Fe)/graphite (25 wt %)	53.30 ± 0.34	2.60 ± 0.01	28.4 ± 0.8	25.3 ± 0.7
MIL-88B(Fe)/graphite (50 wt %)	67.35 ± 0.05	1.65 ± 0.03	18.00 ± 0.24	48.7 ± 0.8
MIL-88B(Fe)/graphite(75 wt %)	84.55 ± 0.06	0.78 ± 0.21	9.5 ± 0.2	77.3 ± 0.7

As shown in Table 2, with increasing graphite fraction across the composite series, the carbon mass fraction increases progressively from 43.06 % (12.5 wt % graphite) to 84.55 % (75 wt % graphite), while the hydrogen content decreases correspondingly from 3.1 to 0.78 wt %. The oxygen content decreases monotonically from 32.38 to 9.5 wt % due to the reduced proportion of MIL-88B(Fe) in the sample. The actual graphite content calculated from CHNO data agrees well with the nominal content, with deviations of no more than 1.5 wt % for samples with 25, 50, and 75 wt % graphite. The largest relative deviation is observed for the 12.5 wt % graphite sample, likely due to adsorption of residual solvent (water).

X-Ray Powder Diffraction

The XRD patterns of the synthesized MIL-88B(Fe)/graphite composites (Figure 2) show an intense reflection at $2\theta \approx 26.5°$, corresponding to the (002) reflection of the hexagonal layered graphite structure (JCPDS 75-1621, d002 = 3.354 Å). Weak reflections at 17.4 °, 25.2°, and 28.0° are attributable to terephthalic acid (CCDC 1269122). Formation of this impurity phase is associated with the low aqueous solubility of terephthalic acid [36, 37] and the high rate of acetate-group substitution. As a result, a portion of the ligand is protonated in the acidic medium and does not have sufficient time to be fully incorporated into the framework. It is known that due to the high reaction rates and steric hindrance, acetate groups may not be completely substituted, leading to the formation of defective linkers [38, 39] in the resulting MOF structure. These defective linkers can coordinate to the metal cluster via only one carboxylate group, with the other group protruding into the pore cavity. This favors the retention of organic molecules inside the framework and results in the inclusion of terephthalic acid within the MOF pores, from which it is difficult to remove

even after repeated washing during the synthesis [40–42]. The absence of characteristic MIL-88B(Fe) reflections when water is used as the solvent is related to the reversible contraction of the crystal lattice, referred to as "breathing" [19, 43, 44], which is caused by the formation of hydrogen bonds between the metal-organic framework and guest molecules [45]. To confirm the flexibility of the synthesized MIL-88B(Fe), additional XRD studies were performed. The sample obtained after synthesis in aqueous solution and drying exhibits a diffraction pattern with a broadened signal in the low-angle region ($2\theta < 6.5°$), which does not allow unambiguous identification of the crystalline reflections characteristic of MIL-88B(Fe). This broadening is attributed to the transition of the framework to the closed (dry) form, which is characterized by anisotropic broadening of the (hk0) reflections, up to their complete disappearance, due to disordering in the (ab) plane caused by the removal of guest molecules and a decrease in the a parameter [18]. After soaking the same sample in DMF for 24 h, intense reflections appear at $2\theta \approx 7.12°$ and 8.75° ($d \approx 12.5$ Å and 10.1 Å, respectively), corresponding to a transition to the expanded (open) phase stabilized by DMF molecules and restoration of long-range crystalline order. This observation is consistent with previously reported rotation of metal clusters and phenyl rings around the O–O axis of carboxylate groups (a "knee-type" rotation axis) upon exposure to water molecules in MIL-88B(Fe) [46]. Similar behavior has been reported for MIL−88B(Fe)/Fe_3S_4 composites [47], MIL-88B(Fe)/nanorods [48], and Fe_3O_4/MIL-88B(Fe) [32].

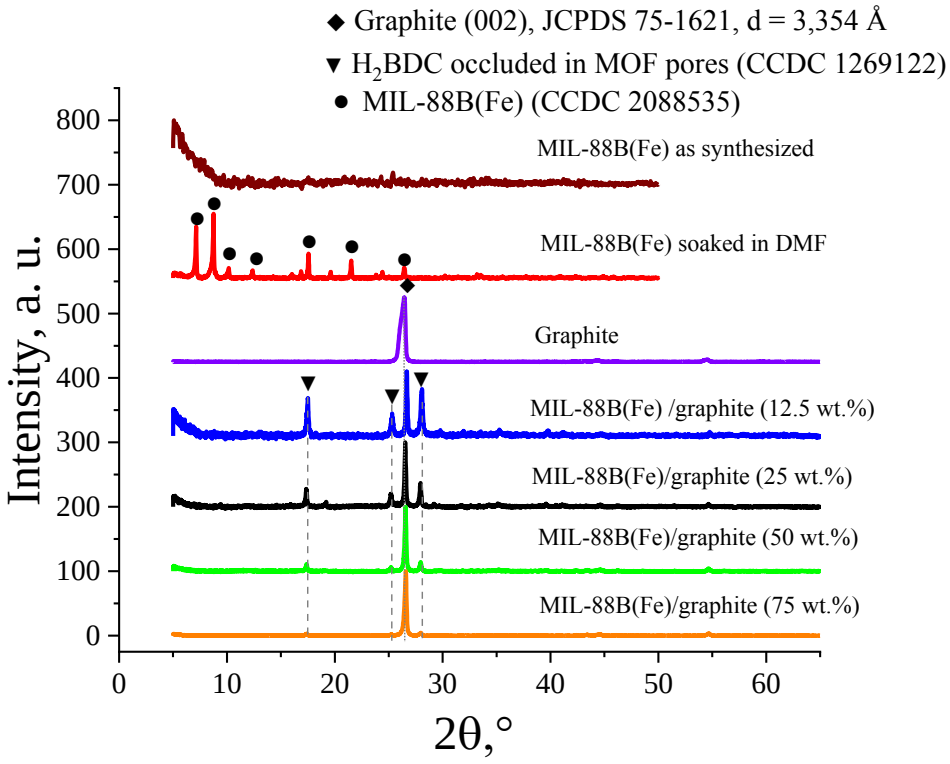

Figure 2. X-ray diffraction patterns of MIL-88B(Fe) and synthesized composites (CuKα, λ = 1.5460 Å)

Infrared Spectroscopy

FTIR spectra of MIL-88B(Fe) and MIL-88B(Fe)/graphite composites with various graphite contents are shown in Figure 3.

The FTIR spectra of the synthesized samples exhibit characteristic bands confirming the formation of MIL-88B(Fe). The symmetric and asymmetric stretching vibrations of the carboxylate groups are observed at 1424 and 1575 cm^{-1}, respectively; the ν(C=C) band of the aromatic ring appears at 1510 cm^{-1}, while the ν(C–O) and ν(C–C) stretching modes are detected at 1287 cm^{-1}. With increasing graphite content, the intensities of all MIL-88B(Fe) bands decrease progressively. Broadening and splitting of both asymmetric and symmetric carboxylate stretching bands is also observed. This splitting indicates the formation of inequivalent COO^- coordination modes in the composites, likely caused by the influence of the graphite surface in proximity to the carboxylate fragments of the metal-organic framework. The presence of a band at 1688 cm^{-1}, assigned to ν(C=O) of free carboxylic groups, indicates the presence of defective (dangling) link-

ers coordinated to the metal cluster through only one carboxylate group [49]. The bands at 668 and 528 cm^{-1} are characteristic of Fe–O stretching vibrations and Fe–O–Fe bridging modes [50], confirming the retention of the trimeric oxoacetate cluster. A broad band in the range of 3200–3600 cm^{-1} with a maximum at 3435 cm^{-1}, whose intensity increases with rising MIL-88B(Fe) content, is attributed to O–H stretching vibrations of hydroxyl groups involved in intermolecular hydrogen bonding [50].

The spectrum of MIL-88B(Fe) displays all characteristic bands of an iron-based carboxylate MOF [50,51]. Intense bands at 1546 and 1387 cm^{-1} correspond to the asymmetric and symmetric stretching vibrations of the carboxylate groups coordinated to the Fe_3O clusters. The absorption band at 725 cm^{-1} is assigned to the C–H bending (out-of-plane) vibrations of the disubstituted aromatic ring. The presence of the aromatic moiety is further confirmed by the band at 3060 cm^{-1}, attributed to the =C–H stretching vibrations [52]. In the spectrum of H_2BDC, the most intense bands are observed at 725, 878, and 779 cm^{-1}, characteristic of out-of-plane C–H deformation modes in the 1,4-disubstituted benzene ring, along with the ν(C=O) band of the free carboxyl group at 1671 cm^{-1} [51, 52]. The frequency difference between the asymmetric and symmetric carboxylate stretching vibrations ($\Delta\nu = \nu_{as} - \nu_{sym} \approx 151–159\ cm^{-1}$) is indicative of a bidentate bridging coordination mode of the carboxylate ions [53] and is in full agreement with literature data for MIL-88B(Fe).

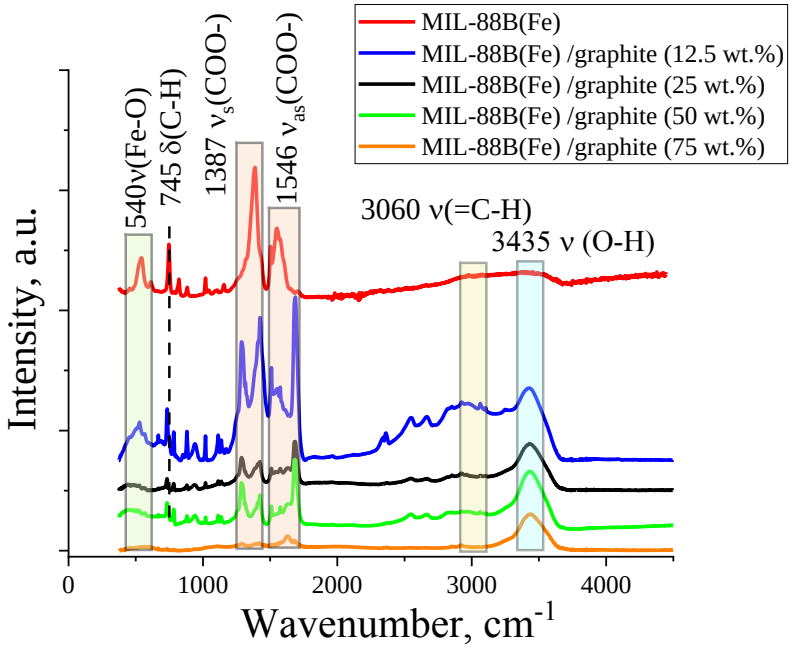

Figure 3. FTIR spectra of MIL-88B(Fe) and MIL-88B(Fe)/graphite composites (KBr pellets, 0.7 wt %)

Raman Spectroscopy

Raman spectroscopy was performed for additional phase identification and assessment of the structural features of the MIL-88B(Fe)/graphite composites (Figure 4). The spectra are presented in the range of 1000–1700 cm^{-1}, covering the characteristic vibrational modes of the graphite and the organic linker of the MOF. As seen in Figure 4a, the pristine graphite shows a D band at ~1350 cm^{-1}, assigned to the A_{1g}-symmetric vibration of defective sp^2-carbon sites, which becomes Raman-active only upon symmetry breaking through a double-resonance process [54]. To assess the degree of disorder and crystallite size, the I_D/I_G ratio is commonly used, where I_G is the intensity of the G peak at ~1580 cm^{-1}, corresponding to the C–C stretching vibrations in an ideal plane [54, 55]. The integrated area ratio of the corresponding graphite peaks was 0.255, indicating a low concentration of structural defects [54, 55]. Using the Tuinstra–Koenig equation applied to the peak height ratio (~0.162), the calculated crystallite size of graphite was 27 nm, which is characteristic of nanocrystalline graphite with low defect density [54]. For the composite with 12.5 wt % graphite, an increase in the integrated intensity ratio of the corresponding graphite peaks (~0.41) is observed, indicating an increase in the defect concentration in graphite during the synthesis of the composite. For samples with higher graphite content (25, 50, and 75 wt %), significant overlap of the D and G bands of graphite with the bands of the aromatic linker of MIL-88B(Fe) is observed. Nevertheless, qualitative analysis of the Raman spectra

indicates that the graphite structure is preserved in the composites, while the observed changes in the defect density suggest an interfacial interaction between graphite and the MOF, likely of a physical nature.

In the Raman spectra of both pristine MIL-88B(Fe) and the MIL-88B(Fe)/graphite (12.5 wt %) composite, characteristic bands of the terephthalate linker are observed. The band in the region of 1600–1615 cm^{-1} has been assigned by some authors to the asymmetric stretching vibrations of the carboxylate group, $\nu_{as}(COO^-)$ [56, 57], while others attribute it to the C=C stretching vibrations of the benzene ring [25, 58]. In the literature, the symmetric carboxylate stretching vibrations $\nu_s(COO^-)$ of MIL-88B(Fe) appear in the Raman spectrum at ~1455 cm^{-1}, whereas the broad absorption in the range of 1300–1430 cm^{-1} is assigned to the C–C and C–O vibrations of the aromatic ring of the terephthalate linker [56, 57]. In the present study, a shift of the carboxylate stretching band to lower wavenumbers (~1427 cm^{-1}) is observed, likely due to formation of partially substituted structures upon interaction with graphite, consistent with FTIR data. Upon the introduction of graphite, the intensity of these bands initially increases (12.5 wt % graphite) and then decreases due to the shielding effect and the reduced MOF fraction in the composite, which correlates with the FTIR results. The band in the range of 1132–1138 cm^{-1} is attributed to the C–C bond vibrations between the benzene ring and the carboxylate group [56].

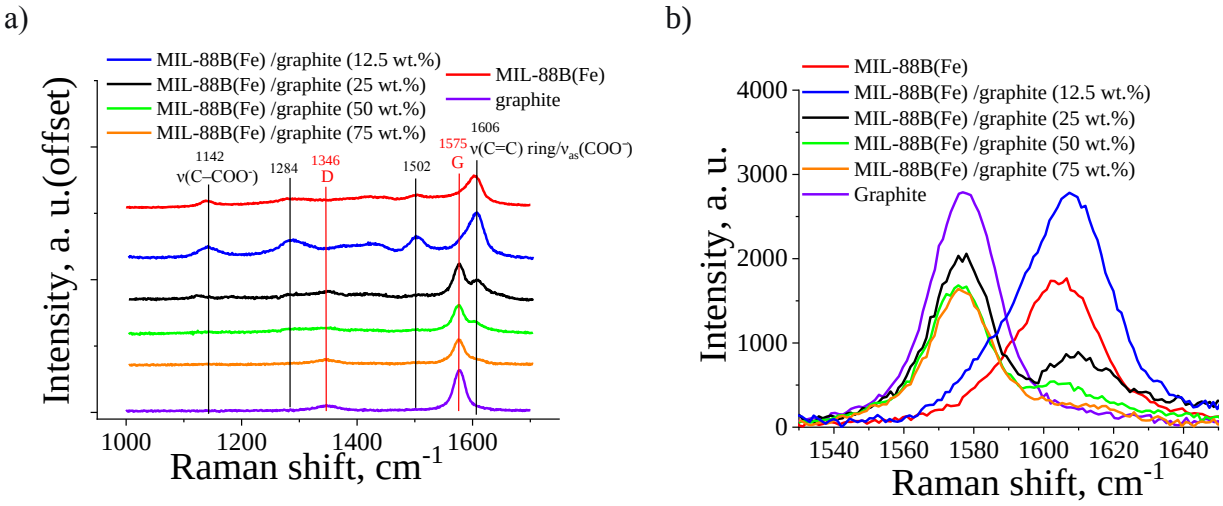

Figure 4. Raman spectra of graphite, MIL-88B(Fe), and MIL-88B(Fe)/graphite composites with various graphite contents (a), and a fragment of the Raman spectra in the range of 1540–1640 cm^{-1} showing the overlap of the graphite G peak and the MIL-88B(Fe) bands (b)

In Raman spectroscopy, the intensity of a band is proportional to the square of the derivative of polarizability with respect to the normal coordinate of the vibration. For low-frequency modes, such as Fe–O stretching vibrations and out-of-plane C–H bending vibrations of the aromatic ring (γ(C–H)), the change in polarizability during vibration is relatively small. Consequently, these modes exhibit a small Raman scattering cross-section and produce weak signals (Figure S1), especially against the background of the intense D and G bands of graphite, which possess high scattering cross-sections.

Specific Surface Area and Pore Size Analysis

Results of low-temperature nitrogen adsorption are summarized in Table 3. Pristine MIL-88B(Fe) exhibits a Type IV nitrogen adsorption–desorption isotherm according to the IUPAC classification, with a hysteresis loop (Figure 5), indicative of capillary condensation in mesopores, with a high specific surface area (S_{BET} = 220 m^2/g) and an average pore diameter of 3.6 nm. The specific surface area of MIL-88B(Fe) is comparable to literature data for MIL-88B(Fe), which range from 15 to 428 m^2/g depending on the synthesis and activation conditions [59–61].

Table 3

Specific surface area (S_{BET}), pore volume (V_{BJH} and V_{QSDFT}) and average pore diameter (d_{BJH} and d_{QSDFT}) of MIL-88B(Fe)/graphite composites

Sample	S_{BET}, m^2/g	V^*_{total}, cm^3/g *(p/p_o =0.99)	V_{BJH}, cm^3/g	d_{BJH}, nm	V_{QSDFT}, cm^3/g	d_{QSDFT}, nm
MIL–88B(Fe)[a]	220	0.32	0.25	3.6	0.25	4.6
MIL-88B(Fe)/graphite (12.5 wt %)	93	0.10	0.07	3.5	0.08	3.1
MIL-88B(Fe)/graphite (25 wt %)	48	0.06	0.05	3.5	0.05	3.1
MIL-88B(Fe)/graphite (50 wt %)	41	0.07	0.06	3.6	0.06	3.1
MIL-88B(Fe)/graphite (75 wt %)	15	0.04	0.04	3.5	0.03	3.1
Graphite	12	0.04	0.04	3.4	0.03	2.8

[a] *according to t-plot analysis V_{micro}=0.018 cm^3/g, S_{micro}=46 m^2/g, S_{ext}=174 m^2/g.*

As can be seen from Table 3, the *in situ* synthesis leads to a non-monotonic decrease in the specific surface area with increasing graphite content. For the sample with 12.5 wt % graphite, the BET-specific surface area was found to be 92.5 m^2/g, which is less than half the theoretical value for a physical mixture (194 m^2/g). The most pronounced drop in S_{BET} is observed upon increasing the graphite content from 12.5 to 25 wt % (from 92.5 to 48.2 m^2/g), which may be attributed to agglomeration of MIL-88B(Fe) particles, blockage of the MOF surface by graphite sheets, or changes in the morphology or defect formation in the MOF structure in the presence of graphite, consistent with the FTIR data. The Type IV isotherms with H3-type hysteresis reflect mesoporosity and interparticle voids, as the intrinsic micropores of flexible MIL-88B(Fe) contract upon guest removal (Figure 5a) [18–20]. The t-plot analysis shows a minor micropore volume of 0.018 cm^3/g for the MIL-88B(Fe) and zero microporosity for the composites. According to QSDFT analysis (Table 3), the pore diameter shifts from 4.6 nm for pure MIL-88B(Fe) to a stable peak maximum at 3.1 nm for all composites (Figure 5b). This consistent position indicates that the internal crystalline framework of the MOF is preserved during the *in situ* synthesis, while the graphite layers introduce a geometric constraint that governs the interstitial mesoporous space.

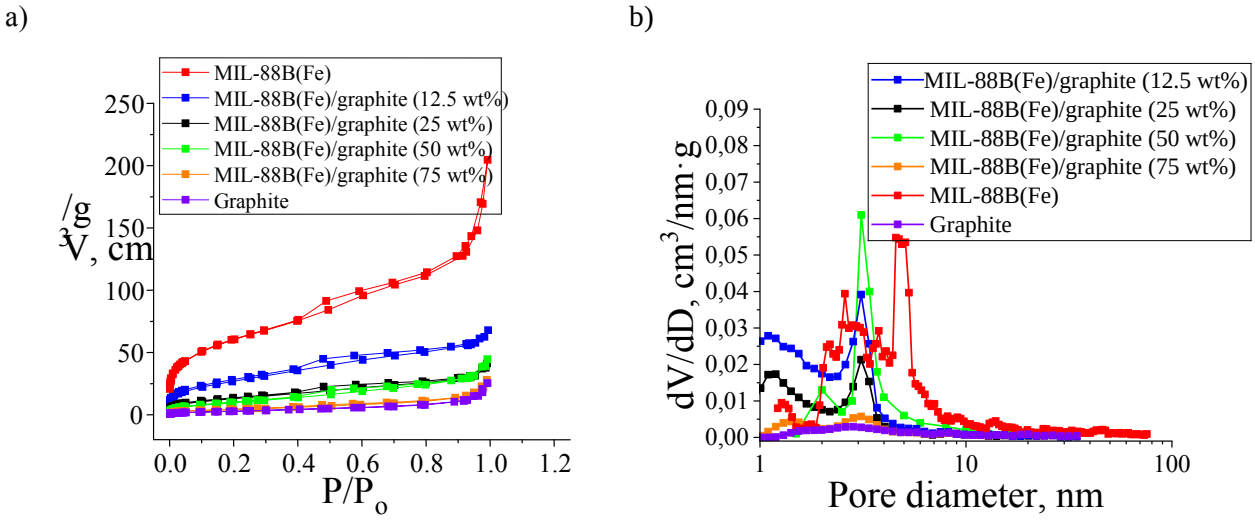

Figure 5. Nitrogen adsorption–desorption isotherms at 77 K (a) and differential pore size distribution curves for MIL-88B(Fe)/graphite composites (b)

Thermogravimetric Analysis

The thermal behavior of the samples was investigated by thermogravimetric analysis (TGA) in the range of 25–600 °C under a nitrogen atmosphere. All samples containing MIL-88B(Fe) exhibit a multistage weight loss. The data on the stages and temperature characteristics are summarized in Tables 4 and 5.

Table 4

Main stages of thermal decomposition of the MIL-88B(Fe)/graphite composites according to TGA data

Sample	Stage	Temperature range, °C	Mass loss, %
MIL–88B(Fe)	I	31-234	11.01
	II	235-372	8.19
	III	373-600	32.55
MIL-88B(Fe)/graphite (12.5 wt %)	I	31-250	6.33
	II	251-358	24.66
	III	359-600	19.13
MIL-88B(Fe)/graphite (25 wt %)	I	31-254	5.13
	II	255-355	15.97
	III	356-600	18.05
MIL-88B(Fe)/graphite (50 wt %)	I	31-264	5.44
	II	265-338	14.6
	III	339-600	19.11
MIL-88B(Fe)/graphite(75 wt %)	I	31-247	1.85
	II	248-327	4.63
	III	328-600	7.31
Graphite	I	31-600	1.95

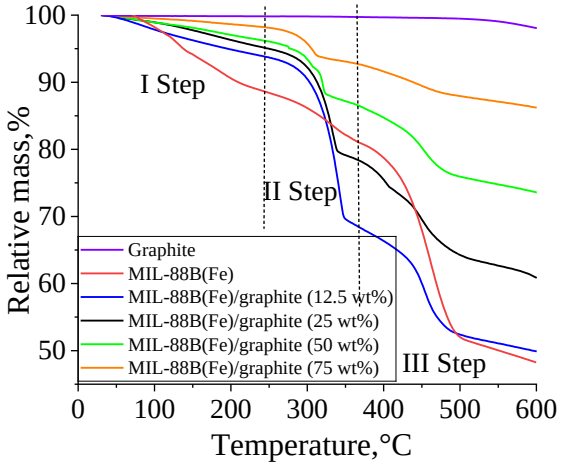

Figure 6. TGA curves of MIL-88B(Fe) and its composites, recorded at a heating rate of 10 °C/min under a nitrogen atmosphere

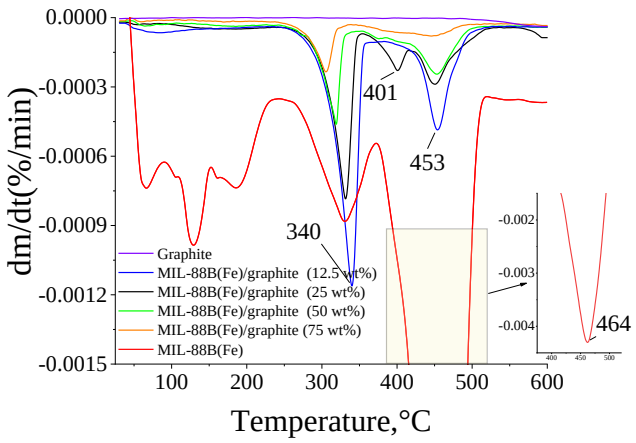

Figure 7. DTG curves of pristine MIL-88B(Fe) and its composites

Table 5

TGA data and residual mass at 600 °C (wt.%) for MIL-88B(Fe) and MIL-88B(Fe)/graphite composites

Sample	TGA data, °C						Residual mass at 600 °C, wt. %
	$T_{5\,\%}$	$T_{10\,\%}$	$T_{20\,\%}$	$T_{30\,\%}$	T_{max1}	T_{max2}	
MIL–88B(Fe)	138	209	386	444	336	464	48.3
MIL-88B(Fe)/graphite (12.5 wt %)	195	303	333	348	340	453	49.9
MIL-88B(Fe)/graphite (25 wt %)	249	313	338	447	330	401;451	60.9
MIL-88B(Fe)/graphite (50 wt %)	277	320	451	-	319	453	73.6
MIL-88B(Fe)/graphite(75 wt %)	305	439	-	-	305	446	86.2
T_i % — temperature of i % weight loss; Tmaxj — temperature of the maximum decomposition rate according to the DTG curve.							

For MIL-88B(Fe), three main decomposition stages are observed (Figure 6). The first stage (up to 234 °C, mass loss 11.0 %) corresponds to the removal of physically adsorbed and coordinated water from the framework pores. The second stage (8.2 %, 235–372 °C) is attributed to decarboxylation of the organic linker. The most significant mass loss occurs in the third stage (32.6 %, 373–600 °C) and is associated with complete decomposition of the terephthalate ligand to form Fe_2O_3 [62].

Comparison of the TGA data (Table 4) and elemental CHNO analysis (Table 2) reveals quantitative correlations between the actual graphite content and the thermal behavior of the MIL-88B/graphite composites. For all graphite-containing composites, the onset of the third decomposition stage is shifted to lower temperatures, specifically 328–359 °C, and its intensity regularly decreases with increasing graphite fraction. The mass loss in the third stage decreases from 19.13 % for the sample containing 12.5 wt. % graphite to 7.31 % for the sample with 75 wt% graphite, which is directly proportional to the decrease in the MOF content. An inverse linear correlation is observed between the graphite content and the mass loss in the first stage (30–250 °C), attributed to dehydration. For the sample with 75 % graphite, the mass loss in the first stage is only 1.85 wt. %, indicating a sharp decrease in surface hydrophilicity at high hydrophobic graphite loadings. Notably, the sample containing 8.3 % graphite, as determined by elemental analysis, shows a higher specific mass loss during the second decarboxylation stage than the pristine MOF. However, the introduction of 8 % graphite, corresponding to the MIL-88B/graphite composite with 12.5 wt. % graphite, already reduces the high-temperature loss in stage III from 32.6 % to 19.1 %, while further increasing the graphite fraction up to 50 % causes no additional decrease in mass loss. Overall, with increasing graphite weight fraction, the rate of mass loss associated with decarboxylation decreases (Figure 7).

The temperature of 5 % mass loss ($T_{5\,\%}$) increases from 138 °C for MIL-88B(Fe) to 305 °C for the MIL-88B(Fe)/graphite (75 wt. %) sample. A similar trend is observed for T10 %, which increases from 209 to 439 °C. This is due to the fact that the mass loss of pristine graphite up to 600 °C is only 1.95 %, which accounts for the increased apparent thermal stability of the composite. The residual mass at 600 °C monotonically increases from 48.25 to 86.21 %, reflecting the combined contribution of Fe_2O_3 and partially retained graphite (Table 5).

The DTG curves reveal two main maxima of the mass loss rate (T_{max1} and T_{max2}). The first maximum shifts from 131 °C for MIL-88B to 305–340 °C for the samples with 50–75 % graphite, indicating a change in the dehydration mechanism in the presence of graphite (Figure 7). The second maximum lies in the range of 446–464 °C for the entire composite series and can be attributed to the decomposition of the organic linker. For the composition with 25 % graphite, two mass loss rate maxima are observed at 401 and 451 °C, which may indicate heterogeneity of the resulting composite. For the graphite-containing samples, the residual mass includes both Fe_2O_3 from the MOF component and graphite partially retained under the experimental conditions (600 °C).

Morphology and Homogeneity of Component Distribution

In the optical micrographs (Figure 8, Figure S2), MOF particles are visualized as uniformly distributed orange inclusions against a dark background of graphite particles. Due to the color contrast between the MOF particles and the graphite matrix, automatic image segmentation with threshold-based object detection was performed. The linear particle size was calculated from the measured cross-sectional area, assuming a spindle-shaped elongated elliptical morphology with an aspect ratio of k = 2 [63] (S1). With increasing graphite content from 12.5 to 75 wt. %, the average particle length decreases from 3.05 ± 0.54 μm to 1.45 ± 0.49 μm (Figure S3). The observed decrease in particle size with increasing graphite content can be attributed to spatial confinement, where the excess graphite surface hinders further growth of MOF crystals and increases the number of nucleation sites.

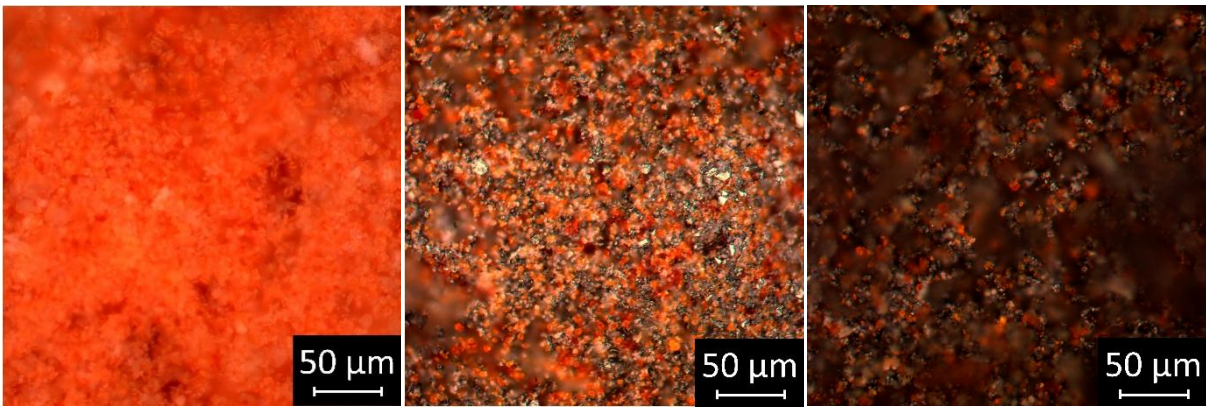

MIL-88B (Fe) | MIL-88B(Fe)/graphite (12,5 wt%) | MIL-88B(Fe)/graphite (25 wt%)

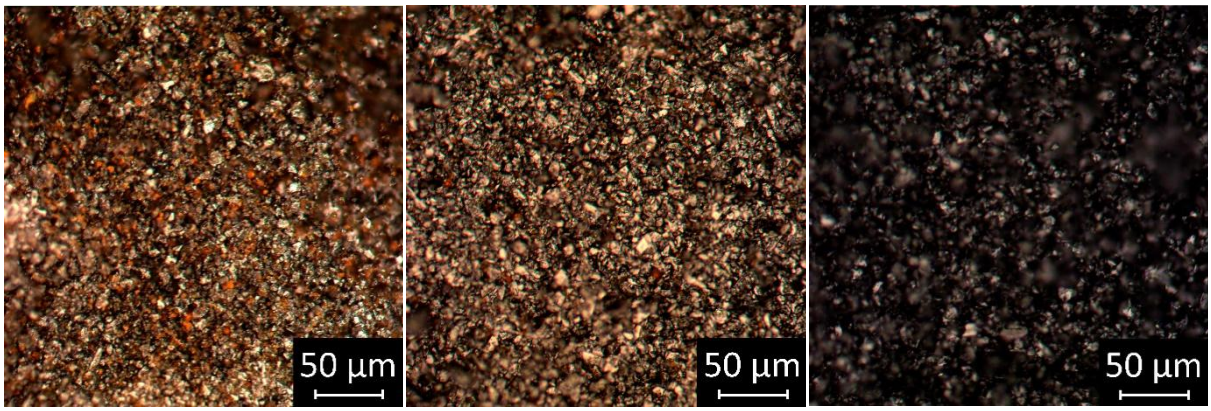

MIL-88B(Fe)/graphite (50 wt%) | MIL-88B(Fe)/graphite (75 wt%) | Graphite

Figure 8. Optical micrographs of MIL-88B(Fe)/graphite composites with different graphite contents (×50 objective, 925x magnification)

As can be seen from the SEM images (Figure 9a), MIL-88B(Fe) consists of needle-like elongated crystals with an average length of 7.27 ± 0.03 µm, whereas pristine graphite exhibits a flaky morphology (Figure 8f) with a particle size of 7.6 ± 0.2 µm and a tendency to aggregate. In the composites, even at 12.5 wt% graphite, aggregates with sharp edges are formed (Figure S4), with an average size of 12.8 ± 4.8 µm. At 25 wt% graphite, the particle size increases to 28.8 ± 8.6 µm, indicating enhanced aggregation. Further increases in graphite content to 50 and 75 wt% lead to a decrease in the average size to 9.0 ± 3.9 and 10.0 ± 2.0 µm, respectively, due to the dominance of the fine graphite phase. The observed non-monotonic particle size variation results from the balance between MOF crystal aggregation at low graphite contents and the dominance of the fine graphite phase at higher loadings.

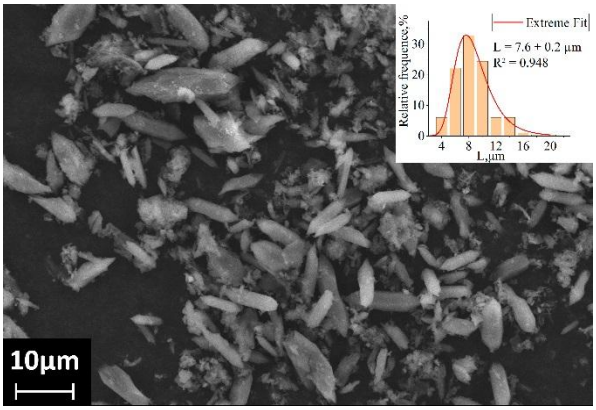

a) MIL-88B (Fe)

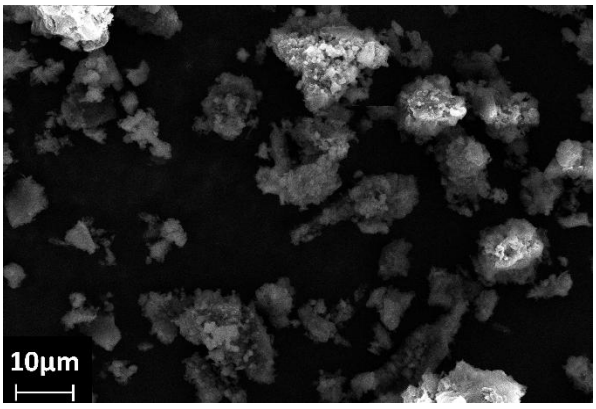

b) MIL-88B(Fe)/graphite (12,5 wt%)

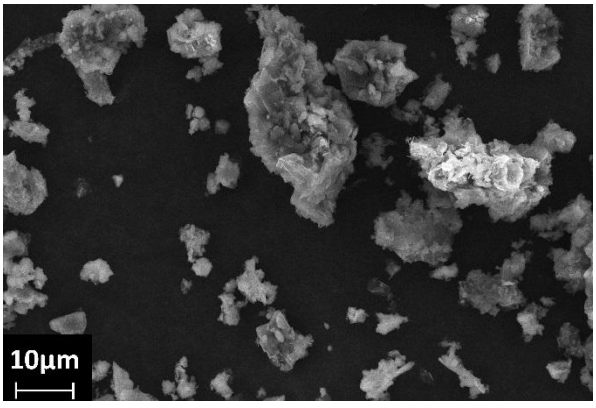

c) MIL-88B(Fe)/graphite (25 wt%)

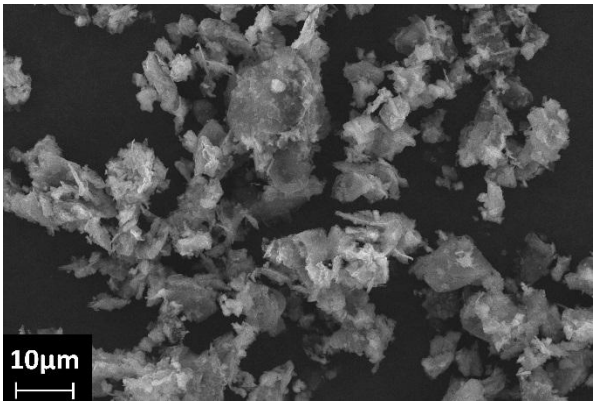

d) MIL-88B(Fe)/graphite (50 wt%)

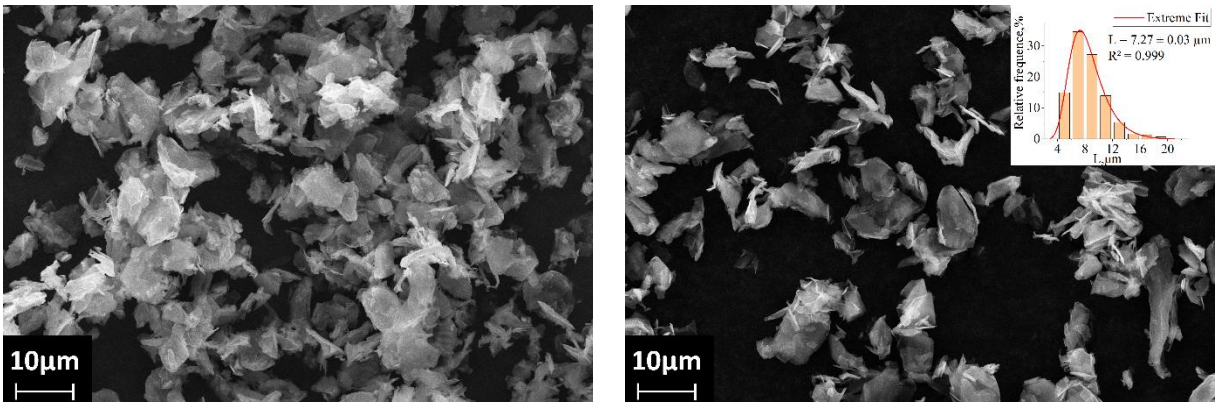

e) MIL-88B(Fe)/graphite (75 wt%) f) graphite

Figure 9. SEM images of the samples:a) MIL-88B(Fe); b) MIL-88B(Fe)/graphite (12.5 wt%); c) MIL-88B(Fe)/graphite (25 wt%); d) MIL-88B(Fe)/graphite 50 wt%); e) MIL-88B(Fe)/graphite (75 wt%); f) pristine graphite

Electrochemical Studies

The electrochemical properties of the synthesized materials were examined using cyclic voltammetry. Figure 10 shows the CV curves recorded over a wide potential range from -1.1 to 1.0 V in a 0.01 M NaOH solution. The oxygen reduction reaction region is observed at E < -0.5 V, and the oxygen evolution reaction region — at E > 0.8 V[64]. Pure MIL-88B(Fe) applied onto the working electrode exhibited low currents due to its poor electrical conductivity. An increase in the graphite content leads to an enhancement of the Faradaic currents on the CV curves (see curve for MIL-88B(Fe)/graphite (50 wt%) as a representative sample). Nevertheless, the addition of 50 wt% carbon black to pure MIL-88B(Fe) to improve the conductivity of the active layer leads to higher capacitive currents in the 0–0.4 V region compared to the MIL-88B(Fe)/graphite composite, despite their identical carbon content and mass loading. This observation indicates a smaller specific surface area for the graphite-based composite, which correlates with the BET data (Table 3). Moreover, the redox reactions within the carbon black-containing layer initiated at lower overpotentials compared to those for the graphite-containing composite.

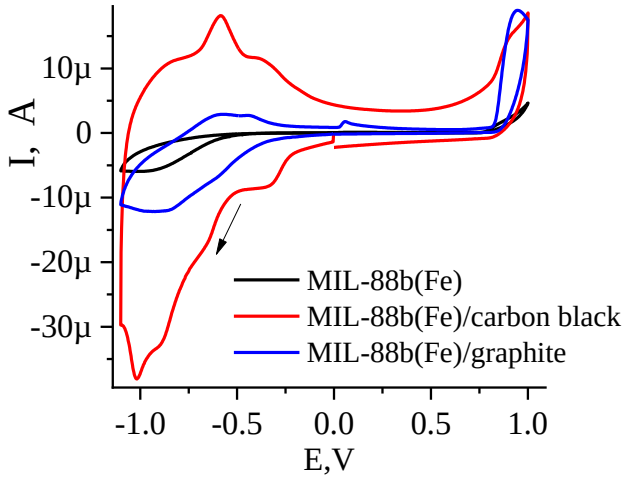

Figure 10. Cyclic voltammograms (scan rate 0.02 V/s) for the test strips with a graphite working electrode modified with MIL-88B(Fe), MIL-88B(Fe)/carbon black and MIL-88B(Fe)/graphite (50 wt%) composite in 0.01 M NaOH + 0.15 M NaCl.

Among the studied conditions, electrocatalytic activity toward glucose oxidation was observed exclusively for the MIL-88B(Fe)/carbon black in the alkaline medium (0.01 M NaOH), whereas this material remained inactive in acidic and neutral electrolytes. The use of the MIL-88B(Fe)/carbon black composition for electroanalytical testing is a rational way to avoid increasing the MOF content in the active layer, which

would otherwise lead to an increase in its thickness and ohmic resistance. As seen from the CV curves (Fig. 11a), an electrooxidation wave appears at E > 0.4 V in the presence of glucose. The chronoamperometric curves were recorded at an applied potential of 0.5 V (Fig. 11b). The steady-state currents increased with glucose concentration up to 5 mM, whereas higher concentrations did not lead to a further rise in current. The linear detection range (LDR), for the SPE modified with the MIL-88B(Fe)/carbon black composition, estimated from current values at 5 s, was 0.5...5 mM of glucose (R^2 = 0.9531). The sensitivity calculated from the linear regression in the LDR was 23 μA mM^{-1} cm^{-2}, the glucose detection limit was 0.17 mM.

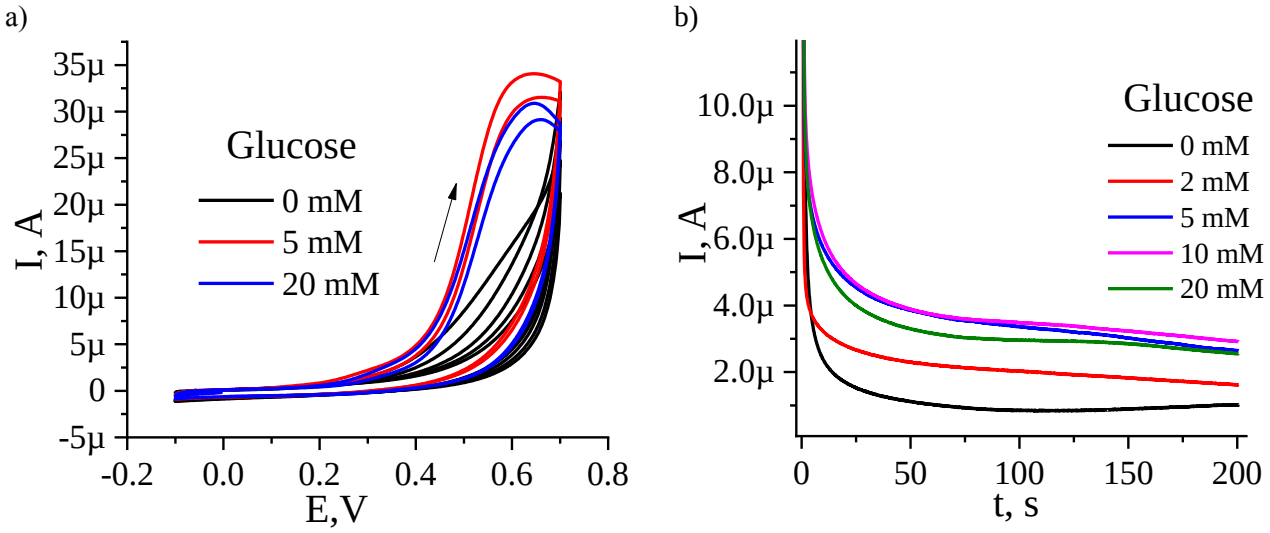

Figure 11. Cyclic voltammograms (scan rate 0.02 V/s) (a) and chronoamperometric curves recorded at 0.5 V (b) for test strips with a graphite working electrode modified with the MIL-88B(Fe)/carbon black in 0.01 M NaOH + 0.15 M NaCl containing glucose.

To sum up, keeping in mind that the LDR of modern glucose sensors is 1–30 mM, the sensor systems based on MIL-88B(Fe) require further optimization. For instance, the use of a flow-limiting membrane could be considered in the future to expand the linear detection range of the sensors based on MIL-88B(Fe) composites. However, it should be noted that the high anodic polarization used for glucose detection leads to a significant increase in cross-sensitivity; therefore, modifying the MOF composition is necessary to optimize the electroanalytical performance.

Conclusions

For the first time, a series of electrically conductive MIL-88B(Fe)/graphite composites with graphite contents ranging from 12.5 to 75 wt.% was successfully prepared using trinuclear iron(III) acetate as the precursor. According to BET analysis, the specific surface area non‑monotonically decreases from 220 m^2/g for MIL-88B(Fe) to 15.2 m^2/g for MIL‑88B(Fe)/graphite (75 wt.%), while the calculated QSDFT pore diameter shifts from 4.6 nm for pure MIL-88B(Fe) to a stable 3.1 nm for the composites. Importantly, this suggests that graphite is localized on the external surface of the MOF crystals without significant penetration into the pores. Furthermore, XRD confirmed the absence of secondary iron oxide phases in the proposed synthesis route, indicating the high phase purity of the MIL-88B(Fe)/graphite composites. FTIR spectroscopy of the MIL-88B(Fe)/graphite composites revealed splitting of the carboxylate stretching vibration bands and the appearance of a band at 1688 cm^{-1}, indicating the presence of dangling linkers coordinated to the metal cluster via only one carboxylate group. This is attributed to incomplete substitution of carboxylate fragments during the *in situ* synthesis in the presence of graphite. Raman spectroscopy confirmed the presence of the graphite phase in the composites and showed an increase in graphite defectiveness upon synthesis. The characteristic bands of the terephthalate linker of MIL-88B(Fe) (~1603, 1502, 1427, 1284, and 1132 cm^{-1}) were identified, confirming the preservation of the MOF structure. Scanning electron microscopy showed that aggregates are already formed in the composites at 12.5 wt% graphite, and the particle size exhibits a non‑monotonic behavior reflecting the competition between MOF aggregation and graphite phase distribution. An inverse linear correlation was found between the graphite content and the mass loss in the first de-

composition stage, attributed to dehydration. With increasing graphite weight fraction, the rate of mass loss associated with decarboxylation decreases, and the decomposition intensity regularly diminishes. As the MOF content in the composite increases, both the total number of particles and their degree of aggregation increase. Electrocatalytic activity of MIL-88B(Fe) toward glucose in alkaline medium was observed for the first time; however, further studies are required to improve the sensing performance.

Supporting Information

The Supporting Information is available free at https://ejc.buketov.edu.kz/ejc/article/view/776/419

Funding

This research was supported by a grant from the Russian Science Foundation (RSF), Project No. 26-13-00404 (https://rscf.ru/project/26-13-00404/).

*Author Information**

**The authors' names are presented in the following order: First Name, Middle Name and Last Name*

Rose Baimuratova Kurmangalievna (*corresponding author*) — Candidate of Chemical Sciences, Researcher, Federal Research Center of Problems of Chemical Physics and Medicinal Chemistry Russian Academy of Sciences, Ac. Semenov avenue 1, 142432, Chernogolovka, Moscow region, Russia; e-mail: roz_baz@mail.ru; https://orcid.org/0000-0002-8389-6871

Ravil Nailevich Bazargulov — Student, Department of Fundamental Physical and Chemical Engineering, Lomonosov Moscow State University, 1 Leninskie Gory, Build. 51, 119991 Moscow, Russian Federation; Research Trainee at the Federal Research Center of Problems of Chemical Physics and Medicinal Chemistry, Russian Academy of Sciences, 142432, Chernogolovka, Moscow Region, Russia; e-mail: elektrosolbox@gmail.com

Sofia Alekseevna Kleinikova — Candidate of Chemical Sciences, Junior Researcher, Federal Research Center of Problems of Chemical Physics and Medicinal Chemistry Russian Academy of Sciences, Ac. Semenov avenue 1, 142432, Chernogolovka, Moscow region, Russia; e-mail: s.a.kleinikova@icp.ac.ru; https://orcid.org/0000-0001-7802-4967

Ekaterina Viktorovna Zolotukhina — Doctor of Chemical Sciences, Deputy Director for Research, Head of Laboratory, Federal Research Center of Problems of Chemical Physics and Medicinal Chemistry Russian Academy of Sciences, Ac. Semenov avenue 1, 142432, Chernogolovka, Moscow region, Russia; e-mail: zolek@icp.ac.ru; https://orcid.org/0000-0002-1735-0264

Konstantin Vladimirovich Gor'kov — Candidate of Chemical Sciences, Researcher, Federal Research Center of Problems of Chemical Physics and Medicinal Chemistry Russian Academy of Sciences, Ac. Semenov avenue 1, 142432, Chernogolovka, Moscow region, Russia; e-mail: gorkovk@yandex.ru; https://orcid.org/0000-0003-1946-8597

Mikhail Vladimirovich Zhidkov — Candidate of Technical Sciences, Researcher, Federal Research Center of Problems of Chemical Physics and Medicinal Chemistry Russian Academy of Sciences, Ac. Semenov avenue 1, 142432, Chernogolovka, Moscow region, Russia; e-mail: zhidkov@icp.ac.ru; https://orcid.org/0000-0001-7513-2057

Gulzhian Iskakovna Dzhardimalieva — Doctor of Chemical Sciences, Head of Laboratory of Metallopolymers, Federal Research Center of Problems of Chemical Physics and Medicinal Chemistry Russian Academy of Sciences, Ac. Semenov avenue 1, 142432, Chernogolovka, Moscow region, Russia; Professor, Moscow Aviation Institute (National Research University), 4 Volokolamskoe Highway, 125993, Moscow, Russia; e-mail: dzhardim@icp.ac.ru; https://orcid.org/0000-0002-4727-8910

Author Contributions

The manuscript was written through contributions of all authors. All authors have given approval to the final version of the manuscript. CRediT: **Baimuratova Rose Kurmangalievna** conceptualization, methodology, data curation, investigation, writing-original draft; **Ravil Nailevich Bazargulov** investigation, valida-

tion, visualization; **Sofia Alekseevna Kleinikova** investigation, visualization, writing-original draft; **Ekaterina Viktorovna Zolotukhina** methodology, data curation, supervision, writing-review & editing; **Konstantin Vladimirovich Gor'kov** investigation, data curation, validation; **Mikhail Vladimirovich Zhidkov** investigation, data curation; **Gulzhian Iskakovna Dzhardimalieva** conceptualization, data curation, funding acquisition, resources, supervision, writing-review & editing.

Acknowledgments

Low-temperature nitrogen adsorption and IR spectroscopy were carried out by using the equipment of the Multi-User Analytical Center of Federal Research Center of Problems of Chemical Physics and Medicinal Chemistry Russian Academy of Sciences.

Conflicts of Interest

The authors declare no conflict of interest.

References

1 Raveendran, A. V., Chandran, M., & Dhanusuraman, R. (2023). A comprehensive review on the electrochemical parameters and recent material development of electrochemical water splitting electrocatalysts. *RSC Advances*, *13*, 3843–3876. https://doi.org/10.1039/d2ra07642j

2 Water electrolysis: From textbook knowledge to the latest scientific strategies and industrial developments. (2022). *Chemical Society Reviews*, *51*, 4583–4762. https://doi.org/10.1039/d0cs01079k

3 Zhai, Q., Huang, H., Lawson, T., Xia, Z., Giusto, P., Antonietti, M., Jaroniec, M., Chhowalla, M., Baek, J. -B., Liu, Y., Qiao, S., & Dai, L. (2024). Recent Advances on Carbon-Based Metal-Free Electrocatalysts for Energy and Chemical Conversions. *Advanced Materials*, *36*. https://doi.org/10.1002/adma.202405664

4 Fan, L., Xia, C., Yang, F., Wang, J., Wang, H., & Lu, Y. (2020). Strategies in catalysts and electrolyzer design for electrochemical CO2 reduction toward C2+ products. *Science Advances*, *6*. https://doi.org/10.1126/sciadv.aay3111

5 Overa, S., Ko, B., Zhao, Y., & Jiao, F. (2022). Electrochemical Approaches for CO2 Conversion to Chemicals: A Journey toward Practical Applications. *Accounts of chemical research*. https://doi.org/10.1021/acs.accounts.1c00674

6 Singh, S., Yadav, R. K., Kim, T. W., Singh, C., Singh, P., Chaubey, S., Rose, B., Gulzhian, D., & Khare, P. (2022). In Situ Prepared NRCPFs as Highly Active Photo Platforms for in Situ Bond Formation Between Aryldiazonium Salts and Heteroarenes. *Photochemistry and Photobiology*, *98*(4), 748–753. https://doi.org/10.1111/php.13639

7 Ferreira, A. P. R. A., Oliveira, R. C. P., Mateus, M., & Santos, D. (2023). A Review of the Use of Electrolytic Cells for Energy and Environmental Applications. *Energies*. https://doi.org/10.3390/en16041593

8 Azari, P., Hasheminejad, H., & Zarean Mousaabadi, K. (2025). Synthesis and characterization of MIL-88 A (Fe)/C composite for treatment of dairy factory's wastewater by enhanced electro-Fenton method. *Scientific Reports*, *15*(1), 8503. https://doi.org/10.1038/s41598-025-92765-4

9 Dhara, K., & Mahapatra, D. (2017). Electrochemical nonenzymatic sensing of glucose using advanced nanomaterials. *Microchimica Acta*, *185*, 1–32. https://doi.org/10.1007/s00604-017-2609-1

10 Li, H., Xiao, N., Jiang, M., Long, J., Li, Z., & Zhu, Z. (2024). Advances of Transition Metal-Based Electrochemical Nonenzymatic Glucose Sensors for Glucose Analysis: A Review. *Critical Reviews in Analytical Chemistry*, *55*, 1099–1135. https://doi.org/10.1080/10408347.2024.2339955

11 Zhang, J., Xiong, Q., & Xu, J. (2024). Research progress in non-precious metal oxide/compound-based electrodes for non-enzymatic electrochemical glucose sensor applications. *Materials Science in Semiconductor Processing*. https://doi.org/10.1016/j.mssp.2024.108643

12 Batten, S. R., Champness, N. R., Chen, X. -M., Garcia-Martinez, J., Kitagawa, S., Öhrström, L., O'Keeffe, M., Paik Suh, M., & Reedijk, J. (2013). Terminology of metal–organic frameworks and coordination polymers (IUPAC Recommendations 2013). *Pure and Applied Chemistry*, *85*(8), 1715–1724. https://doi.org/10.1351/PAC-REC-12-11-20

13 Gao, Q., Sheng, Q., Zhang, S., & Tang, Y. (2025). Recent trends on MIL-88(Fe) metal–organic frameworks: Synthesis and applications in pollutant removal and detection. *RSC Advances*, *15*(32), 26184–26200. https://doi.org/10.1039/D5RA03049H

14 Channab, B. -E., El Ouardi, M., Ait Layachi, O., Marrane, S. E., El Idrissi, A., BaQais, A., & Ait Ahsaine, H. (2023). Recent trends on MIL-Fe metal–organic frameworks: Synthesis approaches, structural insights, and applications in organic pollutant adsorption and photocatalytic degradation. *Environmental Science: Nano*, *10*(11), 2957–2988. https://doi.org/10.1039/d3en00332a

15 Huang, Q., Zeb, A., Xu, Z., Sahar, S., Zhou, J. -E., Lin, X., Wu, Z., Reddy, R. C. K., Xiao, X., & Hu, L. (2023). Fe-based metal-organic frameworks and their derivatives for electrochemical energy conversion and storage. *Coordination Chemistry Reviews*, *494*, 215335. https://doi.org/10.1016/j.ccr.2023.215335

16 Morozan, A., & Jaouen, F. (2012). Metal organic frameworks for electrochemical applications. *Energy & Environmental Science*, *5*(11), 9269–9290. https://doi.org/10.1039/C2EE22989G

17 Ishimoto, T., Ogura, T., Koyama, M., Yang, L., Kinoshita, S., Yamada, T., Tokunaga, M., & Kitagawa, H. (2013). A Key Mechanism of Ethanol Electrooxidation Reaction in a Noble-Metal-Free Metal–Organic Framework. *The Journal of Physical Chemistry C*, *117*(20), 10607–10614. https://doi.org/10.1021/jp4031046

18 Serre, C., Mellot-Draznieks, C., Surblé, S., Audebrand, N., Filinchuk, Y., & Férey, G. (2007). Role of solvent-host interactions that lead to very large swelling of hybrid frameworks. *Science*, *315*(5820), 1828–1831.

19 Horcajada, P., Serre, C., Maurin, G., Ramsahye, N. A., Balas, F., Vallet-Regí, M., Sebban, M., Taulelle, F., & Férey, G. (2008). Flexible Porous Metal-Organic Frameworks for a Controlled Drug Delivery. *Journal of the American Chemical Society*, *130*(21), 6774–6780. https://doi.org/10.1021/ja710973k

20 Ma, M., Bétard, A., Weber, I., Al-Hokbany, N. S., Fischer, R. A., & Metzler-Nolte, N. (2013). Iron-Based Metal–Organic Frameworks MIL-88B and NH2-MIL-88B: High Quality Microwave Synthesis and Solvent-Induced Lattice "Breathing". *Crystal Growth & Design*, *13*(6), 2286–2291. https://doi.org/10.1021/cg301738p

21 Gao, F., Yan, R., Shu, Y., Cao, Q., & Zhang, L. (2022). Strategies for the application of metal–organic frameworks in catalytic reactions. *RSC Advances*, *12*(16), 10114–10125. https://doi.org/10.1039/D2RA01175A

22 Zhu, Q. -L., & Xu, Q. (2014). Metal–organic framework composites. *Chem. Soc. Rev.*, *43*(16), 5468–5512. https://doi.org/10.1039/C3CS60472A

23 Liew, A. S. Y., Nguang, S. Y., Minggu, L. J., Tahir, N., & Moh, P. Y. (2021). Graphene oxide incorporated amino-functionalized iron terephthalate composite as a heterogeneous Fenton-like catalyst. *Journal of the Chinese Chemical Society*, *68*(10), 1887–1896. https://doi.org/10.1002/jccs.202100183

24 Elmowafy, M. E., Zorainy, M., Abuzalat, O., Baraka, A., Sadek, R., & Tantawy, H. (2025). A novel double-layer MIL-88B (Fe/Co)/RGO composite as a superior microwave shielding material. *Journal of Nanoparticle Research*, *27*(8), 211. https://doi.org/10.1007/s11051-025-06393-0

25 Abazari, R., Sanati, S., & Morsali, A. (2022). Mixed metal Fe2Ni MIL-88B metal–organic frameworks decorated on reduced graphene oxide as a robust and highly efficient electrocatalyst for alkaline water oxidation. *Inorganic Chemistry*, *61*(8), 3396–3405.

26 Jia, D., Shen, Z., Lv, Y., Chen, Z., Li, H., Yu, Y., Qiu, J., & He, X. (2024). In situ electrochemical tuning of MIL-88B (V)@ rGO into amorphous V2O5@ rGO as cathode for high-performance aqueous zinc-ion battery. *Advanced Functional Materials*, *34*(2), 2308319. https://doi.org/10.1002/adfm.202308319

27 Zhang, C., Weiqiang, H., Jiang, H., Chang, J. -K., Zheng, M. -S., Wu, Q., & Dong, Q. (2017). Electrochemical performance of MIL-53(Fe)@RGO as an Organic Anode Material for Li-ion Batteries. *Electrochimica Acta*, *246*. https://doi.org/10.1016/j.electacta.2017.06.059

28 Jin, Y., Zhao, C., Lin, Y., Wang, D., Chen, L., & Shen, C. (2017). Fe-Based Metal-Organic Framework and Its Derivatives for Reversible Lithium Storage. *Journal of Materials Science & Technology*, *33*(8), 768–774. https://doi.org/10.1016/j.jmst.2016.11.021

29 Zhang, H., Chen, S., Zhang, H., Fan, X., Gao, C., Yu, H., & Quan, X. (2019). Carbon nanotubes-incorporated MIL-88B-Fe as highly efficient Fenton-like catalyst for degradation of organic pollutants. *Frontiers of Environmental Science & Engineering*, *13*(2), 18. https://doi.org/10.1007/s11783-019-1101-z

30 Qin, W., He, L., Zhang, Y., Li, B., Han, L., & Xu, Y. (2024). Synchronous wrapping and inward-etching strategy on constructing yolk-shell MIL-88A@ NiFe-PB heterostructures for electrochemical non-enzymatic glucose detection. *Microchemical Journal*, *196*, 109641. https://doi.org/10.1016/j.microc.2023.109641

31 Baimuratova, R. K., Zhinzhilo, V. A., Uflyand, I. E., Dmitriev, A. I., Zhidkov, M. V., Ovanesyan, N. S., Kugabaeva, G. D., & Dzhardimalieva, G. I. (2023). Low-Temperature Synthesis of Metal–Organic Coordination Polymers Based on Oxo-centered Iron Complexes: Magnetic and Adsorption Properties. *Russian Journal of Physical Chemistry A*, *97*(4), 735–748. https://doi.org/10.1134/S0036024423040064

32 Sidorov, V. I., Baimuratova, R. K., Korchagin, D. V., Ivanov, A. I., Kydralieva, K. A., & Dzhardimalieva, G. I. (2024). Magnetically Separable Fe3O4/γ-Fe2O3@MIL-88b(Fe) and Fe3O4/γ-Fe2O3@NH2-MIL-88b(Fe) Composites for the Photocatalytic Degradation of Congo Red Dye. *Eurasian Journal of Chemistry*, *29*(3 (115)), 130–147. https://doi.org/10.31489/2959-0663/3-24-5

33 Collins, T. J. (2007). ImageJ for microscopy. *Biotechniques*, *43*(sup1), S25–S30.

34 Chen, Z., Hanna, S. L., Redfern, L. R., Alezi, D., Islamoglu, T., & Farha, O. K. (2019). Reticular chemistry in the rational synthesis of functional zirconium cluster-based MOFs. *Coordination Chemistry Reviews*, *386*, 32–49. https://doi.org/10.1016/j.ccr.2019.01.017

35 Kumar, P., & Bohidar, H. B. (2010). Aqueous dispersion stability of multi-carbon nanoparticles in anionic, cationic, neutral, bile salt and pulmonary surfactant solutions. *Colloids and Surfaces A: Physicochemical and Engineering Aspects*, *361*(1–3), 13–24.

36 Agola, P., & Taddei, M. (2026). A water-based synthetic route to the metal–organic framework UiO-66 starting from PET-derived terephthalate esters. *RSC Sustainability*, *4*(1), 466–476. https://doi.org/10.1039/D5SU00463B

37 Sánchez-Sánchez, M., Getachew, N., Díaz, K., Díaz-García, M., Chebude, Y., & Díaz, I. (2015). Synthesis of metal–organic frameworks in water at room temperature: Salts as linker sources. *Green Chemistry*, *17*, 1500–1509. https://doi.org/10.1039/c4gc01861c

38 Kondo, Y., Kuwahara, Y., Mori, K., & Yamashita, H. (2021). Dual role of missing-linker defects terminated by acetate ligands in a zirconium-based MOF in promoting photocatalytic hydrogen peroxide production. *The Journal of Physical Chemistry C*, *125*(51), 27909–27918. https://doi.org/10.1021/acs.jpcc.1c07735

39 Shearer, G. C., Chavan, S., Bordiga, S., Svelle, S., Olsbye, U., & Lillerud, K. P. (2016). Defect Engineering: Tuning the Porosity and Composition of the Metal–Organic Framework UiO-66 via Modulated Synthesis. *Chemistry of Materials*, *28*(11), 3749–3761. https://doi.org/10.1021/acs.chemmater.6b00602

40 Pangestu, A., Lestari, W. W., Wibowo, F. R., & Larasati, L. (2022). Green Electro-Synthesized MIL-101(Fe) and Its Aspirin Detoxification Performance Compared to MOF-808. *Journal of Inorganic and Organometallic Polymers and Materials*, *32*(5), 1828–1839. https://doi.org/10.1007/s10904-022-02235-x

41 Chávez, A. M., Rey, A., López, J., Álvarez, P., & Beltrán, F. (2021). Critical aspects of the stability and catalytic activity of MIL-100(Fe) in different advanced oxidation processes. *Separation and Purification Technology*, *255*. https://doi.org/10.1016/j.seppur.2020.117660

42 Wang, K. -Y., Yang, Z., Zhang, J., Banerjee, S., Joseph, E., Hsu, Y. -C., Yuan, S., Feng, L., & Zhou, H. (2022). Creating hierarchical pores in metal–organic frameworks via postsynthetic reactions. *Nature Protocols*, *18*, 604–625. https://doi.org/10.1038/s41596-022-00759-7

43 Schneemann, A., Bon, V., Schwedler, I., Senkovska, I., Kaskel, S., & Fischer, R. A. (2014). Flexible metal–organic frameworks. *Chem. Soc. Rev.*, *43*(16), 6062–6096. https://doi.org/10.1039/C4CS00101J

44 Li, Y., Wang, Y., Fan, W., & Sun, D. (2022). Flexible metal–organic frameworks for gas storage and separation. *Dalton Transactions*, *51*(12), 4608–4618. https://doi.org/10.1039/D1DT03842G

45 Pallach, R., Keupp, J., Terlinden, K., Frentzel-Beyme, L., Kloß, M., Machalica, A., Kotschy, J., Vasa, S. K., Chater, P. A., Sternemann, C., Wharmby, M. T., Linser, R., Schmid, R., & Henke, S. (2021). Frustrated flexibility in metal-organic frameworks. *Nature Communications*, *12*(1), 4097. https://doi.org/10.1038/s41467-021-24188-4

46 Mellot-Draznieks, C., Serre, C., Surblé, S., Audebrand, N., & Férey, G. (2005). Very Large Swelling in Hybrid Frameworks: A Combined Computational and Powder Diffraction Study. *Journal of the American Chemical Society*, *127*(46), 16273–16278. https://doi.org/10.1021/ja054900x

47 Ye, Z., Zhang, W., Lanzalaco, S., Zhao, L., Sirés, I., Xia, P., Zhai, J., & He, Q. (2023). Ultra-uniform MIL-88B(Fe)/Fe3S4 hybrids engineered by partial sulfidation to boost catalysis in electro-Fenton treatment of micropollutants: Experimental and mechanistic insights. *Chemical Engineering Journal*, *455*, 140757. https://doi.org/10.1016/j.cej.2022.140757

48 Zhang, S., Zhuo, Y., Ezugwu, C. I., Wang, C., Li, C., & Liu, S. (2021). Synergetic Molecular Oxygen Activation and Catalytic Oxidation of Formaldehyde over Defective MIL-88B(Fe) Nanorods at Room Temperature. *Environmental Science & Technology*, *55*(12), 8341–8350. https://doi.org/10.1021/acs.est.1c01277

49 Karagiaridi, O., Vermeulen, N. A., Klet, R. C., Wang, T. C., Moghadam, P. Z., Al-Juaid, S. S., Stoddart, J. F., Hupp, J. T., & Farha, O. K. (2015). Functionalized defects through solvent-assisted linker exchange: Synthesis, characterization, and partial postsynthesis elaboration of a metal–organic framework containing free carboxylic acid moieties. *Inorganic chemistry*, *54*(4), 1785–1790. https://doi.org/10.1021/ic502697y

50 Nakamoto, K. (2009). *Infrared and Raman spectra of inorganic and coordination compounds* (6th ed). Wiley. https://doi.org/10.1002/9780470405840

51 Aizyatullov, A. S., Baimuratova, R. K., Sidorov, V. L., Spirin, M. G., Shilov, G. V., Dremova, N. N., & Dzhardimalieva, G. I. (2026). Engineering TiO2/MIL-88b(Fe) heterostructures for enhanced photocatalytic degradation of organic dyes. *Materials Science in Semiconductor Processing*, *211*, 110725. https://doi.org/10.1016/j.mssp.2026.110725

52 Hollauer, E., Mondragon, M. A., & Castaño, V. M. (2001). Fourier transform infrared and Raman spectra, vibrational assignment and ab initio calculations of terephthalic acid and related compounds. *Spectrochimica Acta Part A: Molecular and Biomolecular Spectroscopy*, *57*(5), 993–1007. https://doi.org/10.1016/s1386-1425(00)00428-5

53 Deacon, G. B., & Phillips, R. J. (1980). Relationships between the carbon-oxygen stretching frequencies of carboxylato complexes and the type of carboxylate coordination. *Coordination chemistry reviews*, *33*(3), 227–250. https://doi.org/10.1016/s0010-8545(00)80455-5

54 Tuinstra, F., & Koenig, J. L. (1970). Raman spectrum of graphite. *The Journal of chemical physics*, *53*(3), 1126–1130. https://doi.org/10.1063/1.1674108

55 Ferrari, A. C., & Robertson, J. (2000). Interpretation of Raman spectra of disordered and amorphous carbon. *Physical review B*, *61*(20), 14095. https://doi.org/10.1103/physrevb.61.14095

56 Nguyen, V. H., Nguyen, T. D., Bach, L. G., Hoang, T., Bui, Q. T. P., Tran, L. D., Nguyen, C. V., Vo, D. -V. N., & Do, S. T. (2018). Effective Photocatalytic Activity of Mixed Ni/Fe-Base Metal-Organic Framework under a Compact Fluorescent Daylight Lamp. *Catalysts*, *8*(11), 487. https://doi.org/10.3390/catal8110487

57 Hadjiivanov, K. I., Panayotov, D. A., Mihaylov, M. Y., Ivanova, E. Z., Chakarova, K. K., Andonova, S. M., & Drenchev, N. L. (2020). Power of infrared and Raman spectroscopies to characterize metal-organic frameworks and investigate their interaction with guest molecules. *Chemical Reviews*, *121*(3), 1286–1424. https://doi.org/10.1021/acs.chemrev.0c00487

58 Banerjee, P. C., Lobo, D. E., Middag, R., Ng, W. K., & Et., A. (2015). Electrochemical Capacitance of Ni-Doped Metal Organic Framework and Reduced Graphene Oxide Composites: More than the Sum of Its Parts. *ACS Applied Materials & Interfaces*. https://doi.org/10.1021/am508119c

59 Guo, M., & Li, H. (2021). The Hydrolyzed Mil-88B(Fe) With Improved Surface Area for High-Capacity Lithium Ion Battery. *Frontiers in Energy Research*, *9*, 781008. https://doi.org/10.3389/fenrg.2021.781008

60 Hou, S., Wu, Y., Feng, L., Chen, W., Wang, Y., Morlay, C., & Li, F. (2018). Green synthesis and evaluation of an iron-based metal–organic framework MIL-88B for efficient decontamination of arsenate from water. *Dalton Transactions*, *47*(7), 2222–2231. https://doi.org/10.1039/C7DT03775A

61 Morsy, M., Hassan, S. S., Shaker, H. M., & Ismail, K. M. (2025). Synthesis and characterization of MIL-88B(Fe) MOF for high-performance humidity sensing. *Sensors and Actuators B: Chemical*, *438*, 137806. https://doi.org/10.1016/j.snb.2025.137806

62 Zorainy, M. Y., Kaliaguine, S., Gobara, M., Elbasuney, S., & Boffito, D. C. (2022). Microwave-Assisted Synthesis of the Flexible Iron-based MIL-88B Metal–Organic Framework for Advanced Energetic Systems. *Journal of Inorganic and Organometallic Polymers and Materials*, *32*(7), 2538–2556. https://doi.org/10.1007/s10904-022-02353-6

63 Xu, B., Yang, H., Cai, Y., Yang, H., & Li, C. (2016). Preparation and photocatalytic property of spindle-like MIL-88B (Fe) nanoparticles. *Inorganic Chemistry Communications*, *67*, 29–31. https://doi.org/10.1016/j.inoche.2016.03.003

64 Bhardwaj, U., Janjani, P., Sharma, R., & Kushwaha, H. S. (2023). Investigation of Single-Metal Fe-Based Metal–Organic Framework as an Electrocatalyst for a Rechargeable Zinc-Air Battery. *Journal of Electronic Materials*, *52*(2), 917–924. https://doi.org/10.1007/s11664-022-10106-x

How to Cite: Vissurkhanova, Ya.A., Ivanova, N.M., Soboleva, Ye.A., & Muldakhmetov, Z.M. (2026). Comparison of the Influence of Polymer Additives on the Thermal and Electrochemical Reduction of Copper Ferrites and Electrocatalytic Activity of the Formed Fe-Cu Composites. *Eurasian Journal of Chemistry, 31, 3(123), 117–128.* https://doi.org/10.31489/2959-0663/3-26-6

Article

Received: 1 June 2026 | Revised: 14 August 2026 |
Accepted: 24 August 2026 | Published online: 28 August 2026

UDC 546.562+541.64+546.562+544.653.3 https://doi.org/10.31489/2959-0663/3-26-6

Yakha A. Vissurkhanova[1,2*], Nina M. Ivanova[1], Yelena A. Soboleva[1], Zainulla M. Muldakhmetov[1]

[1]*LLP "Institute of Organic Synthesis and Coal Chemistry of the Republic of Kazakhstan", Karaganda, Kazakhstan*
[2]*Buketov Karaganda National Research University, Karaganda, Kazakhstan*
*(*Corresponding author's e-mail: yakhavisurkhanova@bk.ru)*

Comparison of the Influence of Polymer Additives on the Thermal and Electrochemical Reduction of Copper Ferrites and Electrocatalytic Activity of the Formed Fe-Cu Composites

The conducted studies compared the influence of polymers (PVA, PVP, PEG and g-C_3N_4) added to the copper(II) and iron(III) cations co-precipitation environment during the preparation of copper(II) ferrite precursors on the phase compositions of $CuFe_2O_4$ + Polymer samples heat-treated at 700 °C, their electrochemical reduction, and the electrocatalytic activity of the resulting Fe-Cu composites. The structure and morphological features of $CuFe_2O_4$ + Polymer samples after heat treatment (HT) and electrochemical experiments were studied using XRD analysis and electron microscopy. Thermogravimetric studies were performed for the polymers and copper ferrite precursors. The results indicate that the thermal degradation products of PVA and g-C_3N_4 polymers induce a partial decomposition of copper ferrites during HT, yielding crystalline phases of copper and iron, thereby significantly decreasing the duration of the subsequent electrochemical reduction of these samples. "Pure" $CuFe_2O_4$ and samples containing other polymers remain stable at 700 °C. Electrochemical reduction of $CuFe_2O_4$ + PVP and $CuFe_2O_4$ + PEG samples result in a more complete reduction of iron cations than in other samples, which is favourable for intensifying the electrohydrogenation of 4-nitrophenol on Fe-Cu composites formed from these samples. The fabrication of a single product, 4-aminophenol, is confirmed by UV-vis spectra.

Keywords: copper ferrite, polymer additives, co-precipitation, heat treatment, electrochemical reduction, Fe-Cu composites, electrocatalytic hydrogenation, 4-nitrophenol

Introduction

Copper ferrite (II) ($CuFe_2O_4$) is a typical iron-based cubic spinel with high chemical stability, moderate non-toxicity, low cost, and excellent magnetic properties [1, 2]. Copper ferrite, like other transition metal ferrites, is widely utilized in applications ranging from environmental remediation and drug delivery to high-density magnetic storage and catalysis [3–6]. Copper ferrite nanoparticles are used as catalysts in classical thermocatalytic and electrocatalytic processes. The properties of copper ferrite are highly dependent on the synthesis parameters, such as the Fe/Cu ratio, calcination temperature and time, and the use of different stabilizers of copper ferrite nanoparticles or their supports.

Copper ferrite is produced by various methods, the main ones being ceramic technologies using metal oxide powders, CuO and Fe_2O_3 [7, 8]. However, these methods are quite laborious, especially when producing nanosized samples. In methods such as sol-gel, hydro/solvothermal, co-precipitation, and others, various organic compounds, including polymers, are often used to stabilize copper ferrite nanoparticles. For example, paper [9] describes the production of copper(II) ferrite nanoparticles by a hydrothermal method, in which salts of both metals were dissolved in an aqueous solution of ethylene glycol, then the pH of the mixture was adjusted to 12 using sodium hydroxide and it was kept at 180 °C for 6 h. It was found that with an increase in the ethylene glycol content in the reaction mixture, crystalline phases of $CuFe_2O_4$ and Cu are present in the composite. The appearance of copper is explained by the interaction of ethylene glycol with sodium hydroxide and the subsequent reduction of copper cations from copper(I) oxide.

Copper(II) ferrite was also prepared by the sol-gel method using a polymer (the so-called simple polymer-assisted sol-gel method) [10]. For this purpose, copper(II) and iron(III) nitrates in stoichiometric ratios were added to an aqueous solution of polyvinylpyrrolidone. The mixture was then kept at 80 °C until a gel-like precipitate formed, which was then kept at 250 °C for 15 min to remove organic components. The pre-

© 2026 The Authors. This is an open access article under the CC BY-NC-ND license (http://creativecommons.org/licenses/by-nc-nd/4.0/)

cipitate thus prepared was heat-treated at 750 and 950 °C. As a result, ferrite $CuFe_2O_4$ with a tetragonal structure was obtained, which also contained crystalline phases of CuO and Fe_2O_3 in small quantities. It was established that elevated temperatures and extended calcination durations promote the complete crystallization of copper ferrite, which simultaneously causes the nanoparticles to sinter into large agglomerates exceeding 1 μm in size. Furthermore, previous findings [11] regarding solid-phase synthesis with sodium oxalate and polyethylene glycol indicate that $CuFe_2O_4$ undergoes partial degradation into copper(II) and iron(III) oxides when temperatures surpass 400 °C. Soluble impurities were specifically removed before heat treatment at 400 °C.

Copper ferrite samples were produced by autocombustion using natural honey as a reducing and stabilizing agent [12]. Precursors synthesized by co-precipitation of copper and iron cations with sodium hydroxide in the presence of honey were treated at 400 and 800 °C for 4 h. The authors explained the voids between copper ferrite particles by the release of gaseous substances (N_2 and CO_2) formed as a result of the decomposition of glucose and fructose contained in honey. Moreover, the copper ferrite obtained at 400 °C contained crystalline phases of $CuFe_2O_4$ and oxides CuO and α-Fe_2O_3, whereas after heat treatment at 800 °C the sample was single-phase and contained only $CuFe_2O_4$ [12]. That is, no reduced metals were detected in the copper ferrite samples.

In [13], $CuFe_2O_4$ nanoparticles were synthesized by co-precipitation in an aqueous solution with the addition of polyethylene glycol. The resulting precipitate was thoroughly washed, dried, and then treated at 700ºC in a flow of oxygen in a tubular furnace. X-ray diffraction analysis revealed the presence of CuO, Fe_2O_3, and Fe_3O_4 oxides in the $CuFe_2O_4$ samples, the formation of which was explained by the oxidation of copper precipitated by polyethylene glycol, and insoluble FeO. A copper ferrite sample, the precursors of which were dried in a microwave oven, contained fewer impurities.

The given examples show that the addition of organic compounds to the reaction environment for the synthesis of copper ferrite promotes the stabilization of its nanoparticles and the appearance of both metals oxides, and, in rare cases, reduced metals in its composition. Apparently, this is due not only to the heat treatment temperature, the removal of impurities before heat treatment, or the heat treatment conditions, but also to the nature of the added organic stabilizers. In our previous studies devoted to the creation of Fe-Cu composites based on copper ferrite, it was found that the synthesis of copper ferrite by the method of co-precipitation of copper and iron cations in the presence of polymers [14] and carbon nanomaterials [15] followed by heat treatment leads to a change in its phase composition with the formation of not only oxides of both metals, but also reduced metals. Of course, this method is not a suitable synthesis option for obtaining stable crystalline copper ferrite, but for carrying out further electrochemical reduction of copper ferrite to produce catalytically active Fe-Cu composites, the introduction of such additives contributes to a noticeable decrease in the duration of the metal cations reduction process.

The present work aims to investigate the effect of polymer additives such as polyvinyl alcohol (PVA), polyvinylpyrrolidone (PVP), polyethyleneglycol (PEG) and graphitic carbon nitride (g-C_3N_4) on the structural changes in copper ferrite samples under thermal treatment at 700 °C. Additionally, the electrochemical reduction of both metals to form of Fe-Cu composites and their electrocatalytic activity in the model electrohydrogenation of 4-nitrophenol were analyzed.

Experimental

Materials

Copper(II) nitrate trihydrate ($Cu(NO_3)_2 \cdot 3H_2O$), iron(III) nitrate nonahydrate ($Fe(NO_3)_3 \cdot 9H_2O$) and sodium hydroxide (NaOH) were supplied by "Ridder" LLP (Karaganda, Kazakhstan). Dicyandiamide (CAS 461-58-5), polyvinyl alcohol (CAS 9002-89-5, 9,000-10,000 Mw), polyvinylpyrrolidone (CAS 9003-39-8, 10,000 Mw) and polyethylene glycol (CAS 25322-68-3, 10,000 Mw) were purchased from Sigma-Aldrich (USA) and used as received without further purification.

Synthesis of Graphitic Carbon Nitride g-C_3N_4

Graphitic carbon nitride g-C_3N_4 was synthesized following a previously reported procedure [15]. Briefly, 6 g of dicyandiamide was heated under an ambient air atmosphere to 550 °C and held at this temperature for 3 h. The obtained yellow product was ground into a fine powder.

Synthesis of Copper Ferrite and its Samples with Polymer Additives

Syntheses of "pure" copper ferrite and its samples with polymer additives (PVA, PVP, PEG, or g-C_3N_4) were performed by co-precipitation of metal cations from their nitrate salts and subsequent heat treatment (HT) using procedures similar to those described in our previously published works [14, 15]. The HT temperature (700 °C) and its duration (2 hours) for the prepared copper ferrite sample precursors were selected based on previously obtained results on the change in phase compositions of similar samples during HT.

Electrochemical and Electrocatalytic Experiments

Copper ferrite samples prepared with and without the addition of the polymers to the co-precipitation reaction medium and subsequent heat treatment were first reduced in an electrochemical cell. The resulting Fe-Cu composites were then used as electrocatalysts in the electrohydrogenation of 4-nitrophenol (4-NPh). The details regarding the electrochemical and electrocatalytic experiments can be found in our previous study [15]. The initial concentration of 4-NPh in the alcohol-aqueous-alkaline catholyte was 0.162 mol/L.

Characterization

Thermogravimetric measurements (TGA) were performed on a LabSYS evo TGA/LTA/DSC analyzer (Setaram Instrumentation, France). The samples were heated from 25 to 900 °C at a constant heating ramp of 10 °C/min under an air atmosphere. To identify the crystalline phases of the prepared composites, XRD analysis was carried out on a Rigaku SmartLab diffractometer (Rigaku, Japan) with CuKα radiation. The diffraction data were collected over a 2θ span of 5-90°. Their morphological features were studied on a TESCAN MIRA 3 (Tescan, Czech Republic) scanning electron microscope using secondary (SE) and backscattered (BSE) electron detectors. Elemental microanalysis of the samples was performed using an X-Act energy dispersive detector (Oxford Instruments, UK). Surface morphology of $CuFe_2O_4$ + g-C_3N_4 (700 °C) samples were studied using a scanning electron microscope JSM-IT 800 (JEOL, Japan). The samples were analyzed after deposition of conductive gold layer. The formation of 4-aminophenol as a product of electrocatalytic hydrogenation of 4-nitrophenol was established by its UV-Vis spectra recorded in the 250-500 nm wavelength range on a SHIMADZU UV-1900i spectrophotometer (Japan).

Results and Discussion

Figure 1 illustrates the chemical structures of the polymers employed to stabilize the copper ferrite precursor nanoparticles, which consist of copper and iron oxides and hydroxides formed during the co-precipitation of metal salts.

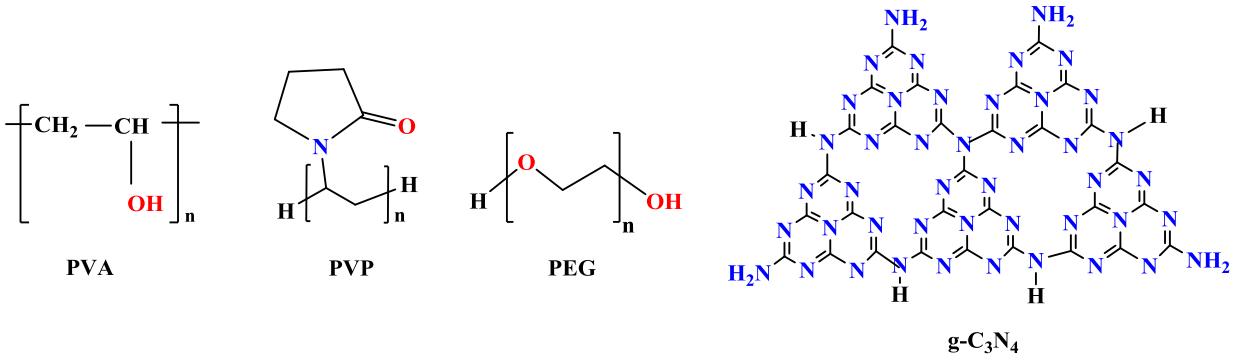

Figure 1. Structural formulas of the polymeric stabilizers employed during copper ferrite precursor synthesis

The PVA, PVP, and PEG polymers are characteristically known for their solubility in water. When the resulting precursors are washed, some of these polymers are removed, leaving behind, apparently, the portion that interacts with the precursor particles at the molecular level. The possibility of such an interaction was demonstrated by quantum-chemical calculations using the example of the PVA + $(CuO)_n$ system (n = 1-4) [16]. It was found that PVA is adsorbed on the surface of copper oxide particles through van der Waals and coordination interactions, as well as intramolecular hydrogen bonding. Polymeric graphitic carbon nitride, g-C_3N_4, on the contrary, is stable in an aqueous-alkaline environment, and the resulting precursors are deposited on its layered surface, reminiscent of graphite sheets [17, 18]. Therefore, graphitic carbon nitride not only acts as a stabilizer for copper ferrite precursor particles, but also serves as their carrier.

During heat treatment of the prepared precursors, the behaviour of the polymer stabilizers remaining after synthesis also varies. According to thermogravimetric analysis in air (Figure 2, curve *1*), the main decomposition of the PVA polymer occurs in the temperature range of 290-450 °C with a loss of ~80 % of the initial mass. The main products of the thermal-oxidative decomposition of PVA are water, acetaldehyde, carbon oxides (CO and CO_2), ethanol and other organic compounds, and at temperatures above 500 °C there are methane and hydrogen [19, 20].

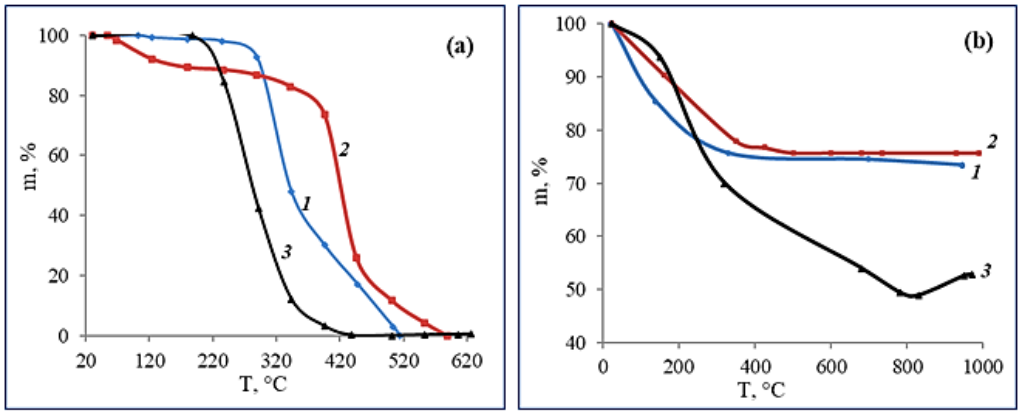

Figure 2. TG curves for (a) PVA (*1*), PVP (*2*), PEG (*3*) polymers; (b) $CuFe_2O_4$ (*1*), $CuFe_2O_4$ + PVP (*2*), $CuFe_2O_4$ + PVA (*3*) in the air

The TGA data (Figure 2(a), curve *2*) reveals that the primary degradation of the PVP polymer takes place between 320 and 450 °C, accompanied by a mass loss of ~75 %. The decomposition products are pyrrolidone, CO_2, hydrocarbons of various structures, and traces of ammonia [21, 22]. Above 450 °C, oxidation processes occur, releasing CO_2 and H_2O and completely burning the residue. Thermal decomposition of PEG polymer in air occurs at lower temperatures than that of PVA and PVP polymers: it begins at ~200 °C, indicating the low molecular weight of the polymer, and is almost fully completed to 390 °C (Figure 2, curve *3*). The main products of its decomposition in this temperature range can be aldehydes (formaldehyde, acetaldehyde), formic acid, ethylene glycol, methanol, ethanol, water, CO_2, CO, etc. [23].

According to the TGA experiment, graphitic carbon nitride produced by treating with dicyandiamide at 550 °C remains stable up to almost 512 °C (Figure 3, curve 1). It then decomposes almost completely to 835 °C, leaving behind approximately 5 % nitrogen-doped carbon (N-C).

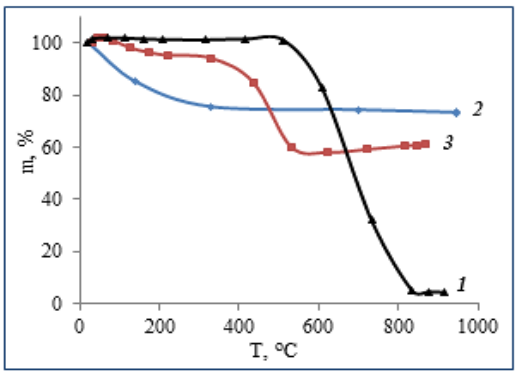

Figure 3. TG curves for g-C_3N_4 (*1*), $CuFe_2O_4$ (*2*), $CuFe_2O_4$ + g-C_3N_4 (*3*)

It can be assumed that all existing impurities (for example, NaOH) and the decomposition products of polymer stabilizers can influence the formation of the ferrite structure, weakening interatomic interactions and leading to the detachment of O_2 and reduction of metal cations.

The thermal behavior of the prepared copper ferrite precursors synthesized with and without the addition of polymer stabilizers, was also studied using TGA. Figure 2(b) shows that the $CuFe_2O_4$ and $CuFe_2O_4$ + PVP samples experience mass losses of 25 % and 22 % of the initial mass at temperatures up to 320-350 °C, respectively, whereas the $CuFe_2O_4$ + PVA samples experience a mass loss of 30 % of the initial mass. This is

due to the removal of their contained water and its loss during the transformation of metal hydroxides into their oxides. Metal ferrites then form as a result of the interaction of their oxides. With a further increase in temperature, the structures of the formed copper ferrites in the $CuFe_2O_4$ and $CuFe_2O_4$ + PVP samples remain unchanged and remain stable up to 950-990 °C. In contrast, in the $CuFe_2O_4$ + PVA sample, the mass loss continues up to 830 °C reaching almost 50 %, confirming the partial degradation of the copper ferrite itself. For the $CuFe_2O_4$ + g-C_3N_4 sample (Figure 3, curve *3*), a major weight loss step of ~40 % was recorded within the 330–530 °C thermal interval, which points to an incomplete decomposition of the ferrite.

The phase compositions of "pure" copper ferrite and its samples synthesized in the presence of polymers and then heat-treated at 700 °C were determined using X-ray diffraction analysis. At 700 °C, a solid-state reaction occurs between the copper and iron oxides, leading to the formation of the ferrimagnetic copper ferrite phase according to the following equation:

$$CuO + Fe_2O_3 \xrightarrow{700°C} CuFe_2O_4 \quad (1)$$

As copper ferrite is a stable ferrimagnetic phase under these conditions, its formation induces the magnetic response of the resulting composite. Therefore, the heat treatment at 700 °C does not cause a loss of magnetism, but rather enables the synthesis of the magnetically active phase from the initial amorphous metal oxides and hydroxides. As a result, the "pure" $CuFe_2O_4$ sample contains crystalline phases of cubic copper ferrite itself and a small amount of copper(II) oxide (Figure 4, (a)).

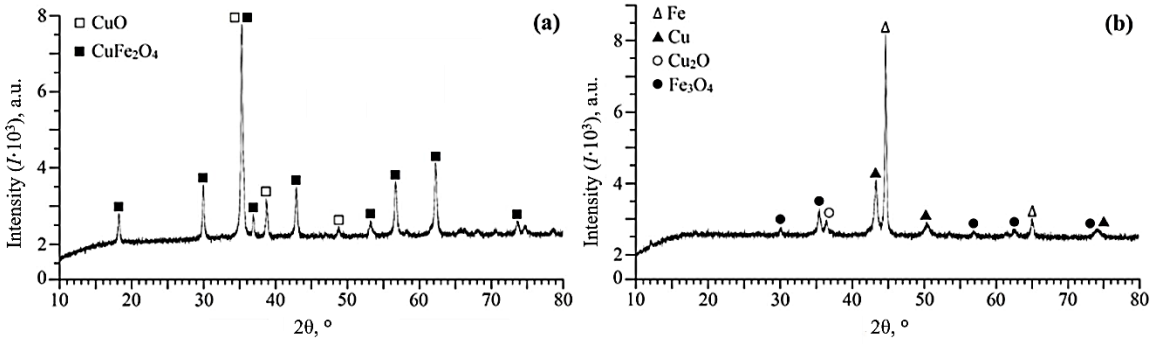

Figure 4. XRD patterns of $CuFe_2O_4$ (a) after HT at 700 °C and (b) after electrochemical experiments

The X-ray diffraction (XRD) pattern (Figure 5, 1(a)) indicate that heat-treating the $CuFe_2O_4$ + PVA precursor causes partial copper ferrite decomposition, generating reduced crystalline phases of Cu^0 and Fe^0 with well-defined, intense peaks. In addition to the remaining copper ferrite, this sample may also contain iron oxide Fe_3O_4 (magnetite), all of whose peaks overlap with those of $CuFe_2O_4$. The formation of Fe_3O_4 occurs as a result of the decomposition of copper ferrite, apparently under the influence of PVA decomposition products and other impurities (e.g., NaOH): $3CuFe_2O_4 \rightarrow 3Cu^0 + 2Fe_3O_4 + 2O_2$. According to [24], high-temperature reduction of Fe_3O_4 with a gas mixture (H_2/CO) occurs stepwise, through the formation of FeO (wüstite), which is then reduced to pure iron.

XRD patterns of $CuFe_2O_4$ + PVP (Figure 5, 2(a)) and $CuFe_2O_4$ + PEG (Figure 5, 3(a)) samples show that they contain crystalline phases of copper ferrite, copper(II) oxide, and small amounts of iron oxides, Fe_2O_3, and FeO. Apparently, PVP and PEG polymers are more soluble in water than PVA, and when the samples prepared after synthesis are washed, most of them are lost to the filtrates, and the concentration of the remaining polymers is insufficient to affect the copper ferrite and decompose it.

During the preparation of precursors for the $CuFe_2O_4$ + g-C_3N_4 sample, graphitic carbon nitride was taken in a 1:1 mass ratio to the theoretical yield of copper ferrite. After thermal treatment at 700 °C, according to XRD analysis, only ~15 % of the carbon remaining in the sample, formed from g-C_3N_4, with possible nitrogen doping (N-C). The XRD pattern of this sample, taken after thermal treatment, shows (Figure 5, 4(a)) that, as with the copper ferrite sample with PVA, the heat treatment process leads to partial copper ferrite decomposition, generating metallic copper and iron phases. The resulting composite also incorporates copper (I, II) oxides, carbon, and residual $CuFe_2O_4$ alongside co-existing Fe_3O_4.

In the electrochemical cell, under the specified conditions, copper ferrite is reduced to form crystalline phases of copper and iron, as confirmed by XRD analysis (Figure 5, 1(b)-4(b)). As follows from the XRD patterns, iron cations are more completely reduced in the $CuFe_2O_4$ + PVP and $CuFe_2O_4$ + g-C_3N_4 samples, which follows from the comparatively lower content of Fe_3O_4 oxide in these samples (Figure 5, 2(b) and

4(b)). Copper cation reduction is more complete in the $CuFe_2O_4$ + PVA and $CuFe_2O_4$ + g-C_3N_4 samples, according to the absence of Cu_2O oxide in their compositions after electrochemical experiments (Figure 5, 1(b) and 4(b)).

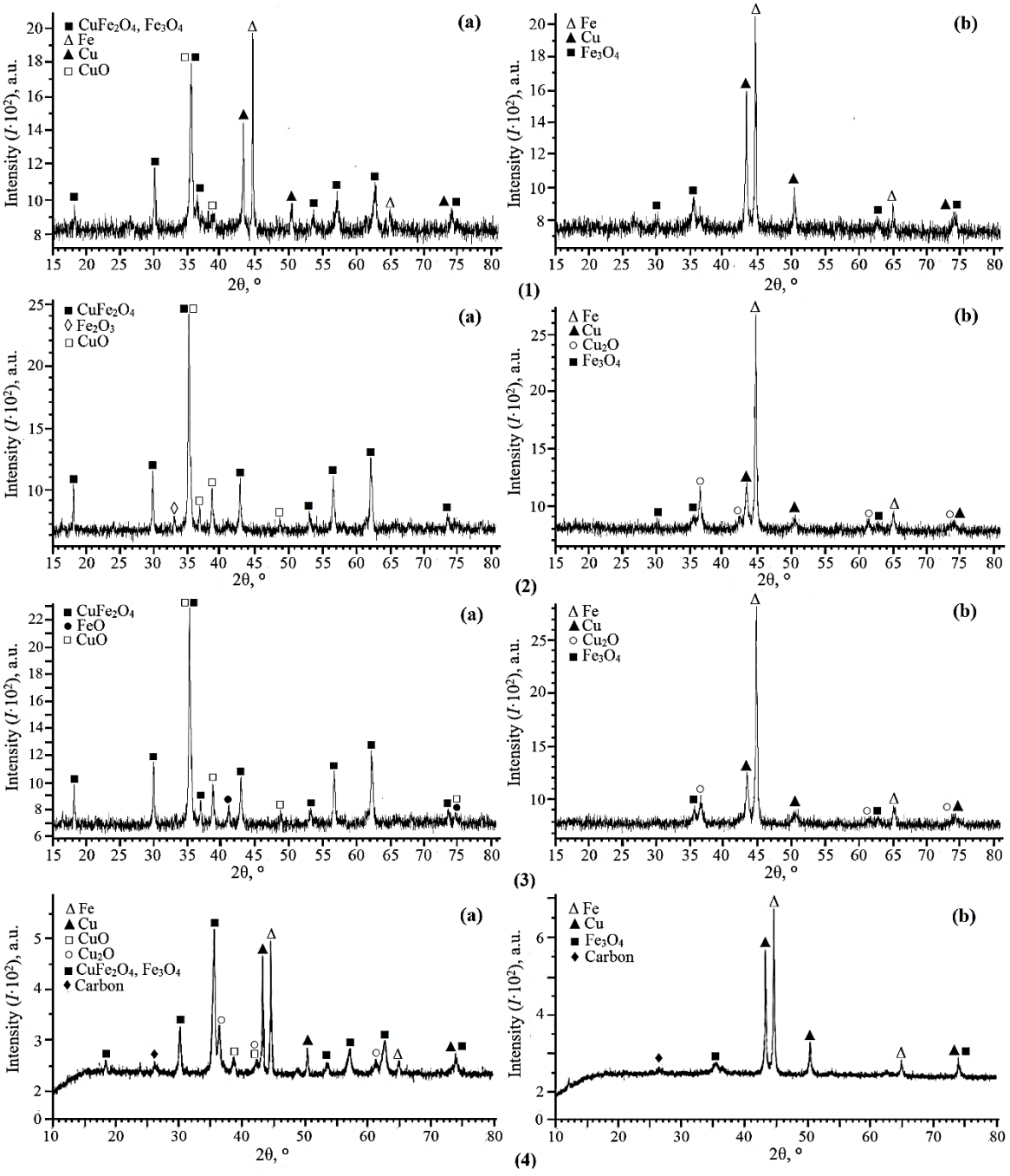

Figure 5. XRD patterns of $CuFe_2O_4$ + PVA (**1**), $CuFe_2O_4$ + PVP (**2**), $CuFe_2O_4$ + PEG (**3**), and $CuFe_2O_4$/g-C_3N_4 (**4**) after HT at 700 °C (a) and (b) after electrochemical experiments

Figures 6–9 display the SEM images of the copper ferrite samples prepared in the presence of polymer additives and annealed at 700 °C. The micrographs were taken using two electron detectors: a secondary electron (SE) detector, which allows one to study the relief and topography of the sample surface, and a backscattered electron (BSE) detector, which provides information on compositional contrast, i.e., areas with heavy elements appear brighter in the image than lighter elements. The BSE image of the C $CuFe_2O_4$ + PVA sample (Figure 6) contains areas of varying brightness: dark areas, apparently belonging to oxygen-containing compounds ($CuFe_2O_4$, Fe_3O_4), and lighter areas containing metallic particles, as established by

XRD analysis (Figure 5, 1(a)). EDS analysis also revealed areas of this sample's particles with higher and lower oxygen contents, and revealed a small carbon content (point spectra in Figure 6).

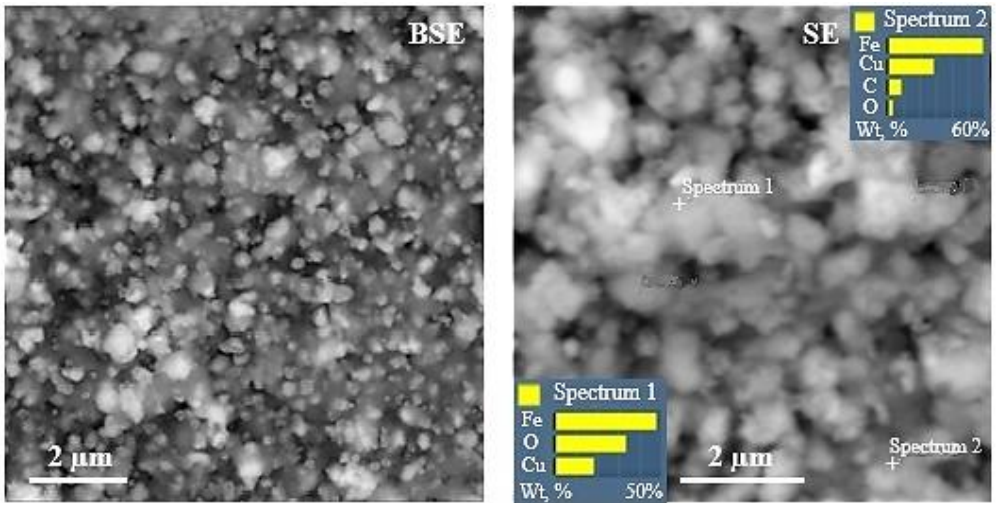

Figure 6. SEM images of $CuFe_2O_4$ + PVA (700 °C) sample

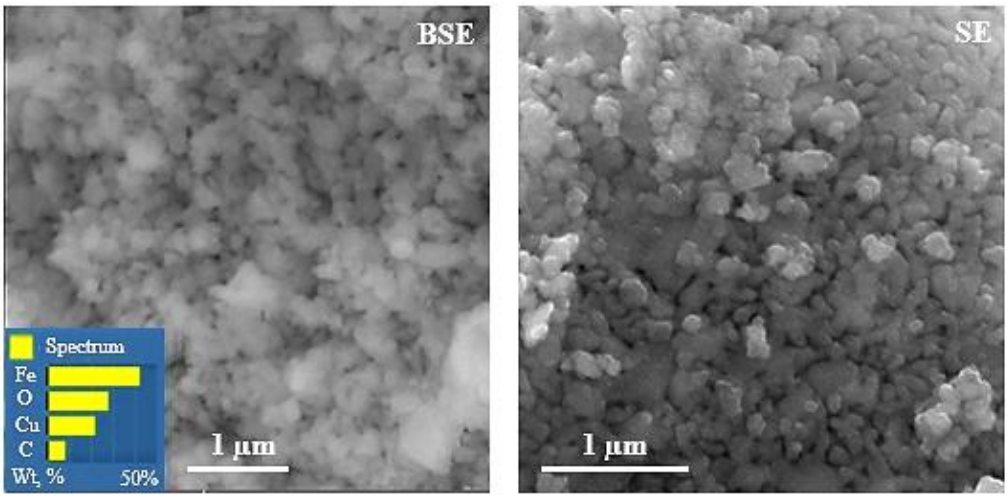

Figure 7. SEM images of $CuFe_2O_4$ + PVP (700 °C) sample

The $CuFe_2O_4$ + PVP and $CuFe_2O_4$ + PEG samples in BSE images (Figures 7 and 8) appear more compositionally uniform compared to the $CuFe_2O_4$ + PVA sample and consist primarily of copper ferrite particles. These particles are composed of smaller rounded or plate-like formations and resemble short sausages shaped to merge with each other, forming a hole in the centre (torus-like). In the $CuFe_2O_4$ + PEG sample (Figure 8), these toroidal formations are smaller. EDS analysis revealed the presence of carbon in both of these samples.

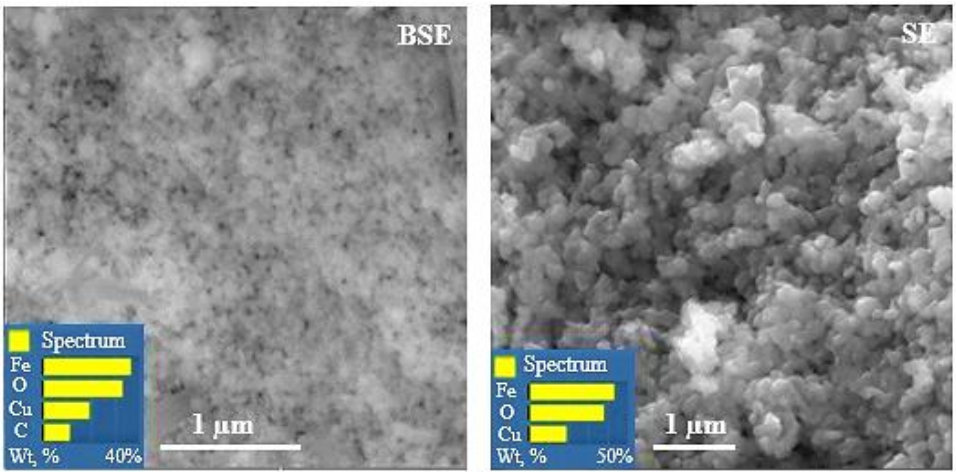

Figure 8. SEM images of $CuFe_2O_4$ + PEG (700 °C) sample

According to SE images of the $CuFe_2O_4$ + g-C_3N_4 sample (Figure 9), its composition contains particles of varying sizes and shapes: tetragonal pyramids of copper ferrite, layered formations of graphitic carbon nitride residues, and large balls twisted from plate-like copper oxide formations. EDS analysis of the selected area revealed a relatively high carbon content and a negligible nitrogen content (spectrum in the SE micrograph in Figure 9). This diverse composition of this sample after thermal treatment is well confirmed by its XRD analysis (Figure 5, 4(a)).

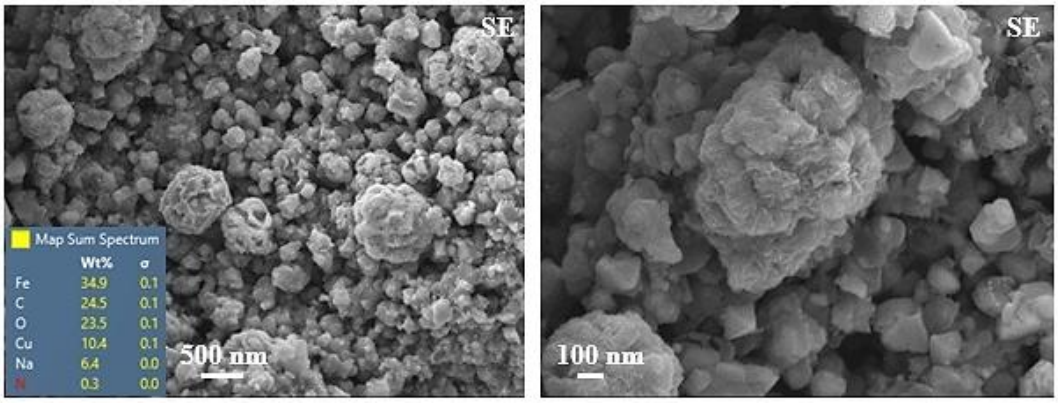

Figure 9. SEM images of $CuFe_2O_4$ + g-C_3N_4 (700 °C) sample

The copper ferrite samples prepared with and without the addition of polymers and obtained after thermal treatment were first reduced in an electrochemical cell. The Fe-Cu composites formed during the reduction were then tested for electrocatalytic activity in the electrohydrogenation of 4-nitrophenol. Notably, 4-NPh is classified as a pollutant, and its reduced form, 4-aminophenol, is a feedstock for the production of several pharmaceuticals, including paracetamol. Therefore, 4-NPh is a frequent subject of catalytic studies, primarily using sodium borohydride as a reducing agent [25-27].

Table 1 presents the results of the studies on the electrochemical reduction (EChR) of heat-treated copper ferrite samples and the electrocatalytic hydrogenation of 4-NPh on Fe-Cu composites. The key parameters evaluating both electrochemical processes are listed below: their durations (t_1 and t_2), the volume of oxygen released (ΔV_{O2}) in the copper ferrite EChR processes, the average 4-NPh hydrogenation rate (W) during the initial period (α = 0.25), the hydrogen utilization coefficient (η), close in its values to the faradaic efficiency, and 4-NPh conversion (α). Table 1 presents the experimental data expressed as the arithmetic mean values ($\bar{X}$) ± standard deviation (±δ) calculated across four independent runs (n = 4) calculated using well-known methods for the statistical processing of experimental data. For comparison, the parameters characterizing 4-nitrophenol electrochemical reduction on a bare copper cathode (in the absence of catalyst composites) are summarized in Table 1.

Table 1

Electrochemical reduction of copper(II) ferrite composites and electrocatalytic hydrogenation of 4-nitrophenol using Fe-Cu containing composites

Copper ferrite samples	EChR of copper ferrite samples		Electrocatalytic hydrogenation of 4-NPh			
	t_1, min	ΔV_{O2}, mL	t_2, min	W, mL H_2/min	η, %	α, %
Cu cathode	–	–	95.00±5.77	5.15±0.13	31.23±1.94	95.45±0.86
$CuFe_2O_4$, 700 °C	170.00±8.16	146.18±3.25	35.00±5.77	14.78±0.28	89.50±1.89	98.38±0.68
$CuFe_2O_4$ + PVA, 700 °C	70.00±8.16	96.25±2.43	35.00±5.77	14.90±0.29	89.54±1,78	98.40±0.63
$CuFe_2O_4$ + PVP, 700 °C	200.00±8.16	156.55±4.00	35.00±5.77	14.95±0.84	91.35±3.83	97.65±1.80
$CuFe_2O_4$ + PEG, 700 °C	208.75±8.54	153.70±6.62	35.00±5.77	15.70±0.55	93.75±3.20	97.10±2.06
$CuFe_2O_4$(1) + g-C_3N_4(1), 700 °C	95.00±9.13	115.78±8.72	36.30±4.79	13.20±0.79	80.15±5.17	97.68±1.72

The XRD data confirm that under the specified conditions, the thermally treated copper ferrite samples deposited on a Cu cathode undergo reduction, yielding Fe-Cu composites that still retain minor metal oxide residues (Figures 4(b) and 5, 1(b)-4(b)). As was shown previously [14], the electrochemical reduction of cations of both metals occurs in parallel. Possible electronic processes with the formation of assumed intermediate copper and iron oxides are described in a recently published article [15]. From the data in Table 1 it follows that the duration of electrochemical reduction of copper ferrite in the studied samples differs significantly. Shorter values of EChR duration are found for the copper ferrite samples synthesized using PVA and g-C_3N_4 polymers, i.e. these are just the ones that, during heating at 700 °C, underwent partial decomposition with the formation of copper and iron in a zero-valent state (Figure 5, 1(b) and 4(b)). In the samples with PVP and PEG polymers, in which thermal decomposition of copper ferrites did not occur (Figure 5, 2(b) and 3(b)), on the contrary, the EChR duration even increased slightly compared to pure $CuFe_2O_4$, which is also stable at 700 °C (Figure 4, (b)). This, firstly, may indicate a retarding effect of the carbon-containing residues of these polymers on the electrochemical reduction of metal cations in copper ferrite. Secondly, the recorded volumes of oxygen, released in addition to the volumes of H_2 and O_2 gases in a 2:1 ratio, also increased slightly, which may indicate more complete reduction of metal cations compared to the pure copper ferrite.

Electrochemical reduction of 4-NPh on a Cu cathode under the given conditions occurs at a rate of 5.15±0.21 mL/min, has a long duration, and has a fairly high degree of 4-NPh conversion (95.45±1.37 %) (Table 1). It can be assumed that this process is accompanied by the formation of by-products, which is typical for nitro compounds in an electrochemical system [28]. However, the UV-Vis spectra of the diluted catholyte after 4-NPh electrohydrogenation (Figure 10, (b), curve *2*) show the presence of a small amount of unreacted 4-NPh (a broad peak in the region of 403 nm) and a high content of 4-aminophenol (4-APh) (a peak in the region of 313 nm). For comparison, Figure 10, (a) shows the UV-vis spectra for aqueous-alkaline solutions of pure 4-NPh and 4-APh compounds. The use of Fe-Cu composites as electrocatalysts in this process, firstly, promotes a nearly threefold acceleration in the 4-NPh hydrogenation rate, thereby substantially shortening the reaction duration; secondly, the 4-NPh conversion reaches its maximum values. The absence of the initial 4-NPh in the catholytes after electrocatalytic hydrogenation on Fe-Cu composites formed from $CuFe_2O_4$ + PVA, $CuFe_2O_4$ + PEG, and pure $CuFe_2O_4$ samples is confirmed by UV-Vis spectra (Figure 10, (b)).

Among all copper ferrite samples, two samples, $CuFe_2O_4$ + PVA and $CuFe_2O_4$ + PEG, shown the highest 4-NPh hydrogenation rate (Table 1). The copper ferrites in these samples did not decompose during thermal treatment at 700 °C (Figures 5, 2(a) and 3(a)). As shown in the XRD patterns of these samples after electrochemical experiments (Figures 5, 2(b) and 3(b)), the diffraction peaks of the unreacted magnetite phase have the lowest intensity. Such a decline points to a near-total conversion of iron ions in these samples, and consequently, the highest content of reduced iron. This likely explains the highest rates of electrocatalytic hydrogenation of 4-NPh on Fe-Cu composites formed from these samples.

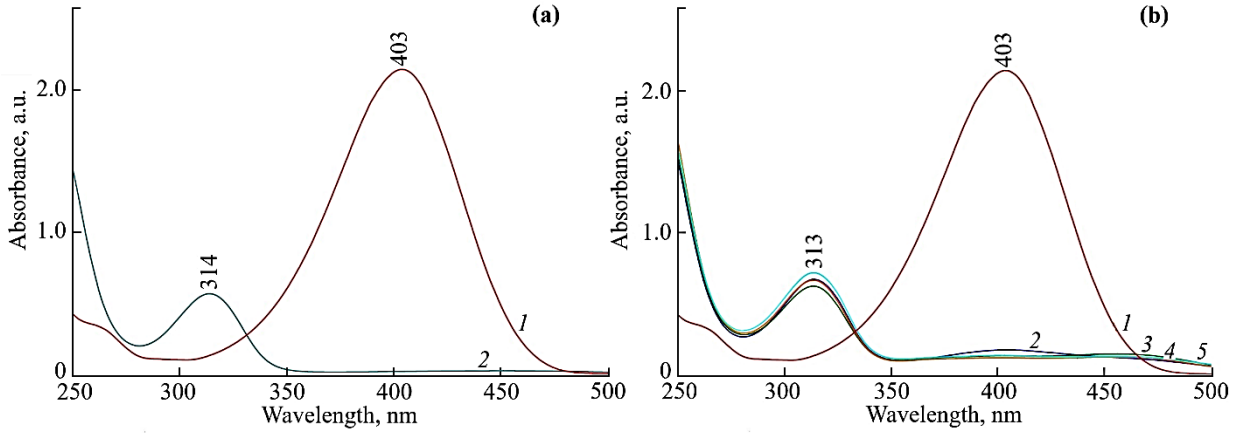

Figure 10. UV-vis spectra of (a) 4-NPh at the beginning of electrohydrogenation (*1*), and pure 4-APh (*2*); (b) catolyte with 4-NPh at the beginning of electrohydrogenation (*1*), catolyte after electrochemical reduction of 4-NPh (*2*), and catolytes after electrocatalytic hydrogenation of 4-NPh on the Fe-Cu composites based on (*3*) $CuFe_2O_4$ (700 °C), (*4*) $CuFe_2O_4$ + 3 % PVA (700 °C), and (*5*) $CuFe_2O_4$ + 3 % PVP (700 °C) samples

The samples synthesized using PVA and g-C_3N_4 polymers contained a large amount of reduced copper (based on the peak ratio in the 2θ = 43-45° angle range) already after the thermal treatment (Figure 5, 1(a) and 4(a)), which further increased after the electrochemical reduction of these samples. The resulting Fe-Cu composites demonstrated superior electrocatalytic performance during the electrohydrogenation of 4-nitrophenol, but slightly lower than that of the other composites (Table 1). Furthermore, it should be noted that the copper ferrite content in the $CuFe_2O_4$ + g-C_3N_4 (700 °C) sample was lower than that in the samples containing other polymers, and, therefore, the amount of reduced metals in the Fe-Cu composite formed from this sample was also lower. This apparently explains the some decrease in the rate of 4-NPh hydrogenation exhibited by this composite in the studied process compared to that of the other composites.

Conclusions

A comparison of the phase compositions of copper(II) ferrites synthesized by co-precipitation in the presence of a number of polymers (PVA, PVP, PEG, and g-C_3N_4) followed by heat treatment at 700 °C revealed the varying effects of these polymers on the subsequent transformation of the resulting copper ferrite samples. It was found that some polymers (PVA, g-C_3N_4) affect the phase compositions of the copper ferrites, leading to their partial decomposition during heat treatment, and their electrochemical reduction decreasing its duration. Other polymers (PVP, PEG) do not have this effect, but a more complete electrochemical reduction of iron cations in their copper ferrite samples prepared with their participation facilitates better intensification of 4-NPh electrohydrogenation with the formation of a single product, 4-aminophenol, which is of great practical importance. The different effects of the polymer additives discussed may be due to their structure, decomposition products during heat treatment, and their interaction with copper ferrite atoms. An additional factor influencing the copper ferrite transformations discussed may be the polymer concentration in co-precipitation reaction environment and their residual content in the copper ferrite precursors.

Funding

This research was funded by the Science Committee of the Ministry of Science and Higher Education of the Republic of Kazakhstan (Program No. BR24992921).

*Author Information**

**The authors' names are presented in the following order: First Name, Middle Name and Last Name*

Yakha Amkhadovna Vissurkhanova (*corresponding author*) — Researcher, Laboratory of Electrocatalysis and Quantum-chemical Research, LLP "Institute of Organic Synthesis and Coal Chemistry of the Republic of Kazakhstan", Alikhanov St., 1, 100000, Karaganda, Kazakhstan; Teacher, Department of Physical and Analytical Chemistry, Buketov Karaganda National Research University, Universitetskaya St., 28, 100024, Karaganda, Kazakhstan; e-mail: yakhavisurkhanova@bk.ru; https://orcid.org/0000-0001-7279-1145

Nina Mikhailovna Ivanova — Doctor of Chemical Sciences, Full Professor, Head of the Laboratory of Electrocatalysis and Quantum-chemical Research, LLP "Institute of Organic Synthesis and Coal Chemistry of the Republic of Kazakhstan", Alikhanov St., 1, 100000, Karaganda, Kazakhstan; e-mail: nmiva@mail.ru; https://orcid.org/0000-0001-8564-8006

Yelena Anatol'evna Soboleva — Candidate of Chemical Sciences, Associate Professor, Leading researcher, Laboratory of Electrocatalysis and Quantum-chemical Research, LLP "Institute of Organic Synthesis and Coal Chemistry of the Republic of Kazakhstan", Alikhanov St., 1, 100000, Karaganda, Kazakhstan; e-mail: esoboleva-kz@mail.ru; https://orcid.org/0000-0002-1089-367X

Zainulla Muldakhmetovich Muldakhmetov — Director of LLP "Institute of Organic Synthesis and Coal Chemistry of the Republic of Kazakhstan", Alikhanov St., 1, 100000, Karaganda, Kazakhstan; e-mail: iosu.rk@mail.ru; https://orcid.org/0000-0001-9497-2545

Author Contributions

The manuscript was written through contributions of all authors. All authors have given approval to the final version of the manuscript. CRediT: **Yakha Amkhadovna Vissurkhanova** investigation, methodology, data curation, visualization; **Nina Mikhailovna Ivanova** conceptualization, writing-original draft, methodology, validation, visualization, writing-review & editing; **Yelena Anatol'evna Soboleva** investigation, data curation, Figures design, resources, visualization; **Zainulla Muldakhmetovich Muldakhmetov** funding acquisition.

Conflicts of Interest

The authors declare no conflict of interest.

References

1 Rashad, M.M., Mohamed, R.M., Ibrahim, M.A., Ismail, L.F.M., Abdel-Aal, E.A. (2012). Magnetic and catalytic properties of cubic copper ferrite nanopowders synthesized from secondary resources. *Adv. Powder Technol., 23*, 315–323. https://doi.org/10.1016/j.apt.2011.04.005

2 Dey, A., Varshney, G., Maity, S., Sengupta, S. (2025). Hydrothermally synthesized ternary copper ferrite ($CuFe_2O_4$) micro-nano particles for high-capacity and long-life anodes in Li-ion batteries. *Mater. Lett., 401*, 139276. https://doi.org/10.1016/j.matlet.2025.139276

3 Wang, K., Yang, P., Guo, R., Yao, X., Yang, W. (2019). Photothermal performance of MFe_2O_4 nanoparticles. Chinese Chem. Lett., 30, 2013–2016**.** https://doi.org/10.1016/j.cclet.2019.04.005

4 Kharisov, B.I., Dias, H.V.R., Kharisova, O.V. (2019). Mini-review: Ferrite nanoparticles in the catalysis. *Arabian J. Chem., 12*, 1234–1246. http://dx.doi.org/10.1016/j.arabjc.2014.10.049

5 Dippong, T., Levei, E.A., Kadar, O. (2021). Recent advances in synthesis and applications of MFe_2O_4 (M = Co, Cu, Mn, Ni, Zn) nanoparticles. *Nanomaterials, 11*, 1560. https://doi.org/10.3390/nano11061560

6 Salih, S.J., Tahseen, Z.S. (2026). Spinel ferrite nanoparticles in environmental remediation: Adsorption, catalysis, and sustainability perspectives. *Next Sustainability*, *7*, 100240. https://doi.org/10.1016/j.nxsust.2025.100240

7 Goya, G.F., Rechenberg, H.R. (1998). Superparamagnetic transition and local disorder in $CuFe_2O_4$ nanoparticles. *Nanostruct. Mater*., *10*(6), 1001–1011. https://doi.org/10.1016/S0965-9773(98)00133-0

8 Marinca, T.F., Chicinaş, I., Isnard, O. (2012). Synthesis, structural and magnetic characterization of nanocrystalline $CuFe_2O_4$ as obtained by a combined method reactive milling, heat treatment and ball milling. *Ceram. Int.*, *38*(3), 1951–1957. https://doi.org/10.1016/j.ceramint.2011.10.026

9 Astaraki, H., Masoudpanah, S.M., Alamolhoda, S. (2021). Effects of ethylene glycol contents on phase formation, magnetic properties and photocatalytic activity of $CuFe_2O_4/Cu_2O/Cu$ nanocomposite powders synthesized by solvothermal method. *J. Mater. Res. Technol., 14*, 229–241. https://doi.org/10.1016/j.jmrt.2021.06.046

10 Calvo-de la Rosa, J., Segarra, M. (2019). Optimization of the synthesis of copper ferrite nanoparticles by a polymer-assisted sol-gel method. *ACS Omega*, *4*(19), 18289–18298. https://doi.org/10.1021/acsomega.9b02295

11 Wu, X., Zhou, K., Wu, W., Cui, X., Li, Y. (2013). Magnetic properties of nanocrystalline $CuFe_2O_4$ and kinetics of thermal decomposition of precursor. *J. Therm. Anal. Calorim*., *111*(1), 9–16. https://doi.org/10.1007/s10973-011-2104-6

12 Divakara, S. G., Jayanna, B. K., Mahesh, B., Anil Kumar, H. G., Reddy, M.A.H., Narasimhaswamy, N. (2026). Honey-assisted synthesis of $CuFe_2O_4$ nano pebbles: a sustainable approach to photocatalytic and antibacterial activity. *J. Exp. Nanosci*., *21*(1), 2630356. https://doi.org/10.1080/17458080.2026.2630356

13 Kanagaraj, M., Sathishkumar, P., Selvan, K., In, P., Arumugam, S. (2014). Structural and magnetic properties of $CuFe_2O_4$ as-prepared and thermally treated spinel nanoferrites. *Indian J. Pure Appl. Phys*., *52*(2), 124–130.

14 Ivanova, N.M., Soboleva, E.A., Visurkhanova, Ya.A., Muldakhmetov, Z. (2020). Electrochemical synthesis of Fe–Cu composites based on copper(II) ferrite and their electrocatalytic properties. *Russ. J. Electrochem.*, *56*, 533–543. http://doi.org/10.1134/S1023193520070034

15 Vissurkhanova, Ya.A., Ivanova, N.M., Soboleva, Ye.A., Muldakhmetov, Z.M. (2026). Fabrication and electrocatalytic activity of Fe-Cu/C composites based on copper ferrite modified with graphene oxide and graphitic carbon nitride. *Materials*, *19*, 2273. https://doi.org/10.3390/ma19112273

16 16. Vissurkhanova, Ya.A, Abulyaissova, L.K., Ivanova, N.M., Minaev, B.F. (2023). Molecular simulation of the interaction of polyvinyl alcohol with potential active centers of copper (II) oxide surface. *News of the Academy of Sciences of RK. Series Chemistry and Technology*, *457*(4), 54–68. https://doi.org/10.32014/2023.2518-1491.192

17 Zhu, J., Xiao, P., Li, H., Carabineiro S.A.C. (2014). Graphitic Carbon Nitride: Synthesis, Properties, and Applications in Catalysis. *ACS Appl. Mater. Interfaces*, *6*, 16449−16465. https://doi.org/10.1021/am502925j

18 Praus, P., Svoboda, L., Ritz, M., Troppova, I., Sihor, M., Koci, K. (2017). Graphitic carbon nitride: Synthesis, characterization and photocatalytic decomposition of nitrous oxide. *Mater. Chem. Phys.*, *193*, 438–446. https://doi.org/10.1016/j.matchemphys.2017.03.008

19 Taghizadeh, M.T., Yeganeh, N., Rezaei, M. (2015). The investigation of thermal decomposition pathway and products of poly(vinyl alcohol) by TG-FTIR. *J. Appl. Polym. Sci.*, *132*(25), 421177. https://doi.org/10.1002/APP.42117

20 Senkevich, S.I., Druzhinina, T.V., Kharchenko, I.M., Kryazhev, Yu.G. (2007). Thermal transformations of polyvinyl alcohol as a source for the preparation of carbon materials. *Solid Fuel Chem*., *41*, 45–51. https://doi.org/10.3103/S0361521907010107

21 Lorı´a-Bastarrachea, M.I., Herrera-Kao, W., Cauich-Rodrı´guez, J.V., Cervantes-Uc, J.M., Va´zquez-Torres, H., A´vila-Ortega, A. (2011). A TGA/FTIR study on the thermal degradation of poly(vinyl pyrrolidone). *A Therm. Anal. Calorim*., *104*, 737–742. https://doi.org/10.1007/s10973-010-1061-9

22 Jablonski, A.E., Lang, A. J., Vyazovkin, S. (2008). Isoconversional kinetics of degradation of polyvinylpyrrolidone used as a matrix for ammonium nitrate stabilization. Thermochimica Acta, 474(1-2), 78–80. https://doi.org/10.1016/j.tca.2008.06.003

23 Kou, Y., Wang, S., Luo, J., Sun, K., Zhang, J., Tan, Z., Shi, Q. (2019). Thermal analysis and heat capacity study of polyethylene glycol (PEG) phase change materials for thermal energy storage applications, *J. Chem. Thermodynamics*, *128*, 259–274. https://doi.org/10.1016/j.jct.2018.08.031

24 Cheng, H., Cao, G., Ba, Z., Hu, D., Wang, Y., Li, Ch., Zhao, J (2026). Magnetite reduction kinetics under H_2 and CO atmospheres at high temperature. *Korean J. Chem. Eng.*, *43*, 1493–1505. https://doi.org/10.1007/s11814-025-00643-6

25 Zhao, P., Feng, X., Huang, D., Yang, D., Astruc, D. (2015). Basic concepts and recent advances in nitrophenol reduction by gold- and other transition metal nanoparticles, *Coord. Chem. Rev.*, *287*, 114–136. https://doi.org/10.1016/j.ccr.2015.01.002

26 Din, M.I., Khalid, R., Hussain, Z., Hussain, T., Mujahid, A., Najeeb, J., Izhar, F. (2020). Nanocatalytic assemblies for catalytic reduction of nitrophenols: A critical review, *Crit. Rev. Anal. Chem.*, *50*(4), 322–338. https://doi.org/10.1080/10408347.2019.1637241

27 Mejía, Y.R., Bogireddy, N.K.R. (2022). Reduction of 4-nitrophenol using green-fabricated metal nanoparticles. *RSC Advances*, *12*(29), 18661–18675. https://doi.org/10.1039/d2ra02663e

28 Simonetti, S.O., Beil, S.B., Waldvogel S.R. (2025). Nitro substrates in reductive electrosynthesis: A review. *ACS Electrochem*., *1*, 805–818. https://doi.org/10.1021/acselectrochem.5c00081

How to Cite: Burkitbayeva, B.D., Adeloye, A.O., Miftakhova, A.F., Jumanova, R.Zh., Beisenova, G.S., Argimbayeva, A.M., Seit, G., Bakhytzhan, Ye.G., & Smail, A.B. (2026). Comparative Electrochemical and Corrosion Inhibition Assessment of Commercial Tannic Acid, Crude Extracts, and *n*-Butanol Fractions of *Quercus robur Stem Bark*. *Eurasian Journal of Chemistry, 31, 3(123), 129–143.* https://doi.org/10.31489/2959-0663/3-26-13

CHEMICAL TECHNOLOGY

Article

Received: 25 June 2026 | Revised: 1 September 2026 |
Accepted: 8 September 2026 | Published online: 10 September 2026

UDC 66.097.8:620.197.3:544.654 https://doi.org/10.31489/2959-0663/3-26-13

Bibisara D. Burkitbayeva[1], Adewale O. Adeloye[1], Alfira F. Miftakhova[1], Raigul Zh. Jumanova[1], Gulmira S. Beisenova[1]*, Akmaral M. Argimbayeva[1], Gulzhan Seit[1], Yeldana G. Bakhytzhan[1], Aruzhan B. Smail[1]

al-Farabi Kazakh National University, Almaty, Kazakhstan
*(*Corresponding author's e-mail: beisenova.gumi@gmail.com)*

Comparative Electrochemical and Corrosion Inhibition Assessment of Commercial Tannic Acid, Crude Extracts, and *n*-Butanol Fractions of Quercus robur Stem Bark

In this study, crude aqueous-ethanolic extract and n-butanol fraction of Quercus robur stem bark were obtained, and their corrosion-inhibition performance on mild steel in 1 M HCl was evaluated while their performances are compared to the commercial tannic acid used as standard. Corrosion inhibition was assessed by potentiodynamic polarization at 200 mg L^{-1} after 1 hour of immersion. The n-butanol fraction exceeded the 71.9 % efficiency of the crude extract, though remaining below the 98.2 % maximum efficiency observed for the tannic acid standard at 1000 mg L^{-1}. Polarization curve shifts support classifying the tannin-containing samples as mixed-type inhibitors. Adsorption-isotherm analysis showed model-dependent behavior: the Freundlich model provided the highest R^2 for the crude extract, while the Langmuir model provided the highest R^2 for the n-butanol fraction and tannic acid. These fits represent empirical descriptions of concentration-dependent inhibition rather than direct molecular mechanisms. For commercial tannic acid, the standard Gibbs free energy of adsorption ΔG^0_{ads} as approximately -33.3 kJ mol^{-1}, indicating thermodynamically favorable adsorption. Overall, solvent fractionation improved inhibition performance. These findings indicate the n-butanol fraction's potential as a plant-derived inhibitor. Further phytochemical investigation, isolation and characterization are required to properly identify the active constituents underlying the adsorption mechanisms.

Keywords: *Quercus robur*, *n*-butanol fraction, commercial tannic acid, corrosion inhibitor, mild steel, potentiodynamic polarization, adsorption isotherms.

1 Introduction

Corrosion of metals and alloys remains a critical, resource-intensive challenge across industrial sectors such as oil and gas production, pipeline infrastructure, construction, and water supply systems. Beyond causing severe economic losses through structural degradation, corrosion indirectly accelerates global greenhouse gas emissions. While conventional corrosion mitigation relies heavily on inorganic inhibitors (such as chromates, phosphates, and silicates) and synthetic organic compounds, their toxicity and severe environmental risks have necessitated a transition toward sustainable alternatives [1, 2]. Consequently, recent research has increasingly focused on biodegradable, plant-derived green inhibitors.

Among naturally occurring plant-derived compounds, tannins extracted from bark, seeds, and leaves have attracted substantial attention due to their structural features and potential corrosion-inhibiting properties. Tannins are polyphenolic compounds generally classified into hydrolysable tannins, which include gallic acid-derived structures, and condensed tannins, consisting mainly of oligomeric and polymeric proanthocyanidins. *Quercus robur* bark has been reported as a source of tannin-containing polyphenolic compounds, including hydrolysable and condensed tannin-related constituents [3-5]. Owing to the presence

© 2026 The Authors. This is an open access article under the CC BY-NC-ND license (http://creativecommons.org/licenses/by-nc-nd/4.0/)

of multiple phenolic hydroxyl groups and aromatic structures, tannin-containing plant materials have attracted increasing interest as potential environmentally compatible corrosion inhibitors. While historically utilized in medicine and leather processing, these polyphenolic materials are increasingly being investigated for applications in materials science, including corrosion protection.

The corrosion-inhibition activity of plant tannins has commonly been attributed to their abundant hydroxyl groups and aromatic rings, which may act as electron-donating sites [6]. Previous studies have proposed that tannin-containing compounds can adsorb on metal surfaces and interact with iron species, potentially forming iron–tannate complexes that contribute to the formation of a protective interfacial layer [7, 8]. Such interactions have been proposed to contribute to corrosion inhibition in aggressive hydrochloric acid environments, which are widely encountered in industrial pickling, acid cleaning, and scale removal. Electrochemical studies have also reported tannin-containing inhibitors as mixed-type inhibitors, based on their effects on both the anodic and cathodic branches of polarization curves [8, 9].

Plant-derived tannins have demonstrated corrosion-inhibition activity under diverse experimental conditions. For instance, Gelam tree bark tannins achieved 89.66 % inhibition efficiency for mild steel in 1 M HCl [10], quebracho tannin extract showed corrosion-inhibition effects in 3.5 % NaCl solution [11], and commercial tannins (TG 3300) reached approximately 85 % inhibition efficiency at pH 10.5 [12]. Previous studies have associated these protective effects with adsorption of tannin-containing species and possible interactions between phenolic constituents and iron species, including the formation of iron–tannate complexes.

In the present study, a crude aqueous-ethanolic extract of *Quercus robur* stem bark was subjected to sequential solvent fractionation, and the resulting *n*-butanol fraction was evaluated for corrosion inhibition of mild steel in 1 M HCl. The crude extract and the *n*-butanol fraction were characterized using FT-IR spectroscopy, and UV-Vis spectrophotometry, while commercial tannic acid was used as a reference material. Their corrosion-inhibition performance was comparatively evaluated by potentiodynamic polarization at different concentrations and immersion times. In addition, the concentration-dependent inhibition data were analyzed using Langmuir, Freundlich, and Temkin adsorption-isotherm models. The study therefore provides a comparative assessment of the crude extract, its *n*-butanol fraction, and commercial tannic acid, with particular emphasis on the effect of solvent fractionation on tannin-equivalent content and corrosion-inhibition performance.

2 Experimental

2.1 Preparation and Extraction of Quercus Robur Bark

Granulated commercial oak (Quercus robur) bark was obtained from Zerde-Fito LLP (Kazakhstan) and used as-supplied. A 1000 g portion of the dried bark was treated with a 1:1 (v/v) water-ethanol solvent mixture (3 L) as illustrated in Figure 1. Following extraction, the liquid suspension was filtered to completely remove residual solid plant biomass. The resulting dark-brown filtrate was subsequently concentrated under reduced pressure using an IKA RV 05 Basic rotary evaporator coupled with an HB4 Basic heating bath (IKA-Werke GmbH & Co. KG, Germany). To protect thermolabile phenolic compounds against thermal degradation, distillation was maintained strictly at a controlled temperature range not exceeding 40–45 ^{o}C [13]. This optimized recovery protocol yielded 83.27 g of a highly concentrated, dark-brown viscous ethanolic extract which was further subjected to solvent-solvent partitioning to obtain the n-butanol fraction used for subsequent characterization and corrosion-inhibition evaluation.

2.2 Liquid-Liquid Fractionation

A portion of the dried extract (50.0 g, dry weight basis) was re-dissolved in 1.0 L of distilled water and successively partitioned using solvents of increasing polarity following a standard phytochemical fractionation procedure [14]: n-hexane (500–600 mL), dichloromethane (1000 mL), ethyl acetate (1400 mL), and n-butanol (1400 mL). Concentration in vacuo yielded the n-hexane fraction (0.85 g), dichloromethane fraction (1.862 g), ethyl acetate fraction (7.705 g), n-butanol fraction (16.332 g), and residual aqueous fraction (20.140 g). This sequential solvent hierarchy — transitioning from non-polar to high-polarity media effectively fractionated the complex phytochemical matrix, with dominant mass recoveries concentrated in the polar n-butanol and aqueous phases, reflecting the inherent abundance of hydroxyl-rich polyphenolic constituents in Quercus robur. The cumulative recovery mass accounted for approximately 93.8 % of the initial extract load, with the minor mass differential (<6.2 %) well within expected technical parameters due to interfacial retention and mechanical transfer losses during multi-step liquid-liquid extraction.

2.3 Thin-Layer chromatography (TLC)

The TLC plates were developed using carefully optimized solvent systems was utilized strictly as a qualitative fingerprinting and comparative tool, rather than a quantitative metric to resolve the polar constituents within the n-butanol fraction. Following development, visualization was achieved via exposure to iodine vapors and subsequent inspection under ultraviolet light at wavelengths of 254 nm and 366 nm to detect UV-active and fluorescent phytochemical metabolites. Distinct, well-resolved spots with reproducible R_f values were successfully recorded, mapping the phytochemical distributions in the fraction as compared to the standard commercial tannic acid.

2.4 Fourier-Transform Infrared (FT-IR) Spectroscopy

FT-IR spectra of commercial tannic acid (ACS reagent, Sigma-Aldrich, Merck KGaA, Germany, catalog no. 403040-100G; manufactured in China), the crude ethanolic extract, and the n-butanol fraction were acquired using an ALPHA II FT-IR spectrometer equipped with an ATR module and the ATR-LIB-COMPLETE spectral library (Bruker, Germany).

2.5 UV-Vis. Absorption Spectrophotometry

The total tannin content in the crude plant material was determined in accordance with the standardized protocol outlined in the State Pharmacopoeia of the Republic of Kazakhstan, as described in a recent study [15]. Quantitative evaluation of the n-butanol fraction was performed using a Hanon i3 UV-Vis spectrophotometer (Jinan Hanon Instruments Co., Ltd., China). Measurements were conducted at the characteristic absorption maximum of tannins, with quantification established via the linear relationship between solution concentration and absorbance at 290 nm in accordance with the Beer-Lambert law (Equation 1).

2.6 Preparation of Standard and Reagent Solutions

Quantitative estimation of the total tannin content in the crude ethanolic extract and its derived n-butanol fraction was performed spectrophotometrically using tannic acid as the analytical standard. A primary stock standard solution (1.0 g L^{-1}) was prepared by dissolving 1.000 g of analytical-grade tannic acid in distilled water and diluting to a final volume of 1000 mL. To prevent oxidative degradation of the polyphenolic structures during the assay, a freshly prepared 0.2 % (w/v) sodium bisulfite solution was utilized throughout the procedure.

A reference blank solution was prepared by dissolving 0.042 g of benzoic acid in 100 mL of distilled water, from which a 2.0 mL aliquot was further diluted to 10.0 mL with distilled water. For calibration, precise working aliquots ranging from 6.0 mL to 6.8 mL of the stock tannic acid solution were transferred into volumetric flasks. Each mixture was treated with 50.0 mL of the 0.2 % sodium bisulfite protective solution, 2.5 mL of a 0.01 M $FeCl_3$ chromogenic reagent, and 50.0 mL of distilled water, followed by thorough homogenization and dilution to volume.

Absorbance measurements of the resulting ferric-tannate complexes were recorded at a wavelength of 290 nm using 1 cm quartz cuvettes against the prepared reference blank for baseline correction. Final concentrations and total tannin yields were quantified in strict accordance with the Beer-Lambert law.

$$A = \varepsilon cl \quad (1)$$

where A is the absorbance, ε is the molar absorptivity coefficient, c is the concentration, and l is the optical path length.

2.7 Electrochemical Measurements

The corrosion-inhibition performance of the investigated tannin-containing samples was evaluated using potentiodynamic polarization, which is based on the continuous variation of the electrode potential at a predetermined scan rate while recording the resulting current response. This method enables evaluation of corrosion-inhibition performance and assessment of changes in the anodic and cathodic polarization behavior of the steel.

Electrochemical measurements were performed using an Autolab PGSTAT302N potentiostat/galvanostat. All experiments were conducted in a conventional three-electrode electrochemical cell consisting of a mild steel working electrode with an exposed surface area of 0.1256 cm^2, a platinum counter electrode, and an Ag/AgCl reference electrode.

Potentiodynamic polarization measurements were carried out in the potential range from –0.30 to +0.30 V relative to the open-circuit potential (OCP) at a scan rate of 2 mV s^{-1}. For each inhibitor concentration and immersion condition, three independent electrochemical measurements were performed using three

separate mild-steel specimens (n = 3). Each specimen was freshly prepared and polished prior to an individual electrochemical measurement. The reported electrochemical parameters are presented as mean ± standard deviation (SD) of the three independent measurements.

All electrochemical measurements were performed at room temperature (approximately 25 °C). Prior to testing, steel specimens were sequentially polished with abrasive papers of different grit sizes, rinsed with distilled water and acetone, and finally dried in air. This procedure was used to remove surface contaminants and obtain comparable initial surface conditions for the electrochemical measurements.

To evaluate the inhibitory performance of the investigated extracts, steel specimens were immersed in 1 M HCl solutions containing inhibitor concentrations ranging from 200 to 1200 mg L^{-1}. Polarization measurements were performed either immediately after immersion or after 1 h of immersion.

For Tafel analysis, linear portions of the anodic and cathodic polarization branches approximately 50–100 mV from the corrosion potential (E_{corr}) were used for extrapolation.

The inhibition efficiency was evaluated from the polarization parameters and corrosion rates calculated from the electrochemical data according to the following equation 2 [10]:

$$\eta(\%) = \frac{j_{corr}^{0} - j_{corr}}{j_{corr}^{0}} \times 100\% \quad (2)$$

where j_{corr}^{0} s the corrosion current density in the uninhibited solution (A cm^{-2}), and j_{corr} is the corrosion current density in the presence of the tannin-containing inhibitor (A cm^{-2}).

3 Results and Discussion

3.1 Extraction, Solvent-Solvent Partitioning of Quercus robur Bark and TLC profiles

The systematic workflow for the extraction and sequential solvent-solvent partitioning of the Quercus robur bark ethanolic extract is detailed in Figure 1. Sequential solvent-solvent partitioning facilitated a polarity-directed fractionation of the crude extract. The negligible yield recorded for the n-hexane fraction reflects a sparse concentration of non-polar constituents, such as aliphatic lipids and waxes, within the Quercus robur bark matrix. Conversely, the prominent quantitative recoveries observed across the ethyl acetate, n-butanol, and the residual aqueous fractions underscore a strong predominance of polar metabolites. This macroscopic distribution pattern aligns directly with the chemical profile of polyhydroxylated phenolic compounds, whose numerous hydroxyl groups and extensive hydrogen-bonding capacity govern their preferential partitioning into polar media, such structural features further corroborated by prominent infrared (IR) spectroscopic signals, notably the broad O-H stretching and aromatic C=C skeletal vibrations [16].

While exhaustive isolation of individual pure phytochemical constituents fell outside the immediate scope of this investigation, we optimized mobile phase systems established via preliminary TLC screening successfully mapped the complex phytochemical distribution of the crude matrix where solvent systems for column chromatography were developed. Typical thin-layer chromatography (TLC) profiles of crude ethanolic extract (A1), ethyl acetate fraction (A2), n-butanol fraction (A3) and commercial tannic acid (A4) are shown (Figure 2).

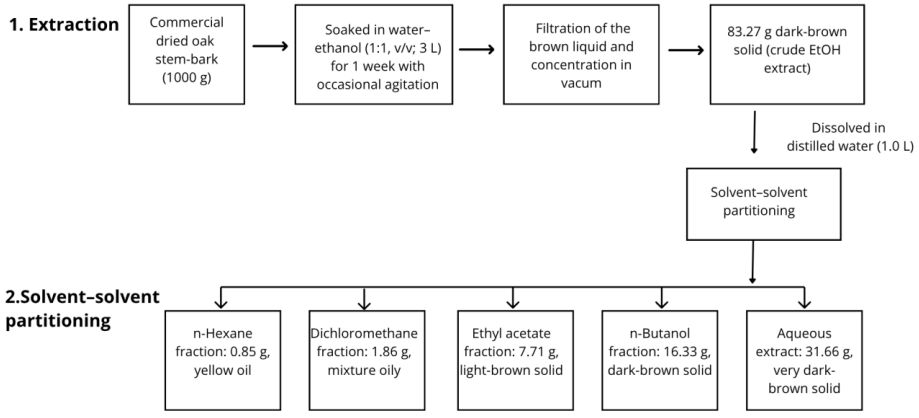

Figure 1. Extraction and Fractionation Scheme of *Quercus robur* Bark

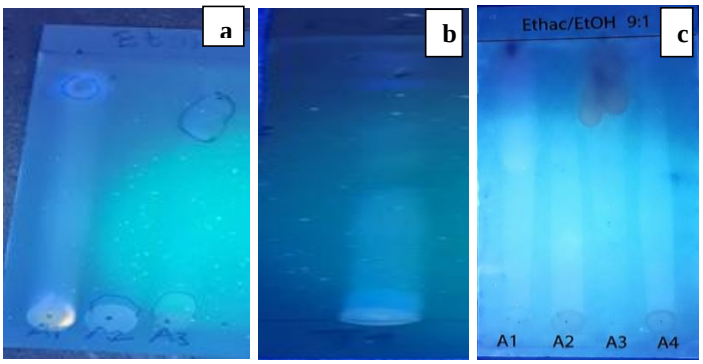

Figure 2. A typical TLC plates used for solvent system development and phytochemical constituents evaluation: Plate (a): crude ethanolic extract (**A1**), ethyl acetate (**A2**), *n*-butanol fraction (**A3**); Plate (b): commercial tannic acid, (TA)); and Plate (c): (**A1**) crude extract, (**A2**) ethyl acetate fraction, (**A3**) *n*-butanol fraction, and (**A4**) commercial tannic acid in ethyl acetate (100 %, volume, plates (a) and (b)); or ethyl acetate-ethanol (9:1, v/v). as mobile phase (plate c).

3.2 Comparative Analysis of FTIR Spectroscopic Studies of Commercial Tannic Acid, Crude Extract and n-Butanol fraction

The FT-IR spectral of the crude ethanolic extract and n-butanol fraction recorded within the 4000-400 cm^{-1} region, exhibits characteristic vibrational frequencies that are comparable to the functional groups observed in the FT-IR spectrum of the commercial tannic acid used as standard. For the commercial tannic acid — chemical structure as shown in Figure 3, and previously reported to be a complex and varying mixture of different gallotannins and simpler galloylglucoses [17]. The broad absorption band observed at 3191.22 cm^{-1} is attributed to the stretching vibration of hydroxyl υ(O–H) groups, indicative of an extensive hydrogen-bonding network within the molecular framework. A very weak band detected at 2890.66 cm^{-1} corresponds to the asymmetric and symmetric stretching vibrations of methylene (CH_2) groups.

The prominent sharp peaks resolved at 1701.96 cm^{-1} and 1697.34 cm^{-1} are assigned to carbonyl υ(C=O) stretching modes associated with the galloyl and ester functionalities. The distinct peak at 1604.66 cm^{-1} peak is characteristic of the skeletal aromatic ring stretching vibration υ(C=C). Furthermore, the absorption band at 1442.83 cm^{-1} is assigned to aromatic methine in-plane bending or skeletal vibrations υ(C–H), while the peak at 1306.98 cm^{-1} corresponds to the symmetric stretching mode of carboxylate υ(–COO–) species. Finally, the intense absorption bands observed at 1174.86 cm^{-1} and 1010.23 cm^{-1} are ascribed to the υ(C–O–C) stretching vibrations of the ester and ether linkages inherent to the pyrogallol and glucose core structures [18]. Additional absorption features resolved at 1081.77 cm^{-1}, 864.33 cm^{-1}, and 753.00 cm^{-1} further corroborate the complex aromatic substitution patterns and out-of-plane (C–H) bending modes of the polyphenol network.

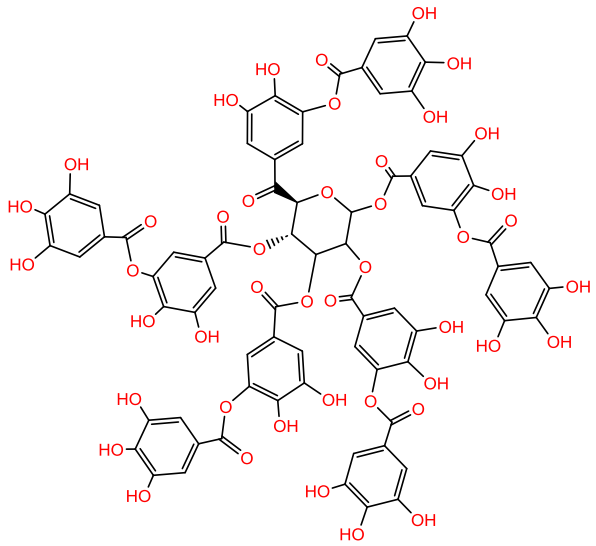

Figure 3. A typical schematic structure of commercial tannic acid used as reference standard

A comparative overlay of the FTIR spectra revealed that the broad ν(O–H) stretching band of reference commercial tannic acid at 3191.22 cm^{-1} shifted to 3246.65 cm^{-1} in the crude ethanolic extract and 3311.53 cm^{-1} in the n-butanol fraction of Quercus robur stem bark (Figures 4 and 5). In contrast, among the three samples, this band was very weak in the crude ethanolic extract, yet mostly pronounced and of the highest intensity in the n-butanol fraction, indicating a potential higher abundance of (O–H) groups. Similarly, prominent υ(C–H) stretching peaks were observed at 2927.62 and 2870.13 cm^{-1} for the n-butanol fraction; whereas a clear band in this region was difficult to resolve in the crude extract. Furthermore, carbonyl υ(C=O) stretching bands were identified at 1706.07 cm^{-1} and 1701.96 cm^{-1} in the crude extract and n-butanol fraction, respectively.

The FT-IR spectra also display key absorption frequencies that closely resemble those of the reference tannic acid. Specifically, the peaks observed at 1609.02 cm^{-1} and 1606.78 cm^{-1} correspond to aromatic υ(C=C) stretching vibrations. This correspondence extends to the band at 1442.83 cm^{-1} υ(C–H) methine bending), the signals at 1330.36 cm^{-1} and 1304.98 cm^{-1} assigned to the symmetric υ(–COO–) stretching), and the ether linkages identified by bands at 1174.86 cm^{-1} and 1010.23 cm^{-1} υ(C–O–C) groups).

It is observed that specific vibrational bands present in the *n*-butanol fraction are absent in the crude extract. This phenomenon is likely due to a combination of concentration effects, the removal of overlapping or masking species, and matrix effects. As bioactive compounds in plant materials exist as complex multicomponent mixtures, their effective separation and characterization often present significant analytical challenges [19, 20]. Furthermore, discrepancies between the n-butanol fraction and the commercial tannic acid spectrum were observed; specifically, certain peaks appearing in the *n*-butanol fraction were absent in the pure tannic acid as reference. This variation is attributed to the presence of co-extracted secondary metabolites within the fraction, which act as impurities relative to the purified commercial standard. Consequently, further purification via column chromatography will be employed to isolate the target constituents.

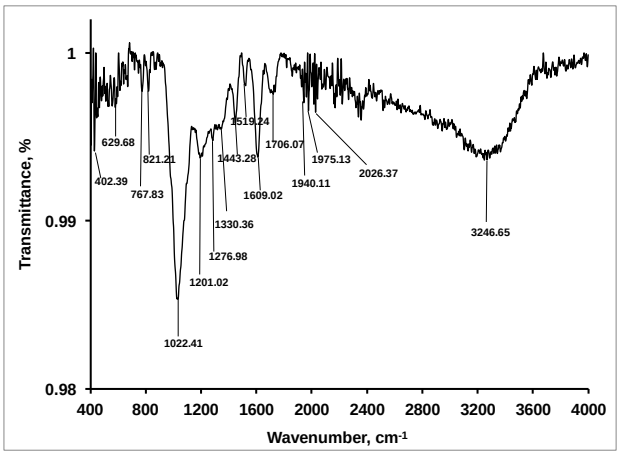

Figure 4. FT-IR of crude ethanolic extract of *Quercus robur*

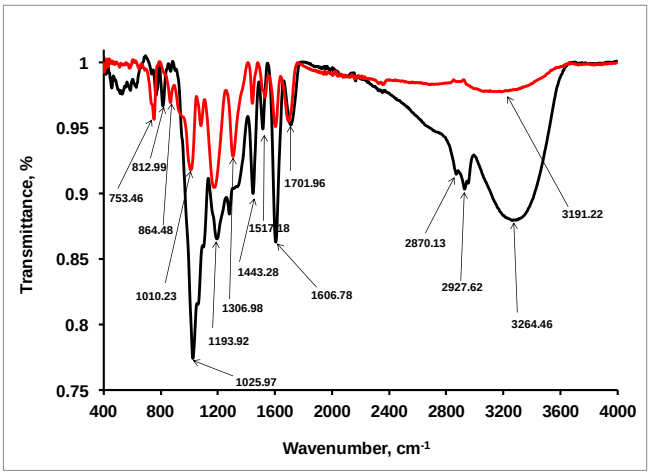

Figure 5. Comparative FT-IR of Commercial Tannic acid and *n*-Butanol fraction

3.3 Quantitative Determination of Tannin Contents by UV-Visible Spectrophotometry

The total tannin content (TTC) of both the crude extract and n-butanol fraction was determined spectrophotometrically and expressed as tannic acid equivalents (TAE) per gram of dry weight. Initially, the TTC of the crude aqueous-ethanol extract of Quercus robur stem bark was calculated as 70.8 mg TAE/g^{-1} of dry weight (7.08 % w/w). After liquid-liquid fractionation of the total crude extract to obtain n-butanol fraction, the resulting fraction was analyzed under previous identical conditions for the crude ethanolic extract. Using the standard calibration curve (A = 0.012C + 0.02) and linearity range (57.3 to 80.8 mg L^{-1}), the measured absorbance (A = 0.87) corresponded to a solution concentration of 70.83 mg L^{-1}. Taking into account the initial sample mass, final volumetric dilution, and dilution factor, the total tannin content (TTC) of the n-butanol fraction was calculated as 225.0 mg TAE g^{-1} dry weight (22.5 % w/w on a dry weight basis). This reflects a successful and approximately threefold enrichment of the active polyphenolic components in the n-butanol fraction compared to the primary crude ethanolic extract. This significant enhancement is fundamentally attributed to selective solvent-solvent partitioning, where polar polyphenolic components (including tannins) are preferentially extracted into the n-butanol fraction while all extraneous, non-active matrix components are separated out.

3.4 Potentiodynamic Polarization Analysis of St3 Steel in 1.0 M HCl

The inhibitory properties of the crude ethanolic extract and the n-butanol fraction of Quercus robur were evaluated using potentiodynamic polarization and compared against commercial tannic acid. Potentiodynamic polarization curves were recorded for both extracts and the reference control in 1.0 M HCl.

Potentiodynamic polarization measurements were conducted to compare the corrosion-inhibition performance of the crude ethanolic extract and the n-butanol fraction of Quercus robur bark against a commercial tannic acid control. As shown in Figures 6-8, the polarization curves enabled comparison of the corrosion-inhibition performance of the investigated samples and assessment of changes in the anodic and cathodic polarization behavior.

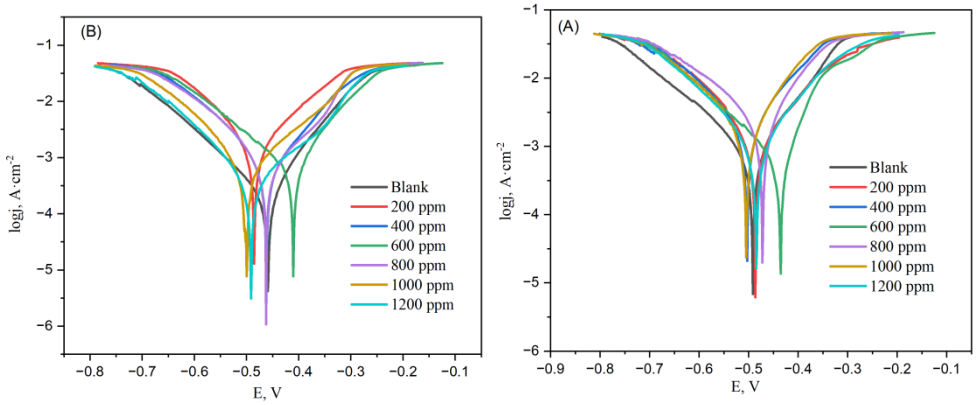

Figure 6. Potentiodynamic polarization curves of mild steel in 1 M HCl solution at different concentrations of the crude ethanolic extract after 0 h (A) and 1 h (B) immersion at 298 K

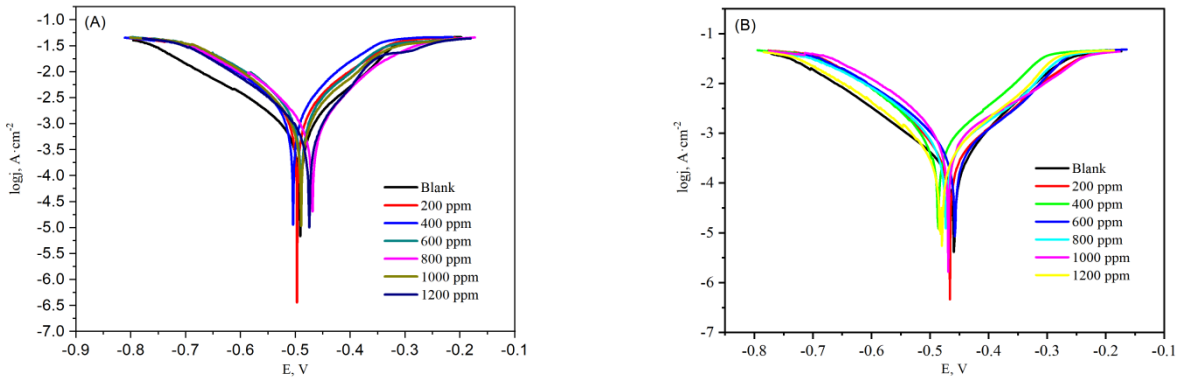

Figure 7. Potentiodynamic polarization curves of mild steel in 1 M HCl solution at different concentrations of the *n*-butanol fraction after 0 h (A) and 1 h (B) immersion at 298 K

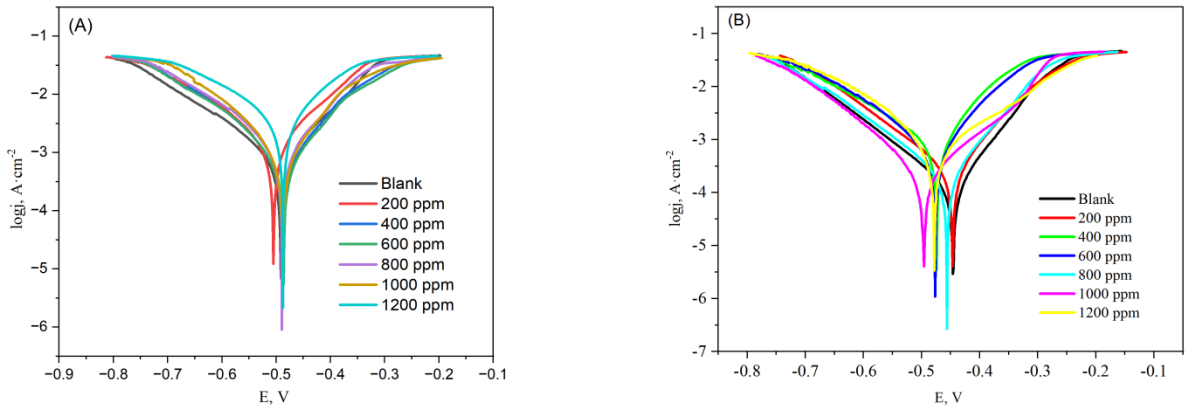

Figure 8. Potentiodynamic polarization curves of mild steel in 1 M HCl solution at different concentrations of commercial tannic acid after 0 h (A) and 1 h (B) immersion at 298 K

A comparative analysis of the potentiodynamic polarization curves revealed that the addition of both the crude ethanolic extract and the *n*-butanol fraction produced changes in both the anodic and cathodic polarization branches, while displacing the corrosion potential (E_{corr}), indicating changes in the electrochemical corrosion behavior. Consequently, the corrosion rate (C_R) decreased while the inhibition efficiency (η) improved across both treatments (Tables 1-6). Although the *n*-butanol fraction elicited a more substantial reduction in corrosion current density than the crude extract, consistent with its higher inhibition efficiency compared with the crude extract, both natural extracts demonstrated a comparatively attenuated inhibitory effect relative to commercial tannic acid, as evidenced by the magnitude of current density reduction and polarization curve displacement.

These observed disparities in inhibitory efficacy are plausibly ascribed to differences in chemical composition and the relative abundance of active constituents contributing to the observed corrosion inhibition behavior. Furthermore, these findings substantiate the capacity of both the crude extract and the *n*-butanol fraction to suppress electrochemical corrosion, underscoring the viability of investigating these botanical extracts as sustainable, eco-friendly corrosion inhibitors.

Table 1

Electrochemical polarization potentiodynamic data for mild steel at different concentrations of crude ethanolic extract, in 1 M HCl, at 298 K, at 0 hour immersion time

C_{inh}, mg L^{-1}	E_{corr}, mV	j_{corr}, μA/cm^2	β_a	β_c	C_R, mm/year	η, %
0	-491.94 ± 2.16	752.52 ± 10.74	148.76 ± 1.80	83.93 ± 2.57	8.74 ± 0.02	
200	-503.78 ± 3.25	850.48 ± 14.23	60.30 ± 1.76	49.24 ± 1.98	9.88 ± 0.01	-
400	-485.52 ± 1.98	695.80 ± 10.92	65.17 ± 1.35	74.10 ± 2.63	8.08 ± 0.02	7.54 ± 0.78
600	-436.68 ± 2.36	673.49 ± 12.67	121.24 ± 1.56	67.77 ± 2.19	7.83 ± 0.03	10.50 ± 0.65
800	-471.46 ± 2.76	619.70 ± 13.02	34.54 ± 1.33	33.85 ± 1.79	7.20 ± 0.03	17.65 ± 0.89
1000	-504.19 ± 1.63	553.87 ± 11.89	32.54 ± 1.89	36.21 ± 2.08	6.62 ± 0.02	26.39 ± 0.90
1200	-484.41 ± 1.85	496.42 ± 10.77	57.46 ± 1.27	37.17 ± 1.65	5.61 ± 0.03	34.03 ± 0.91

Table 2

Electrochemical polarization potentiodynamic data for mild steel at different concentrations of crude ethanolic extract, in 1 M HCl, at 298 K, at 1 hour immersion time

C_{inh}, mg L^{-1}	E_{corr}, mV	j_{corr}, μA/cm^2	β_a	β_c	C_R, mm/year	η, %
0	-458.74 ± 1.86	723.12 ± 12.87	143.75 ± 1.09	135.65 ± 1.87	8.69 ± 0.01	
200	-487.64 ± 2.32	506.98 ± 11.69	34.52 ± 1.67	40.00 ± 2.19	5.89 ± 0.02	29.89 ± 0.74
400	-461.96 ± 3.45	453.57 ± 13.42	63.98 ± 1.84	72.63 ± 2.78	5.27 ± 0.02	37.27 ± 0.86
600	-411.86 ± 1.99	321.88 ± 10.98	46.25 ± 1.49	40.86 ± 2.93	3.74 ± 0.01	55.48 ± 0.91
800	-463.90 ± 2.35	285.95 ± 11.83	42.29 ± 1.78	42.04 ± 1.98	3.32 ± 0.03	60.46 ± 0.87
1000	-502.21 ± 2.78	245.72 ± 11.69	199.88 ± 1.91	27.27 ± 1.84	2.86 ± 0.01	66.02 ± 0.68
1200	-490.21 ± 1.97	203.15 ± 12.86	60.70 ± 1.69	52.44 ± 2.09	2.36 ± 0.03	71.91 ± 0.79

Table 3

Electrochemical polarization potentiodynamic data for mild steel at different concentrations of *n*-BuOH fraction, in 1 M HCl, at 298 K, at 0 hour immersion time

C_{inh}, mg L^{-1}	E_{corr}, mV	j_{corr}, μA/cm^2	β_a	β_c	C_R, mm/year	η, %
0	-491.94 ± 2.16	752.52 ± 10.74	148.76 ± 1.80	83.93 ± 2.57	8.74 ± 0.02	
200	-499.64 ± 1.96	739.66 ± 12.43	50.14 ± 1.43	50.48 ± 1.78	8.59 ± 0.02	1.71 ± 0.76
400	-505.89 ± 2.56	728.30 ± 11.87	54.29 ± 1.56	40.09 ± 1.66	8.46 ± 0.03	3.22 ± 0.84
600	-490.54 ± 2.54	688.75 ± 13.21	44.87 ± 1.67	44.40 ± 2.07	8.00 ± 0.03	8.47 ± 0.59
800	-470.39 ± 1.99	671.38 ± 11.65	80.00 ± 1.75	62.32 ± 1.91	7.80 ± 0.01	10.78 ± 0.92
1000	-489.43 ± 3.14	533.13 ± 12.36	47.01 ± 1.86	41.26 ± 1.77	6.19 ± 0.02	29.15 ± 0.89
1200	-475.58 ± 1.95	479.12 ± 12.86	93.04 ± 1.98	47.15 ± 1.87	5.56 ± 0.02	36.33 ± 0.77

Table 4

Electrochemical polarization potentiodynamic data for mild steel at different concentrations of *n*-BuOH fraction, in 1 M HCl, at 298 K, at 1 hour immersion time

C_{inh}, mg L^{-1}	E_{corr}, mV	j_{corr}, μA/cm^2	β_a	β_c	C_R, mm/year	η, %
0	-458.74 ± 1.86	723.12 ± 12.87	143.75 ± 1.09	135.65 ± 1.87	8.69 ± 0.01	
200	-468.28 ± 1.99	493.82 ± 12.06	142.70 ± 1.86	142.38 ± 1.93	5.73 ± 0.01	31.71 ± 0.74
400	-488.07 ± 2.78	376.70 ± 11.67	88.95 ± 2.31	134.37 ± 1.58	5.53 ± 0.02	47.91 ± 0.86
600	-504.36 ± 1.87	265.04 ± 13.85	83.85 ± 1.73	113.17 ± 1.85	3.08 ± 0.03	63.35 ± 0.91
800	-473.07 ± 3.04	220.12 ± 11.98	37.76 ± 2.34	47.39 ± 1.90	2.56 ± 0.02	69.56 ± 0.78
1000	-470.18 ± 3.46	215.64 ± 12.75	23.64 ± 1.84	35.25 ± 1.88	2.50 ± 0.01	70.17 ± 0.82
1200	-480.58 ± 2.54	148.43 ± 13.09	50.78 ± 1.98	19.52 ± 1.49	1.72 ± 0.02	79.47 ± 0.67

Table 5

Electrochemical polarization potentiodynamic data for mild steel at different concentrations of commercial tannic acid, in 1 M HCl, at 298 K, at 0 hour immersion time

C_{inh}, mg L^{-1}	E_{corr}, mV	j_{corr}, μA/cm^2	β_a	β_c	C_R, mm/year	η, %
0	-491.94 ± 2.16	752.52 ± 10.74	148.76 ± 1.80	83.93 ± 2.57	8.74 ± 0.02	
200	-505.86 ± 2.75	1065.02 ± 15.04	62.50 ± 1.97	50.41 ± 1.98	12.37 ± 0.02	-
400	-488.86 ± 1.97	790.45 ± 12.76	138.38 ± 2.04	106.74 ± 1.85	9.18 ± 0.03	-
600	-487.82 ± 2.67	408.38 ± 11.87	66.78 ± 1.67	65.54 ± 1.76	4.75 ± 0.03	45.73 ± 0.85
800	-489.40 ± 3.09	354.68 ± 13.89	33.46 ± 1.84	33.59 ± 2.12	3.42 ± 0.01	52.87 ± 0.76
1000	-487.86 ± 2.86	211.28 ± 11.67	26.78 ± 1.56	24.46 ± 1.86	2.45 ± 0.02	71.92 ± 0.91
1200	-487.91 ± 1.94	92.87 ± 12.88	6.05 ± 1.95	8.21 ± 1.69	1.07 ± 0.02	87.66 ± 0.87

Table 6

Electrochemical polarization potentiodynamic data for mild steel at different concentrations of commercial tannic acid, in 1 M HCl, at 298 K, at 1 hour immersion time

C_{inh}, mg L^{-1}	E_{corr}, mV	j_{corr}, μA/cm^2	β_a	β_c	C_R, mm/year	η, %
0	-458.74 ± 1.86	723.12 ± 12.87	143.75±1.09	135.65 ± 1.87	8.69 ± 0.01	
200	-459.72 ± 2.05	224.90 ± 13.76	74.52±1.37	60.22 ± 1.65	2.61 ± 0.02	68.89 ± 0.62
400	-425.64 ± 1.98	196.67 ± 12.87	99.23±1.62	70.65 ± 1.50	2.28 ± 0.03	72.80±0.76
600	-451.00 ± 2.67	104.94 ± 14.64	122.75 ± 1.39	83.59 ± 1.47	2.15 ± 0.03	85.45 ± 0.81
800	-441.35 ± 1.83	14.76 ± 1.60	13.69±1.73	13.19 ± 2.61	0.17±0.03	97.95 ± 0.56
1000	-473.16 ± 3.17	12.75 ± 0.99	7.19±2.17	5.78 ± 2.58	0.15±0.02	98.23 ± 0.77
1200	-447.11 ± 2.74	28.72 ± 4.07	4.10±1.89	5.37 ± 1.94	0.33 ± 0.01	96.03 ± 0.85

The influence of exposure duration on corrosion-inhibition efficiency was systematically evaluated. Commercial tannic acid, evaluated as a reference standard, achieved a maximum inhibition efficiency of

98.2 % at 1000 mg L^{-1} after 1 hour of immersion. A further increase in concentration to 1200 mg L^{-1} resulted in a slight decrease in inhibition efficiency to 96.2 %, indicating a non-monotonic concentration response at the highest investigated concentration. The origin of this decrease cannot be determined from the present potentiodynamic polarization data alone.

The *n*-butanol fraction showed higher inhibition efficiency than the crude ethanolic extract under the investigated conditions. At 800 mg L^{-1}, its inhibition efficiency reached 69.5 %, increasing to 79.5 % at 1200 mg L^{-1}. This trend is consistent with the higher tannic-acid-equivalent content measured for the *n*-butanol fraction, although the specific chemical constituents responsible for the improved inhibition performance were not identified in the present study.

Both the crude ethanolic extract and the *n*-butanol fraction showed lower inhibition efficiencies than commercial tannic acid. This difference may reflect differences in chemical composition and the relative abundance of electrochemically active constituents in the investigated samples. However, because the crude extract and the *n*-butanol fraction are complex multicomponent mixtures, the contribution of individual constituents to the observed inhibition behavior cannot be resolved from the present data.

Changes were observed in both the anodic and cathodic branches of the polarization curves for the investigated samples. Together with the relatively small shifts in E_{corr}, not exceeding 85 mV in either direction, these observations support classification of the tannin-containing samples as mixed-type inhibitors. The polarization data therefore indicate an influence on both anodic and cathodic corrosion processes. However, the present measurements do not directly establish the formation of a specific protective adsorption layer, blocking of individual active sites, or changes in elementary electrochemical steps. Such mechanisms may be consistent with previous reports on tannin-containing corrosion inhibitors but would require complementary surface-sensitive or impedance measurements for direct confirmation.

3.5 Adsorption Isotherms

To investigate the concentration-dependent adsorption behavior of the inhibitor species on the mild-steel surface, the apparent surface-coverage data were fitted using the Langmuir, Freundlich, and Temkin adsorption isotherm models [21]. These models were compared using their respective fitting parameters and coefficients of determination (R^2) [22].

The apparent surface coverage (θ) was estimated from the inhibition efficiency obtained after 1 h of immersion in 1 M HCl according to:

$$\theta = \frac{\eta}{100} \tag{3}$$

where η is the inhibition efficiency expressed as a percentage. Because the surface coverage was derived from electrochemical inhibition efficiency rather than measured directly, the calculated θ values are referred to here as apparent surface coverage [21].

The calculated apparent surface coverage generally increased with increasing inhibitor concentration. For commercial tannic acid, θ reached 0.982 at 1000 mg L^{-1}, whereas the corresponding values for the crude ethanolic extract and the n-butanol fraction at 1200 mg L^{-1} were 0.719 and 0.795, respectively.

Table 7

Inhibition efficiency-derived apparent surface coverage values for the crude ethanolic extract, n-BuOH fraction, and commercial tannic acid on mild steel in 1 M HCl at 298 K after 1 h of immersion

C_{inh}, mg L^{-1}	Crude ethanolic extract, θ	*n*-BuOH fraction, θ	Commercial Tannic acid, θ
200	0.299 ± 0.008	0.317 ± 0.007	0.689 ± 0.005
400	0.373 ± 0.004	0.479 ± 0.006	0.728 ± 0.008
600	0.555 ± 0.006	0.633 ± 0.004	0.855 ± 0.004
800	0.605 ± 0.007	0.695 ± 0.003	0.979 ± 0.003
1000	0.660 ± 0.004	0.702 ± 0.008	0.982 ± 0.006
1200	0.719 ± 0.005	0.795 ± 0.006	0.962 ± 0.007

The adsorption data were fitted to the linearized forms of the Langmuir, Freundlich, and Temkin isotherms. The Langmuir model was expressed as [22]:

$$\frac{C}{\theta} = \frac{1}{K_{ads}} + C \tag{4}$$

where C is the inhibitor mass concentration expressed in mg L^{-1}, θ is the apparent surface coverage, and K_{ads} is the apparent mass-based adsorption constant.

The Freundlich isotherm was expressed in its linearized form as:

$$\log\theta = \log K_F + \frac{1}{n}\log C \tag{5}$$

where K_F is the Freundlich adsorption constant and n is the Freundlich heterogeneity parameter.

The Temkin isotherm was expressed in its linearized form as:

$$\theta = B_T \ln A_T + B_T \ln C \tag{6}$$

where A_T is the Temkin equilibrium binding constant and B_T is the Temkin constant related to the variation of adsorption energy.

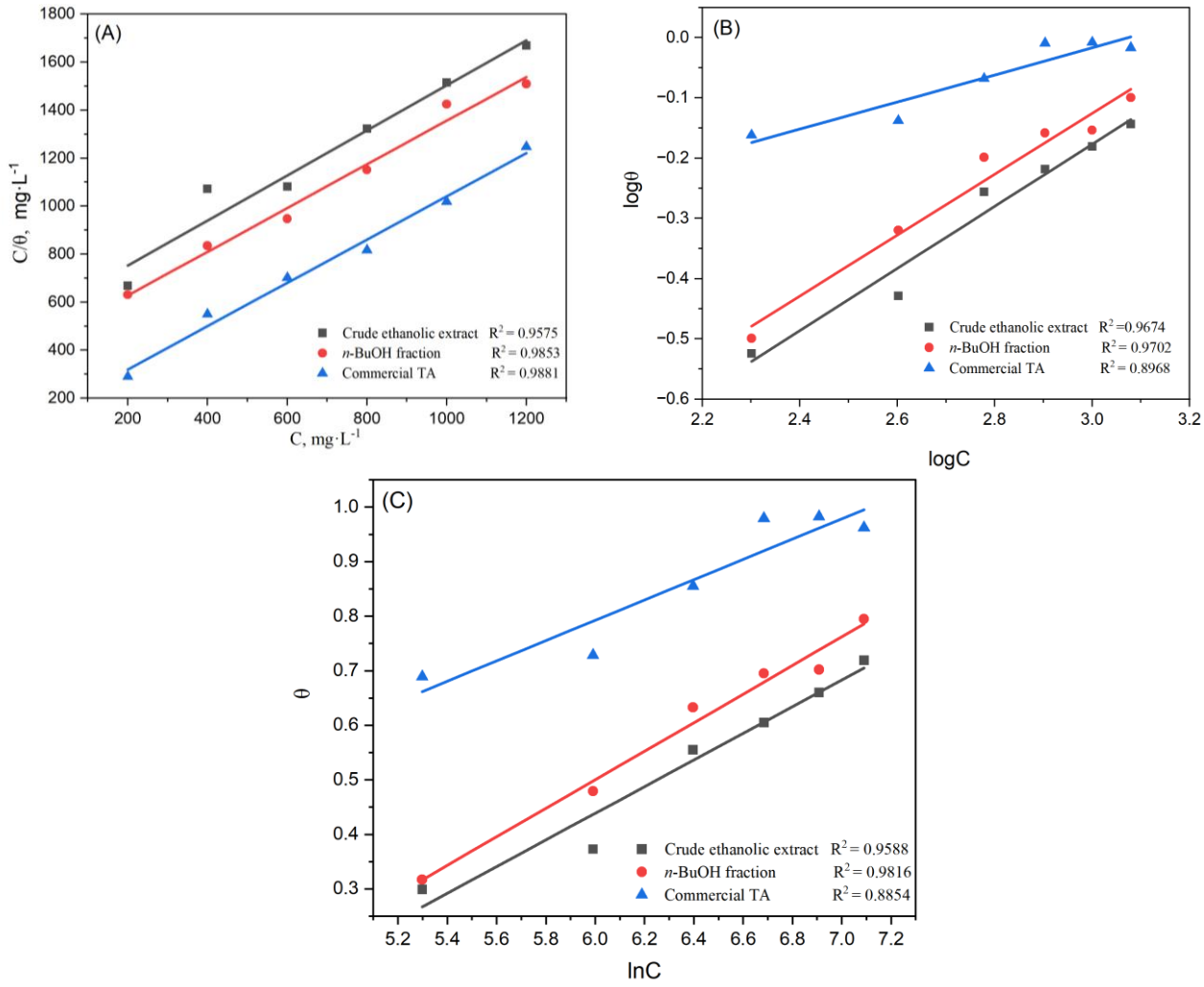

Figure 9. Linearized adsorption-isotherm plots for the crude ethanolic extract, *n*-BuOH fraction, and commercial tannic acid on mild steel in 1 M HCl at 298 K after 1 h of immersion: (A) Langmuir, (B) Freundlich, and (C) Temkin models.

Table 8

Adsorption-isotherm parameters and coefficients of determination (R^2) for the investigated tannin-containing inhibitors on mild steel in 1 M HCl at 298 K

Model	Parameter	Crude extract	n-BuOH fraction	Commercial TA
Langmuir	K_{ads}^{app}, L mg^{-1}	1.77×10^{-3}	2.24×10^{-3}	7.14×10^{-3}
	(R^2)	0.9575	0.9853	0.9881
Freundlich	(K_F)	0.0939	0.0851	0.4736
	(n)	1.78	1.66	2.33
	(R^2)	0.9674	0.9702	0.8968
Temkin	(A_T)	0.0353	0.0389	0.0462
	(B_T)	0.51578	0.50529	0.22492
	(R^2)	0.9588	0.9816	0.8854

Note. All adsorption-isotherm parameters were derived using inhibitor concentrations expressed on a mass-concentration basis (mg L^{-1}). Accordingly, the Langmuir constants are reported as apparent mass-based adsorption constants (K_{ads}^{app}, L mg^{-1}). The Freundlich and Temkin parameters are likewise reported on the same mass-concentration basis and are used primarily for comparison of model fitting.

Comparison of the goodness-of-fit parameters showed that no single adsorption isotherm model provided the best fit for all three investigated samples. For the crude ethanolic extract, the Freundlich model showed the highest coefficient of determination (R^2=0.9674), compared with the Temkin (R^2=0.9588) and Langmuir (R^2=0.9575) models. However, the relatively small differences among the R^2 values indicate that the adsorption behavior of the crude extract cannot be unambiguously assigned to a single model. The slightly better agreement with the Freundlich model may reflect the heterogeneous nature of adsorption from this multicomponent mixture.

For the *n*-BuOH fraction, the Langmuir model provided the highest coefficient of determination (R^2=0.9853), followed closely by the Temkin (R^2=0.9816) and Freundlich (R^2=0.9702) models. For commercial tannic acid, the Langmuir model clearly provided the best fit (R^2=0.9881), whereas considerably lower values were obtained for the Freundlich (R^2=0.8968) and Temkin (R^2=0.8854) models.

Overall, these results indicate that the adsorption behavior depends on the composition of the inhibitor system. Nevertheless, because the surface coverage values were derived from electrochemical inhibition efficiencies rather than measured directly, the adsorption-isotherm fits should be regarded as empirical descriptions of the concentration-dependent inhibition behavior rather than definitive evidence of a particular molecular adsorption mechanism.

The Langmuir adsorption constants presented in Table 8 were derived using inhibitor concentrations expressed on a mass-concentration basis (mg L^{-1}). Accordingly, the obtained constants are reported as apparent mass-based Langmuir adsorption constants (K_{ads}^{app}). The K_{ads}^{app} values were 1.77×10^{-3}, 2.24×10^{-3}, and 7.14×10^{-3} L mg^{-1} for the crude ethanolic extract, the *n*-BuOH fraction, and commercial tannic acid, respectively.

The crude ethanolic extract and the *n*-BuOH fraction are chemically complex mixtures for which a unique molar mass cannot be defined. Therefore, their experimentally applied mass concentrations were not converted to molar concentrations, and molar adsorption equilibrium constants were not calculated for these samples. Consequently, standard Gibbs free energies of adsorption (ΔG_{ads}^{0}) were not calculated for the crude ethanolic extract or the *n*-BuOH fraction. The corresponding Kadsapp values should instead be interpreted as model-dependent, mass-based parameters describing their concentration-dependent adsorption behavior under the investigated conditions.

On the same mass-concentration basis, the *n*-BuOH fraction exhibited a somewhat higher apparent Langmuir adsorption constant than the crude ethanolic extract (2.24×10^{-3} versus 1.77×10^{-3} L mg^{-1}). This observation is consistent with the generally higher inhibition efficiency of the *n*-BuOH fraction. However, the comparison should be interpreted cautiously because both materials are multicomponent mixtures and the Langmuir model was not the best-fitting model for the crude ethanolic extract. Therefore, these mass-based apparent constants should not be interpreted as directly comparable thermodynamic adsorption affinities.

For commercial tannic acid, which was used as the reference material, the mass concentration was additionally converted to molar concentration using the molecular weight of 1701.20 g mol^{-1} specified by the

manufacturer (Sigma-Aldrich). On this basis, the mass-based Langmuir adsorption constant (K_{ads}^{app} =7.14×10^{-3} L mg^{-1}) corresponds to a molar adsorption constant of 1.22×10^{4} L mol^{-1}.

The standard Gibbs free energy of adsorption for commercial tannic acid was calculated according to:

$$\Delta G_{ads}^{0} = -RTln\left(55.5K_{ads}\right) \quad (7)$$

where R is the universal gas constant, T is the absolute temperature (298 K), and 55.5 mol L^{-1} represents the molar concentration of water. The calculated ΔGads◦ value was approximately -33.3 kJ mol^{-1}, indicating that adsorption of commercial tannic acid on the mild-steel surface is thermodynamically favorable under the investigated conditions.

In contrast, ΔG_{ads}^{0} was not calculated for the crude ethanolic extract or the *n*-BuOH fraction because these samples are complex mixtures without uniquely defined molar masses; therefore, conversion of their experimentally applied mass concentrations to a physically meaningful molar concentration would require an arbitrary molecular-weight assumption.

4 Conclusions

This study establishes a streamlined extraction and solvent partitioning protocol for *Quercus robur* bark, yielding a crude ethanolic extract and a polyphenolic-(tannin) enriched *n*-butanol fraction. Rather than pursuing the isolation of individual pure constituents, this is a preliminary approach coupled fractional separation with Fourier-transform infrared (FT-IR) spectroscopic profiling to gain vital insights into the functional chemical features driving the corrosion-inhibition performance.

Potentiodynamic polarization measurements demonstrated that the *n*-butanol fraction exhibited higher corrosion-inhibition efficiency than the crude ethanolic extract under the investigated conditions. After 1 h of immersion, the maximum inhibition efficiency of the *n*-butanol fraction reached 79.5 % at 1200 mg L^{-1}, compared with 71.9 % for the crude extract at the same concentration. Commercial tannic acid showed the highest inhibition performance, reaching 98.2 % at 1000 mg·L^{-1}.

Changes in both the anodic and cathodic polarization branches support the classification of the investigated tannin-containing samples as mixed-type inhibitors under the experimental conditions.

Adsorption-isotherm analysis showed model-dependent behavior. The Freundlich model provided the highest R^2 for the crude ethanolic extract, whereas the Langmuir model provided the highest R^2 for the *n*-butanol fraction and commercial tannic acid. Because the apparent surface coverage was derived from electrochemical inhibition efficiency rather than measured directly, these fits should be regarded as empirical descriptions of the concentration-dependent inhibition behavior rather than direct evidence of a specific molecular adsorption mechanism. For chemically defined commercial tannic acid, the calculated ΔG_{ads}^{0} of approximately –33.3 kJ·mol^{-1} indicated thermodynamically favorable adsorption under the investigated conditions.

Overall, solvent fractionation resulted in an *n*-butanol fraction with higher tannic-acid-equivalent content and improved corrosion-inhibition performance compared with the crude ethanolic extract. However, identification of the individual active constituents and direct elucidation of the surface-inhibition mechanism require further phytochemical characterization and complementary surface-sensitive and electrochemical studies.

Funding

This research has been funded by the Ministry of Science and Higher Education of the Republic of Kazakhstan, Grant No. AP 26102663.

*Author Information**

*The authors' names are presented in the following order: First Name, Middle Name and Last Name

Bibisara Dzhalmukhamedovna Burkitbayeva — Doctor of Chemical Sciences, Professor, Head of Laboratory, Chief Research Scientist, Center of Physical-Chemical Methods of Analysis, Al-Farabi Kazakh National University, 050040, Almaty, Kazakhstan; e-mail: bibisaraburkit@gmail.com; https://orcid.org/0000-0002-9113-4471

Adewale Olufunsho Adeloye — Associate Professor, Al-Farabi Kazakh National University, 050040, Almaty, Kazakhstan; e-mail: adeloye.adewale@kaznu.edu.kz; https://orcid.org/0000-0003-1736-5738

Alfira Farukhovna Miftakhova — Candidate of Chemical Sciences, Senior Lecturer, Al-Farabi Kazakh National University, 050040, Almaty, Kazakhstan; e-mail: alfira.miftakhova1@gmail.com; https://orcid.org/0000-0001-5518-7384

Raigul Zhumakhanovna Jumanova — PhD, Lecturer, Al-Farabi Kazakh National University, 050040, Almaty, Kazakhstan; e-mail: raigul0907@gmail.com; https://orcid.org/0009-0007-7320-3676

Gulmira Sembaykyzy Beisenova (*corresponding author*) — PhD, Senior Lecturer, Al-Farabi Kazakh National University, 050040, Almaty, Kazakhstan; e-mail: beisenova.gumi@gmail.com; https://orcid.org/0000-0002-6751-9451

Akmaral Mukhambetovna Argimbayeva — Candidate of Chemical Sciences, Associate Professor, Head of the Department of Analytical, Colloid Chemistry and Technology of Rare Elements, Al-Farabi Kazakh National University, 050040, Almaty, Kazakhstan; e-mail: akmaral.argimbayeva@gmail.com; https://orcid.org/0000-0002-2467-8241

Gulzhan Seit — 2nd-year Doctoral Student, Al-Farabi Kazakh National University, 050040, Almaty, Kazakhstan; e-mail: gulzhan.seit2024@gmail.com; https://orcid.org/0009-0004-0373-3872

Yeldana Galymzhankyzy Bakhytzhan — PhD, Senior Lecturer, Al-Farabi Kazakh National University, 050040, Almaty, Kazakhstan; e-mail: bakhytzhan.yeldana@gmail.com; https://orcid.org/0000-0002-3217-5927

Aruzhan Bekezhankyzy Smail — 2nd-year Master's Student, Al-Farabi Kazakh National University, 050040, Almaty, Kazakhstan; e-mail: arusmail0807@mail.ru; https://orcid.org/0009-0009-4294-1611

Author Contributions

The manuscript was written through contributions of all authors. All authors have given approval to the final version of the manuscript. CRediT: **Bibisara Dzhalmukhamedovna Burkitbayeva** conceptualization, data curation, investigation, methodology, validation, visualization, writing-review & editing; **Adewale Olufunsho Adeloye** formal analysis, methodology, writing-original draft, writing-review & editing; **Alfira Farukhovna Miftakhova** writing-original draft, investigation, data curation, visualization; **Raigul Zhumakhanovna Jumanova** writing-original draft, investigation, data curation, formal analysis, writing-review & editing; **Gulmira Sembaykyzy Beisenova** supervision, project administration, funding acquisition, resources, writing–review & editing; **Akmaral Mukhambetovna Argimbayeva** investigation, validation, formal analysis; **Gulzhan Seit** investigation, data curation, formal analysis; **Yeldana Galymzhankyzy Bakhytzhan** methodology, resources, validation, visualization; **Aruzhan Bekezhankyzy Smail** investigation, visualization, formal analysis.

References

1 Rahim, A., & Kassim, J. (2008). Recent Development of Vegetal Tannins in Corrosion Protection of Iron and Steel. *Recent Patents on Materials Sciencee, 1(3),* 223-231 https://doi.org/10.2174/1874464810801030223

2 Agi, A., Junin, R., Rasol, M., et al. (2018) Treated *Rhizophora mucronata* tannin as a corrosion inhibitor in chloride solution. *PLoS One, 13(8),* e0200595 https://doi.org/10.1371/journal.pone.0200595

3 Scutareanu, P., & Lingeman, R. (1994). Natural Content of Phenols and Tannin in Quercus Robur Leaves Related to Development of Euproctis Chrysorrhoea Caterpillars. *Acta Horticulturae,* (381), 738–741. https://doi.org/10.17660/actahortic.1994.381.106

4 Ferreira, D., Gross, G.G., Hagerman, A.E., Kolodziej, H., & Yoshida, T. (2008) Tannins and related polyphenols: Perspectives on their chemistry, biology, ecological effects, and human health protection. *Phytochem. 69*, 3006-3008 https://doi.10.1016/j.phytochem.2008.10.018.

5 Gonzalez-Iglesias, D., Rubio, L., Martinez-Vazquez, F., Castillo, A., Celeiro, M., Garcia-Jares, C., Lores, M. (2025). Phytochemical and antioxidant comparison of Quercus ilex and Quercus robur acorn extracts obtained by matrix solid-phase dispersion. *RSC Advances, 15(16),* 12538–12546. https://doi.org/10.1039/d4ra08675a.

6 Qi, C., Li, Z., Bi, H., & Dam-Johansen, K. (2024) Towards sustainable steel corrosion protection: expanding the applicability of natural hydrolyzable tannin in epoxy coatings via metal complexation. *Electrochimica Acta*, *497*, 144546. https://doi.org/10.1016/j.electacta.2024.144546

7 Oki, M., Charles, E., Alaka, C., & Oki, T.K. (2011) Corrosion inhibition of mild steel in hydrochloric acid by tannins from *Rhizophora racemosa*. *Mat. Sci. App*., 02, 592–595 https://doi.10.4236/msa.2011.26079

8 Proença, C.S., Serrano, B., Correia, J., & Araújo, M.E.M. (2022) Evaluation of tannins as potential green corrosion inhibitors of aluminium alloy used in aeronautical industry. *Metals*, *12*, 508. https://doi.org/10.3390/met12030508

9 Qi, C., Li, Z., Bi, H., & Dam-Johansen, K (2024) Towards sustainable steel corrosion protection: Expanding the applicability of natural hydrolyzable tannin in epoxy coatings via metal complexation. *Electrochimica Acta*, *497*, Article 144546. https://doi.org/10.1016/j.electacta.2024.144546

10 Kaco, H., Talib, N.A.A., Zakaria, S., Jaafar, S.N.S., Othman, N.K., Chia, C.H., & Gan, S. (2018) Enhanced corrosion inhibition using purified tannin in HCl medium, *Malaysian J. Anal. Sci*., 22, 931 — 942 https://mjas.analis.com.my/wp-content/uploads/2019/06/22_6_2.html

11 Vorobyova V., Sikorsky O., Skiba M., Vasyliev, G. (2023) Quebracho tannin as corrosion inhibitor in neutral media and novel rust conversion agent for enhanced corrosion protection. *S. Afr. J. Chem. Eng.*, *44*, 68-80 https://doi.org/10.1016/j.sajce.2023.01.003.

12 Dargahi M., Olsson A.L.J., Tufenkji N., Gaudreault R. (2015) Green technology: tannin-based corrosion inhibitor for protection of mild steel. *Corr. Sci.*, *71*, 1321-1329. https://doi.org/10.5006/1777

13 Azmir, J., Zaidul, I. S. M., Rahman, M. M., Sharif, K. M., Mohamed, A., Sahena, F., Jahurul, M. H. A., Ghafoor, K., Norulaini, N. A. N., & Omar, A. K. M. (2013) Techniques for extraction of bioactive compounds from plant materials: A review. *J. Food Eng.*, *117*, 426-436 https://doi.org/10.1016/j.jfoodeng.2013.01.014

14 Awe, E.O., Adeloye, A., Idowu, T., Olajide, O.A., & Makinde J. (2008). Antinociceptive effect of *Russelia equisetiformis* leave extracts: Identification of its active constituents, *Phytomedicine*, *15*, 301–305. https://doi.org/10.1016/j.phymed.2007.03.012

15 Litvinenko, Y. A., Sassykova, L. R., Sassykova, A. R., Konysbayev, A. T., Aitbayeva, R. R., Abildin, T. S., Kanapiyeva, F. M., Zhakirova, N. K., Zhussupova, A. K., Sendilvelan, S., Bhaskar, K., Gomathi, K., & Hua, R. (2026). Elemental composition, heavy metal accumulation and biologically active substances in wild plants of Kazakhstan. *Sci*, *8*(6), Article 123. https://doi.org/10.3390/sci8060123

16 Dai J., Mumper R.J. (2010) Plant phenolics: extraction, analysis and their antioxidant and anticancer properties. *Molecules*, *15*, 7313-7352. https://doi.org/10.3390/molecules15107313

17 Sylla, T., Pouységu, L., Dacosta, G., Deffieux, D., Monti, J. P., & Quideau, S. (2015) Gallotannins and tannic acid: first chemical syntheses and *in-vitro* inhibitory activity on Alzheimer's amyloid β-peptide aggregation. *Angew. Chem., Int. Ed.*, *54*, 8217-8221 https://doi.org/10.1002/anie.201411606

18 Khanbabaee, K., & van Ree, T (2001) Tannins: Classification and definition. Natural Product Reports, 18(6), 641–649. https://doi.org/10.1039/b101061l

19 Chua, L.S., Lau, C.H., Chew, C.Y., Dawood, D.A.S. (2019) Solvent fractionation and acetone precipitation for crude saponins from *Eurycoma longifolia* extract. *Molecules, 24*, 1416. https://doi.org/10.3390/molecules24071416

20 Vargas-Ramella, M., Ely, J., Favaro-Trindade, C.S., Alves dos Santos, B., Campagnol, P.C.B., Lorenzo, J.M. (2026) Analytical characterization and quantification of plant-derived antioxidants focusing on methods, limitations, and data comparability. *Food Anal. Met*., *19*, 162. https://doi.org/10.1007/s12161-026-03075-y

21 Abeng, F.E., Oji, N.N., Osuwa, K.A. et al. (2026) Thermodynamic study and adsorption characteristics of mild steel corrosion inhibition in 0.1 M solution by orange peels (*Citrus sinensis*). *Discov. Chem*., *3*, 81. https://doi.org/10.1007/s44371-026-00546-3

22 Akinbulumo, O. A., Odejobi, O. J., & Odekanle, E. L. (2020). Thermodynamics and adsorption study of the corrosion inhibition of mild steel by Euphorbia heterophylla L. extract in 1.5 M HCl. Results in Materials, 5, 100074. https://doi.org/10.1016/j.rinma.2020.100074